

Reconstructing Biogeochemical Cycles During and After the Late Ediacaran DOUNCE/Shuram Excursion

Zheyu Tian



A dissertation submitted to University College London in accordance with the requirements for award of the degree of Doctor of Philosophy in the Faculty of Science

Department of Earth Sciences
Date of Submission: December 19, 2021

Author's Declaration

I, Zheyu Tian, confirm that the work presented in this thesis is my own. Where information has been derived from other sources, I confirm that this has been indicated in the thesis.

ZHEYU TIAN

December 19, 2021

Abstract

In this thesis, I made carbon, oxygen, and sulfur chemostratigraphic study of three representative sections in South China (Lianghong, Sishang and Qinglinkou sections). These data confirm that the DOUNCE/Shuram (EN4) was a basin-wide event; Data from the Qinglinkou section also confirm the other negative excursions (EN1=CANCE, EN2=WANCE, EN3=BAINCE).

Field observations and C isotope data from the Qinglinkou section suggest that the ‘middle carbonate’ unit, which occurs between two black shale layers of the upper Doushantuo Formation, corresponds to a slumped unit that likely derives from the overlying Hamajing Member (Lower Dengying Formation).

I designed and compared three Carbonate-associated sulfate (CAS) extraction methods to minimize the influence caused by contaminants. My results suggest that a sequential NaOCl, H₂O₂, and NaCl pre-leaching method is most effective for eliminating contaminants. For purer carbonate samples, more traditional sequential leaching of NaCl and DI water should be sufficient.

My CAS data illustrates that sulfate $\delta^{34}\text{S}$ (~21‰), $\Delta\delta^{34}\text{S}_{\text{sulfate-sulfide}}$ (~30‰) and estimated seawater sulfate concentrations (~29mM) show similar values to modern levels during the DOUNCE/Shuram. However, after the DOUNCE/Shuram, the sulfate reservoir shrank to pre-excursion levels (as low as 0.6 mM), influencing the S cycling pathways and resulting in a decoupled C-S isotope trend. The seawater $^{87}\text{Sr}/^{86}\text{Sr}$ during the DOUNCE/Shuram suggests high continental weathering during that interval, which would have contributed to elevated nutrient, Fe, and sulfate fluxes into the ocean. In summary, my work shows how global tectonic forces might have driven the DOUNCE/Shuram.

I also analyzed the representative samples for U isotope and redox-sensitive trace elements (RSTE), e.g., U, Mo, V, concentrations. Overall, the data reveal a pulsed oxygenation history in late Ediacaran and indicate that the DOUNCE/Shuram interval is not a simple oxygenation event. Moreover, a final oxygenation event of the late Ediacaran was recognized that might directly link with the ‘Cambrian Explosion’.

Impact Statement

Firstly, this PhD thesis's main beneficiaries are Earth scientists especially interested in understanding the 'co-evolved' environment and life in Earth history. My work covers a wide range of disciplines: sedimentology, geochemistry, structural geology, paleobiology, tectonics, geology.

In particular, my lab experiments on CAS extraction methods built up a robust protocol to eliminate contaminant sulfur and help better reconstruct the paleo sulfur cycle. This work has been submitted to *Chemical Geology*. Each main chapter will be one paper that is currently in preparation for publication. The work presented in Chapter 6 has been presented at the internationally regarded Goldschmidt conference. The field observations, measurements, and laboratory experiments in this thesis reveal the possible links between life evolution and the changing of the surface system ~500 million years ago. In the ancient past, our planet experienced huge changes, including climate change, oxygen level change, tectonic activities, and volcanism, which closely influenced the life living on it. The past can be a mirror of the future. Furthering our understanding of the paleo world not only solves some existing scientific problems but may also provide new insight into the modern or future Earth system and how environmental changes will influence human beings.

Secondly, non-academic beneficiaries of this research include:

1. This study includes collaborating with scientists in China and so may help foster improved relationships between the UK and China. People may gain better knowledge of each other's cultures and ways of thinking, leading to less conflict and misunderstandings between the two countries.
2. This work refreshes people's conception of how important it is to protect our environment. To protect the environment is to protect us all.
3. My work might change our understanding of Earth history and might help inspire more people into Earth Sciences.

I dedicate this thesis to my parents in China.

Acknowledgments

Four years PhD journey comes to an end. Throughout the whole journey, I have learned a lot and experienced a lot. This unforgettable memory will always be my treasure for the rest of my life.

I would like to firstly thank my supervisors Prof. Graham A. Shields and Dr. Ying Zhou, who has given me so much help in academics and life. I have experienced confusion and self-doubt, but they always gave me trust, support and led me through the fog.

I would also thank all the people who have helped me during this long journey. A special thanks to Prof. Maoyan Zhu and Dr. Miao Lu, who shared the samples and data with me. Without their help, this research could not have been finished. Other special thanks to Prof. Chao Li and Dr. Wei Shi for their support for my fieldwork in Hubei Province. The lab works benefited from the help provided by Dr. Anirban Basu, Dr. Alexander Dickson, Dr. Aubrey Zerkle, Gary Tarbuck, Jim Davy. Other supports were provided by Dr. Fred Bowyer, Dr. Tianchen He, Dr. Weiqi Yao, Dr. Huan Cui, Dr. Fuencisla Canadas, Dr. Colin Mettam, Dr. Philip Pogge von Strandmann, Dr. Anne-Lise Jourdan. I also want to thank my friends Liangxuan Jiao, Guang Ouyang, Xi Chen, Kun Zhang, and all the roommates in the last four years.

I would thank the China Scholarships Council (CSC)-UCL studentship award for supporting my cost in the last four years. And finally, I want to thank my parents, who always have the trust and unconditional support.

When I look back, all the memory still be vivid as they happened yesterday. At the end of this journey, it is time to pack up again and start a new adventure. I would like to commemorate this journey with a small poem written by myself.

The wind

You

Like the wind,

Blew my hair,

Strong and cool.

When you are back,

I know it's not you anymore,

Soft and warm.

Table of Contents

Author's Declaration	2
Abstract	3
Impact Statement	4
Acknowledgments	6
Glossary of Common Abbreviations	10
List of Figures	12
List of Tables	20
Chapter 1 Introduction	21
1.1 Overview of the Project	21
1.2 Late Ediacaran Biological Evolution	23
1.3 Neoproterozoic Oxygenation Event (NOE)	26
1.4 Carbon Isotopes	27
1.5 Sulfur Isotopes	31
1.6 Uranium Isotopes.....	33
1.7 Redox Sensitive Trace Elements.....	34
1.8 Late Ediacaran DOUNCE/Shuram Excursion and Its Aftermath.....	36
1.9 Global Correlation.....	39
1.10 Research Aims	40
Chapter 2 Geological Background and Sample Locations	41
2.1 Paleogeographic Setting of South China Block	41
2.2 Tectonic Settings	41
2.3 Ediacaran Stratigraphy in South China	42
2.4 Studied Sections	45
2.4.1 Lianghong Section	46
2.4.2 Sishang Section	47
2.4.3 Qinglinkou Section	49
2.4.4 The Age Framework of the Ediacaran Excursions in South China	50
Chapter 3 Chemostratigraphy of the Qinglinkou Section, compared with the Lianghong and Sishang Section	52
Abstract	52
3.1 Introduction	53
3.2 Geological Background	54
3.2.1 Geological Background of the Yangzi Gorges Area	54
3.2.2 Qinglinkou Section	56
3.3 Methods.....	60
3.4 Results	61
3.4.1 Petrography of the Samples.....	61
3.4.1.1 Lianghong Section	61
3.4.1.2 Sishang Section	61
3.4.1.3 Qinglinkou Section	63
3.4.2 Carbon, Oxygen Isotope and Elemental Data.....	65
3.4.2.1 Lianghong Section	65
3.4.2.2 Sishang Section	67

3.4.2.3	Qinglinkou Section.....	69
3.5	Discussion	72
3.5.1	The Wide Occurrence of Faults/slumps and Folds.....	72
3.5.2	Petrographic Correlation of the Middle Carbonate.....	75
3.5.3	Chemostratigraphic Correlation	76
3.5.3.1	Diagenetic Evaluation.....	76
3.5.3.2	C-isotope Chemostratigraphy	78
3.5.3.3	Elemental Correlation	82
3.6	Conclusions.....	83
Chapter 4 Large-scale Slumping in the Western Region of the Huangling Anticline Area, South China.....		84
	Abstract.....	84
4.1	Introduction	85
4.2	Geological Background	86
4.3	Stratigraphic Correlation of the Surrounding Sections	87
4.4	The Existence of the ‘Mirror plane’ at the Qinglinkou Section	88
4.5	Chemostratigraphic Correlation	91
4.6	Slide Dimensions and Paleogeographic Recovery	94
4.7	Possible Evolution History	96
4.8	Future Plans for Developing the Models.....	101
4.9	Conclusions.....	101
Chapter 5 Experimental Comparisons of Carbonate-associated Sulfate Extraction Methods.....		102
	Abstract.....	102
5.1	Introduction	103
5.2	Sample Selection, Pre-treatment, and Analytical Methodology	105
5.3	Refined NaCl Leaching Method (method 1)	107
5.4	Three Newly Designed Methods.....	108
5.4.1	H ₂ O ₂ and NaOCl Leaching (methods 2a and 2b).....	108
5.4.2	Combined NaOCl-H ₂ O ₂ Leaching (method 3).....	109
5.5	Results.....	110
5.6	Discussion	112
5.6.1	Diagenetic Evaluation.....	112
5.6.2	Evaluation of the Three New Methods	113
5.6.3	Contaminant Sulfur Evaluation.....	115
5.6.4	Comparing the New Data with Published CAS Data.....	118
5.6.5	Rethinking the ‘Superheavy Pyrite’	120
5.7	Conclusions.....	122
Chapter 6 Reconstructing the Late Ediacaran Sulfur Cycle Using New Data from South China		123
	Abstract.....	123
6.1	Introduction	124
6.2	Methods	125
6.3	Results.....	126
6.3.1	CAS Concentration-[CAS].....	126
6.3.2	CAS Sulfur Isotope Values ($\delta^{34}\text{S}_{\text{CAS}}$).....	126

6.3.3	Correlation with Carbon Isotope Data.....	127
6.3.4	Diagenetic Evaluation	129
6.4	Discussion.....	132
6.4.1	Estimation of Seawater Sulfate Concentration-‘Rate method’ Model	132
6.4.2	Underestimated Seawater Sulfate Concentration in the Late Ediacaran	134
6.4.3	Tectonic Controls on the DOUNCE/Shuram.....	139
6.4.4	Carbon and Sulfur Cycling before and during the DOUNCE/Shuram	140
6.4.5	Carbon and Sulfur Cycling after the DOUNCE/Shuram.....	142
6.4.6	Global Correlation and S Isotope Chemostratigraphy	144
6.5	Conclusions	147
Chapter 7	Marine Redox Oscillations during the Late Ediacaran	148
	Abstract	148
7.1	Introduction	149
7.2	Redox Proxies Background.....	151
7.3	Methods.....	151
7.3.1	Trace Elements	151
7.3.2	Uranium Isotopes	151
7.3.3	The LOWESS Fit	152
7.4	Results	152
7.4.1	Redox Sensitive Trace Elements (RSTE).....	152
7.4.2	Uranium Isotopes	155
7.5	Discussion.....	157
7.5.1	Diagenetic Evaluation	157
7.5.2	Ocean Redox Oscillations during the DOUNCE/Shuram.....	159
7.5.3	Ocean Redox Oscillations after the DOUNCE/Shuram	162
7.5.4	Global Ocean Paleo-redox Shifts and Life Evolutions	164
7.6	Conclusions	166
Chapter 8	Towards a Conceptual Model of Ocean Evolution through the	
	DOUNCE/Shuram Interval.....	167
8.1	Pre-DOUNCE/Shuram Period (EP3)	167
8.2	Onset Period of the DOUNCE/Shuram (EN4a)	168
8.3	During the DOUNCE/Shuram (EN4b)	169
8.4	The Recovery Period of the DOUNCE/Shuram (EN4c)	170
8.5	The DOUNCE/Shuram Aftermath (EP4a).....	171
8.6	The DOUNCE/Shuram Aftermath (EP4b).....	171
Chapter 9	Conclusions and Future Work.....	173
9.1	Conclusions	173
9.2	Future Studies	177
	REFERENCES	178
	APPENDIX A: ROCK DESCRIPTIONS.....	202
	APPENDIX B: RAW DATA FROM ICP-OES TEST.....	208
	APPENDIX C: RAW DATA FROM ICP-MS TEST.....	223
	APPENDIX D: CARBON, OXYGEN, SULFUR, URANIUM ISOTOPES	
	DATA.....	238

Glossary of Common Abbreviations

BSR	Bacterial Sulfate Reduction
MSR	Microbial Sulfate Reduction
TSR	Thermochemical Sulfate Reduction
DOC	Dissolved Organic Carbon
DOM	Dissolved Organic Matter
CAS	Carbonate Associate Sulfate
[CAS]	Carbonate Associate Sulfate Concentration
GYP	Gypsum
PY	Pyrite
ICP-MS	Inductively Coupled Optical Emission Spectrometry
ICP-OES	Inductively Coupled Plasma Optical Emission Spectrometer
LOGIC	London Geochemistry & Isotope Centre
Ma/Myr	Million years
NIGPAS	Nanjing Institute of Geology and Palaeontology, Chinese Academy of Sciences
PPL	Plane-polarized Light
XPL	Cross-polarized Light
RL	Reflected Light
REY	Rare Earth Elements and Yttrium
SAS	Secondary Atmospheric Sulfate
SW	Seawater
SCB	South China Block
$\delta^{13}\text{C}$	Ratio of Heavy (^{13}C) to Light (^{12}C) Stable Carbon Isotope
$\delta^{34}\text{S}$	Ratio of Heavy (^{34}S) to Light (^{32}S) Stable Sulfur Isotope
$\Delta^{34}\text{S}_{\text{SW-PY}}$	Difference in Isotopic Composition of Seawater Sulphate and Coeval Pyrite
Ce/Ce*	Cerium anomaly
DOUNCE	Doushantuo negative carbon isotope excursion
BAINCE	Baiguoyuan negative carbon isotope excursion
WANCE	Weng'an negative carbon isotope excursion
CANCE	Cap carbonate negative carbon isotope excursion
PAL	Present Atmospheric Level

DST	Doushantuo Formation
DY	Dengying Formation
HMJ	Hamajing Member
SBT	Shibantan Member
BMT	Baimatuo Member
SMTZ	Sulfate-methane Transition Zone
DI water	Deionized water

List of Figures

- Fig. 1. 1 A summary photo of the typical fossils of each biota in Ediacaran in South China. A: Algal fossil from the Lantian biota (Yuan et al., 2012); B: Scanning electron microscope images from the Weng'an biota: (1) *Eocyathispongia*, a putative sponge; (2) *Tianzhushania*, in division stage (Cunningham et al., 2017). C: *Eoandromeda octobrachiata* from the Miaohu & Wenghui biota (Zhu et al., 2008; Xiao et al., 2013). D: *Vendotaenia pavimentipes* and the restored picture from the Shibantan biota (Yang et al., 2018). E: (3) Fossil record of coiling and phototaxis from the Gaojiashan biota: (1) Magnified photo of 3; (2) Trail pattern of *Dictyostelium discoideum* slugs with fruiting bodies (Zhuravlev et al., 2009). 25
- Fig. 1. 2 The evolution history of Earth's atmospheric oxygen content. The shaded red zone is my study period. The top figure summarizes carbon (black) and multiple sulfur (grey and red) isotope data in earth history. Modified from (Lyons et al., 2014). 27
- Fig. 1. 3 Schematic diagram shows the long-term carbon cycle with each flux's average carbon isotope compositions during the Phanerozoic. From (Kump and Arthur, 1999). 29
- Fig. 1. 4 A box model of the long-term carbon cycle. From (Berner, 1999). 29
- Fig. 1. 5 Long-term carbon isotope mass balance. Modified from (Shields, 2017). The red arrow starts from 1 to 2 means the steady-state changes from 1 to 2. 30
- Fig. 1. 6 Biochemical isotope fractionation processes in an open system show that with the help of sulfide oxidation and disproportionation, sulfides can be more depleted in ^{34}S than the single sulfate reduction process. Modified from (Canfield and Thamdrup, 1994). 32
- Fig. 1. 7 A simple diagram showing the marine sulfur cycle and the main control fluxes. The blue arrows show the sulfur input fluxes, whereas the black arrows represent the output fluxes. The thickness of the arrows represents the relative proportion of each flux. Flux and isotopic parameters from (Canfield, 2004; Bottrell and Newton, 2006; Fike et al., 2015). 33
- Fig. 1. 8 Modern uranium budget and major ^{238}U fluxes to the ocean. From (Lau et al., 2019). 34
- Fig. 1. 9 Ediacaran and Cambrian stratigraphy, fossil records, life evolution history of South China. From (Zhu and Li, 2017). 1. bedded cherts; 2. black shale; 3. silty shale; 4. siltstone; 5. sandstone; 6. thick-bedded and massive dolostone; 7. thin- or medium-bedded dolostone; 8. limestone; 9. phosphorite; 10. phosphatic nodules. 38
- Fig. 1. 10 Comparison of the $\delta^{13}\text{C}$ record of the DOUNCE/Shuram with other parts of the world. From (Lu et al., 2013). Yellow = dolostone; Blue = limestone. 39
- Fig. 2. 1 Paleogeographic reconstruction of the SCB, India, Australian blocks, East Antarctica, and Tarim at ca. 570-560 Ma (a) and ca. 505Ma. From (Zhang et al., 2015). 41
- Fig. 2. 2 Stratigraphic column, carbon, strontium, and oxygen isotope data of the Ediacaran Doushantuo and Dengying Formations from the Jiulongwan-Shipai section in the Yangtze Gorges area. From (Jiang et al., 2007). 44
- Fig. 2. 3 Simplified geological map and paleogeographic reconstruction of South China Block. Modified from (Lu et al., 2013; Cui et al., 2016b; Lan et al., 2019). The red star shows the location of the three sections (Lianghong, Sishang, and Qinglinkou section) in this study. 45
- Fig. 2. 4 Simplified geological map shows the location of the Lianghong section and adjacent terranes. Pt₂ Mesoproterozoic, Pt₃ Neoproterozoic. 46

- Fig. 2. 5 Stratigraphic column of the Lianghong section and $\delta^{13}\text{C}$ (‰, VPDB) and $\delta^{18}\text{O}$ (‰, VPDB). Modified from (Lu et al., 2013). A: Banded limestone; B: Edgewise limestone; C: a sequence boundary with the lithological transition from thick-bedded dolostone to thin-bedded dolomitic limestone at the basal part of the DOUNCE. The yellow arrows point to the samples at the lower part. 47
- Fig. 2. 6 Simplified geological map showing the location of the Sishang section and adjacent terranes. 48
- Fig. 2. 7 Stratigraphic column of the Sishang section and $\delta^{13}\text{C}$ (‰, VPDB) and $\delta^{18}\text{O}$ (‰, VPDB) profiles. Modified from (Lu et al., 2013). A: thin-bedded dolomitic limestone; B and C: thin-bedded limestone; D: the sequence boundary (dashed line) at the base of the DOUNCE in the section. The coin is 25 mm, and the hammer is 32 cm. 48
- Fig. 2. 8 Simplified geological map showing the location of the Qinglinkou section and adjacent terranes. 49
- Fig. 2. 9 The comparison of the time model of the Ediacaran period around the world. Modified from (Yang et al., 2016). Published ages in South China are from (Condon et al., 2005; Zhu et al., 2007; Narbonne, 2011; Wang et al., 2012c; An et al., 2015; Yang et al., 2016; Gong et al., 2017; Zhou et al., 2017a; Huang et al., 2020); Data in Oman are from (Bowring et al., 2007; Rooney et al., 2020); Data in Namibia are from (Grotzinger et al., 1995; Bowring et al., 2007; Wood et al., 2015; Linnemann et al., 2019); Data in South Australia are from (Ireland et al., 1998; Minguez and Kodama, 2017; Williams and Schmidt, 2018). 51
- Fig. 3. 1 Geological map of the Yangtze Gorges area shows the Qinglinkou section's location and other sections in the Huangling Anticline area. Two dashed lines divide the Huangling area into three regions. Modified from (An et al., 2015; Zhou et al., 2017b). 56
- Fig. 3. 2 Outcrop photo showing the deformed contact between the overlying shale II and underlying middle carbonate. Large carbonate concretions occur within the upper shale II layers. 58
- Fig. 3. 3 Outcrop photo showing the folded layers within the Hamajing Member and conformable contact between the upper and lower layers at the Qinglinkou section. 58
- Fig. 3. 4 Stratigraphic column and outcrop photograph of the Qinglinkou Section. A: Nantuo diamictite. B: 4m thick Doushantuo I cap carbonate. C: lower Doushantuo II thin-bedded carbonate layer interbedded with chert bands. D: middle Doushantuo II medium-thin carbonate layer interbedded with black shale layers. E: Doushantuo III medium-thick dolostone. F: the boundary between the shale I and middle carbonate. G: the boundary between upper black shale II and Dengying Hamajing dolostone. (Carbonate concretions bedded in the shale II layers). H: bottom Shibantan thin-bedded limestone with siliceous concretions. I: lower Shibantan dark grey limestone. J: upper Shibantan light grey limestone with calcite veins cut through. The red curve line represents the slumping surface... 59
- Fig. 3. 5 Representative samples and their microphotographs from the Lianghong section. A, C: Fine-grained limestone; B: Fine-grained dolostone with relatively large calcite grains; D: Fine-grained laminated dolostone with large calcite grains. E: Fine-grained dolostone. 61
- Fig. 3. 6 Representative samples and their microphotographs from the Sishang section, the dominant rock type here is laminated limestone. A: Laminated medium-grained limestone with calcite grains and organics (Sample number is 16MJW61.7, $\delta^{13}\text{C}_{\text{carb}} = 1.09\text{‰}$ and $\delta^{18}\text{O}_{\text{carb}} = -5.86\text{‰}$); B: Fine-grained limestone (Sample number is 16MJW40); C: Fine-grained laminated limestone with relatively high pyrite density (Sample number is 16MJW29.5, $\delta^{13}\text{C}_{\text{carb}} = -8.04\text{‰}$ and $\delta^{18}\text{O}_{\text{carb}} = -9.00\text{‰}$); D: Fine-grained laminated limestone, rich with organics

- (Sample number is 16MJW11, $\delta^{13}\text{C}_{\text{carb}} = -9.03\text{‰}$ and $\delta^{18}\text{O}_{\text{carb}} = -10.56\text{‰}$); E: Fine-grained limestone (Sample number is 16ss-96, $\delta^{13}\text{C}_{\text{carb}} = -6.20\text{‰}$ and $\delta^{18}\text{O}_{\text{carb}} = -5.49\text{‰}$)..... 62
- Fig. 3. 7 Typical rock samples and their microphotographs from the Qinglinkou section. (A-C): Dark limestone sample Q178 from the Dengying Shibantan Member, stratigraphic height 199.1m; (D-F): Recrystallized dolostone sample Q174 from the Dengying Hamajing Member, stratigraphic height 194m; (G-I): Shale II sample Q161, stratigraphic height 176.9m. Note the carbonate minerals occupy near 30% of the sample; (J-L): Recrystallized dolostone sample Q154 from middle carbonate unit in between two black shale layers at the Qinglinkou section, stratigraphic height 157.8m; (M-O): Fine-grained dolostone sample Q149 from the Doushantuo Member III, stratigraphic height 145.6m. Cal=Calcite, Py=Pyrite, XPL=cross-polarized light, RL=reflected light. 64
- Fig. 3. 8 Lithostratigraphy, $\delta^{13}\text{C}_{\text{carb}}$, $\delta^{18}\text{O}_{\text{carb}}$, and elemental profiles of the Doushantuo and Dengying Formation at the Lianghong section. Shaded symbols in the C-O isotope profile represent the carbon isotope value, and unshaded symbols represent the oxygen isotope value. C-O isotope data were from (Lu et al., 2013). 66
- Fig. 3. 9 Lithostratigraphy, $\delta^{13}\text{C}_{\text{carb}}$, $\delta^{18}\text{O}_{\text{carb}}$, and elemental profiles of the Doushantuo and Dengying Formation in the Sishang section. Shaded symbols in the C-O isotope profile represent the carbon isotope value, and unshaded symbols represent the oxygen isotope value. C-O data were from (Lu et al., 2013)..... 68
- Fig. 3. 10 Lithostratigraphy, $\delta^{13}\text{C}_{\text{carb}}$, $\delta^{18}\text{O}_{\text{carb}}$, and elemental profiles of the Doushantuo and Dengying Formation at the Qinglinkou section. EN=Ediacaran negative excursion, EP=Ediacaran positive excursion, HMJ=Hamajing Member, BMT=Baimatuo Member. DOUNCE=Doushantuo negative carbon isotope excursion. BAINCE=Baiguoyuan negative carbon isotope excursion. WANCE=Weng'an negative carbon isotope excursion. CANCE=Cap carbonate negative carbon isotope excursion. 71
- Fig. 3. 11 Outcrop photos, structural analysis, and the sketch cross-section graph of the Qinglinkou section. A: normal fault cut the lower Doushantuo Member I (View towards: 339°); B: Z-folds formed by flexural slip during the formation of Huangling Anticline and lower equal-area hemisphere projection of the fold data. The green arrow shows the direction of the main stress σ_1 is NE-SW (View towards: 335°). C: 'S' shape slumping surface showing the upper Doushantuo III layers are disrupted and the lower part laminated (View towards: 335°). D: location shows the occurrence of the first black shale layer (30-60cm), which is not consistent with the upper and lower layers (View towards: 342°). E: location shows the second black shale layer is thicker (18.1m) than the lower one and contains laminated carbonate concretions (View towards: 339°). The red curve lines represent the slumping surface or faults. 74
- Fig. 3. 12 Microscopic photographs comparison of the samples from Doushantuo Member III, middle carbonate, and Hamajing Member. A: fine-crystalline dolomite sample from the upper part of the Doushantuo Member III. B: medium-crystalline dolomite with large calcite grains. C: fine-crystalline dolomite with calcite vein. D: fine-crystalline dolomite from the bottom of the Doushantuo Member III. E: fine-crystalline dolomite from the upper part of the middle carbonate (grain size, ~5-22 μm). F: partial recrystallized medium-crystalline dolomite with a calcite vein. G-H: highly recrystallized saddle dolomite from the bottom of the middle carbonate (grain size, ~50-170 μm). I: highly recrystallized saddle dolomite from the top Hamajing Member (grain size, ~60-260 μm). J-L: fine-crystalline dolomite with calcite grains (grain size, ~40-420 μm). 76
- Fig. 3. 13 Cross-plot of the Qinglinkou section samples with Mn/Sr < 10. DM: dolomite (calcium carbonate content < 70%); DL: dolomitic limestone (calcium carbonate

content >70%; Mg/Ca > 0.025); LM: limestone (calcium carbonate content >70%; Mg/Ca < 0.025). Thresholds for the green shaded area (best-preserved samples) are Mn/Sr < 2, Mg/Ca < 0.257, Sr/Ca > 0.001, Mn/Ca < 0.003, Fe/Ca < 0.01 and Al/Ca < 0.05. 78

- Fig. 3. 14 Lithostratigraphic and chemostratigraphic correlation of the Doushantuo Formation in the Huangling Anticline area. Data from the Qinglinkou section is from this study after the diagenetic screening. Data from the Jiulongwan section is from (Jiang et al., 2007; McFadden et al., 2008). Zhangcunping section data is from (Wang et al., 2017b; Ouyang et al., 2019). Shaded symbols represent the carbon isotope values, and unshaded symbols represent the oxygen isotope values. 81
- Fig. 4. 1 Generalized lithostratigraphic column, TOC vs carbonate proportion column, biostratigraphic column, and carbonate carbon isotope chemostratigraphic column in the Yangtze Gorges area. Fossil records were modified from (Zhu and Li, 2017; Wood et al., 2019). Carbon isotope data from (Wei et al., 2018b). 86
- Fig. 4. 2 3D stratigraphic correlation of the sections around the Huangling Anticline area. The 560 Ma time equivalent line is set as the start of the DOUNCE/Shuram excursion (Gong et al., 2017). The 551 ± 0.7 Ma is dated from the ash bed atop of the shale layer. 89
- Fig. 4. 3 Lithostratigraphy, $\delta^{13}\text{C}_{\text{carb}}$, $\delta^{18}\text{O}_{\text{carb}}$, and elemental profiles of the Doushantuo Formation at the Qinglinkou section. Gray shades identify four negative carbon isotope excursions. The blue line represents the ‘mirror plane’. HMJ, Hamajing Member; BMT, Baimatuo Member. 90
- Fig. 4. 4 Lithostratigraphy and $\delta^{13}\text{C}_{\text{carb}}$ profiles of Ediacaran successions in the western region of the Huangling Anticline area. The red lines represent the stratigraphic correlations. The shaded blue area represents the negative carbon isotope excursion. The grey circles represent the data from the middle carbonate unit and could be recovered to the red circles based on my mirror plane hypothesis. The data of the Qinglinkou section are from this study. $\delta^{13}\text{C}_{\text{carb}}$ profiles of the Jiuqunao and Miaohe section are from (Lu et al., 2013), Zhimaping section is from (An et al., 2015), Liaojiagou and Gaolan section are from (Zhou et al., 2017b). 92
- Fig. 4. 5 Lithostratigraphy and $\delta^{13}\text{C}_{\text{carb}}$ profiles of the Ediacaran successions in the central and eastern region of the Huangling Anticline area. $\delta^{13}\text{C}_{\text{carb}}$ profile of the Jiulongwan section is from (Jiang et al., 2007), Xiangerwan section is from (An et al., 2015), Zhengjiatang section is from (Zhou et al., 2017b), Tianjiayuanzi section is from (Zhou et al., 2012), Baiguoyuan section is from (Zhu et al., 2007), Niuping section is from (Liu et al., 2013). 93
- Fig. 4. 6 A: Paleogeographic recovery of the Huangling Anticline area. Modified from (Wang et al., 2019b). B: Cross-section from W to E. 95
- Fig. 4. 7 The first possible evolution history of the middle carbonate unit. In this hypothesis, slumping occurs after the deposition of the lower HMJ Member. The lower HMJ has been slumped down into the basin, followed by the shale layers. After the deposition of the upper HMJ, which also slumped down and resulted in the sandwiched layers. 97
- Fig. 4. 8 The second possible evolution history of the middle carbonate unit (Shelf-to-basin transect). The red arrows represent the relative moving direction. Modified from (Jiang et al., 2011). 99
- Fig. 4. 9 An example field photo and sketch showing the deformed carbonate unit slumping along the horizontal detachment surface and the NE-dipping Pulivendla Formation backthrust on top of the folded carbonate slumping unit. Figure from (Khan et al., 2020). 100
- Fig. 4. 10 A: Field photograph of the ‘Z’ shape contact surface between the upper shale II and the middle carbonate unit. B: Field photograph showing the uncontinuous

lower shale I layer. C: Schematic sketch showing the lateral occurrence of different lithounits and the controlling structures. The arrows in the figures represent the relative moving directions of the upper shale II layers (red arrows) and the middle carbonate unit (blue arrows).	100
Fig. 5. 1 New designed and tested carbonate-associated sulfate (CAS) pre-leaching and extraction protocols in this study. A: Refined 10% NaCl (aq) pre-leaching method (method 1). B: Single oxidative-NaCl pre-leaching methods: 10% H ₂ O ₂ (aq) leach (method 2a) and 12% NaOCl leach (aq) (method 2b). C: Combined NaOCl-H ₂ O ₂ -NaCl pre-leaching method (method 3). D: Refined CAS extraction protocols.	110
Fig. 5. 2 Cross-plot of the selected samples. DM: dolomite (calcium carbonate content < 70%); DL: dolomitic limestone (calcium carbonate content >70%; Mg/Ca > 0.025); LM: limestone (calcium carbonate content >70%; Mg/Ca < 0.025). Thresholds for the green shaded area (best-preserved samples) are Mn/Sr < 2, Sr/Ca > 0.001, Mg/Ca < 0.257 and Fe/Ca < 0.01.	113
Fig. 5. 3 NaOCl leachates with pink/brown color showing the pyrite has been oxidized.	114
Fig. 5. 4 Comparison and evaluation of four methods results in this study. A: Barite precipitate weight from 3 leachates using method 2a. B: Barite precipitate weight from 3-4 leachates using method 2b (shaded in pink) and 3 (shaded in green). C: Leachate sulfate sulfur isotope values $\delta^{34}\text{S}_{\text{SL}}$. D: Comparison of the final CAS sulfur isotope value $\delta^{34}\text{S}_{\text{CAS}}$ using three different methods (NaCl only, methods 2b, and method 3). E: Comparison between the gradient of CAS $\delta^{34}\text{S}_{\text{CAS}}$ increase from NaCl pre-leaching to method 3 and samples' CRS concentration and TOC content. F: Comparison of the leachate precipitate S isotope value with pyrite S isotope value showing the leachate S isotope values are consistently lower than the coeval pyrite S isotope values. Sample CC3 (dark limestone with the highest pyrite density and AVS + CRS concentration, ~550Ma) has the highest increase of the final $\delta^{34}\text{S}_{\text{CAS}}$ value (and greatest slope), then QLKS6 (dark grey limestone, ~548Ma), then LHA6.5 (grey limestone, ~555Ma).	117
Fig. 5. 5 Comparison of the published $\delta^{34}\text{S}_{\text{CAS}}$ (‰) and the data from this study using method 1 (orange circles) and method 3 (red square). The relative stratigraphic heights of the samples are based on age estimations and carbon isotope values. Sample LHA6.5 is from the Lianghong section. Sample CC3 is from the Zhimaping section. Sample QLKS6 and QLKS18 are from the Qinglinkou section. The blue dots are published data from (Cui et al., 2016a; Shi et al., 2018). GJS = Gaojiashan Member.	119
Fig. 5. 6 A-B: Comparison of published $\delta^{34}\text{S}_{\text{CAS}}$ (blue color) and $\delta^{34}\text{S}_{\text{PY}}$ (orange color) data measured from 'superheavy pyrite' sections. A: Nama Group data from (Tostevin et al., 2017). B: Datangpo Formation data from (Wang et al., 2019a). C: Box plots of corresponding data. The black line and cross symbols in each box show the median and mean values, respectively.	121
Fig. 6. 1 Late Ediacaran $\delta^{13}\text{C}_{\text{carb}}$, $\delta^{18}\text{O}_{\text{carb}}$, and $\delta^{34}\text{S}_{\text{CAS}}$ profiles of three sections in South China. According to the petrology and elemental test (Chapter 3), I separate the carbonate samples into limestone (blue circle), dolomitic limestone (orange square), and dolomite (black triangle) samples (shown in the $\delta^{13}\text{C}_{\text{carb}}$ profiles). The entire DOUNCE/Shuram excursion is divided into three stages (EN4a, 4b, 4c). The blue dashed line represents the 'mirror plane' at the Qinglinkou sections. HMJ-Hamajing Member; BMT-Baimatuo Member; EN-Ediacaran negative excursion; EP-Ediacaran positive excursion. DOUNCE=Doushantuo negative carbon isotope excursion. BAINCE=Baiguoyuan negative carbon isotope excursion. WANCE=Weng'an negative carbon isotope excursion. CANCE=Cap carbonate negative carbon isotope excursion.	128

- Fig. 6. 2 Cross-plots of the $\delta^{13}\text{C}_{\text{carb}}$, $\delta^{18}\text{O}_{\text{carb}}$ and $\delta^{34}\text{S}_{\text{CAS}}$ and elemental ratios of the Lianghong, Sishang and Qinglinkou sections. a. $\delta^{13}\text{C}_{\text{carb}}$ (‰)- $\delta^{18}\text{O}_{\text{carb}}$ (‰) (Lianghong-DST, DY $R^2 = 0.49, 0.19$; Sishang-DST, DY, Cambrian $R^2 = 0.34, 0.2, 0.57$; Qinglinkou-DST, DY $R^2 = 0.33, 0.059$). b. $\delta^{34}\text{S}_{\text{CAS}}$ (‰)- $\delta^{18}\text{O}_{\text{carb}}$ (‰) (Lianghong-DST, DY $R^2 = 0.0028, 0.99$; Sishang-DST, DY, Cambrian $R^2 = 0.20, 0.013, 0.83$; Qinglinkou-DST, DY $R^2 = 0.014, 0.013$). c. $\delta^{34}\text{S}_{\text{CAS}}$ (‰)-carbonate content (‰) (Lianghong-DST, DY $R^2 = 0.0025, 0.41$; Sishang-DST, DY, Cambrian $R^2 = 0.028, 0.171, 0.14$; Qinglinkou-DST, DY $R^2 = 0.046, 0.097$). d. $\delta^{34}\text{S}_{\text{CAS}}$ (‰)-Mg/Ca (w/w) (Lianghong-DST, DY $R^2 = 0.0019, 0.47$; Sishang-DST, DY, Cambrian $R^2 = 0.13, <0.0001, 0.23$; Qinglinkou-DST, DY $R^2 = 0.0074, 0.18$). e. $\delta^{34}\text{S}_{\text{CAS}}$ (‰)-[CAS] (ppm) (Lianghong-DST, DY $R^2 = 0.064, 0.50$; Sishang-DST, DY, Cambrian $R^2 = 0.15, 0.016, 0.15$; Qinglinkou-DST, DY $R^2 = <0.0001, 0.16$). f. $\delta^{34}\text{S}_{\text{CAS}}$ (‰)-Mn/Sr (w/w) Lianghong-DST, DY $R^2 = 0.035, 0.082$; Sishang-DST, DY, Cambrian $R^2 = <0.0001, 0.20, 0.018$; Qinglinkou-DST, DY $R^2 = 0.030, 0.19$). g. [CAS] (ppm)-Mg/Ca (w/w) (Lianghong-DST, DY $R^2 = 0.26, 0.67$; Sishang-DST, DY, Cambrian $R^2 = 0.0003, 0.0031, 0.5654$; Qinglinkou-DST, DY $R^2 = 0.78, 0.074$). h. [CAS] (ppm)-Mn/Sr (w/w) (Lianghong-DST, DY $R^2 = 0.0093, 0.76$; Sishang-DST, DY, Cambrian $R^2 = 0.029, 0.0003, 0.073$; Qinglinkou-DST, DY $R^2 = 0.21, 0.057$). Carbonate content (‰): weight percentages of HCl-leachable CaCO_3 and $\text{CaMg}(\text{CO}_3)_2$131
- Fig. 6. 3 The compilation of $\Delta^{34}\text{S}$ values versus sulfate concentration in the euxinic system. From (Gomes and Hurtgen, 2015)132
- Fig. 6. 4 The simplified box model of the sulfur cycle. GYP = gypsum and PY = pyrite. The sulfur isotope composition for each parameter is from (Fike et al., 2015).133
- Fig. 6. 5 Comparisons of bulk rock CAS and pyrite S isotope value of the late Ediacaran (~560-541Ma) samples from different sections around the world. A: The histogram shows $\delta^{34}\text{S}_{\text{CAS}}$ during late Ediacaran has an average value of $27.7 \pm 10.0\text{‰}$; B: The histogram shows $\delta^{34}\text{S}_{\text{PY}}$ during late Ediacaran has an average value of $4.5 \pm 20.5\text{‰}$. The CAS and pyrite data compiled here including this study and data from (Hurtgen et al., 2005; Fike et al., 2006; Fike and Grotzinger, 2008; McFadden et al., 2008; Ries et al., 2009b; Wu et al., 2015; Cui et al., 2016a; Wang et al., 2017a; Shi et al., 2018; Wang et al., 2020).135
- Fig. 6. 6 ‘Rate method’ model of maximum seawater sulfate concentration in late Ediacaran (~560- 541 Ma). A: Lianghong section B: Sishang section. C: Qinglinkou section. The blue, orange and grey curves represent the estimated seawater sulfate concentration with 0.2Ma smoothing grids when $\delta^{34}\text{S}_{\text{PY}} = -6.3\text{‰}$, -11.5‰ , and -16.7‰ , respectively. The green pointed curve represents the estimated sulfate concentration with 0.4Ma smoothing grids and $\delta^{34}\text{S}_{\text{PY}} = -11.5\text{‰}$. The yellow curve represents the CAS concentration curve of the samples. The grey shaded area connects the baseline of the model lines and represents the best estimation of the seawater sulfate concentration.138
- Fig. 6. 7 Summary of carbonate carbon isotope $\delta^{13}\text{C}_{\text{carb}}$, CAS sulfur isotope $\delta^{34}\text{S}_{\text{CAS}}$ from the Lianghong, Sishang, Qinglinkou section and compiled $^{87}\text{Sr}/^{86}\text{Sr}$ ratios profile (Li et al., 2017) during the late Ediacaran (~565- 541 Ma).140
- Fig. 6. 8 Box plots of bulk rock CAS $\delta^{34}\text{S}_{\text{CAS}}$ and pyrite S isotope $\delta^{34}\text{S}_{\text{PY}}$ values of the late Ediacaran (~570-541Ma) samples from this study and around the world. The red, orange, and blue lines represent the CAS sulfur isotope curves (mean values) of the Lianghong, Sishang, and Qinglinkou section samples, respectively. The green and black lines represent the global CAS sulfur and pyrite sulfur isotope profiles, respectively. The blue and red shaded areas represent the difference between the CAS sulfur and pyrite sulfur isotope values $\Delta\delta^{34}\text{S}_{\text{CAS-PY}}$. The data compiled here include the data from this study and data from (Hurtgen et al., 2005; Fike et al., 2006; Fike and Grotzinger, 2008; McFadden et al., 2008; Ries et al.,

- 2009b; Wu et al., 2015; Cui et al., 2016a; Wang et al., 2017a; Shi et al., 2018; Wang et al., 2020). 144
- Fig. 6. 9 Compilation of the carbonate carbon isotope $\delta^{13}\text{C}_{\text{carb}}$, barite sulfur $\delta^{34}\text{S}_{\text{barite}}$, evaporite sulfur $\delta^{34}\text{S}_{\text{evaporite}}$, other mineral bound sulfate $\delta^{34}\text{S}_{\text{other}}$, CAS sulfur $\delta^{34}\text{S}_{\text{CAS}}$, and pyrite sulfur $\delta^{34}\text{S}_{\text{py}}$ isotope composition from published papers and this study from Cryogenian to middle Cambrian. Carbonate carbon isotope data from global sections are from (Cox et al., 2016; Bowyer et al., 2017; Wood et al., 2019). South China data from (Jiang et al., 2011; Wang et al., 2012b; Gamper et al., 2015). Barite data from (Misi and Veizer, 1998; Peng et al., 2011; Crockford et al., 2016). Evaporite data from (Gorjan et al., 2000; Strauss et al., 2001; Peryt et al., 2010; Crockford et al., 2019). CAS data from (Fike and Grotzinger, 2008; Hurtgen et al., 2009; Ries et al., 2009b; Bao et al., 2012; Wu et al., 2015; Cui et al., 2016a; Tostevin et al., 2017; Shi et al., 2018). Other mineral bound sulfate data from (Shields et al., 1999; Walter et al., 2000; Shields et al., 2004; Goldberg et al., 2005a; Hough et al., 2006). Pyrite sulfur data from (Sahoo et al., 2012; Tostevin et al., 2017; Shi et al., 2018; Wang et al., 2021). The red dashed line in figure B represents the modern seawater sulfate S isotope value ($\sim 21\%$) (Tostevin et al., 2014; Cui et al., 2016a). The compiled data set can be accessed by contacting the author. 146
- Fig. 7. 1 The geochemical profiles of the redox-sensitive trace elements across the DOUNCE/Shuram at the Lianghong section. 154
- Fig. 7. 2. The geochemical profiles of the redox-sensitive trace elements across the DOUNCE/Shuram at the Sishang section. 154
- Fig. 7. 3 The geochemical profiles of the redox-sensitive trace elements across the Ediacaran Period at the Qinglinkou section. 155
- Fig. 7. 4. Ediacaran $\delta^{13}\text{C}_{\text{carb}}$, $\delta^{18}\text{O}_{\text{carb}}$, and $\delta^{238}\text{U}$ profiles of the carbonate samples of the studied sections from this study. The red-dashed line represents the modern seawater $\delta^{238}\text{U}$ value $-0.392 \pm 0.005\%$. The red-dashed shaded area represents the modern Bahama carbonate ($0.27 \pm 0.14\%$ heavier than modern seawater) (Tissot and Dauphas, 2015; Chen et al., 2018). 156
- Fig. 7. 5 Cross-plots of the $\delta^{238}\text{U}$, $\delta^{18}\text{O}_{\text{carb}}$ and elemental ratios of the Lianghong, Sishang and Qinglinkou sections. a. $\delta^{238}\text{U}$ ($\%$)- $\delta^{18}\text{O}_{\text{carb}}$ ($\%$) (Lianghong $R^2 = 0.016$; Sishang $R^2 = 0.22$; Qinglinkou $R^2 = 0.002$); b. $\delta^{238}\text{U}$ ($\%$)-Mn/Sr (Lianghong $R^2 = 0.38$; Sishang $R^2 = 0.0002$; Qinglinkou $R^2 = 0.294$); c. $\delta^{238}\text{U}$ ($\%$)-Carbonate content ($\%$) (Lianghong $R^2 = 0.012$; Sishang $R^2 = 0.087$; Qinglinkou $R^2 = 0.365$); d. $\delta^{238}\text{U}$ ($\%$)-Mg/Ca (Lianghong $R^2 = 0.0032$; Sishang $R^2 = 0.040$; Qinglinkou $R^2 = 0.211$); e. $\delta^{238}\text{U}$ ($\%$)-U/Sc (Lianghong $R^2 = 0.088$; Sishang $R^2 = 0.15$; Qinglinkou $R^2 = 0.086$); f. $\delta^{238}\text{U}$ ($\%$)-U/Al (Lianghong $R^2 = 0.070$; Sishang $R^2 = 0.11$; Qinglinkou $R^2 = 0.218$); 158
- Fig. 7. 6 A: Boxplots of Enrichment Factors (U_{EF} , Mo_{EF} , and V_{EF}) of the carbonate samples from each period during pre-DOUNCE to early Cambrian. N = number of samples. The blue, black, and orange curve lines represent the average U_{EF} , Mo_{EF} , and V_{EF} values, respectively. B: The enrichment factor index (ΣEF) profile of each section. C: Uranium isotope $\delta^{238}\text{U}$ profile of the studied sections (Lianghong, Sishang, and Qinglinkou section). D: Iron speciation data from Yanjia section, Daotuo drillcore, Jiulongwan section, and Three Gorges Core ($\text{Fe}_{\text{HR}}/\text{Fe}_{\text{T}} > 0.38$; $\text{Fe}_{\text{PY}}/\text{Fe}_{\text{T}} > 0.8$ indicate euxinic water-column). The red curves are LOWESS smoothed profiles. 163
- Fig. 7. 7 Compilation of the $\delta^{238}\text{U}$ (A), U_{EF} (B), and Mo_{EF} (C) from carbonate samples and shale samples from published papers and this study. (D) Estimated bottom water oxygen levels based on published iron speciation data. (E) Biotic evolution records cross Cryogenian-Cambrian, modified from (Wood et al., 2019). Oxidic condition $[\text{O}_2] > 2 \text{ ml/l}$ ($\text{O}_2/\text{H}_2\text{O}$); Suboxic condition $0.2 < [\text{O}_2] < 2 \text{ ml/l}$ ($\text{O}_2/\text{H}_2\text{O}$);

Anoxic condition $[O_2] < 0.2 \text{ ml/l } (O_2/H_2O)$; Ferruginous condition $[O_2] < 0.1 \text{ ml/l } (O_2/H_2O)$; Euxinic $[O_2] = 0 \text{ ml/l } (O_2/H_2O)$ (Tyson and Pearson, 1991; Tribovillard et al., 2006). Compiled data includes (Dahl et al., 2014; Azmy et al., 2015; Kendall et al., 2015; Lau et al., 2017; Wei et al., 2018a; Zhang et al., 2018; Dahl et al., 2019; Tostevin et al., 2019; Zhang et al., 2019; Cheng et al., 2020; Li et al., 2020; Wei et al., 2020a; Wei et al., 2021a). The compiled data set can be accessed by contacting the author.....	165
Fig. 8. 1 Conceptual model showing the seawater oxygenation state during the pre-excursion period (EP3). The pyrite formation zone (PFZ) is shaded in yellow.	168
Fig. 8. 2 Conceptual model showing the seawater oxygenation state during the onset period of the DOUNCE/Shuram (EN4a). The pyrite formation zone (PFZ, euxinic) is shaded in yellow. This period lasted around 1.6 Ma in South China.	169
Fig. 8. 3 Conceptual model showing the seawater oxygenation state during the DOUNCE/Shuram (EN4b). This period lasted around 7.3 Ma in South China.	170
Fig. 8. 4 Conceptual model showing the seawater oxygenation state during the recovery period of the DOUNCE/Shuram (EN4c). This period lasted around 1.1 Ma in South China.	171
Fig. 8. 5 Conceptual model showing the seawater oxygenation state during the DOUNCE/Shuram aftermath (EP4a). This period lasts around 3.1 Ma in South China and is characterized by coupled C-S trend.	172
Fig. 8. 6 Conceptual model showing the seawater oxygenation state during the DOUNCE/Shuram aftermath (EP4b). This period lasts around 3.7 Ma in South China and is characterized by the decoupled C-S trend.	172

List of Tables

Table 1. 1 Simple classification of the paleoredox conditions (Tyson and Pearson, 1991; Tribovillard et al., 2006).	35
Table 1. 2 Characteristic of redox-sensitive trace elements in the modern ocean (U, V, Mo). Data from (McLennan, 2001; Tribovillard et al., 2006; Och and Shields-Zhou, 2012; Partin et al., 2013).	36
Table 4. 1 Comparison between the decreasing magnitude of the $\delta^{13}\text{C}_{\text{carb}}$ from the middle carbonate unit and the Hamajing Member.	97
Table 5. 1 Selected carbonate samples. Age estimation is based on its stratigraphic height and geological unit. QLKS = Qinglinkou section, CC = Zhimaping section, LH = Lianghong section.	107
Table 5. 2 Leachate precipitate weight, sulfur isotope composition, and final CAS sulfur isotope values from different pre-leaching methods together with the TOC content, AVS, CRS concentration, and its sulfur isotope values of the samples. “-” means too low to get a reliable value. SL = solution. S isotope values are reported in the δ notation against V-CDT.	111
Table 5. 3 Elemental concentrations of the acid-soluble fractions of the samples measured by ICP-OES. Carbonate content (%): weight percentages of acid-leachable content ($\text{CaCO}_3 + \text{MgCO}_3$).	112
Table 5. 4 Comparisons between CAS sulfur isotope values $\delta^{34}\text{S}_{\text{CAS}}$ and $\Delta\delta^{34}\text{S}_{\text{CAS-PY}}$ from this study and published data. ‘n’ indicates the sample number. Errors are one standard deviation.	120
Table 6. 1 Comparison between pyrite sulfur isotope values $\delta^{34}\text{S}_{\text{PY}}$ and $\Delta\delta^{34}\text{S}_{\text{CAS-PY}}$ from this study and published data during the DOUNCE/Shuram aftermath. Errors are one standard deviation.	137

Chapter 1 Introduction

1.1 Overview of the Project

In Earth history, life and oxygen played a crucial role in shaping our planet, such as climatic changes, biological evolution, and the weathering of the continents. The Ediacaran Period (c. 635 – c. 541 Ma) witnessed a series of important events: the Neoproterozoic Oxygenation Event (NOE, ~850 to 541 Ma); the Gaskiers glacial event (~580 Ma); biological innovations, such as the first appearance of animal fossils (~574 Ma), trace fossils (c. ~565 Ma) and biomineralization (c. ~550 Ma); the breakup of Rodinia and assemblage of the Gondwanaland (~630 - 530 Ma), the most extreme negative carbon isotope excursion (DOUNCE/Shuram Excursion, c. ~570 Ma – 551 Ma) and oxygenation of the deep ocean. These events make the Ediacaran Period a key time interval to investigate the links between environmental changes and life evolution on our planet.

During the Ediacaran, life forms became more complex when the Ediacaran biota (large, benthic, multicellular, animal grade organisms) emerged and flourished (Och and Shields-Zhou, 2012; Zhu and Li, 2017). The widespread record of trace fossils (from ~565 Ma) from upper Ediacaran strata shows evidence of increased mobility of the fauna: some trail patterns show self-avoiding behavior and coiling, which might indicate that they either needed higher O₂ levels in the surrounding area or that they required efficient O₂ extracting ways (Martin et al., 2000; Narbonne and Gehling, 2003; Zhuravlev et al., 2009; Cui et al., 2015).

Carbon isotopes are the most widely used geochemical proxy for oxygenation events and global chemostratigraphic correlation of different sections. A series of carbon isotopic records of different sections were published in recent studies, such as the Jiulongwan, Miaohu, Dongdahe sections (Ishikawa et al., 2008; Lu et al., 2013), which helped to look into the carbon cycle during the Ediacaran Period. The late Ediacaran DOUNCE (DOUshantuo Negative Carbon isotope Excursion) occurs widely in South China and can be correlated to the most significant negative carbon isotope excursion in Earth history: the Shuram-Wonoka $\delta^{13}\text{C}$ negative excursion (down to -12‰) (Burns and Matter, 1993; Condon et al., 2005; Le Guerroue, 2006; Lu et al., 2013).

A plausible explanation of the negative carbon isotope excursion is the

oxidation of a large dissolved organic carbon (DOC) reservoir stored in seawater (Jiang et al., 2007; Shields, 2017). However, considering the low paleo oxygen level (0.01-1%PAL) (Lyons et al., 2014), the oxygen could be quickly exhausted by oxidation of the DOC estimated by numerical models (Bristow and Kennedy, 2008). Therefore, diagenetic or localized explanations of this event are favored by some scientists (Derry, 2010; Grotzinger et al., 2011; Cui et al., 2017). To better understand the carbon cycle and the oxygenation history during the DOUNCE/Shuram event, sulfur and uranium isotopes and redox-sensitive elements (RSTE) were chosen as paleoenvironmental redox proxies.

Carbonate Associated Sulfate (CAS) refers to trace sulfate incorporated into calcium-carbonate minerals during their precipitation (Marengo et al., 2008a), which means that it is relatively resistant to later diagenetic alteration (He et al., 2019). Carbonate deposits occur widely in normal marine settings and - in younger time intervals - contain fossils that serve as chronological constraints. These features make CAS an ideal proxy for understanding how ancient seawater sulfate $\delta^{34}\text{S}_{\text{sw}}$ has changed over time (Marengo et al., 2008a; Tostevin et al., 2017; Shi et al., 2018). In the marine system, sulfate concentration and sulfur isotope composition are mainly controlled by two fluxes: riverine input and pyrite burial. The oceanic reservoir and pyrite burial flux are both redox-sensitive, which means that redox imbalances should imprint both the sulfate concentration and sulfur isotope composition, thus allowing us to trace redox changes through Earth history (Tostevin et al., 2017; Lyu et al., 2019). As with carbonate $\delta^{13}\text{C}_{\text{carb}}$, $\delta^{34}\text{S}_{\text{CAS}}$ can be used, if unaffected by later isotopic exchange, to represent the paleo seawater values and reflect the redox balance in past oceans.

Uranium isotopes are also a robust global ocean redox proxy against diagenetic influences (Andersen et al., 2016; Lau et al., 2017; Zhang et al., 2019). Uranium has a longer residence time (~500 kyr) than the ocean mixing time (~1 kyr), the uranium isotope composition of marine carbonates can provide global average redox conditions for the paleo-seafloor. The principles are based primarily on the fact that uranium solubility is controlled by oxygen levels (U^{6+} is soluble and U^{4+} is relatively insoluble), and that ^{238}U is preferentially removed in suboxic and anoxic environments compared to ^{235}U (Lau et al., 2016; Tostevin et al., 2019; Zhang et al., 2020b). This means that low uranium concentration [U] and $\delta^{238}\text{U}$ values might indicate anoxic scavenging of uranium.

Biological extinction, evolution, and radiation seem to be tightly linked to marine environmental changes, such as oceanic oxygenation events, tectonically induced nutrient flux changes, and climate changes (Och and Shields-Zhou, 2012; Lenton et al., 2014; Song et al., 2014; Lau et al., 2017). This study presents a detailed stratigraphic and chemostratigraphic study of the Yangtze Gorges Area and high-resolution and high-fidelity C-O, CAS sulfur, U isotope, and RSTE concentration data of three representative sections during and after the DOUNCE/Shuram excursion with an aim to further understand the interactions between marine environmental changes and life and establishing a faithful stratigraphic and chemostratigraphic framework of the late Ediacaran strata in South China.

1.2 Late Ediacaran Biological Evolution

In this thesis, the ‘Late Ediacaran period’ refers to the period after the Gaskiers glaciation in the Ediacaran (c. ~580 Ma - 541 Ma). The focus of my research is the late Ediacaran, which plays an important role in the biological evolution history on Earth (Butterfield, 2007). The Ediacaran biota (c. ~574 - 541 Ma) was described as “The Dawn of Animal Life” by Glaessner (Glaessner, 1985; Seilacher et al., 2003) and is famous for tubular, frondose, and flat-bodied organisms of uncertain affinity as well as the first appearance of definitive animals (complex multicellular organisms) (Grotzinger et al., 1995; Bobrovskiy et al., 2018; Wood et al., 2019). Ediacaran type fossils first appeared at around 574 Ma from Mistaken Point Ecological Reserve (MPER) in Newfoundland (Matthews et al., 2020), which is after the Gaskiers glaciation (c. 579.63 ± 0.15 Ma – 579.88 ± 0.44 Ma), and are thought to have become extinct by the Cambrian radiation of skeletal animals (Saylor et al., 1995; Narbonne and Gehling, 2003; Canfield et al., 2007; Pu et al., 2016; Sial et al., 2018). It is a special and lonely taxonomic classification that has even been described as “As strange as life on another planet” (Bobrovskiy et al., 2018). However, because the life forms are non-skeletal, our paleontological knowledge about the Ediacaran organisms is relatively poor.

South China has a complete stratigraphic succession of the Ediacaran Period and well-preserved Ediacaran biota fossil records. From bottom to top, the strata are divided into the Doushantuo Formation (ca. 635-551 Ma) and Dengying Formation (ca. 551-541 Ma). These fossil biotas include (Fig. 1.1):

- (1) Lantian biota (c. ~620 - 582 Ma): Located at Lantian Town of Xiuning County, Anhui Province, China. The Lantian biota contains algae and putative animals, preserved as carbonaceous compressions, and yield the oldest Ediacaran benthic sessile macroorganisms (Yuan et al., 2012). Before the Marinoan snowball Earth event (c. 650 – 635 Ma), eukaryotic life comprised mostly single-celled microscopic algae, simple globular and tubular forms (Yuan et al., 2012), some of which can be confidently assigned to green algae (Zhang and Pratt, 2015), red algae (Xiao et al., 2004) or testate amoebae (Porter and Knoll, 2000). The Lantian biota recorded the rapid development of eukaryotes after the Marinoan glaciation, but some argued that it probably does not belong to the Ediacaran biota (Narbonne, 2011).
- (2) Weng'an biota (c. ~590 – 570 Ma): Located at Weng'an County, the central part of Guizhou Province, China. The Weng'an biota is hosted in phosphorite of the Doushantuo Formation and contains a diverse assemblage of microscopic, multicellular soft-bodied eukaryote fossils, multicellular algae, and acanthomorphic acritarchs (Xiao et al., 2014; Cunningham et al., 2017; Zhou et al., 2017a). It has been interpreted as being deposited in an outer-shelf environment (Jiang et al., 2011).
- (3) Miaohu & Wenghui biota (c. ~575 - 551 Ma): The Miaohu biota is located at Miaohu Town, Zigui County, Hubei Province, China. The Wenghui biota is located at Wenghui Village, Jiangkou County, northeastern Guizhou Province, China (26°50'07"N, 109°01'20"E). The Miaohu & Wenghui biota were found in the uppermost Doushantuo Formation and are likely to have been marine benthic organisms that lived in the photic zone (Xiao et al., 2013). These include mainly benthonic megascopic algae, organic tubes of cnidarian *scyphopolyps* and Ediacaran type *Eoandromeda octobrachiata* (Zhao et al., 2004; Zhou et al., 2018).
- (4) Shibantan biota (c. ~551 – 541 Ma): Located at Wuhe, Yangtze Gorges area, China. The Shibantan biota was found in the middle Dengying Formation and is known to contain abundant trace fossils and other marine organisms such as *Pteridinium*, *Rangia*, *Charniodiscus*, *Hiemalora*, and annulated tubes (*Wutubus*) (Chen et al., 2014; Duda et al., 2014).
- (5) Gaojiashan biota (c. ~552 – 544 Ma): Located at Hujiaba town, southern Shaanxi Province, China. The Gaojiashan biota was found in the middle

Dengying Formation and is known for the appearance of *Cloudina* biomineralized tubes and self-avoiding behavior among trace fossils (not overlapping) (Zhuravlev et al., 2009).

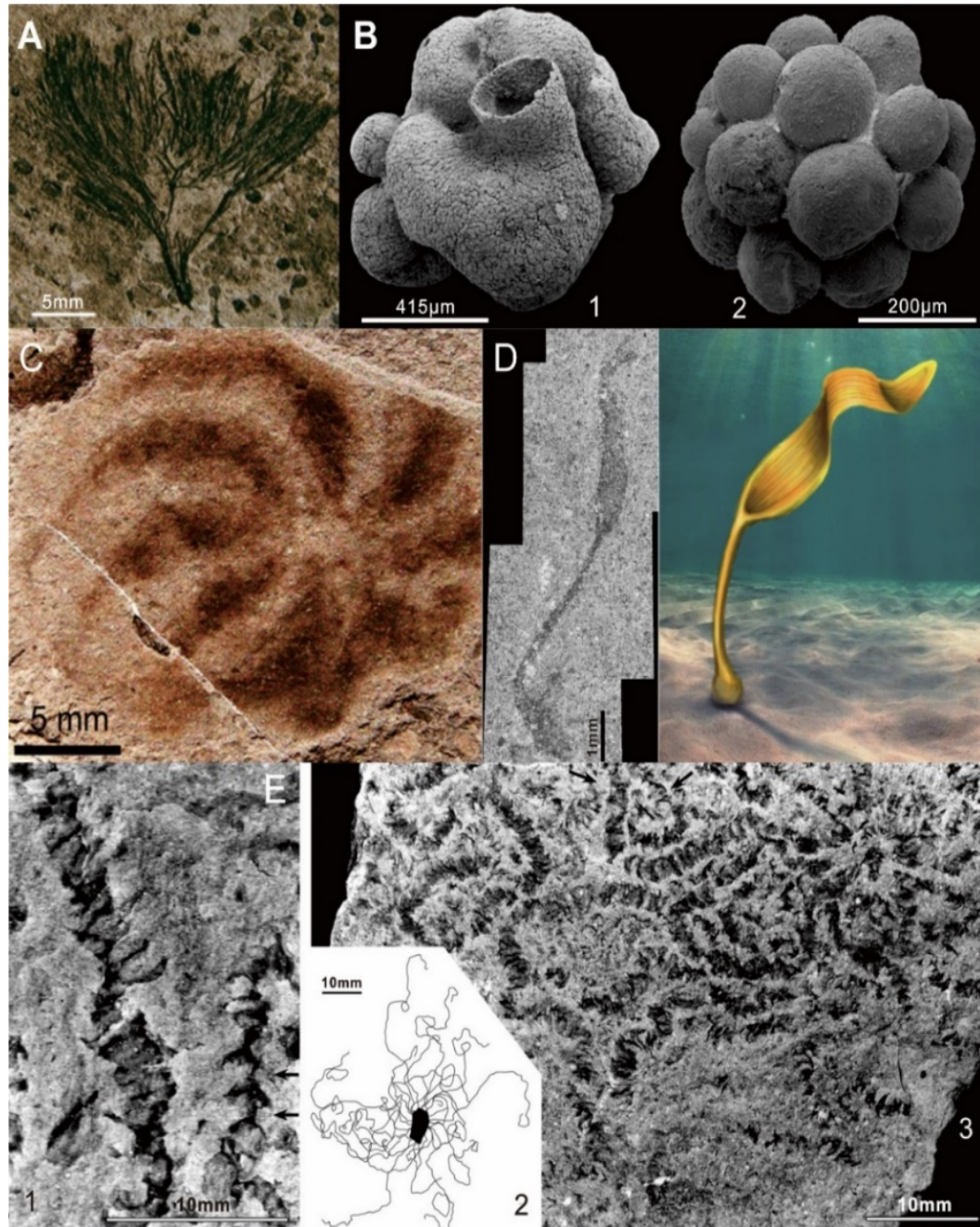


Fig. 1. 1 A summary photo of the typical fossils of each biota in Ediacaran in South China. A: Algal fossil from the Lantian biota (Yuan et al., 2012); B: Scanning electron microscope images from the Weng'an biota: (1) *Eocyathispongia*, a putative sponge; (2) *Tianzhushania*, in division stage (Cunningham et al., 2017). C: *Eoandromeda octobrachiata* from the Miaohu & Wenghui biota (Zhu et al., 2008; Xiao et al., 2013). D: *Vendotaenia pavimentipes* and the restored picture from the Shibantan biota (Yang et al., 2018). E: (3) Fossil record of coiling and phobotaxis from the Gaojiashan biota: (1) Magnified photo of 3; (2) Trail pattern of *Dictyostelium discoideum* slugs with fruiting bodies (Zhuravlev et al., 2009).

1.3 Neoproterozoic Oxygenation Event (NOE)

The oxygenation history of our planet can be divided into two major episodes, as mentioned before, the Great Oxidation Event/Episode (GOE, ~2.32 to 2.22 Ga) (Holland, 2002; Poulton et al., 2021) and the Neoproterozoic Oxygenation Event (NOE, ~850 to 541 Ma) (Fig. 1.2) (Och and Shields-Zhou, 2012; Lyons et al., 2014). During the GOE, the atmosphere oxygen level increased dramatically to 0.1 - 0.5 times the present atmospheric level (PAL) in a short time interval and then decreased again to a plateau around 0.001 – 0.1 PAL in the following ~1 Ga (Lyons et al., 2014; Planavsky et al., 2014). The major character of the GOE is the permanent loss of the multiple sulfur isotopes (MIF-S) signal in marine sediments.

The Neoproterozoic Era (~1000-541 Ma) witnessed turbulent environmental change, especially the carbon isotope records (Shields, 2018; Canfield et al., 2020). The unusually high $\delta^{13}\text{C}$ values (~5‰) before the glaciations during 850 Ma to 720 Ma indicates that the proportion of organic carbon burial flux was elevated, which might have resulted in the drawdown of atmospheric CO_2 and elevated O_2 (Knoll, 2003; Lenton et al., 2014). It is believed that during this period, the split of the Rodinia supercontinent (ca. 800 Ma) might trigger this decreasing of atmospheric $p\text{CO}_2$ and the coming of an icehouse environment (Shields-Zhou and Och, 2011). The Sturtian glaciation event is also closely linked to the diversification of eukaryotic plankton, which changed the nature of organic matter production (Knoll, 2003). From this event, we can see that the evolution of our planet and the evolution of life are not isolated. They are tightly linked and influenced in a way by each other.

The NOE happened in multiple stages after the end of the global glaciations during the Cryogenian Period. The NOE has been studied using multiple proxies, including C, S, U, isotopes, Fe-speciation, Ce anomaly, and redox-sensitive elements (Condon et al., 2005; Zhou et al., 2012; Shi et al., 2018; Wei et al., 2021b). The increase of the seawater $^{87}\text{Sr}/^{86}\text{Sr}$ indicates that continental influence becomes increasingly dominant (Cox et al., 2016; Li et al., 2017). Elevated physical weathering potentially brought more nutrients into the ocean, which might have triggered the flourishing of primary producers and produced more O_2 into the Earth system. Moreover, the increasing of negative Ce anomalies towards the Ediacaran-Cambrian boundary is interpreted as evidence for localized progressive oxygenation in South China (Ling et al., 2013). The enrichment of Mo and V in black shales can

further support a rise in oceanic oxygen (Scott et al., 2008; Sahoo et al., 2012; Och et al., 2016).

In between these two episodes is a long period of environmental stability, which is known as the ‘Boring Billion’ (c. $\sim 1.85 - 0.85$ Ga) (Fig. 1.2) (Holland, 2006; Lenton et al., 2014; Mukherjee et al., 2018). This period is also marked by the prolonged stable environmental conditions (nutrient, climate, atmospheric and tectonic stability) (Mukherjee et al., 2018). During this time interval, the continents have nearly no ice sheets, and the oxygen levels in the atmosphere might also have been relatively steady and low between 0.001 - 0.1 PAL (Canfield, 2005; Och and Shields-Zhou, 2012). Moreover, the deep ocean also remained anoxic, and even the photic zone might have turned sulphidic at times (Brocks et al., 2005). Because of the low oxygen level, the evolution of complex life is believed to be delayed during the Boring Billion (Mukherjee et al., 2018).

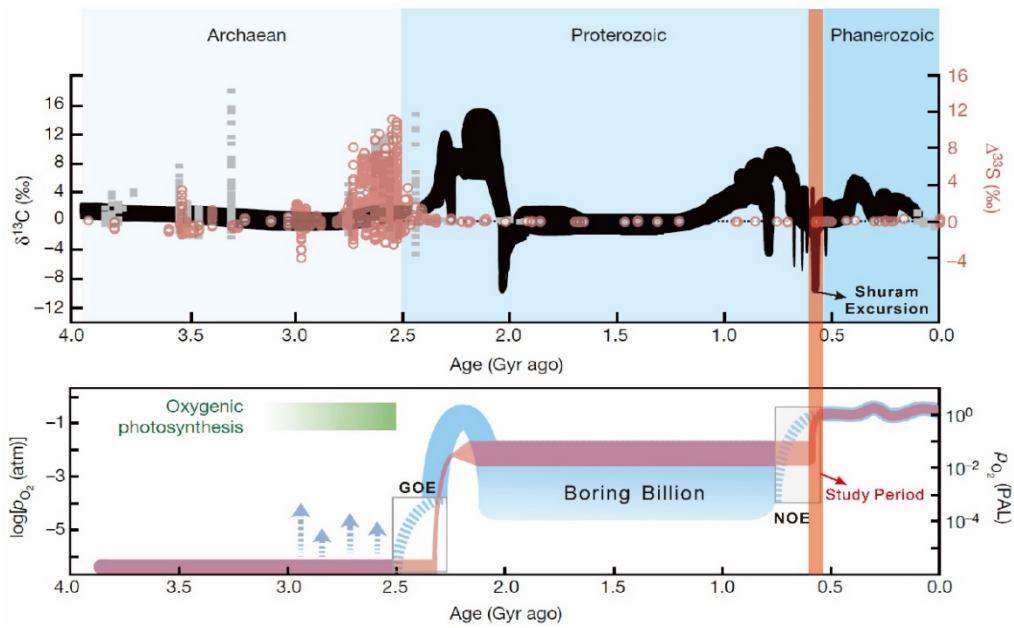


Fig. 1. 2 The evolution history of Earth's atmospheric oxygen content. The shaded red zone is my study period. The top figure summarizes carbon (black) and multiple sulfur (grey and red) isotope data in earth history. Modified from (Lyons et al., 2014).

1.4 Carbon Isotopes

Carbon isotopes are widely used as a geochemical proxy for oxygenation events and global correlation of Precambrian-Cambrian (Pc-C) boundary strata (Knoll et al., 1986; Rothman et al., 2003; Ishikawa et al., 2008; Hoefs, 2015; Shields, 2017). Carbon has two stable isotopes: ^{12}C (98.93%) and ^{13}C (1.07%) (Rosman and Taylor, 1998; Hoefs, 2015). Carbon isotope composition can be expressed as $\delta^{13}\text{C}$ (The international standard δ -value is the V-PDB-standard) (Hoefs, 2015):

$$\delta^{13}C = \left[\frac{(^{13}C/^{12}C_{sample})}{(^{13}C/^{12}C_{standard})} - 1 \right] * 1000 \quad \text{Equation 1.1}$$

Carbon isotope fractionation refers to the processes that could affect the relative abundance of carbon isotopes (Kendall and Caldwell, 1998; Hoefs, 2015). Because carbonate has a similar carbon composition with the coeval seawater carbon values, $\delta^{13}C_{carb}$ is used to reflect $\delta^{13}C_{sw}$ (Keith and Weber, 1964). The reviews by O'Leary (1981) and Farquhar et al. (1989) have pointed out the biochemical background of the C isotope fractionation. During photosynthesis, the light carbon ^{12}C is preferentially taken up by organisms ($\sim -20\text{‰}$), driving the residual seawater to be relatively depleted in light carbon (modern ocean, 0‰) (Keith and Weber, 1964; Berner, 2003). This phenomenon causes the $\delta^{13}C$ depth gradients in the modern ocean. Through photosynthesis, shallow seawater can become depleted in the lighter isotope, while respiration and oxidation of the organic matter may cause the deeper ocean to be enriched in the lighter carbon isotope (Hoefs, 2015).

The long-term carbon cycle is defined by Berner (1999) as the cycle that involves the slow exchange of carbon between rocks and the surficial system, which includes the biosphere, oceans, biota, and soils. Fig. 1.3 shows the average carbon isotope values of a steady-state carbon cycle during the Phanerozoic. Two fluxes control the carbon isotope composition in the ocean: 1. Input fluxes; 2. Output fluxes. For the input flux, the average carbon isotope composition of each component is degassing (-5‰), rock weathering ($\sim 0\text{‰}$), and organic weathering/oxidation ($\sim -22\text{‰}$). For output fluxes, the average carbonate burial value is 1‰ , and organic burial is -29‰ (Kump and Arthur, 1999).

The carbon cycle exerts the main control over atmospheric CO_2 , ocean nutrients, and oxygen (Berner, 1999), which has long been implicated in the evolution of life (Brasier and Lindsay, 1998; Berner, 2003; Shields, 2017). The diagram below shows a box model of the carbon cycle (Fig. 1.4). This diagram shows that carbon enters the ocean-atmosphere system through organic matter weathering, carbonate weathering, volcanic-metamorphic degassing of carbonate, and organic carbon. Over a long time scale ($>$ carbon residence time-about 10^5 y), the sum of all input fluxes and output fluxes should be very close to each other to satisfy mass balance (Berner, 1999). The mass balance equation is shown in Equation 1.2 (f_{org} : The proportion that organic carbon burial makes up of total carbon burial):

$$\delta^{13}C_{in} = \delta^{13}C_{org} \cdot f_{org} + \delta^{13}C_{carb}(1-f_{org}) \quad \text{Equation 1.2}$$

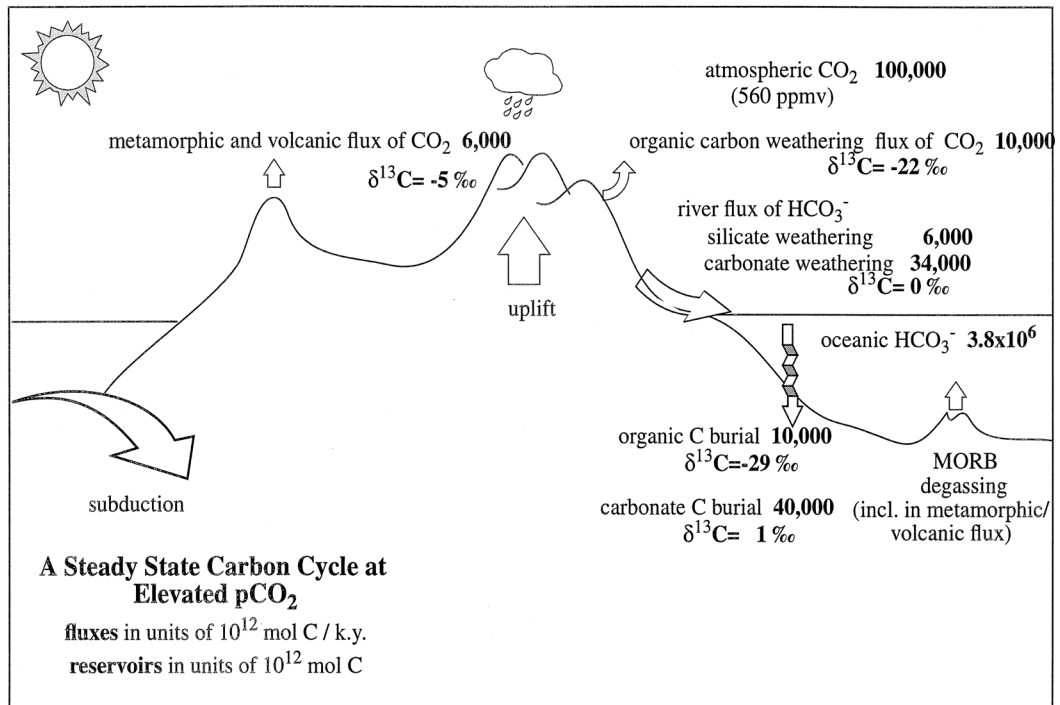


Fig. 1. 3 Schematic diagram shows the long-term carbon cycle with each flux's average carbon isotope compositions during the Phanerozoic. From (Kump and Arthur, 1999).

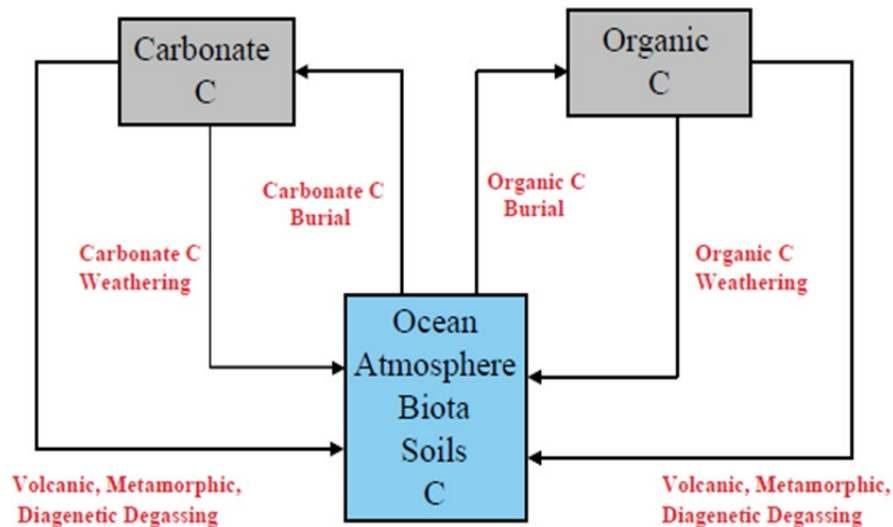


Fig. 1. 4 A box model of the long-term carbon cycle. From (Berner, 1999).

Assuming that the $\delta^{13}\text{C}_{\text{in}}$ is constant and around -6‰ ($\pm 1\text{‰}$) (canonical mantle composition), we can deduce the proportion of organic carbon burial with Equation 1.3. Δ_c is the difference in carbon isotope composition between the inorganic and organic carbon depositional sink (Equation 1.4). Combining Equation 1.3 and 1.4, we can deduce Equations 1.5 and 1.6, which show the $\delta^{13}\text{C}_{\text{carb}}$ and $\delta^{13}\text{C}_{\text{org}}$ and have a linear relationship with f_{org} (Blue lines, Fig. 1.5).

If the steady-state changes from $\delta^{13}\text{C} = +4\text{‰}$ to -8‰ (red arrow 1 to 2), from this figure, this can be related to a change in $\delta^{13}\text{C}_{\text{in}}$ from -6‰ to -12‰ and a change in f_{org} from 0.33 to 0.13 (Shields, 2017). This means that a negative carbon excursion can be caused by a change to an isotopically lighter carbon input flux and/or lower organic matter burial proportion (Rothman et al., 2003).

$$f_{\text{org}} = \frac{\delta^{13}\text{C}_{\text{carb}} - \delta^{13}\text{C}_{\text{in}}}{\delta^{13}\text{C}_{\text{carb}} - \delta^{13}\text{C}_{\text{org}}} \quad \text{Equation 1.3}$$

$$\Delta_c \equiv \delta^{13}\text{C}_{\text{carb}} - \delta^{13}\text{C}_{\text{org}} \quad \text{Equation 1.4}$$

$$\delta^{13}\text{C}_{\text{carb}} = \Delta_c f_{\text{org}} + \delta^{13}\text{C}_{\text{in}} \quad \text{Equation 1.5}$$

$$\delta^{13}\text{C}_{\text{org}} = \Delta_c f_{\text{org}} + \delta^{13}\text{C}_{\text{in}} - \Delta_c \quad \text{Equation 1.6}$$

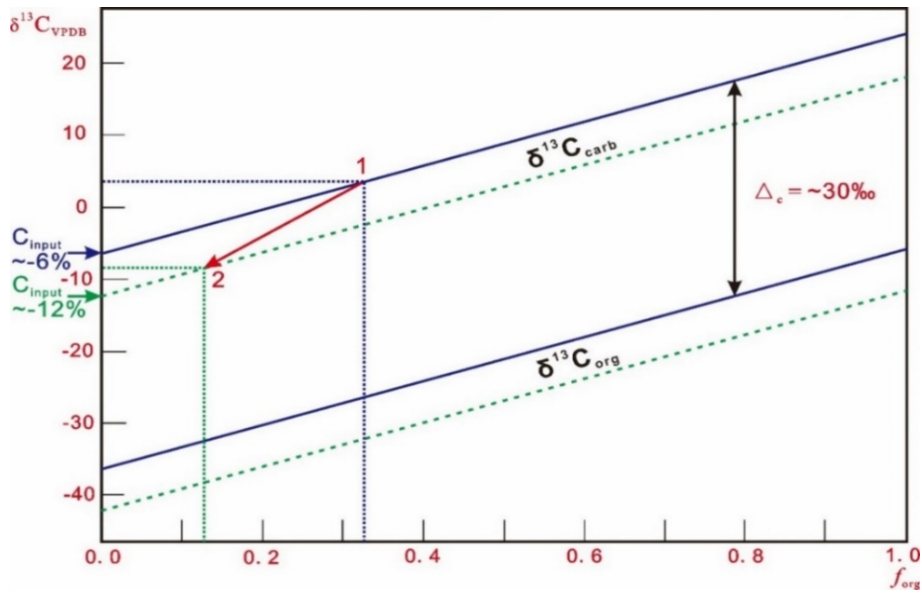


Fig. 1. 5 Long-term carbon isotope mass balance. Modified from (Shields, 2017). The red arrow starts from 1 to 2 means the steady-state changes from 1 to 2.

In summary, negative $\delta^{13}\text{C}$ excursions are conventionally interpreted as being caused by a decrease in biological activity and/or a net increase in weathering/oxidation of organic matter (Knoll et al., 1986; Rothman et al., 2003; Hoefs, 2015; Tostevin, 2015; Shields, 2017). Long-lived negative carbon excursions in seawater ($\delta^{13}\text{C}_{\text{sw}}$), below the canonical mantle value, such as the Shuram-Wonoka anomaly, imply prolonged surplus of organic carbon oxidation over burial that would result in an oxygen deficit, if not compensated by increased oxidant supply in the form of sulfate via weathering (Shields et al., 2019). Alternative explanation is that negative carbon isotope excursions are caused by diagenetic alteration (Bristow and Kennedy, 2008; Derry, 2010; Oehlert and Swart, 2014). However, not all the negative carbon isotope excursions in Earth history show evidence for alteration and several can be correlated globally (Lu et al., 2013; Lee et al., 2015; Lan et al., 2019).

On the other hand, positive carbon excursion might be caused by the overall rate of organic carbon burial exceeding the overall organic matter weathering rate. This means that the net oxygen production rate is high during that period, potentially causing a decrease in the atmosphere-ocean carbon reservoir and global cooling.

1.5 Sulfur Isotopes

Sulfur has four stable isotopes: ^{32}S (95.04%), ^{33}S (0.75%), ^{34}S (4.20%), and ^{36}S (0.01%). Mass-independent fractionation (MIF) of the sulfur isotope refers to a deviation of the measured value of $\delta^{33}\text{S}$ from that expected from $\delta^{34}\text{S}$ and is defined as $\Delta^{33}\text{S} \approx \delta^{33}\text{S} - 0.515 \times \delta^{34}\text{S}$, which is commonly recorded in rocks older than ~ 2.3 Ga (Hulston and Thode, 1965; Pavlov and Kasting, 2002). The preservation of MIF-S signatures indicates a fundamental change of the sulfur cycle and commonly represents the existence of an anoxic atmosphere before ~ 2.3 Ga (Kurzweil et al., 2013; Ono et al., 2013). However, this study mainly focuses on the late Ediacaran period and will not further discuss the MIF-S during the Archean.

Sulfate in the ocean has a residence time of ~ 20 M (modern seawater) (Rees et al., 1978; Claypool et al., 1980; Newton et al., 2004; Tostevin et al., 2014), which means the sulfur isotopic composition of carbonate-associated sulfate (CAS) can be used to interpret ancient seawater $\delta^{34}\text{S}_{\text{sw}}$ and as a global archive of the sulfur cycle (Paytan et al., 1998; Paytan et al., 2004; Böttcher et al., 2007). The ratio between the isotopes ^{32}S and ^{34}S is a good indicator of sulfur biogeochemical cycling in the Earth system. In our environment, sulfur isotope fractionation is mainly controlled by microbial sulfate reduction (MSR: $\text{SO}_4^{2-} \rightarrow \text{S}^{2-}$), which involves anaerobic sulfur-reducing bacteria (Canfield and Thamdrup, 1994). Bacteria excrete H_2S enriched in ^{32}S that can then be buried in pyrite, leaving the sulfate left in seawater isotopically heavier (Fig. 1.6).

In an open system, laboratory experiments show the isotope fractionation $\Delta\delta^{34}\text{S}_{\text{sulfate-sulfide}}$ can be as high as $+45\text{‰} \sim 66\text{‰}$ under high sulfate concentration conditions ($[\text{SO}_4^{2-}] = 28\text{mM}$, modern seawater) (Canfield, 2001b; Sim et al., 2011). With the help of sulfide oxidation ($\text{S}^{2-} \rightarrow \text{S}^0$) and disproportionation, sulfides can be more depleted in ^{34}S (Fig. 1.6). However, in a restricted or close system, Rayleigh fractionation could cause a lower $\Delta\delta^{34}\text{S}_{\text{sulfate-sulfide}}$ but higher $\delta^{34}\text{S}_{\text{sulfate}}$ and $\delta^{34}\text{S}_{\text{sulfide}}$ (Canfield, 2001a; Fike et al., 2015; Cui et al., 2018).

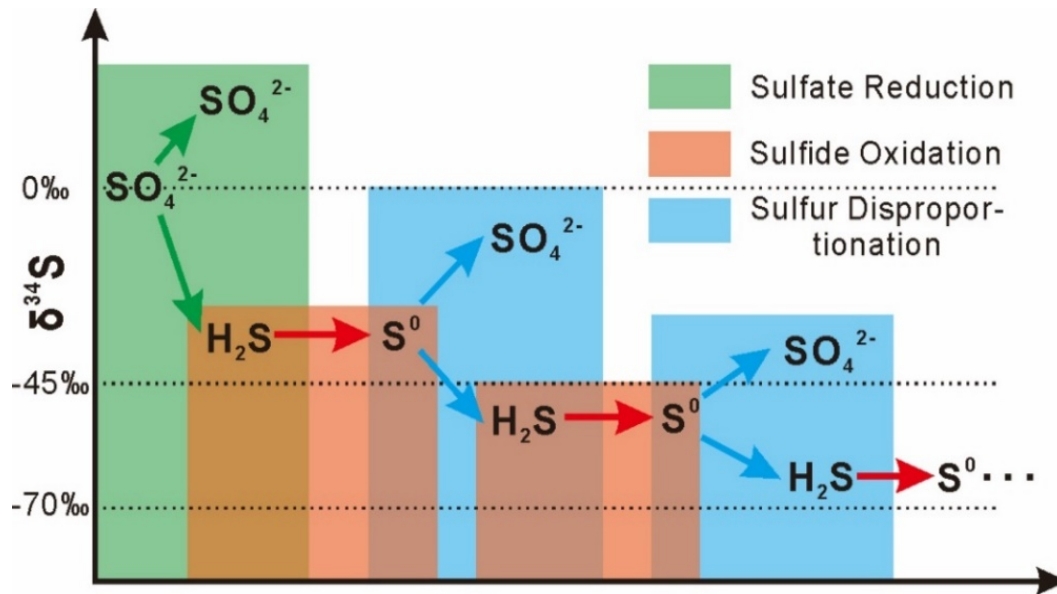


Fig. 1. 6 Biochemical isotope fractionation processes in an open system show that with the help of sulfide oxidation and disproportionation, sulfides can be more depleted in ^{34}S than the single sulfate reduction process. Modified from (Canfield and Thamdrup, 1994).

Another important pathway of sulfate reduction is thermochemical sulfate reduction (TSR), which is an abiotic process (Worden et al., 1995; Machel, 2001; Machel and Buschkuehle, 2008; Cui et al., 2018). Compared with MSR, TSR requires higher temperatures $>110^\circ\text{C}$ and normally has a hydrothermal origin (Machel and Buschkuehle, 2008; Olanipekun and Azmy, 2018). Laboratory experiments show the $\Delta^{34}\text{S}_{\text{sulfate-sulfide}}$ value around $+30 - 40\text{‰}$ at $\sim 200^\circ\text{C}$ (Ohmoto, 1997; Seal, 2006).

The ocean represents a major reservoir of sulfur on earth, with large quantities in the form of dissolved sulfate and sedimentary minerals (e.g., gypsum and pyrite). Two critical fluxes in control of the seawater $[\text{SO}_4^{2-}]$ and $\delta^{34}\text{S}_{\text{sw}}$ are riverine input from the dissolution of gypsum ($\text{CaSO}_4 \cdot 2\text{H}_2\text{O}$), anhydrite (CaSO_4), and oxidative weathering of pyrite (Fe_2S) and marine output through pyrite burial (evaporite and carbonate precipitation has no fractionation with seawater) (Fig. 1.7). Sulfate reduction is the main cause of sulfur isotope fractionation. Being reduced by bacteria, sulfide still has the potential to be re-oxidized again, but if buried as pyrite, isotopically light sulfur could be removed more permanently and efficiently. However, if the pyrite buried in pool water, the pyrite S isotope values could be much higher during Rayleigh distillation (Canfield, 2001a; Fike et al., 2015). By comparing with coeval pyrite sulfur isotopes, we can know more about redox conditions, sulfate concentrations, and biogeochemical cycling.

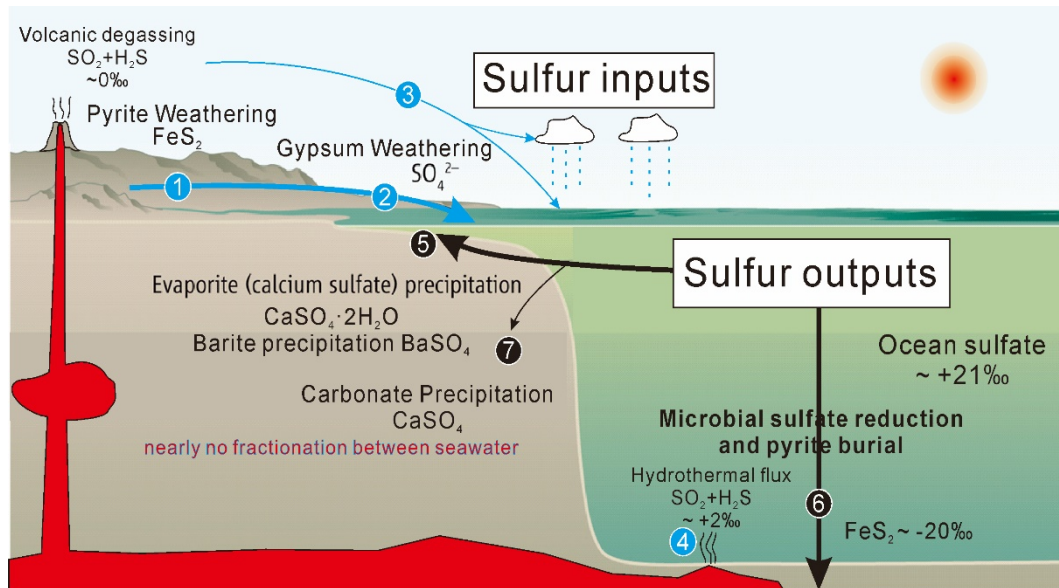


Fig. 1. 7 A simple diagram showing the marine sulfur cycle and the main control fluxes. The blue arrows show the sulfur input fluxes, whereas the black arrows represent the output fluxes. The thickness of the arrows represents the relative proportion of each flux. Flux and isotopic parameters from (Canfield, 2004; Bottrell and Newton, 2006; Fike et al., 2015)

1.6 Uranium Isotopes

Uranium isotopes can provide global average redox conditions of the paleo seawater because U has a longer residence time (~ 450 kyr in the modern ocean) than the ocean mixing time (~ 1 kyr) and has a homogenous value of $\delta^{238}\text{U}_{\text{seawater}} = -0.392 \pm 0.005\text{‰}$ (modern seawater) (Tissot and Dauphas, 2015; Lau et al., 2017; Zhang et al., 2020b; Wei et al., 2021b).

Uranium has two redox states, U^{6+} (soluble and forms uranyl bi-carbonate complexes in natural waters) and U^{4+} (relatively insoluble) (Andersen et al., 2014). Fig. 1.8 shows, in the uranium cycle, that the major input is from rivers (88%), and outputs are suboxic and anoxic sediments ($\sim 26\%$) and carbonate ($\sim 23\%$) (Andersen et al., 2014). In modern seawater, it seems that the reduction of Uranium is dominated by biotic activity with the process caused by the nuclear volume effect (NVE) (Bigeleisen, 1996). Recent work also pointed that limited U isotope fraction could be caused by fast reduction rate of the U and aqueous Ca concentrations (Brown et al., 2018). Despite this potential influences, it is commonly agreed that ^{238}U is preferentially removed in a suboxic and anoxic environment compared to ^{235}U (Weyer et al., 2008; Zhang et al., 2020b). This means that if seawater anoxia increases globally, the uranium concentration ($[\text{U}]$) and uranium isotopic composition ($\delta^{238}\text{U}$) captured in well preserved marine carbonate minerals should

decrease simultaneously (Lau et al., 2017).

Although these seawater $\delta^{238}\text{U}$ signals can potentially be recorded in rocks, marine carbonates are slightly isotopically heavier than seawater by 0.2 - 0.4‰ (Fig. 1.8) because of pore water anoxia influence during early diagenesis (Romaniello et al., 2013; Wei et al., 2018a; Zhang et al., 2018).

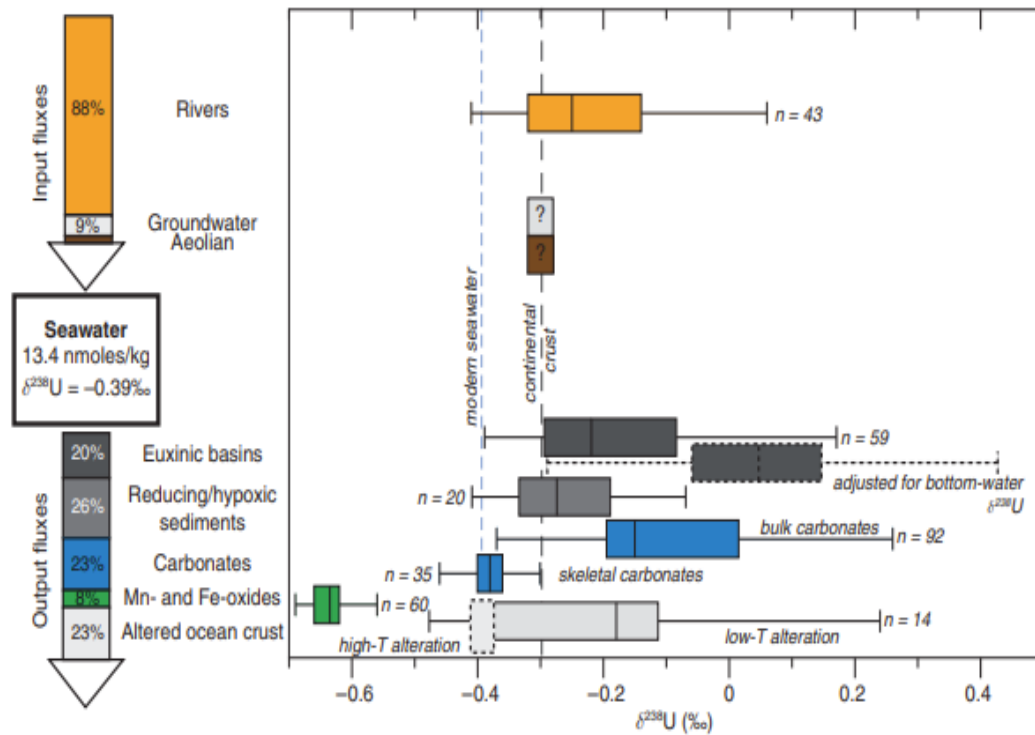


Fig. 1. 8 Modern uranium budget and major ^{238}U fluxes to the ocean. From (Lau et al., 2019).

1.7 Redox Sensitive Trace Elements

Redox-sensitive trace elements (RSTE) (such as U, V, Mo) are sensitive to the redox status of the water column (Emerson and Husted, 1991; Tribovillard et al., 2006; Ansari et al., 2020). These three elements have long residence times in the modern ocean, much longer than the ocean mixing time ($\sim 1\text{kyr}$) (Table 1.2), which makes them good indicators to track the global average conditions (Tribovillard et al., 2006; Gómez-Peral et al., 2019). Except for oxic and anoxic conditions, suboxic and euxinic (water column present free H_2S) are commonly used to describe the paleoredox conditions (Table 1.1). Moreover, anoxic conditions can be euxinic or ferruginous when H_2S occurs in the water column or not.

Table 1. 1 Simple classification of the paleoredox conditions (Tyson and Pearson, 1991; Tribovillard et al., 2006).

Redox state	Oxic	Suboxic	Anoxic	Euxinic
Bottom water oxygen concentration	$[O_2] > 2$ (ml O_2/H_2O)	$2 > [O_2] > 0.2$ (ml O_2/H_2O)	$[O_2] < 0.2$ (ml O_2/H_2O)	$[O_2] = 0$ (ml O_2/H_2O)

Uranium can be reduced from highly soluble U^{6+} in the seawater to relatively insoluble U^{4+} with active sulfate reduction and enriched or precipitated in the sediments (Tribovillard et al., 2006; Schroder and Grotzinger, 2007). It has been noted that reoxidation could lower the sediments' uranium concentration and might shift its isotopic composition (Schroder and Grotzinger, 2007).

Vanadium presents as HVO_4^{2-} and $H_2VO_4^-$ (soluble V^{5+}) in the oxic water column (Table 1.2). In mildly reducing conditions, V(V) can be reduced to VO^{2+} (IV), $VO(OH)^{3-}$ and insoluble $VO(OH)_2$ (Tribovillard et al., 2006). Under euxinic conditions, V (IV) can be further reduced to solid V_2O_3 or $V(OH)_3$ (III) (Wanty and Goldhaber, 1992).

The molybdenum concentration in the seawater is relatively high compared to the crustal values (Table 1.2), which means it is more robust to clastic input and can record seawater values (Schroder and Grotzinger, 2007). Similar to uranium, the main source of the molybdenum in the ocean is riverine input (Tribovillard et al., 2006; Ye et al., 2020). Molybdenum can be slowly absorbed on Mn/Fe-oxyhydroxides (as MoO_4^{2-}) in the oxic water column (amounting to 50% of the total Mo sink) and released again in a reducing environment (Och et al., 2016). In the anoxic environment, fixation of the molybdenum occurs with the help of excess HS^- in the water column, whereby molybdate can be converted to particle-reactive thiomolybdates (as MoO_xS_{4-x}), which can be subsequently removed by organic matter or metal-rich particles (taken up to 15% of the total Mo sink) (Och et al., 2016). However, this process is relatively rare in the open marine environment and only occurs in euxinic water columns ($[O_2]_{aq} = 0 \mu M$; $[H_2S]_{aq} \geq 11 \mu M$).

In summary, RSTE are soluble as oxyanions in the oxic water column and could be reduced to more insoluble or particle-reactive under reducing conditions (Burnett et al., 2006; O'Connor et al., 2015).

Investigate the RSTE enrichment in marine seawater might be able to

reconstruct the evolution history of oxygen in the paleo Earth system. Enrichment factors (EF) can provide a way to normalize and compare trace-element proportions with different contents. Typically, EFs are calculated as $X_{EF} = (X/Y)_{\text{sample}} / (X/Y)_{\text{AUCC}}$, in which X is the trace elements, Y is the normalization element (Al, Th, Ti, Sc, Zr could be used as they are associated with non-carbonate components), and AUCC is the average upper crust abundance value (McLennan, 2001; Schroder and Grotzinger, 2007).

Table 1. 2 Characteristic of redox-sensitive trace elements in the modern ocean (U, V, Mo). Data from (McLennan, 2001; Tribovillard et al., 2006; Och and Shields-Zhou, 2012; Partin et al., 2013)

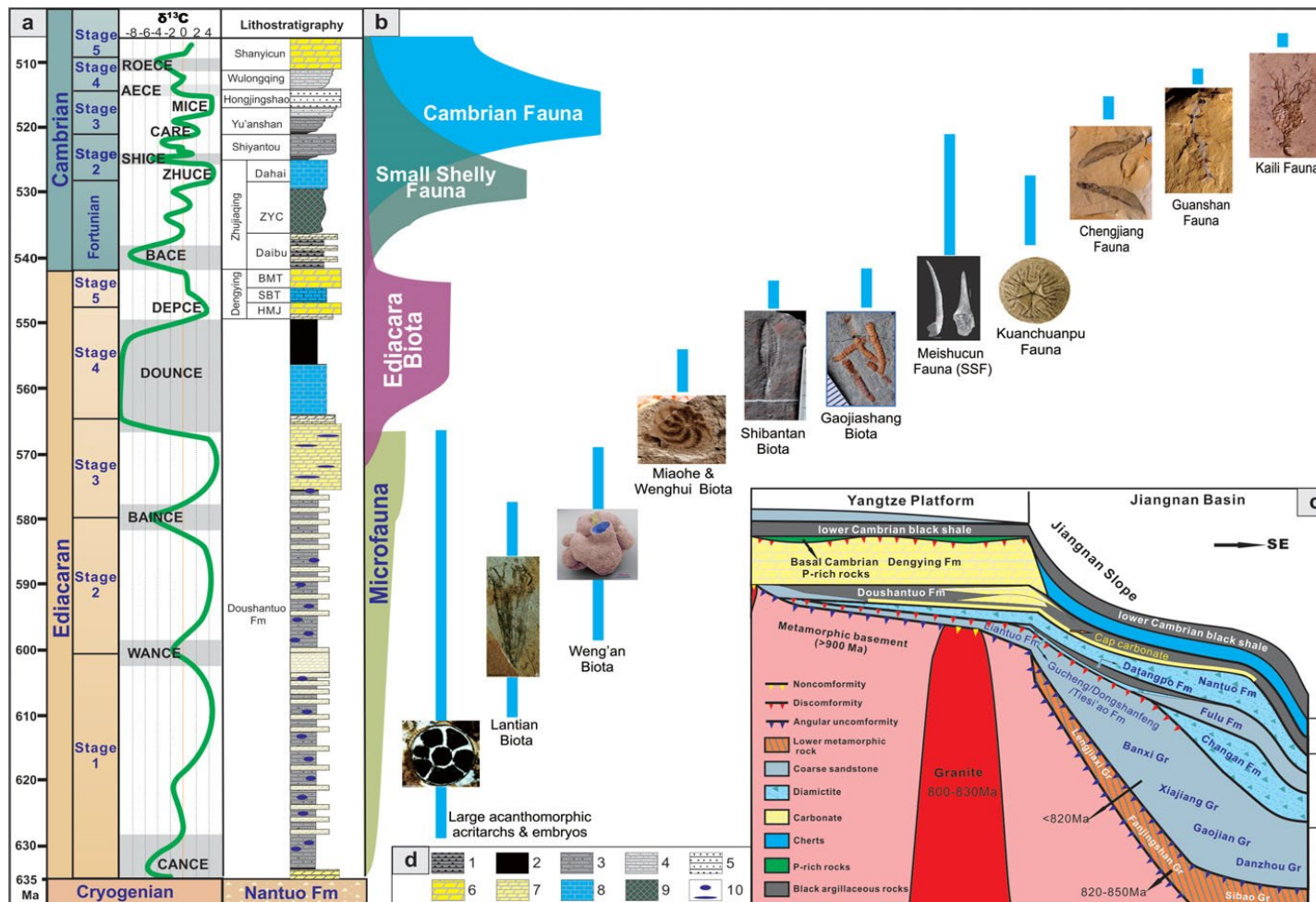
	Uranium	Vanadium	Molybdenum
Residence time (kyr)	450	50	780
Main species in oxic seawater	$\text{UO}_2(\text{CO}_3)_3^{4-}$ /U(VI)	HVO_4^{2-} and H_2VO_4^- /V(V)	MoO_4^{2-} /Mo(VI)
Species in anoxic condition	UO_2 , U_3O_7 or U_3O_8 / U(IV)	VO^{2-} , $\text{VO}(\text{OH})_3^-$, $\text{VO}(\text{OH})_2$, V_2O_3 , $\text{V}(\text{OH})_3$ /V(IV)	Thiomolybdates $\text{MoO}_x\text{S}_{4-x}$ (x=0-3)
Average concentration in the ocean (nmol/kg)	13.4	39.3	107
Average upper crust abundance (ug/g)	2.8	107	1.5

1.8 Late Ediacaran DOUNCE/Shuram Excursion and Its Aftermath

The late Ediacaran negative carbon isotope excursion, the Shuram-Wonoka Excursion (SE), is a major negative $\delta^{13}\text{C}_{\text{carb}}$ anomaly (down to -12‰), which is recorded worldwide in Oman, Siberia, Northern India, South Australia, and South China (Burns and Matter, 1993; Calver, 2000; Condon et al., 2005; Fike et al., 2006; Lu et al., 2013; Shields, 2017). The SE was firstly observed from the Wonoka Formation in South Australia (Jansyn, 1990) and further proved by Urlwin (1992), Pell et al. (1993), and Calver (2000). The SE was also found from the Shuram Formation in Oman (Burns and Matter, 1993) and observed globally in marine carbonate rocks (Le Guerroue, 2006). This negative shift recorded in carbonate rocks stabilized at its nadir for millions of years before returning to pre-event levels (Wang et al., 2012b). The name DOUNCE is used for what is commonly presumed to be the same excursion on the South China Craton, beginning within the upper part of

Doushantuo Member III and ending towards the top of Doushantuo Member IV (Lu et al., 2013; Cui et al., 2015). In most areas, the carbon isotope profiles of the Shuram Excursion show a similar pattern, starting with a sharp shift to the lowest $\delta^{13}\text{C}$ values followed by a more prolonged recovery (Fig. 1.9) (Zhou et al., 2017b).

The DOUNCE/Shuram Excursion is the most severe negative carbon isotope excursion recorded after the Gaskiers glaciation and is commonly interpreted to represent an ocean and/or atmospheric oxygenation event (Fike et al., 2006; Och and Shields-Zhou, 2012). It is believed that the net storage of dissolved organic carbon pool began to accumulate during the Boring Billion (Bartley and Kah, 2004; Paulasantos et al., 2021). The oxidation of such a light $\delta^{13}\text{C}$ DOC pool could have caused negative shifts in the $\delta^{13}\text{C}$ composition of seawater as recorded in sedimentary carbonate rocks, which means that the DOUNCE/Shuram Excursion possibly results from a global oxygenation event that oxidized part of the large DOC pool (Fike et al., 2006; Shields, 2017).



1.9 Global Correlation

Many studies have shown that some major carbon isotope excursions can be used for global stratigraphic correlation because they occurred almost everywhere within the same period, such as the Shuram Excursion (DOUNCE) in this study (Lu et al., 2013; Shields, 2017).

The Shuram Excursion is found in northern India, South Australia, Oman, Scotland, Scandinavia, southeastern Siberia, and western Laurentia and recorded most completely in South China and Oman (Fig. 1.10) (Lu et al., 2013). This negative carbon isotope event is preserved mainly in limestone, and the base of the excursion can be used in chemostratigraphic correlation based on the litho-, bio-, and sequence stratigraphic framework correlation examined by (Zhou and Xiao, 2007). However, both diagenetic alteration and local variation need to be carefully assessed. In South China, the carbon isotopic composition of DOUNCE shifted gradually in a short stratigraphic interval and remained at its anomalously low value for a relatively thicker interval, then followed with a sharp recovery (Fig. 1.10). Although the magnitude of the recorded Shuram Excursion varies among sections, the $\delta^{13}\text{C}_{\text{carb}}$ anomalies can be correlated with other sections in the world (Jiang et al., 2011).

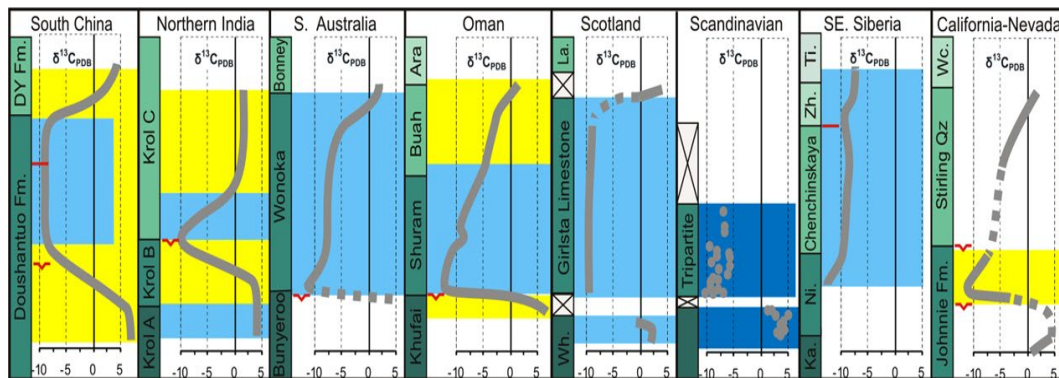


Fig. 1. 10 Comparison of the $\delta^{13}\text{C}$ record of the DOUNCE/Shuram with other parts of the world. From (Lu et al., 2013). Yellow = dolostone; Blue = limestone

1.10 Research Aims

This project is designed to establish a high-fidelity stratigraphic and isotopic chemostratigraphic framework of the late Ediacaran succession in order to improve our understanding of the relationship between paleoenvironmental changes, the carbon cycle, sulfur cycle, oxygenation history, and bio-evolutionary events during that time interval. This research is based on the uppermost Ediacaran strata on the South China Block to establish the paleoenvironmental changes using traditional geologic observations (field, hand specimen, and microscopic observations), geochemistry (C, O, S, U, major and trace elements), and numerical models. This thesis is presented as a series of different research topics. Each chapter will be or has been submitted to scientific journals. The research aims are to:

- Identify possible global isotopic events and trends through the late Ediacaran.
- Improve global stratigraphic and chemostratigraphic correlation through this key interval of Earth history.
- Improve the existing CAS extraction method and establish a robust protocol for CAS extraction.
- Better understand the carbon and sulfur cycles during the DOUNCE/Shuram Excursion and its aftermath.
- Better understand the weathering history during the DOUNCE/Shuram Excursion and its aftermath.
- Better understand the oxygenation history during the DOUNCE/Shuram Excursion and its aftermath.
- And also, combined with these geochemical proxies, build a conceptual model of paleoenvironmental changes during the DOUNCE/Shuram Excursion and its aftermath, incorporating their relationship with the evolution of life.

Chapter 2 Geological Background and Sample Locations

2.1 Paleogeographic Setting of South China Block

Many studies have been conducted to reconstruct the paleo-locations of the South China Block (SCB) during the Ediacaran Period (Li et al., 2013b; Zhang et al., 2013; Yao et al., 2014; Zhang et al., 2015). However, the paleogeographic relationship of the SCB with other continents, in particular, with the India Block and the Australia Block is still not settled yet. The most recent paleomagnetic data from Doushantuo Member III place the SCB close to northwestern India during the Ediacaran and establish that it progressively moved towards northwestern Australia in the late Ediacaran and Early Cambrian (Fig. 2.1) (Zhang et al., 2015).

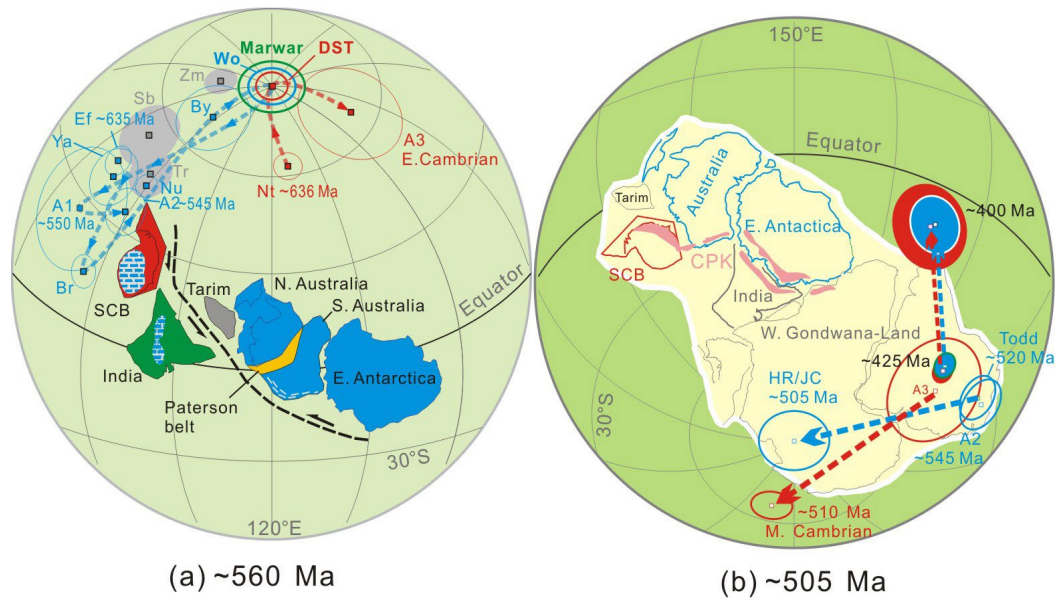


Fig. 2. 1 Paleogeographic reconstruction of the SCB, India, Australian blocks, East Antarctica, and Tarim at ca. 570-560 Ma (a) and ca. 505Ma. From (Zhang et al., 2015).

2.2 Tectonic Settings

In the Late Precambrian, the Earth likely experienced two major tectonic movements. The first one was the break-up of the Rodinia supercontinent (c. 825 Ma – 740 Ma), with episodic superplume magmatic activity at c. 825 Ma, c. 780 Ma, and c. 750 Ma (Li et al., 2008). These superplume events are believed to have been the major driving force that led to the break-up of Rodinia (Wang and Li, 2003; Li et al., 2008). Palaeomagnetic data suggest that Rodinia eventually moved from high

latitudes to equatorial areas at around c. 750 Ma (Li et al., 2004). After that, the global Sturtian glaciation and later Marinoan glaciation occurred during c. 717 – 660 Ma and c. 650 - 635 Ma, respectively (Hoffman et al., 2017). Many scientists have proposed possible links between these snowball Earth events and the break-up of Rodinia, but the matter is still highly controversial (Donnadieu et al., 2004; Rooney et al., 2014; Cox et al., 2016; Shields, 2017).

The subsequent formation of Gondwanaland c. 630 – 530 Ma, which is supported by palaeomagnetic analyses (Li and Powell, 2001), led to intense orogenic movements and continental uplift (Shields, 2017). This event coincided with increasing erosion rates, the rise of oxygen levels, and eukaryotic diversification (Gernon et al., 2016; Shields, 2017).

2.3 Ediacaran Stratigraphy in South China

In South China, the Ediacaran successions comprise the Doushantuo Formation (ca. 635 – 551 Ma) and the overlying Dengying Formation (ca. 551 – 541 Ma) in Hubei, Sichuan, and Yunnan provinces with mainly carbonate rock types. In Hunan and Guizhou provinces, where the paleo depth is deeper, the upper Ediacaran strata comprise the siliceous Liuchapo Formation equivalent to the Dengying Formation (Zhou et al., 2018). In Anhui Province, the Ediacaran strata are named the Lantian Formation and Piyuancun Formation, which are equivalent to the Doushantuo Formation and Liuchapo Formation, respectively.

In the Yangtze Gorges area, the Doushantuo Formation (Fig. 2.2) is around 160m thick at the Jiulongwan section, with an average sedimentation rate of 1.9 m Myr⁻¹. The Doushantuo Formation conformably overlies the Nantuo glaciogenic diamictite and can be divided into four lithostratigraphic Members. One representative stratigraphic and chemostratigraphic profile of Ediacaran successions (Jiulongwan-Shipai section) in South China is shown in Fig 2.2. From bottom to top, the Doushantuo Member I is a 2-6 m cap carbonate unit characterized by sheet cracks, tepee-like structures, macropeloids, and barite crystal fans (Jiang et al., 2003; Och, 2011; Cui et al., 2016b). Member II (c. ~70m) comprises organic-rich shale and thinly interbedded argillaceous dolostone with abundant chert nodules, containing acanthomorphic acritarchs and multicellular algae (Yin et al., 2007; Zhou and Xiao, 2007; Och, 2011). Member III (c. ~40m) is a thin- to thick- bedded unit of alternating

dolostone and limestone beds, in which the onset of the negative $\delta^{13}\text{C}$ DOOUNCE Excursion (=Shuram anomaly) is recorded. Member IV, also referred to as the Miaohu Member, comprises 10-20 m of organic-rich thin black shale layers. However, in the shallow area, this black shale unit is replaced by limestone layers (such as the Zhangcunping section). In the black shale layers, pyrite can be abundant, presenting as pervasive, scattered, or in bands (Sawaki et al., 2010; An et al., 2015; Cui et al., 2015; Zhang et al., 2015).

The Dengying Formation (Fig. 2.2) at the Jiulongwan section is around 540m thick with an average sedimentation rate of 54 m Myr^{-1} . The Dengying Formation overlies the Doushantuo Formation and is characterized by carbonate strata in the Three Gorges area. The bottom and the top are composed of thick-bedded to massive gray dolostone Hamajing Member and Baimatuo Member, respectively. The middle portion comprises the dark thin-bedded limestone Shibantan Member.

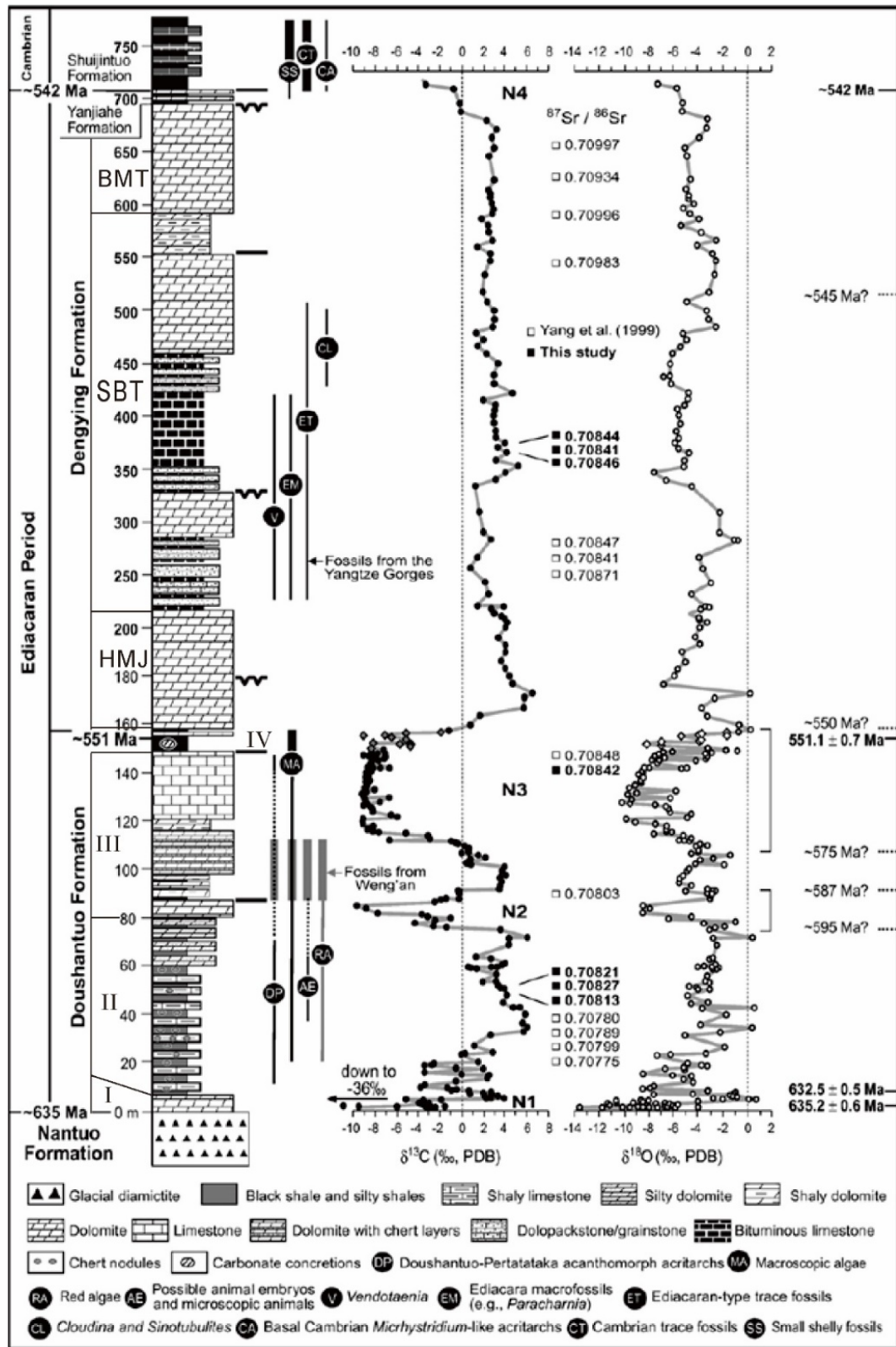


Fig. 2. 2 Stratigraphic column, carbon, strontium, and oxygen isotope data of the Ediacaran Doushantuo and Dengying Formations from the Jiulongwan-Shipai section in the Yangtze Gorges area. From (Jiang et al., 2007).

2.4 Studied Sections

Three sections' samples have been collected in South China. The Qinglinkou section was sampled by me in the summer of 2019. Lianghong and Sishang section samples were collected previously by Dr. Miao Lu (Nanjing Institute of Geology and Palaeontology, Chinese Academy of Sciences).

These three sections cover a wide area in South China and vary in depositional environments. The location of each section can be found in Fig. 2.3. The Qinglinkou section has been interpreted to represent a slope-deep basin, lagoonal setting. The Lianghong section represents a shallow coastal basin environment, and the Sishang section is an open deep-water slope (Lu et al., 2013).

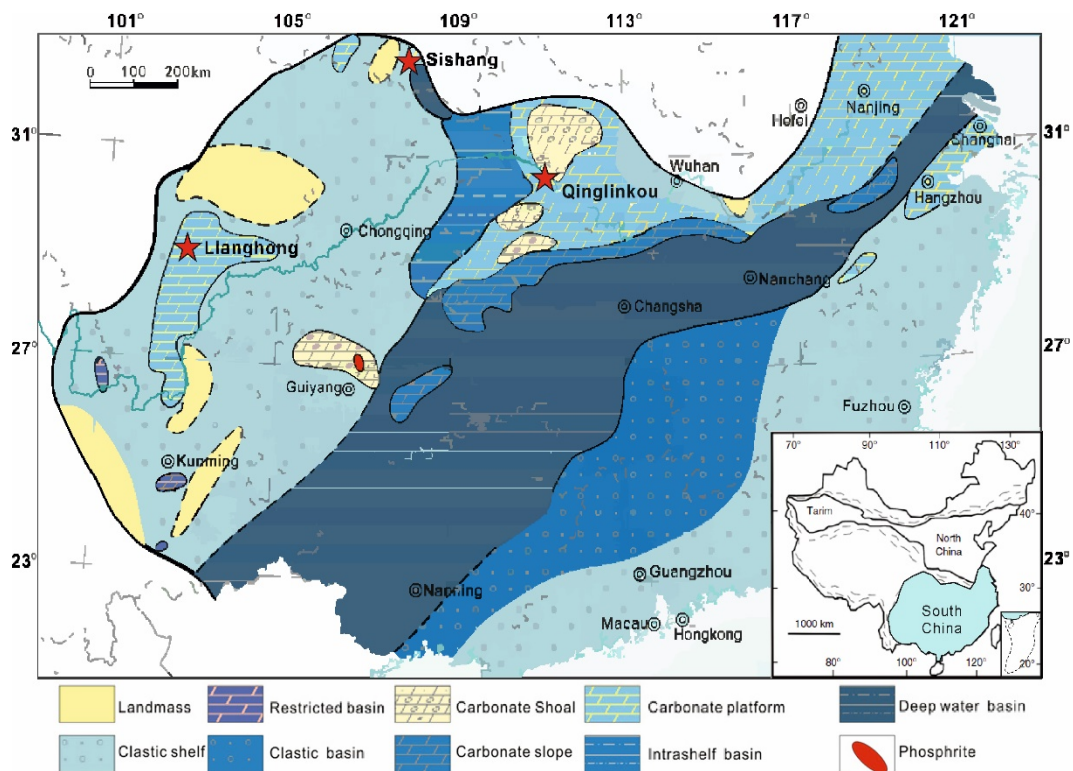


Fig. 2. 3 Simplified geological map and paleogeographic reconstruction of South China Block. Modified from (Lu et al., 2013; Cui et al., 2016b; Lan et al., 2019). The red star shows the location of the three sections (Lianghong, Sishang, and Qinglinkou section) in this study.

2.4.1 Lianghong Section

The Lianghong section samples are provided by Dr. Miao Lu. This section is located at Ganluo County, Sichuan (N29°04'53.2", E102°49'01.7") situated in the southwestern part of SCB (Fig. 2.4). The paleogeographic location is in a restricted shallow coastal basin (Lu et al., 2013). At the bottom part of the Doushantuo Formation in Lianghong (Fig. 2.5-C), the rock type changes from thick-bedded dolostone to thin-bedded dolomitic limestone. This change likely represents a sea-level rise. The middle part comprises edgewise limestone (Fig. 2.5-B), which means the paleoenvironment had shallowed enough to be affected by storms. The top part is composed of banded limestone (Fig. 2.5-A). Detailed petrology descriptions can be found in (Wang et al., 2012b; Lu et al., 2013).

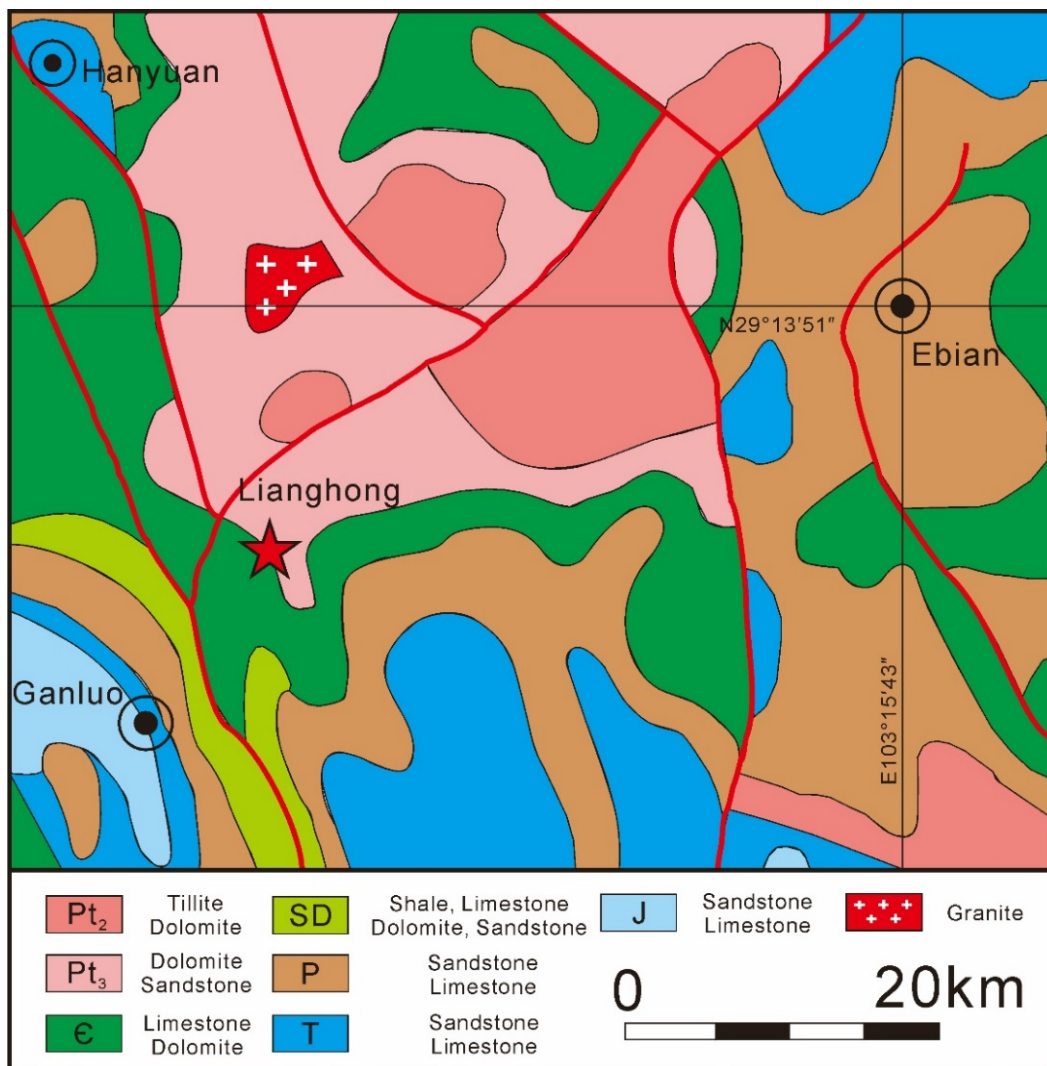


Fig. 2. 4 Simplified geological map shows the location of the Lianghong section and adjacent terranes. Pt₂ Mesoproterozoic, Pt₃ Neoproterozoic.

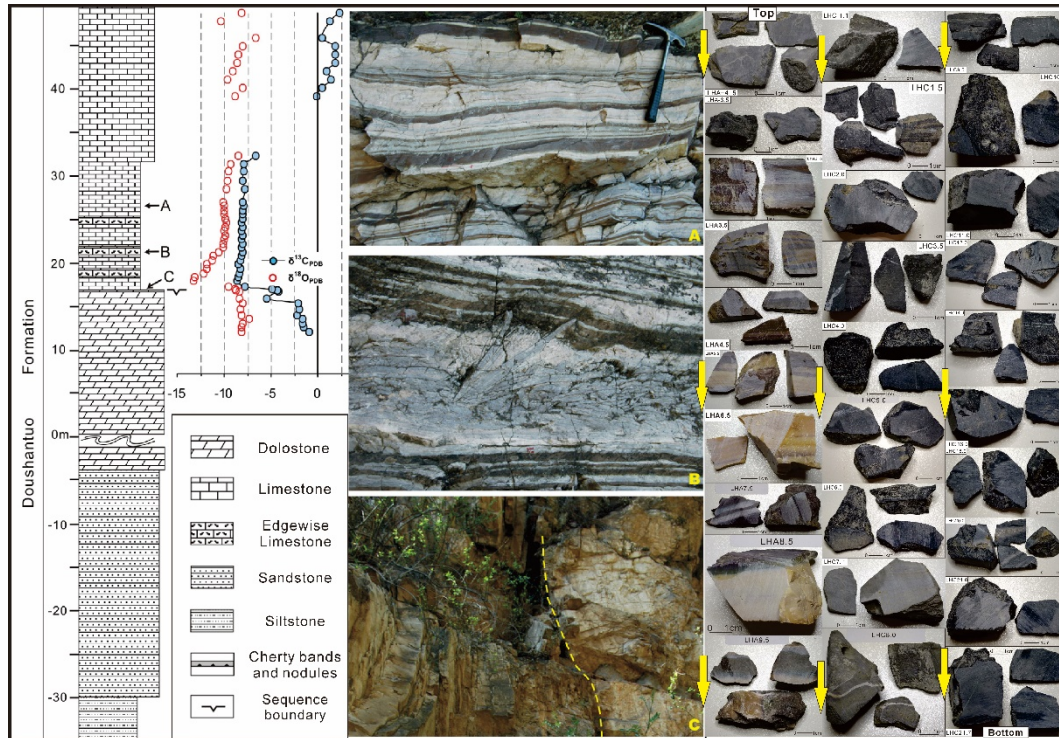


Fig. 2. 5 Stratigraphic column of the Lianghong section and $\delta^{13}\text{C}$ (‰, VPDB) and $\delta^{18}\text{O}$ (‰, VPDB). Modified from (Lu et al., 2013). A: Banded limestone; B: Edgewise limestone; C: a sequence boundary with the lithological transition from thick-bedded dolostone to thin-bedded dolomitic limestone at the basal part of the DOUNCE. The yellow arrows point to the samples at the lower part.

2.4.2 Sishang Section

The Sishang section samples are also from Dr. Miao Lu. This section is located at Sishang, Xixiang County, Shanxi (N32°51'05.7", E107°54'08.2"). The Sishang section is situated at the northwestern part of the SCB (Fig. 2.6). In this section, the rock is mainly thin-bedded limestone with occasionally dark shale interbeds (Fig. 2.7). The Doushantuo Formation is separated by massive dolostone with breccias from the overlying Dengying Formation (Lu et al., 2013). Its paleogeographic location is an open deep-water slope (Lu et al., 2013). Detailed petrology descriptions can be found in (Wang et al., 2012b; Lu et al., 2013).

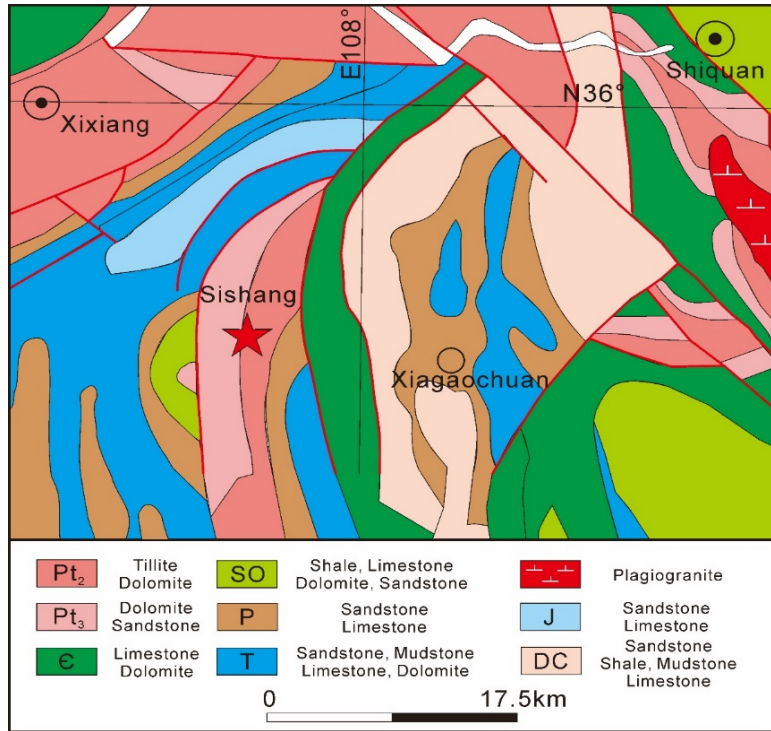


Fig. 2. 6 Simplified geological map showing the location of the Sishang section and adjacent terranes.

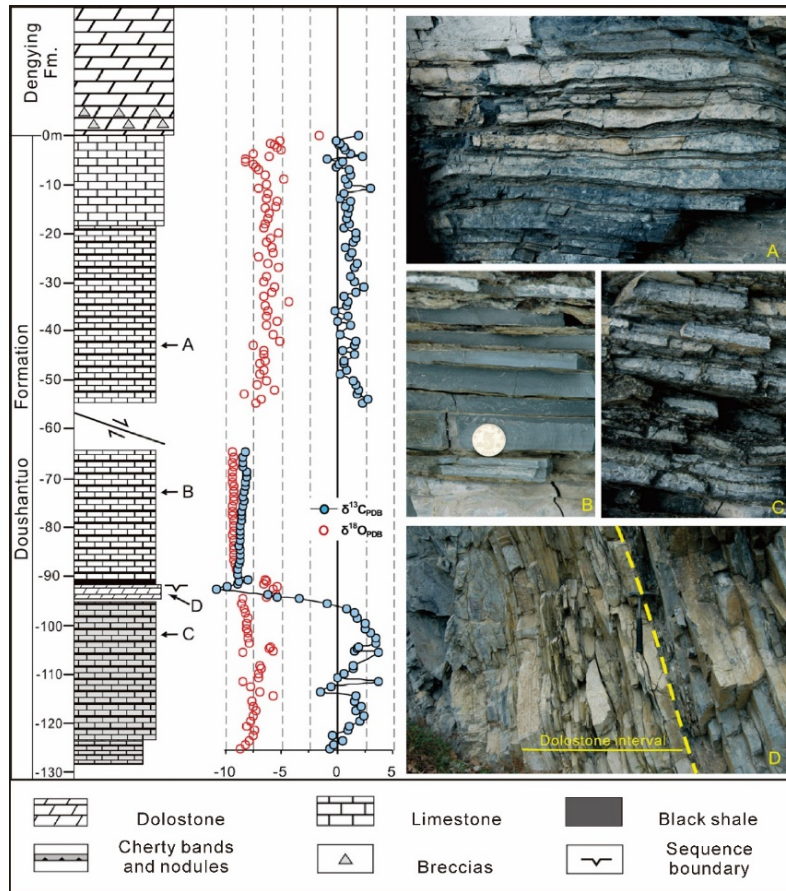


Fig. 2. 7 Stratigraphic column of the Sishang section and $\delta^{13}\text{C}$ (‰, VPDB) and $\delta^{18}\text{O}$ (‰, VPDB) profiles. Modified from (Lu et al., 2013). A: thin-bedded dolomitic limestone; B and C: thin-bedded limestone; D: the sequence boundary (dashed line) at the base of the DOUNCE in the section. The coin is 25 mm, and the hammer is 32 cm.

2.4.3 Qinglinkou Section

The Qinglinkou section is located at Qinglinkou, Zigui county, Hubei Province (N30°47'45.22", E110°55'15.81"). The Qinglinkou section is situated at the southwestern limb of the Huangling Anticline area, containing ~320m thick Ediacaran strata (Fig. 2.8). The paleogeographic location during deposition of the Doushantuo Formation is slop to deep basin and during deposition of the Dengying Formation is carbonate platform. Detailed descriptions can be found in Chapter 3.

This section is newly exposed by excavation for a recent road in 2019. I collected 159 samples in total as follows:

1. Samples were collected nearly every 0.5-1m to obtain relatively high resolution.
2. Collected samples were selected as being the least weathered and least altered material available.
3. GPS locations of sampling localities were recorded.

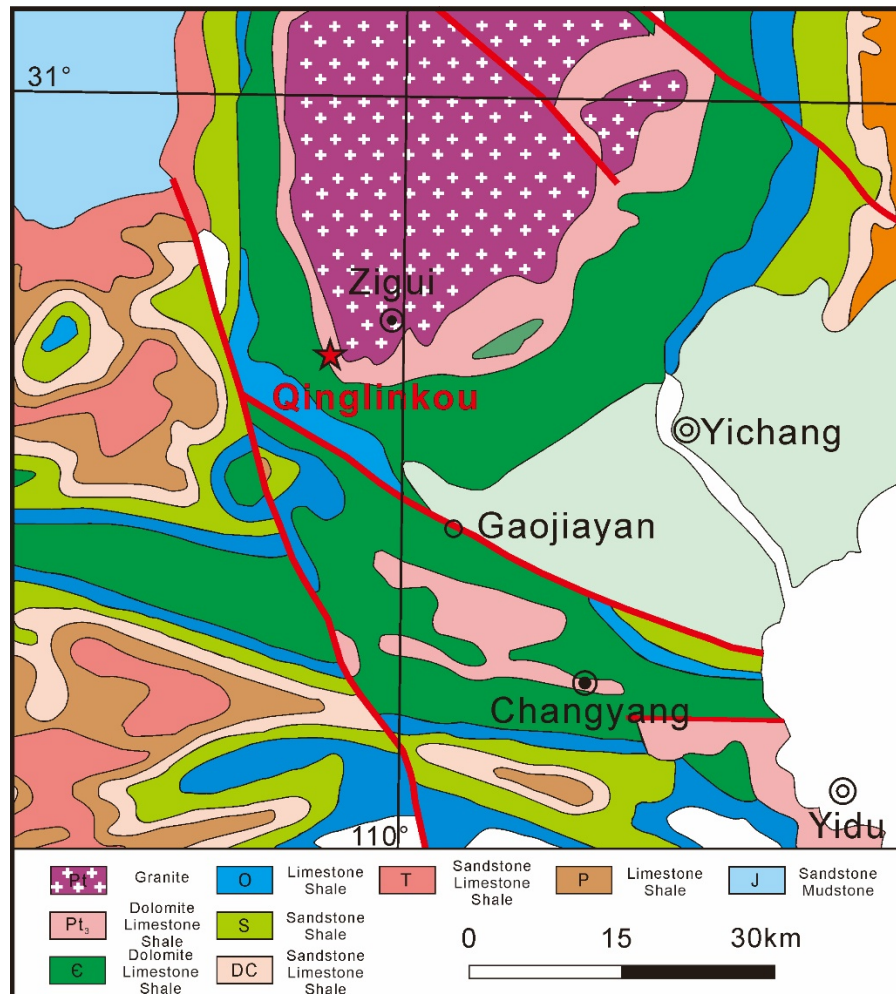


Fig. 2. 8 Simplified geological map showing the location of the Qinglinkou section and adjacent terranes.

2.4.4 The Age Framework of the Ediacaran Excursions in South China

The exact timing of the DOUNCE/Shuram excursion is not fully settled yet. However, a constraint on the termination time is given by the zircon U-Pb dating of the uppermost Doushantuo black shale (Fig. 2.9), which provides an age of $c. 551.07 \pm 0.61$ Ma (Condon et al., 2005). In this study, the upper Hamajing Member recorded the recovery part of the DOUNCE, which might suggest the termination time of the DOUNCE is slightly later than 551 Ma. The onset time of the DOUNCE from stratigraphic analyses and Sr isotope data is younger than $c. 580$ Ma (Sawaki et al., 2010). Whereas the entire excursion was suggested with a range of $ca. 575$ - 551 Ma by (Jiang et al., 2007; Shi et al., 2018). The Re-Os ages suggested that the Shuram excursion in Oman is 578.2 ± 5.9 Ma to 562.7 ± 3.8 Ma, in northwestern Canada is 574.0 ± 4.7 Ma to 567.3 ± 3.0 Ma, in Newfoundland is 574.17 ± 0.66 to 562.5 ± 1.1 Ma (Rooney et al., 2020). The overall duration of the Shuram excursion is less than 11.7 ± 1.3 Ma (Rooney et al., 2020). Condon et al. (2005) reported that the duration of the Shuram Excursion in Oman is < 10 Ma. Cyclostratigraphy indicates the duration of DOUNCE is around $c. 9.1 \pm 1.0$ Myr (Gong et al., 2017; Zhu and Li, 2017) and $c. 8.2 \pm 1.2$ Myr (Minguez et al., 2015). The duration of the Doushantuo Member III is 4.5 Myr based on rock magnetic cyclostratigraphy data (Gong et al., 2017). By comparison in Fig. 2.9, the onset age of this excursion is possibly around $c. 560$ Ma and decreases to the nadir in around 1Ma (Gong et al., 2017). The recovery time is close to 551.07 ± 0.61 Ma. The Baimatuo Member in the Yangtse Gorges area has a U-Pb age of 543.4 ± 3.5 Ma (Huang et al., 2020). The boundary between the Ediacaran and Cambrian has an age of 541.0 ± 1.0 Ma (Yang et al., 2016; Yang et al., 2017).

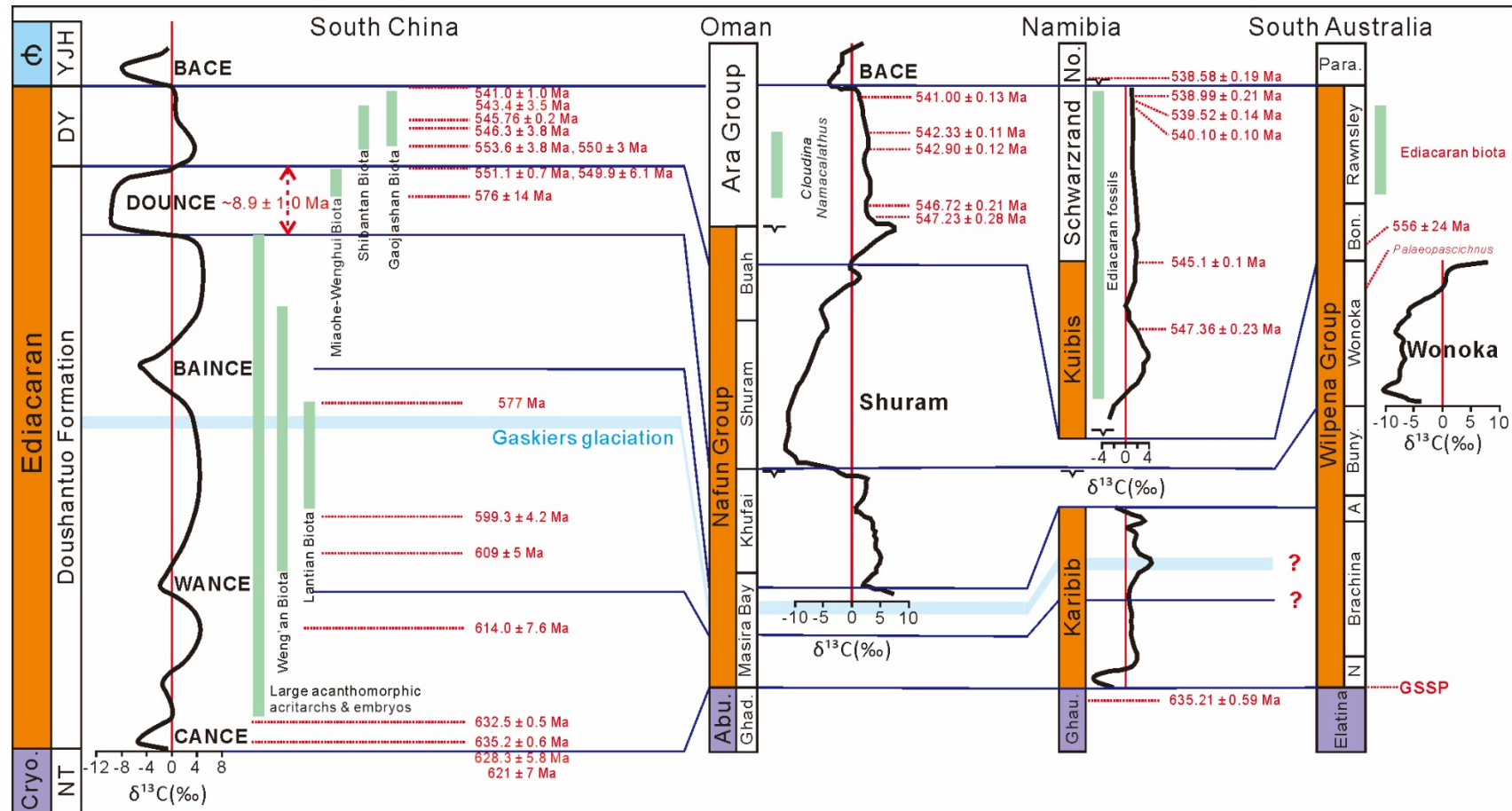


Fig. 2. 9 The comparison of the time model of the Ediacaran period around the world. Modified from (Yang et al., 2016). Published ages in South China are from (Condon et al., 2005; Zhu et al., 2007; Narbonne, 2011; Wang et al., 2012c; An et al., 2015; Yang et al., 2016; Gong et al., 2017; Zhou et al., 2017a; Huang et al., 2020); Data in Oman are from (Bowring et al., 2007; Rooney et al., 2020); Data in Namibia are from (Grotzinger et al., 1995; Bowring et al., 2007; Wood et al., 2015; Linnemann et al., 2019); Data in South Australia are from (Ireland et al., 1998; Minguez and Kodama, 2017; Williams and Schmidt, 2018).

Chapter 3 Chemostratigraphy of the Qinglinkou Section, compared with the Lianghong and Sishang Section

Abstract

The Ediacaran DOUNCE (=Shuram) excursion is the most pronounced negative carbon isotope excursion in Earth history and is thought to reflect a sustained global biogeochemical perturbation. Although the anomaly has been used to correlate late Ediacaran strata worldwide, the occurrence of a carbonate unit with positive $\delta^{13}\text{C}$ values sandwiched between two black shale layers in the western Huangling Anticline area of South China has led some to conclude that the DOUNCE anomaly comprises two separate events. Improved exposure at the Qinglinkou section (Hubei Province) has allowed us to carry out a new structural, sedimentological and chemostratigraphic study, which demonstrates that the middle carbonate is, in fact, a slumped raft that likely derives from the Hamajing Member of the overlying Dengying Formation. In recent decades, the $\delta^{13}\text{C}$ profile has been used widely as a tool for stratigraphic correlation, but my work shows caution must be exercised when using this tool, especially for future workers in the western Huangling Anticline Area.

Author Contributions: The data presented here were mainly from this thesis, but the C and O isotope data from Lianghong and Sishang sections were obtained from (Lu et al., 2013). The samples from the Qinglinkou section were collected with the help of Dr. Wei Shi at CUG in the Summer 2019. The samples from Lianghong and Sishang section were from Dr. Miao Lu and Professor Maoyan Zhu at NIGPAS.

3.1 Introduction

The Ediacaran successions in South China witnessed dramatic paleoenvironmental changes and animal evolution (Lu et al., 2013; Macdonald et al., 2015; Zhu and Li, 2017). Chrono-, bio-, chemo-, litho-stratigraphy, and geochronology have been used to constrain the Ediacaran successions in South China and correlate with other sections globally. Among them, carbon isotope chemostratigraphy has been used as a powerful tool for stratigraphic correlation in many studies because of the lack of Precambrian marker fossils (Lu et al., 2013; Gamper et al., 2015; Zhang et al., 2020c). So far, generally, four major negative excursions have been identified from the previously published carbon isotope profiles in South China Ediacaran successions; they are (from bottom to top): CANCE = Cap carbonate negative carbon isotope excursion, WANCE = Weng'an negative carbon isotope excursion, BAINCE = Baiguoyuan negative carbon isotope excursion, DOUNCE = Doushantuo negative carbon isotope excursion, of which DOUNCE is the most significant negative carbon excursion in Earth history and can be correlated to the global Shuram-Wonoka excursion (Zhu and Li, 2017).

However, due to regional influence, the interpretation and correlation of the $\delta^{13}\text{C}$ records in South China can be very different (Lu et al., 2013; An et al., 2015; Zhou et al., 2017b). Two key factors might cause these different interpretations. The first factor might be mistaken stratigraphic observations. The second factor involves the influence of diagenetic or later alteration processes. However, due to stratigraphy complexity caused by local geological forces, the correlation and interpretation of these published $\delta^{13}\text{C}$ records remain controversial. Furthermore, the argument of the diagenetic effect adds more complications.

Here I focus on the DOUNCE/Shuram excursion. In the Huangling Anticline area, especially in the western region, previous studies have different opinions about the DOUNCE pattern and stratigraphic correlation. Different from the other places in South China, where the DOUNCE shows a much simpler pattern, which starts with a relatively gradual decline of $\delta^{13}\text{C}$ values to a plateau value around -8‰, followed by a variously abrupt or gradual recovery (Lu et al., 2013), sections in the western region of the

Huangling Anticline area seems to contain two negative $\delta^{13}\text{C}$ excursions separated by positive values captured in the middle carbonate layers in between two black shale layers (Lu et al., 2013; An et al., 2015; Zhou et al., 2017b). For this, there are three different interpretations about the stratigraphic and chemostratigraphic correlation. Some scientists (Lu et al., 2013; Zhu et al., 2013) suggest that the middle carbonate layer is a large olistostrome block and the two separate negative carbon isotope excursions are from the same unit; some others (Zhou et al., 2017b) propose that the upper Doushantuo Formation in the western region records two negative $\delta^{13}\text{C}$ excursions rather than one; the third view argues that the negative excursion of the lower black shale layer is equivalent to the DOUNCE, and the upper black shale layer correlates with the Shibantan Member of the Dengying Formation (An et al., 2015), which means the termination of the DOUNCE could be much older than 551.09 ± 1.02 Ma, which derives from the ash bed at the upper black shale layer (Condon et al., 2005; An et al., 2015; Yang et al., 2016).

Qinglinkou section is one of these western Huangling Anticline sections located in the Qinglinkou, Zigui county, Hubei Province ($\text{N}30^{\circ}47'45.22''$, $\text{E}110^{\circ}55'15.81''$) and contains two black shale layers in the upper Doushantuo Formation. A new data set was obtained from samples collected during 2019, just after a new road cutting had been made. The new field observations and the new data set might shed some light on the stratigraphic correlation of the upper Doushantuo Formation.

3.2 Geological Background

3.2.1 Geological Background of the Yangzi Gorges Area

In South China, Ediacaran strata are mainly composed of the Doushantuo (DST) Formation (ca. 635-551 Ma) and Dengying (DY) Formation (ca. 551-541 Ma). The Doushantuo Formation conformably overlies the Nantuo glaciogenic diamictite and can be divided into four lithostratigraphic Members in the Yangtze Gorges area. Dengying Formation consists of three carbonate units. The bottom and the top are composed of thick bedded to massive gray dolostone Hamajing Member and Baimatuo Member,

respectively. The middle portion is comprised of the dark thin-bedded limestone Shibantan Member. The Shibantan Member and Baimatuo Member both contain fossils of the Shibantan biota.

The Huangling Anticline area can be divided into three regions (Fig. 3.1): Western Region, Central Region, and Eastern Region (Zhou et al., 2017b). Briefly, the Eastern region is characterized by dolostone with a very thin black shale unit ($< 1\text{m}$, or even absent) on top of the Doushantuo Formation. The central region is characterized by one black shale unit (Doushantuo Member IV), as shown in Chapter 2 (Fig. 2.2). In the western region, the upper Doushantuo Formation consists of a lower black shale unit (Shale I), a middle dolostone unit, and an upper black shale unit (Shale II). Detailed descriptions can be found in (Zhou et al., 2017b). This research mainly focuses on the western region of the Huangling Anticline Area, more specifically, the Qinglinkou Section.

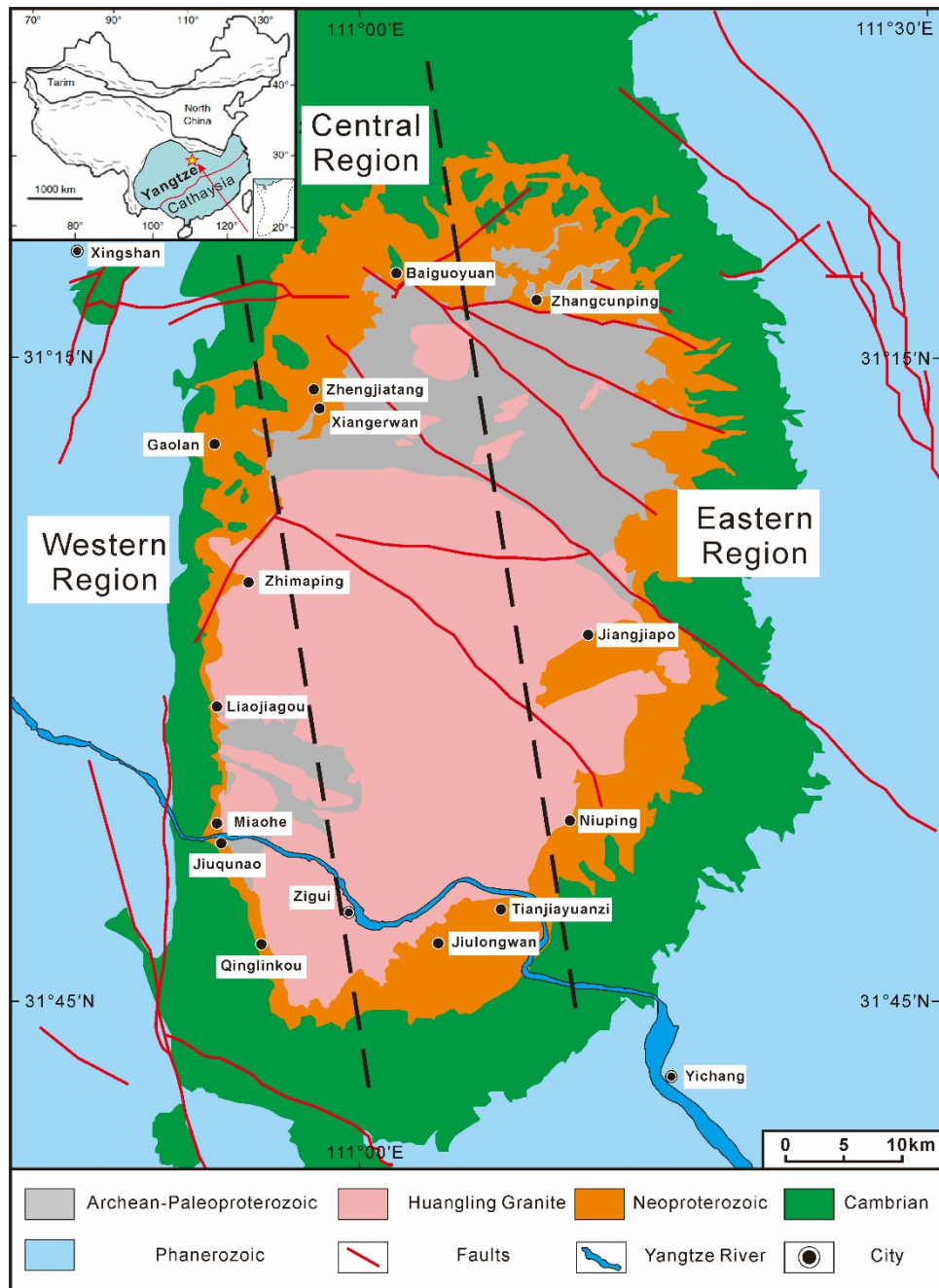


Fig. 3. 1 Geological map of the Yangtze Gorges area shows the Qinglinkou section's location and other sections in the Huangling Anticline area. Two dashed lines divide the Huangling area into three regions. Modified from (An et al., 2015; Zhou et al., 2017b).

3.2.2 Qinglinkou Section

As mentioned above, the stratigraphic framework of the Ediacaran strata in South China is a matter of debate, especially in the western Huangling Anticline area. Qinglinkou section is located at the southwestern limb of the Huangling Anticline area, containing ~320m thick Ediacaran strata. The marker bed of the basal Doushantuo

formation is the cap dolostone (Member I) overlying the Nantuo diamictite (Fig. 3.4-A), which is 4 m thick at the Qinglinkou section (Fig. 3.4-B).

Overlying the cap carbonate is Doushantuo II thin-bedded argillaceous carbonate interbedded with shale layers. The carbonate layer is partially silicified with some chert nodules (size range 3-7cm, Fig. 3.4-C). The upper part of Doushantuo II is thin to medium thick-bedded dolostone interbedded with shale layers. The layers here have been cut by many faults/slumps and exhibit minor folding, especially in the shale layers (Fig. 3.4-D). The thickness of the Doushantuo II is ~116m at the Qinglinkou section

A sharp lithofacies change occurs at level 120m, where the upper part changes to the medium to thick-bedded dolostone layers of the Doushantuo Member III. This rock unit is consistent up to 148m, where the upper layers are disrupted with no bedding observable (Fig. 3.4-E). The lithology of the upper and lower layers shows consistency (similar rock type and color).

At level 160 m, a thin shale layer (30-60cm) occurs, whereby comparison might be the shale I (An et al., 2015). Due to poor exposure and being covered by vegetation, previously, some scientists thought this rock unit to be a consistent, unique layer in the western Huangling Anticline area (Xiao et al., 2012; An et al., 2015; Zhou et al., 2017b). However, my field observations demonstrate that this shale layer is not continuous and sits in unconformable contact with the upper and lower layers (Fig. 3.4-F).

The shale I unit unconformable contact with the overlying middle dolostone unit (Fig. 3.4-F), which is highly disrupted and shows no bedding. The thickness of these middle carbonate layers is ~18.1m (measured from the top of shale I to the base of shale II). Another thick shale layer (shale II, ~9m) lies on top of this middle carbonate (Fig. 3.4-G). This shale layer shows bedding parallel with the overlying Hamajing Member carbonate rocks (7.8m, Fig. 3.3). Large carbonate concretions (20-35cm) are bedded among the shale II layers (~9m, Fig. 3.2). The beds of the Hamajing Member show folding and become more tabular upward into the lower Shibantan (Fig. 3.3). The previous interpretation of the top Hamajing Member is an exposure surface (An et al., 2015), but Fig. 3.3 shows the contact between the Hamajing Member and the lower Shibantan Member is consistent with no exposure textures (such as ripple mark,

desiccation crack, rain-print) and no conglomerate in lower Shibantan Member.

Lithofacies change from the Hamajing Member dolostone to the Shibantan Member thin-bedded limestone at level ~195m. The bottom Shibantan Member contains spherical or elliptical siliceous concretions (6-12cm, Fig. 3.4-H). Lower-middle Shibantan Member is dark thin-bedded limestone (Fig. 3.4-I). However, the upper Shibantan Member shows lighter color with white calcite veins cutting through (Fig. 3.4-J). Shibantan Member in total has a thickness of ~107m at the Qinglinkou section. A detailed lithostratigraphic description is present in Appendix A.



Fig. 3. 2 Outcrop photo showing the deformed contact between the overlying shale II and underlying middle carbonate. Large carbonate concretions occur within the upper shale II layers.

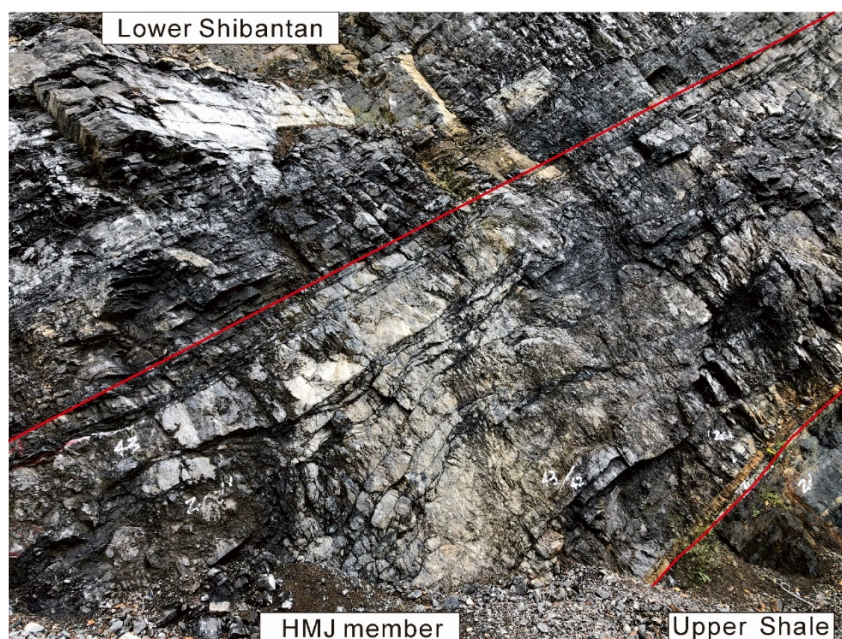


Fig. 3. 3 Outcrop photo showing the folded layers within the Hamajing Member and conformable contact between the upper and lower layers at the Qinglinkou section.

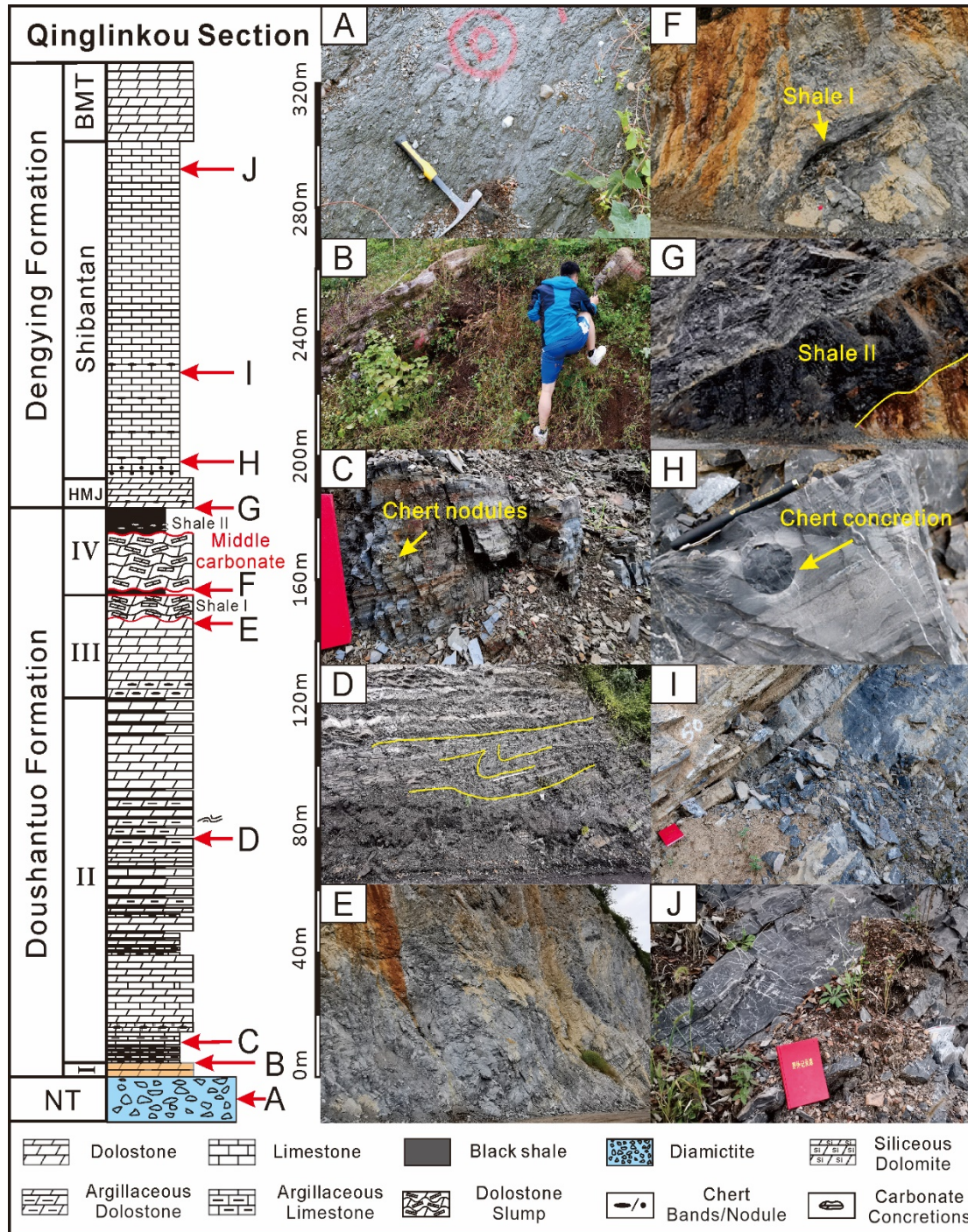


Fig. 3. 4 Stratigraphic column and outcrop photograph of the Qinglinkou Section. A: Nantuo diamictite.

B: 4m thick Doushantuo I cap carbonate. C: lower Doushantuo II thin-bedded carbonate layer interbedded with chert bands. D: middle Doushantuo II medium-thin carbonate layer interbedded with black shale layers. E: Doushantuo III medium-thick dolostone. F: the boundary between the shale I and middle carbonate. G: the boundary between upper black shale II and Dengying Hamajing dolostone. (Carbonate concretions bedded in the shale II layers). H: bottom Shibantan thin-bedded limestone with siliceous concretions. I: lower Shibantan dark grey limestone. J: upper Shibantan light grey limestone with calcite veins cut through. The red curve line represents the slumping surface.

3.3 Methods

A continuous sampling and structural measurement, high-resolution in crucial transitions, has been done at the Qinglinkou section, which is newly exposed by a road cut. Carbonate samples were collected in ~ 0.5-1m stratigraphic intervals. In total, 159 samples were collected for this study. Large block samples were cleaned, crushed into small pieces with a hammer, and carefully selected in China University of Geosciences, Wuhan to minimize mixing with weathered surface and veins. One of the blocks was used for making thin sections at University College London (UCL). The other sample chips were grounded into fine powder ($< 10\mu\text{m}$) using a tungsten carbide Tema Mill. The machine was cleaned carefully with water and acetone to prevent contamination between samples after each crushing process.

For elemental analysis (Ca, Mg, Fe, Mn, Sr, Na, K, Al), 20 mg carbonate rock powder for each sample has been leached with 10ml 2% HNO_3 for 24 h. After centrifugation, the elemental concentration of the supernatant was measured using a Varian® 720 Inductively Coupled Plasma Optical Emission Spectrometer (ICP-OES) at the London Geochemistry and Isotope Centre (LOGIC), University College London. The analytical precisions were better than 5%. Total carbonate/calcite concentrations was calculated based on the Ca concentration and Mg concentration of the sample with the equation: $\text{CaCO}_3 (\%) = [\text{Ca} (\%) - \text{Mg} (\%)] \times 2.5$. Carbonate content (%) was calculated as the weight percentage of the acid leachable CaCO_3 and $\text{CaMg}(\text{CO}_3)_2$ in each carbonate samples.

An aliquot of 300-600 μg of each powder sample has been tested for $\delta^{13}\text{C}$ and $\delta^{18}\text{O}$ analyses at the Bloomsbury Environmental Isotope Facility (BEIF) lab (46 samples from the Doushantuo Member I and II at the Qinglinkou section) in UCL and Department of Geology, University of Tartu. Results are reported as per mil (‰) deviations from the Vienna Pee Dee Belemnite (VPDB) standard.

3.4 Results

3.4.1 Petrography of the Samples

3.4.1.1 Lianghong Section

My sample set mainly covers the upper Doushantuo Formation and part of the Dengying Formation (Fig. 3.5). The dominant rock type here is micrite with few subhedral pyrites (size 5-18 μ m). Detailed outcrop and sample descriptions see (Lu et al., 2013). The grain size and mineral assemblage here show that the Lianghong sections samples are well-preserved with minor diagenesis influence.

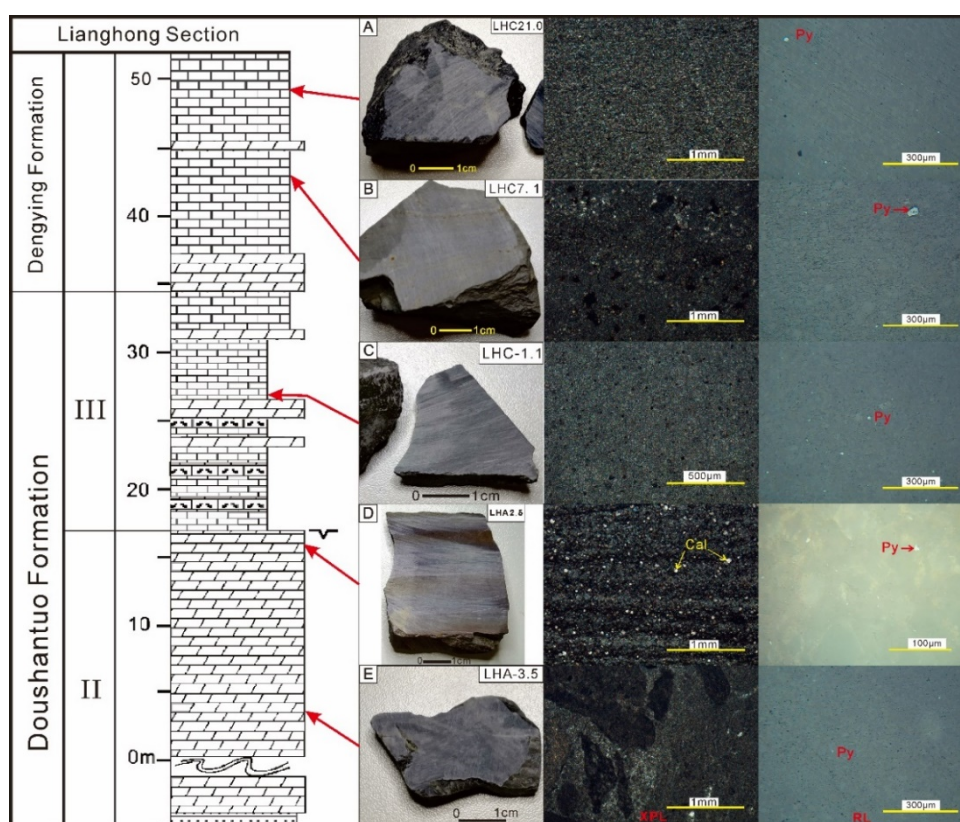


Fig. 3. 5 Representative samples and their microphotographs from the Lianghong section. A, C: Fine-grained limestone; B: Fine-grained dolostone with relatively large calcite grains; D: Fine-grained laminated dolostone with large calcite grains. E: Fine-grained dolostone.

3.4.1.2 Sishang Section

The Sishang section is also dominated by laminated micrite (Fig. 3.6). According to Lu et al. (2013), my sample set mainly covers the upper Doushantuo Formation and part of the Dengying Formation. This section is relatively rich with organics and pyrite

(average size 5-10 μ m). One sample, 16MJW29.5, has larger pyrite crystals with a size range from 10-40 μ m. The grain size and mineral assemblage here show that samples from Sishang sections are well preserved with minor diagenesis influence too.

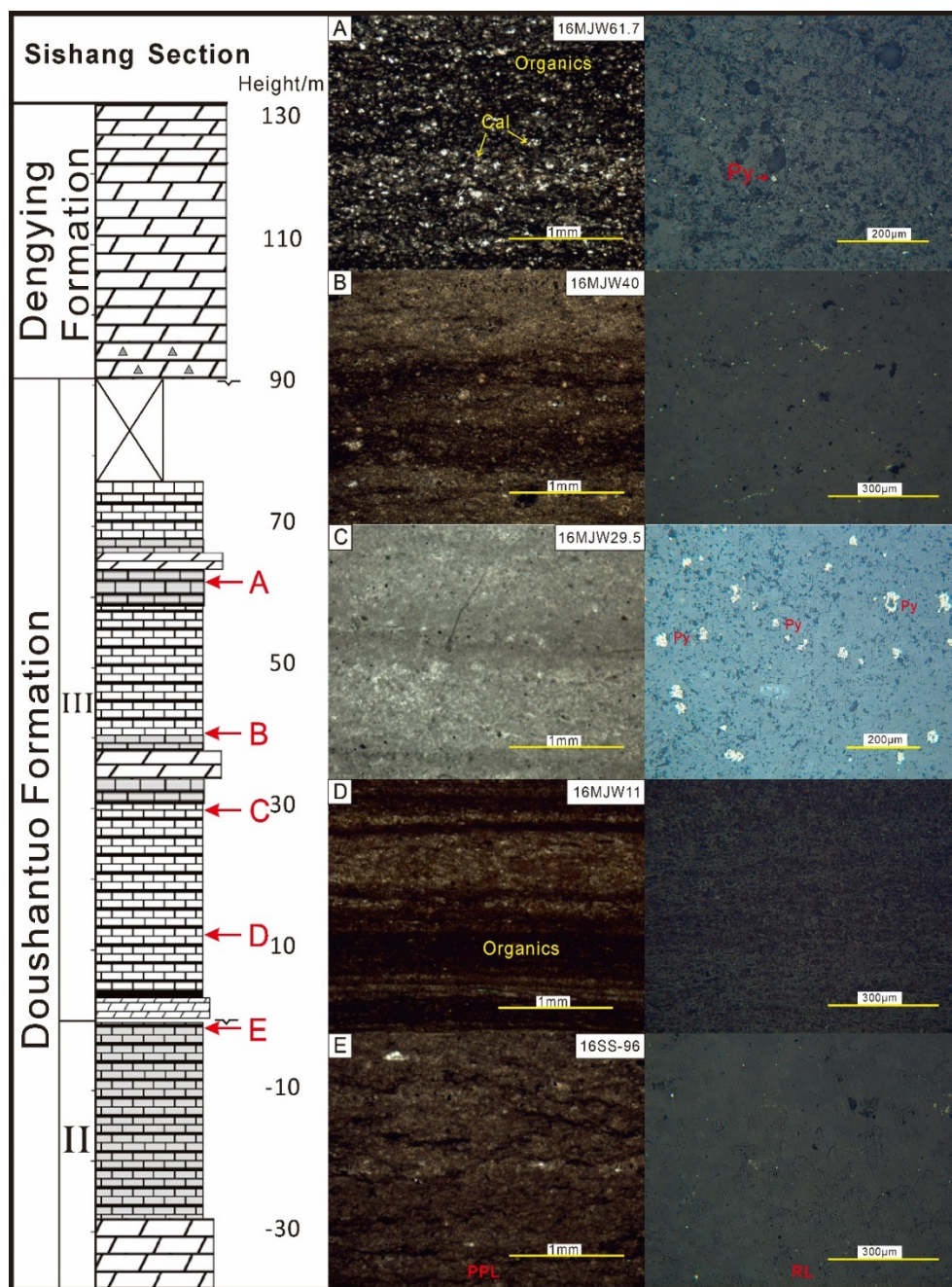


Fig. 3. 6 Representative samples and their microphotographs from the Sishang section, the dominant rock type here is laminated limestone. A: Laminated medium-grained limestone with calcite grains and organics (Sample number is 16MJW61.7, $\delta^{13}\text{C}_{\text{carb}} = 1.09\text{‰}$ and $\delta^{18}\text{O}_{\text{carb}} = -5.86\text{‰}$); B: Fine-grained limestone (Sample number is 16MJW40); C: Fine-grained laminated limestone with relatively high pyrite density (Sample number is 16MJW29.5, $\delta^{13}\text{C}_{\text{carb}} = -8.04\text{‰}$ and $\delta^{18}\text{O}_{\text{carb}} = -9.00\text{‰}$); D: Fine-grained laminated limestone, rich with organics (Sample number is 16MJW11, $\delta^{13}\text{C}_{\text{carb}} = -9.03\text{‰}$ and $\delta^{18}\text{O}_{\text{carb}} = -10.56\text{‰}$); E: Fine-grained limestone (Sample number is 16ss-96, $\delta^{13}\text{C}_{\text{carb}} = -6.20\text{‰}$ and $\delta^{18}\text{O}_{\text{carb}} = -5.49\text{‰}$)

3.4.1.3 Qinglinkou Section

At the Qinglinkou section, shale layers occur interbedded with thin limestone layers at the bottom of Doushantuo Member II and as thick layers containing large carbonate concretions in the upper Doushantuo Formation (Fig. 3.2). The shale samples mainly comprise calcite, organics, pyrite, and some clay minerals (Fig. 3.7). Chert bands are found interbedded with limestone and dolostone at the bottom of the Doushantuo Formation. Siliceous concretions occur at the lower part of the Shibantan Member within the dark thin-bedded limestone layers.

Carbonate is the dominant rock type in this section, which can be further divided into siliceous dolostone, argillaceous dolostone, recrystallized dolostone, and dark limestone (Fig. 3.7). Siliceous dolostone only occurs at the bottom of the Doushantuo Member II. Recrystallized dolostone occurs at the upper Doushantuo Formation and Lower Dengying Formation. The crystal size of the carbonate mineral ranges from 10-50 μ m. However, the recrystallized samples have larger crystal sizes ranging from 40-260 μ m (Fig. 3.7-E, K). Pyrite crystal disseminated as euhedral and framboidal pyrite in the carbonate samples with the size ranging of 5-18 μ m. The shale sample has the most abundant pyrite crystals and the largest pyrite crystals among these samples (Fig. 3.7-I).

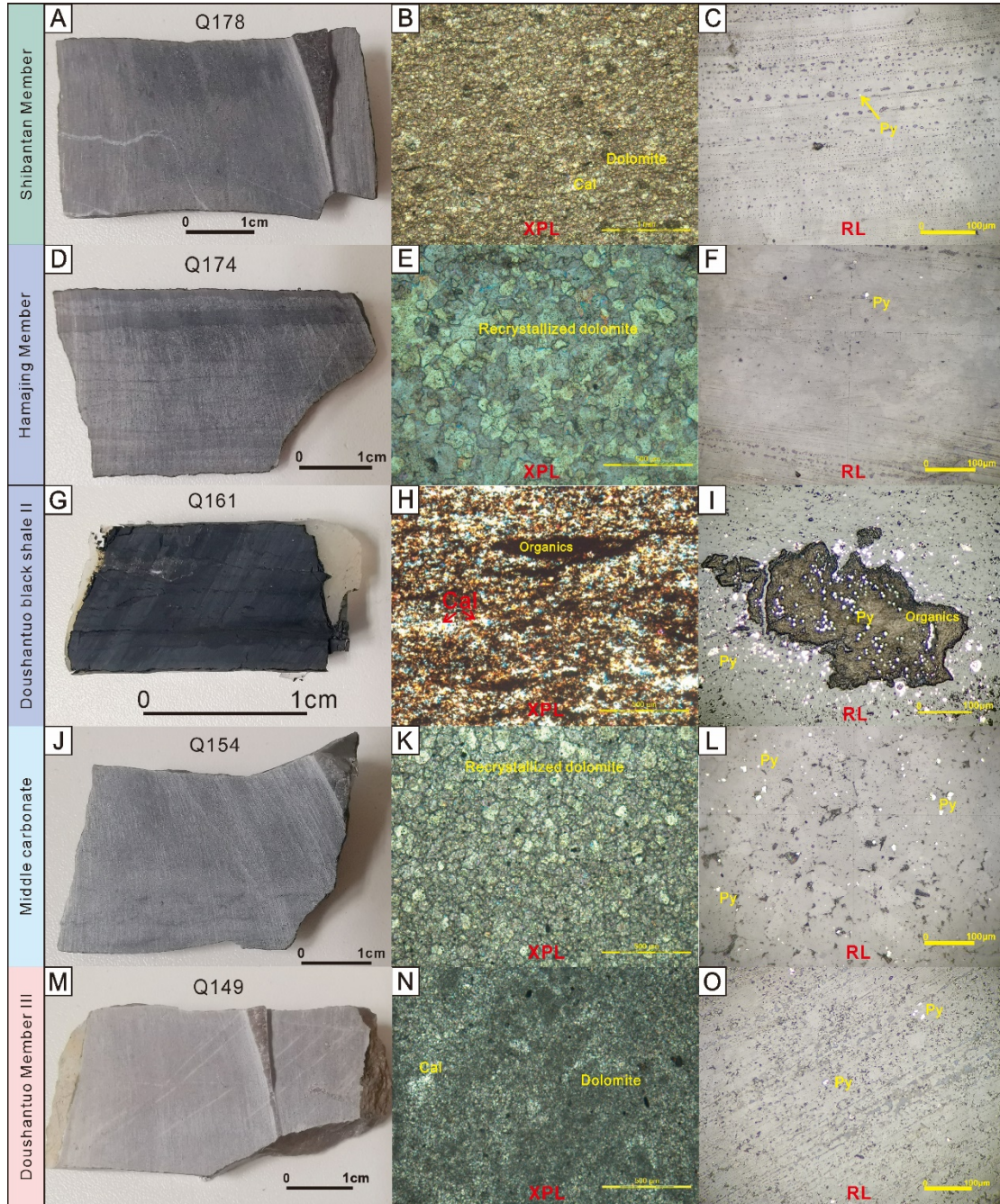


Fig. 3. 7 Typical rock samples and their microphotographs from the Qinglinkou section. (A-C): Dark limestone sample Q178 from the Dengying Shibantan Member, stratigraphic height 199.1m; (D-F): Recrystallized dolostone sample Q174 from the Dengying Hamajing Member, stratigraphic height 194m; (G-I): Shale II sample Q161, stratigraphic height 176.9m. Note the carbonate minerals occupy near 30% of the sample; (J-L): Recrystallized dolostone sample Q154 from middle carbonate unit in between two black shale layers at the Qinglinkou section, stratigraphic height 157.8m; (M-O): Fine-grained dolostone sample Q149 from the Doushantuo Member III, stratigraphic height 145.6m.

Cal=Calcite, Py=Pyrite, XPL=cross-polarized light, RL=reflected light.

3.4.2 Carbon, Oxygen Isotope and Elemental Data

3.4.2.1 Lianghong Section

The $\delta^{13}\text{C}_{\text{carb}}$ and $\delta^{18}\text{O}_{\text{carb}}$ data are published data from (Lu et al., 2013) and also included in Appendix D. Fig. 3.8 show the $\delta^{13}\text{C}_{\text{carb}}$ curve at the Lianghong section reveals extreme negative excursions (range from -9.6‰ to 0.2‰). At level 10-13.7m, the $\delta^{13}\text{C}_{\text{carb}}$ values are relatively constant with an average value $-1.63\text{‰} \pm 0.44\text{‰}$. However, at level 14.4-17m, the $\delta^{13}\text{C}_{\text{carb}}$ decreases dramatically to the lowest value of -8.6‰ and keeps consistently low until level 30m. The level 30-38m is the recovery part of the $\delta^{13}\text{C}_{\text{carb}}$ curve, back to 0.15‰. The Dengying Formation at the Lianghong Section is characterized by positive carbon isotope values around 1.33‰.

The CaCO_3 (wt%) profile and Mg/Ca ratio show the samples below level 16.4m at the Lianghong section are dolostone, but the upper part is mainly limestone interbedded with dolostone. These results coincide with my petrological observation in Fig. 3.5 that most samples at the Lianghong section are limestone.

The Mn/Sr ratios of the Lianghong samples in the upper part of the Dengying Formation are consistently low < 0.5 . The Doushantuo Formation has a higher Mn/Sr ratio, but all the samples have Mn/Sr ratios lower than 10. The Sr concentration and Sr/(Ca+Mg) ratio shows that the Dengying Formation is characterized by high values (average 2365 ppm and 0.0059) compared with the Doushantuo Formation (average 243 ppm and 0.00061). It seems the Sr concentration and Sr/Ca ratio have not been influenced by the lithology shift between samples, especially samples from the Doushantuo Formation. However, the Mn concentration, Mn/(Ca+Mg) ratio, and Fe content, Fe/(Ca+Mg) ratio show a similar pattern with the Mg/Ca pattern, which indicates the dolomitization increase all these four values.

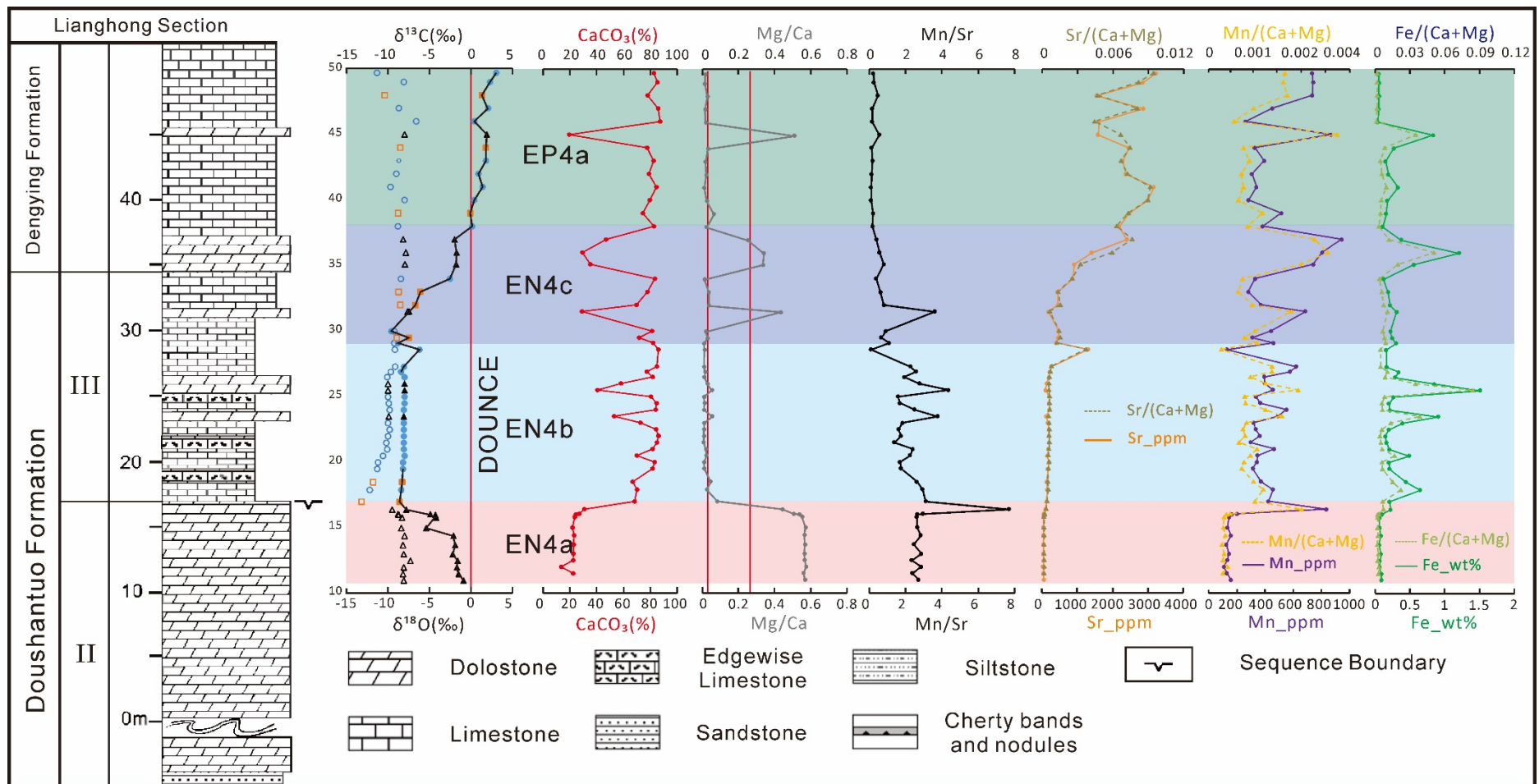


Fig. 3. 8 Lithostratigraphy, $\delta^{13}\text{C}_{\text{carb}}$, $\delta^{18}\text{O}_{\text{carb}}$, and elemental profiles of the Doushantuo and Dengying Formation at the Lianghong section. Shaded symbols in the C-O isotope profile represent the carbon isotope value, and unshaded symbols represent the oxygen isotope value. C-O isotope data were from (Lu et al., 2013).

3.4.2.2 Sishang Section

Fig. 3.9 shows that the $\delta^{13}\text{C}_{\text{carb}}$ curve at the Sishang section reveals extreme negative excursions (from -10.8‰ to 1.9‰). The $\delta^{13}\text{C}_{\text{carb}}$ pattern is similar to the Lianghong Section, which shows a sharp decrease at level -10-0m, before keeping relatively constant at level 0-30m followed with a sharp recovery back to positive values at level 35.5m. The $\delta^{13}\text{C}_{\text{carb}}$ value is constantly high (average 1.1‰) in the upper part of this section except with a minor decrease at level 90m (0.2‰).

The CaCO_3 (wt%) profile and Mg/Ca ratio show that the samples from the Doushantuo Formation at the Sishang section are mainly limestone interbedded with dolostone. The Dengying Formation samples are dolostone. These results coincide with my petrological observation in Fig. 3.6 that most samples at the Sishang section are well-preserved limestone.

The Mn/Sr ratios of the Sishang section samples in the Doushantuo Formation are consistently low <3. However, the Dengying Formation has a higher Mn/Sr ratio, but all the samples have Mn/Sr ratio lower than 10. Different from the Lianghong section, the Sr content and Sr/(Ca+Mg) ratio shows the Dengying Formation here has constant low values (average 69 ppm and 0.00022). The Doushantuo Formation level 32.5-75.4m (average 1558 ppm and 0.0046) shows a different pattern compared with the lower part (average 387 ppm and 0.0012). Similar to the Lianghong section, the lithology shift between samples has not influenced the Sr concentration and Sr/(Ca+Mg) ratio. However, the Mn concentration, Mn/(Ca+Mg) ratio and Fe content, Fe/(Ca+Mg) ratio show a similar pattern with the Mg/Ca pattern.

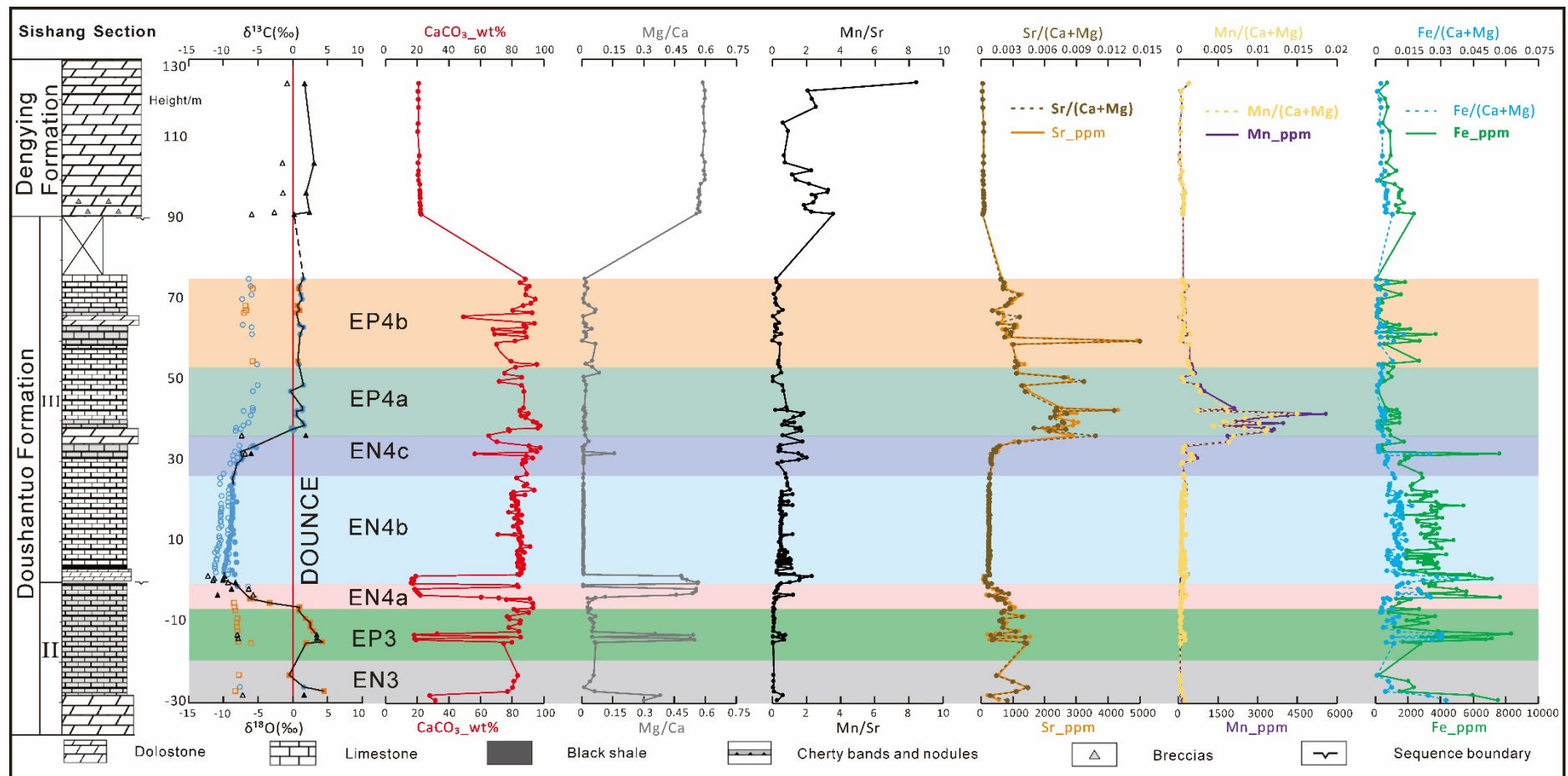


Fig. 3. 9 Lithostratigraphy, $\delta^{13}\text{C}_{\text{carb}}$, $\delta^{18}\text{O}_{\text{carb}}$, and elemental profiles of the Doushantuo and Dengying Formation in the Sishang section. Shaded symbols in the C-O isotope profile represent the carbon isotope value, and unshaded symbols represent the oxygen isotope value. C-O data were from (Lu et al., 2013).

3.4.2.3 Qinglinkou Section

$\delta^{13}\text{C}_{\text{carb}}$ and $\delta^{18}\text{O}_{\text{carb}}$ data are listed in Appendix D. At the Qinglinkou section, the cap carbonate shows a prominent negative $\delta^{13}\text{C}$ excursion with lowest values of -4.4‰ (Fig. 3.10). For the first ~40 m of the Doushantuo Member II, the $\delta^{13}\text{C}_{\text{carb}}$ and $\delta^{18}\text{O}_{\text{carb}}$ values have relatively large fluctuations, which range from -9.3‰ to 4.2‰ and -12.5‰ to -0.9‰, respectively. The $\delta^{13}\text{C}_{\text{carb}}$ and $\delta^{18}\text{O}_{\text{carb}}$ compositions are relatively consistent (~1.8‰ and -4.7‰ respectively) in upper Doushantuo Member II samples in this section except for one negative $\delta^{13}\text{C}_{\text{carb}}$ excursion between 90m-100m, which has the lowest value of -1.0‰. Across the depth from ~137 to 200 m in this section, a mild $\delta^{13}\text{C}_{\text{carb}}$ negative excursion has been recorded at the upper Member III, IV, and Dengying Hamajing Member samples, which can be correlated with the DOUNCE in other sections. The carbonate $\delta^{13}\text{C}_{\text{carb}}$ and $\delta^{18}\text{O}_{\text{carb}}$ values at this depth range from -4.6‰ to 4.4‰ and -7.4‰ to -1.0‰, respectively. In between two black shale layers in Member IV, a positive $\delta^{13}\text{C}_{\text{carb}}$ excursion was recorded in the middle carbonate rock unit from this section. The average $\delta^{13}\text{C}_{\text{carb}}$ and $\delta^{18}\text{O}_{\text{carb}}$ values are 1.20‰ and -1.67‰. Middle and upper Dengying Formation have a narrow range of the $\delta^{13}\text{C}_{\text{carb}}$ and $\delta^{18}\text{O}_{\text{carb}}$ values, which is 1.9‰ to 5.2‰ and -10.3‰ to -4.2‰, respectively.

Major and trace element concentrations of the Qinglinkou section samples display considerable variations. The first ~40 m has quite large fluctuations of the elemental data. The calcium carbonate content and Mg/Ca ratio shows that the carbonate rock among this level is mainly dolomite and interbedded with limestone (Fig. 3.10). The upper part of Doushantuo Member II, III, and Dengying Hamajing Member comprise mainly dolostone samples. However, Dengying Shibantan Member is dominated by pure limestone.

Manganese concentration, Mn/(Ca+Mg) ratio and iron concentration, Fe/(Ca+Mg) ratio displays a similar variation tendency throughout the profile, which decreases from the highest value in the first 40m and then remains constant though Doushantuo Member II and shows a slight rise during the DOUNCE and decrease to the lowest plateau during

the Dengying Formation.

Sr concentration and Sr/(Ca+Mg) ratio display significant variations different from these four values. The profile shows these two values gradually increase from the base cap carbonate and reach the highest value at the middle part of Doushantuo Member II. Then the values decrease again to the lowest value at the middle to upper part of Member III with the mean value of 101.3 ppm and 0.00033, respectively. These two values keep constantly low up until the Dengying Shibantan Member. The Shibantan Member shows a dramatic increase of both the Sr concentration and Sr/(Ca+Mg) with a mean value of 1169.9 ppm and 0.0031, respectively.

To summarize, the $\delta^{13}\text{C}_{\text{carb}}$ curve at the Qinglinkou section reveals four negative excursions EN1-4 recorded in cap carbonate, lower Doushantuo Member II, upper Doushantuo Member II, and Doushantuo Member III, IV & Hamajing Member, respectively.

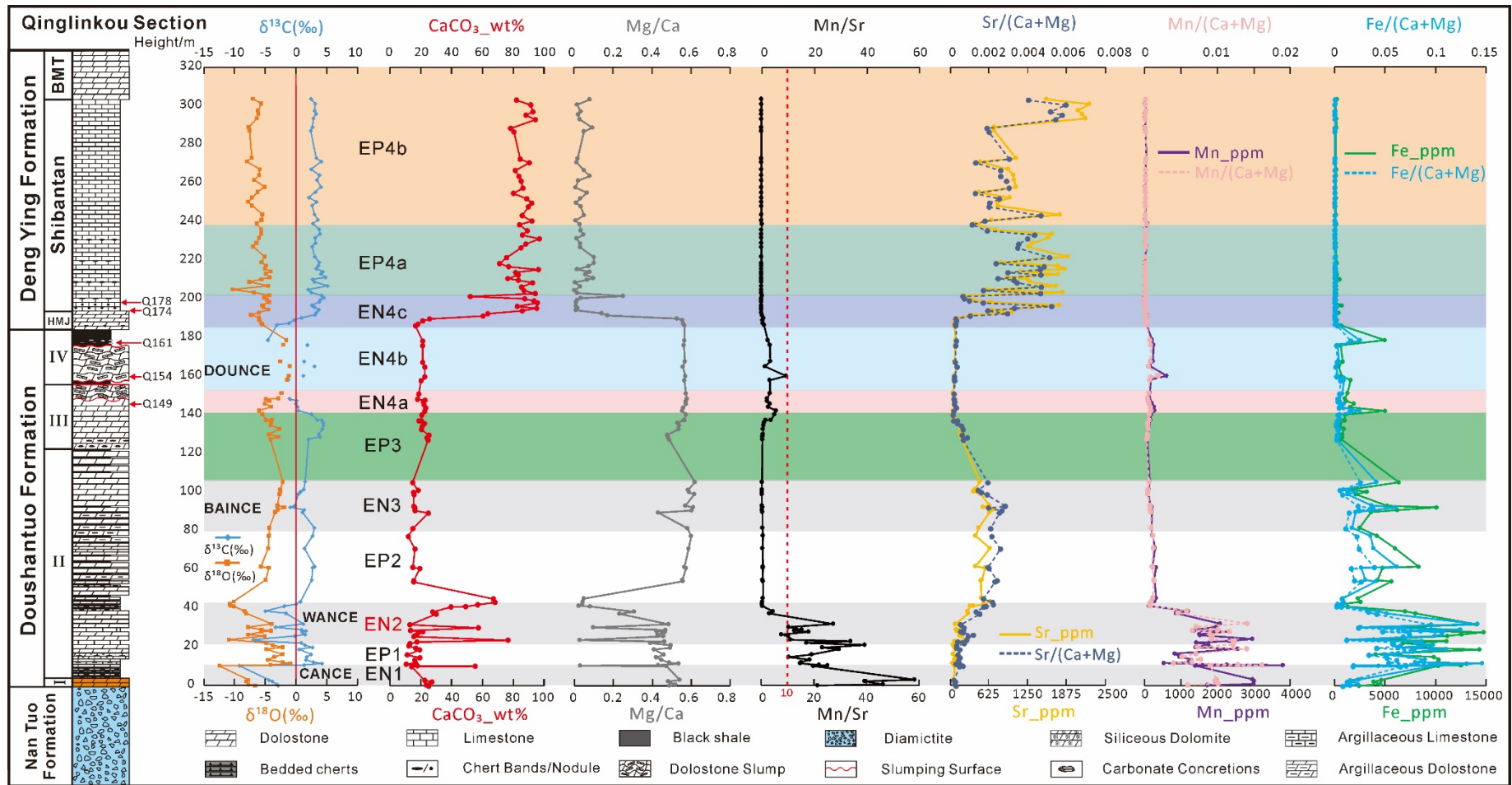


Fig. 3. 10 Lithostratigraphy, $\delta^{13}\text{C}_{\text{carb}}$, $\delta^{18}\text{O}_{\text{carb}}$, and elemental profiles of the Doushantuo and Dengying Formation at the Qinglinkou section. EN=Ediacaran negative excursion, EP=Ediacaran positive excursion, HMJ=Hamajing Member, BMT=Baimatuo Member. DOUNCE=Doushantuo negative carbon isotope excursion. BAINCE=Baiguoyuan negative carbon isotope excursion. WANCE=Weng'an negative carbon isotope excursion. CANCE=Cap carbonate negative carbon isotope excursion.

3.5 Discussion

3.5.1 The Wide Occurrence of Faults/slumps and Folds

Observed and measured in the field, the strata in this section generally dip to SW, and the average angle of dip is 35.8° . At location A (Fig. 3.11-A), a small-scale normal fault has been observed cutting the lower Doushantuo Member I. The hanging wall strata have an orientation of 249° (dip direction)/ 51° (dip angle). However, the footwall layer's orientation is $227^\circ/12^\circ$. The thin-bedded Doushantuo Member II limestone layers are intensely folded with 'Z' shape at location B (Fig. 3.11-B). The angle between the fold's limbs is around 29° and can be divided into tight folds (isoclinal fold) formed by flexural slip. After lower hemisphere projection analysis, the fold axis is oriented $306^\circ/12^\circ$, and the folded plane has the orientation of $042.5^\circ/22.9^\circ$, which shows that the main stress σ_1 is oriented NE-SW. This orientation is parallel to the layers' dip direction, which likely indicates that those folds might have formed together with the tilting of the layers and the forming of the Huangling Anticline. 'Z' shaped folds are well developed among the Doushantuo layers in this section, especially in the thin, soft layers (Appendix A).

The curved 'S' shape glide plane at location C shows that the overlying slumped beds are highly disrupted at location C (Fig. 3.11-C), although the underlying stable deposits are well-bedded dolostone layers. The previous interpretation of this break is an erosional surface (An et al., 2015). However, the upper layers close to the slumping surface are more disrupted than the other parts. No noticeable color changes, exposure textures (such as ripple mark, desiccation crack, rain-print) or basal conglomerate could be observed within this break, which indicates that the erosional surface explanation for this break might not be correct (break S-1 from An et al. (2015)). Moreover, according to the petrological observations, elemental data, and carbon isotope values, the upper disrupted slump unit has a similar rock type and similar carbon isotope values to the lower, bedded layers, which might indicate those rocks are still possibly the Doushantuo Member III but might have been displaced and slumped down, causing layers close to the slumping surface to be more disrupted.

Fig. 3.11-D shows that the lower shale I sharpen to a point at both ends, while the

near left-hand part is thicker than the right part, which indicates that the lower shale I is a slumped rock unit with the slump direction from NE to SW. In between these two black shale layers is the massive dolostone layer (18.1m). The middle carbonate unit shows unconformable contact (Fig. 3.2, 3.11-D, E) with both the upper black shale II and lower black shale I, which suggests that this rock unit is another slumped unit.

The contact between the upper black shale and Hamajing Member seems to show comfortable contact, but the layers within the upper Hamajing Member are folded and become more tabular upward into the lower Shibantan, which suggests that the Hamajing Member might also have been displaced and slumped down along the top surface of the upper black shale. The lithofacies change between the upper black shale layer and the overlying dolostone Hamajing Member is consistent with a significant regression or uplift during formation of the Hamajing dolostone, which might have facilitated submarine movement along detachment surfaces due to reduced frictional strength (Vernhet et al., 2006).

In summary, my observation and analysis show that the middle carbonate unit is unconformably in contact with the upper black shale II and lower shale I layers. Slumping and folds are widely presented in this section. The folds might have formed during the formation of the Huangling Anticline.

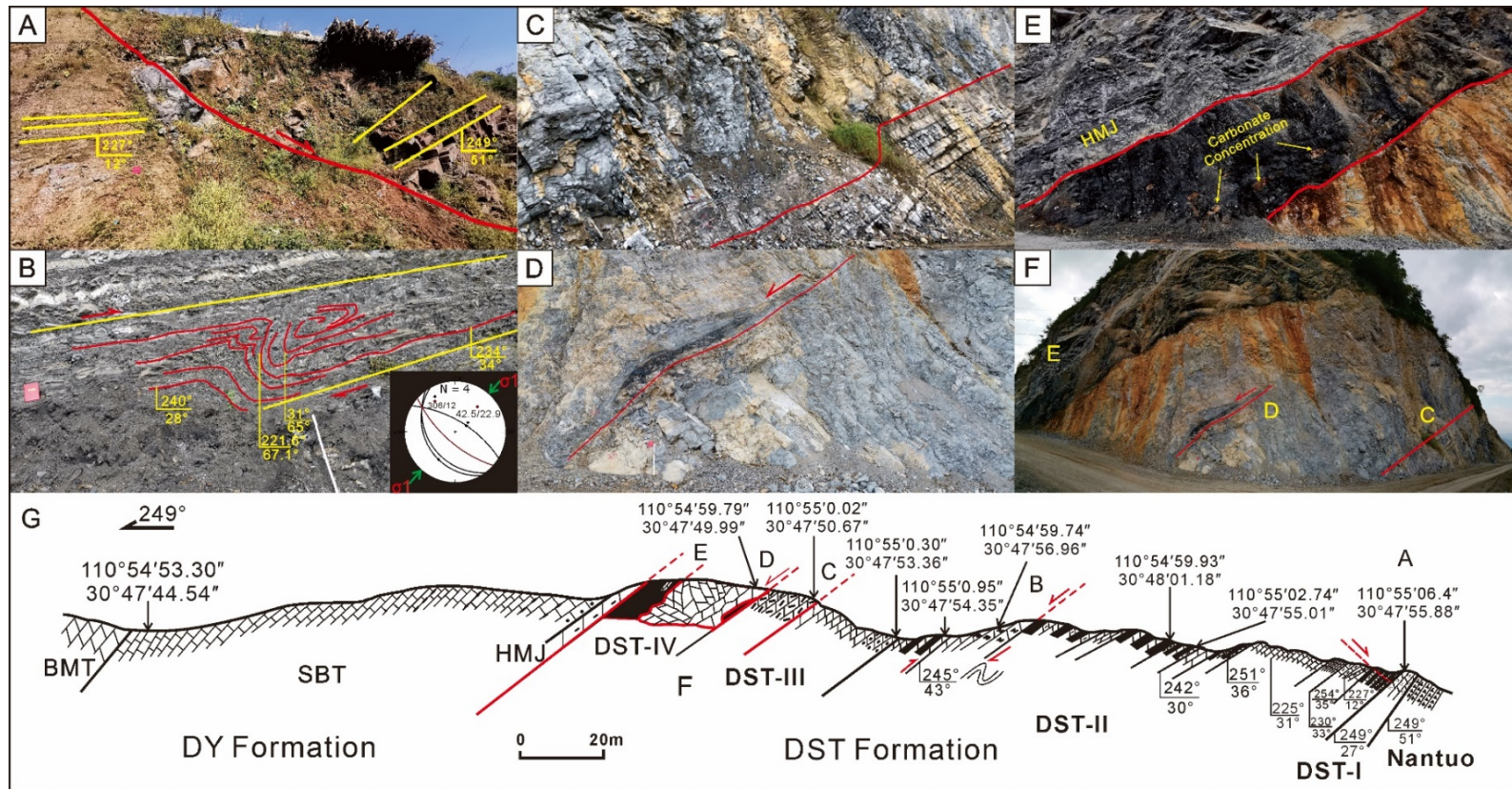


Fig. 3. 11 Outcrop photos, structural analysis, and the sketch cross-section graph of the Qinglinkou section. A: normal fault cut the lower Doushantuo Member I (View towards: 339°); B: Z-folds formed by flexural slip during the formation of Huangling Anticline and lower equal-area hemisphere projection of the fold data. The green arrow shows the direction of the main stress σ_1 is NE-SW (View towards: 335°). C: 'S' shape slumping surface showing the upper Doushantuo III layers are disrupted and the lower part laminated (View towards: 335°). D: location shows the occurrence of the first black shale layer (30-60cm), which is not consistent with the upper and lower layers (View towards: 342°). E: location shows the second black shale layer is thicker (18.1m) than the lower one and contains laminated carbonate concretions (View towards: 339°). The red curve lines represent the slumping surface or faults.

3.5.2 Petrographic Correlation of the Middle Carbonate

My observation shows that the middle carbonate is possibly a slumped dolostone unit. However, which rock unit is the source of this middle carbonate is still not answered. This study conducted detailed petrographic investigations on the Doushantuo Member III, middle carbonate, and Hamajing Member samples (Fig. 3.12).

Samples from the Shibantan Member are dark limestone samples, which are not likely to have been the source of the middle carbonate. Dolomitization is a dissolution and recrystallization process controlled by its precursor mineralogy and crystal size (Al-Aasm and Clarke, 2004). Four types of dolomites have been identified at the Qinglinkou section (from early dolomitization to late-stage dolomitization): 1. Fine-crystalline matrix dolomite (5-50 μ m); 2. Fine-crystalline matrix dolomite with calcite grains; 3. Medium-crystalline pervasive dolomite (10-100 μ m); 4. Saddle dolomite (>100 μ m). Fig. 3.12 shows that the most common dolomite type at the Qinglinkou section is the fine-crystalline matrix dolomite, which proves most of the dolomite samples have undergone very limited further recrystallization.

Samples from the Doushantuo Member III have a lighter color than the middle carbonate (Fig. 3.7). Moreover, the photomicrograph shows that the lower part of the middle carbonate has undergone severe recrystallization (Fig. 3.12-G, H). Similarly, except for the middle carbonate, this recrystallization feature of the dolostone sample only exists in the upper part of the overlying Hamajing Member (Fig. 3.12-I), indicating that the middle carbonate derives from the Hamajing Member, but the rock sequence has been overturned due to slumping.

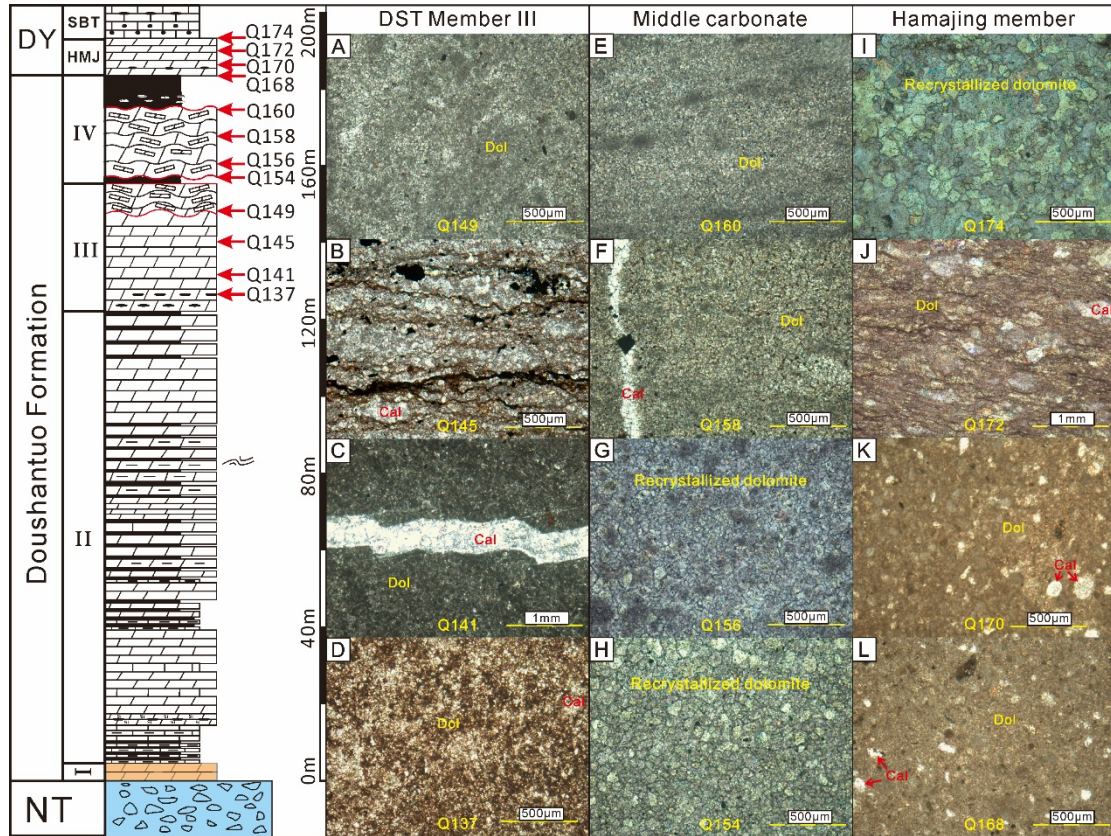


Fig. 3. 12 Microscopic photographs comparison of the samples from Doushantuo Member III, middle carbonate, and Hamajing Member. A: fine-crystalline dolomite sample from the upper part of the Doushantuo Member III. B: medium-crystalline dolomite with large calcite grains. C: fine-crystalline dolomite with calcite vein. D: fine-crystalline dolomite from the bottom of the Doushantuo Member III. E: fine-crystalline dolomite from the upper part of the middle carbonate (grain size, ~5-22µm). F: partial recrystallized medium-crystalline dolomite with a calcite vein. G-H: highly recrystallized saddle dolomite from the bottom of the middle carbonate (grain size, ~50-170µm). I: highly recrystallized saddle dolomite from the top Hamajing Member (grain size, ~60-260µm). J-L: fine-crystalline dolomite with calcite grains (grain size, ~40-420µm).

3.5.3 Chemostratigraphic Correlation

3.5.3.1 Diagenetic Evaluation

Before discussing the chemostratigraphic correlation, it is crucial to evaluate the diagenetic effects first, as it might change the original signal through the fluid-rock interaction with meteoric or hydrothermal fluids (Guo et al., 2013; Chen and Feng, 2019; Zhang et al., 2020c). Such diagenetic alteration of the carbonate rock can sometimes simultaneously lower $\delta^{13}\text{C}_{\text{carb}}$ and $\delta^{18}\text{O}_{\text{carb}}$ values (Zhang et al., 2020c). Samples with

the $\delta^{18}\text{O}_{\text{carb}} < -10\text{‰}$ might get influence from diagenetic alteration (Li et al., 2013a; Gamper et al., 2015; Zhang et al., 2020c).

According to (Lu et al., 2013), the cross-plot of $\delta^{13}\text{C}_{\text{carb}}$ and $\delta^{18}\text{O}_{\text{carb}}$ and Mn/Sr ratios <10 from the Lianghong and Sishang sections indicate those samples are well-preserved samples with a non-diagenetic origin. My diagenetic evaluation of these two sections also supports that those samples are well-preserved (Appendix A, Fig. S1, S2).

Based on the CaCO_3 content and Mg/Ca ratios, the QLK samples are categorized into three groups: limestone (LM) samples: CaCO_3 content higher than 70% and the Mg/Ca ratios lower than 0.025; dolomitic limestone (DL) samples: CaCO_3 content higher than 70% and the Mg/Ca ratios higher than 0.025; dolomite (DM) samples: CaCO_3 content lower than 70% (Fig. 3.13-A).

During dolomitization, major elements Mg, Fe, Mn are assumed to be able to substitute for Ca in the carbonate lattice (Hohl et al., 2015). The Mn/Sr ratio is also a useful tool for evaluating diagenetic alteration (Kaufman and Knoll, 1995; Bartley et al., 1998) (Kaufman and Knoll, 1995; Bartley et al., 1998; Li et al., 2013; Lan et al., 2019) as dissolution and recrystallization processes can raise Mn contents and lower Sr contents. The samples that have Mn/Sr <10 commonly retain near primary signals (Kaufman and Knoll, 1995). However, previously reported Mn/Sr ratios from Cryogenian “cap carbonates” are commonly high, which has been attributed to the unusual coeval seawater chemistry (high Fe and Mn concentration) in anoxic or suboxic depositional environments (Yoshioka et al., 2003; Font et al., 2006). Wu et al. (2019) propose Mn/Sr value of 60 as the cut-off (lower than) for primary preservation, specifically for the cap carbonate. All of the Mn/Sr values from the Doushantuo Member I samples, the cap carbonate at the Qinglinkou section, are lower than 60, possibly representing the original signal. For the rest of the samples, the threshold of Mn/Sr <10 is applied.

Cross-plots of $\delta^{13}\text{C}_{\text{carb}}$ show no correlation with diagenesis indicators shown above, $\delta^{18}\text{O}_{\text{carb}}$ ($R^2 = 9\text{E-}05$), Mg/Ca ($R^2 = 0.18$), Mn/Sr ($R^2 = 0.17$), indicating that the rest of the samples might reflect the primary signals (Fig. 3.13-B, C, D). All the green boxes in Fig. 3.13 represent the best-preserved samples.

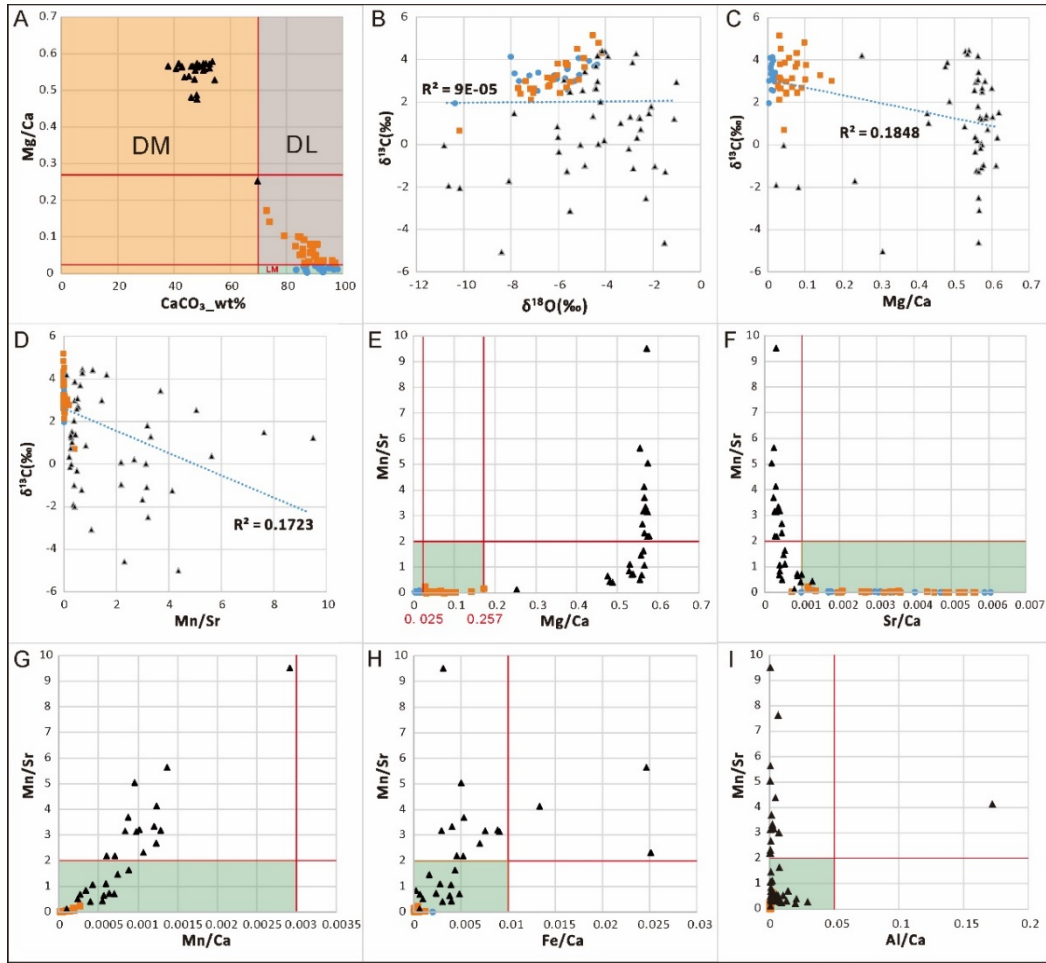


Fig. 3.13 Cross-plot of the Qinglinkou section samples with Mn/Sr < 10. DM: dolomite (calcium carbonate content < 70%); DL: dolomitic limestone (calcium carbonate content > 70%; Mg/Ca > 0.025); LM: limestone (calcium carbonate content > 70%; Mg/Ca < 0.025). Thresholds for the green shaded area (best-preserved samples) are Mn/Sr < 2, Mg/Ca < 0.257, Sr/Ca > 0.001, Mn/Ca < 0.003, Fe/Ca < 0.01 and Al/Ca < 0.05.

3.5.3.2 C-isotope Chemostratigraphy

After diagenesis evaluation and data screening, the carbon isotope $\delta^{13}\text{C}_{\text{carb}}$ profile generated from the well-preserved samples at the Qinglinkou section clearly shows, from bottom to top (Fig. 3.14): (1) Four major negative $\delta^{13}\text{C}_{\text{carb}}$ excursions (NE). The NE1 is recorded in the cap dolostone with the lowest value of -4.4‰, possibly CANCE; The NE2 in the lower to the middle part of Doushantuo Member II layers with the lowest value reached -5.0‰ could be WANCE. The NE3 in the upper part of Doushantuo Member II layers with the lowest value of -0.2‰ could correlate with the reported

BAINCE; The NE4 in the Doushantuo Member III, IV, and Dengying Hamajing Member with the lowest value of -4.6‰ could be the DOUNCE, which is commonly correlated with the Shuram-Wonoka excursion in Oman and Australia respectively (Lu et al., 2013; Wang et al., 2016). (2) In between these negative excursions, there are three positive $\delta^{13}\text{C}_{\text{carb}}$ excursions in the Doushantuo layers and a stable $\delta^{13}\text{C}_{\text{carb}}$ plateau in the middle Dengying Shibantan Member. (3) The positive carbon isotope excursion of middle dolostone layers shows slight fluctuations and an average value of 1.8‰. (4) The magnitude of the negative carbon excursion is much smaller than other sections. (5) These carbon isotope excursions from the Qinglinkou section can be correlated with other sections in South China and can be used to do chemostratigraphic correlation as a useful tool to subdivide and correlate the Ediacaran successions in South China.

The CANCE and BAINCE can be correlated with the EN1 and EN3 at the Jiulongwan section and Zhangcunping section (Fig. 3.14). However, the EN2/WANCE was not reported in previous studies of Doushantuo chemostratigraphy at the Jiulongwan and Zhangcunping sections. In my correlation (Fig. 3.14), the negative carbon isotope values from levels 5-23m could be correlated to WANCE at the Jiulongwan section and level 13-25m at the Zhangcunping section. The fluctuation of the carbon isotope values at this level might result from no/improper data screening. In this study, the lower part of the Doushantuo Member II has been influenced heavily by diagenesis and alteration ($\text{Mn/Sr} > 10$, Fig. 3.10). After a further elemental test of the other sections in the future, we might reveal a clearer negative carbon isotope excursion of the EN2/WANCE in other sections.

The $\delta^{13}\text{C}_{\text{carb}}$ profile from the middle carbonate unit shows a sharp decrease from 1.81‰ to -4.6‰ with no values in between in a short distance (2.5m) between samples from the middle carbonate and carbonate concretions in shale II, which is also evidenced at the Zhimaping section (An et al., 2015). Based on my observation and analysis mentioned above, the interpretation of the two negative carbon isotope excursions of DOUNCE as proposed by (Kaufman et al., 2007; Bergmann et al., 2011; Verdel et al., 2011; Zhou et al., 2017b) might not be accurate.

An et al. (2015) correlated the middle carbonate and shale II with the Dengying

Hamajing and the Shibantan Members, respectively. However, carbonate concretion in the shale II and the Shibantan Member are discrete; The carbon isotope composition of the carbonate concretion in shale II is -4.6‰, while the Shibantan Member $\delta^{13}\text{C}_{\text{carb}}$ values range from 1.93-5.15‰ at the Qinglinkou section. Moreover, the shale II $\delta^{13}\text{C}_{\text{org}}$ values at the Miaohé and Jiuqunao sections (-36.7‰ to -38.3‰ and -37.3‰ to -38.1‰ respectively) (Bridger et al., 2021) are different from the Shibantan Member (-25‰ to -30‰) (Wang et al., 2014). Except for these, the fossil assemblages from the Miaohé Member and Shibantan Member are distinct too (Zhou et al., 2017b). Therefore, the inferred correlation of the shale II with the younger Shibantan Member should be rejected.

The $\delta^{13}\text{C}_{\text{carb}}$ profile supports the correlation of the middle carbonate with the Hamajing Member (Fig. 3.14). However, the $\delta^{13}\text{C}_{\text{carb}}$ pattern of the middle carbonate at the Miaohé and Jiuqunao sections, which shows first increase to positive values and then decrease to negative again (as low as -12.83‰), makes it difficult to correlate the middle carbonate to the Hamajing Member (the decreasing trend is very minor to -0.51‰ at the Xiangdangping section (Zhu et al., 2013) and -1.29‰ at the Jiulongwan section (An et al., 2015)). But this study proves the middle carbonate is a slump, which might be overturned based on the petrography correlation mentioned above. Moreover, I noticed that the thickness of the middle carbonate has a doubled relationship between the Hamajing Member (18.1m and 7.8m, respectively), which is also shown in other sections (An et al., 2015). It is possible to infer that the middle carbonate is a slumped unit from the Hamajing Member with a doubled thickness due to slumping and ‘Z’ shape folds.

The Dengying Formation Shibantan Member has constant high carbon isotope values (average 3.3‰) with minor fluctuation. This rock unit is comparable to the Gaojiashan Member in the southern Shaanxi Gaojiashan area (Chen et al., 2015; Cui et al., 2016a) and the Nama Group in Namibia (Tostevin et al., 2017).

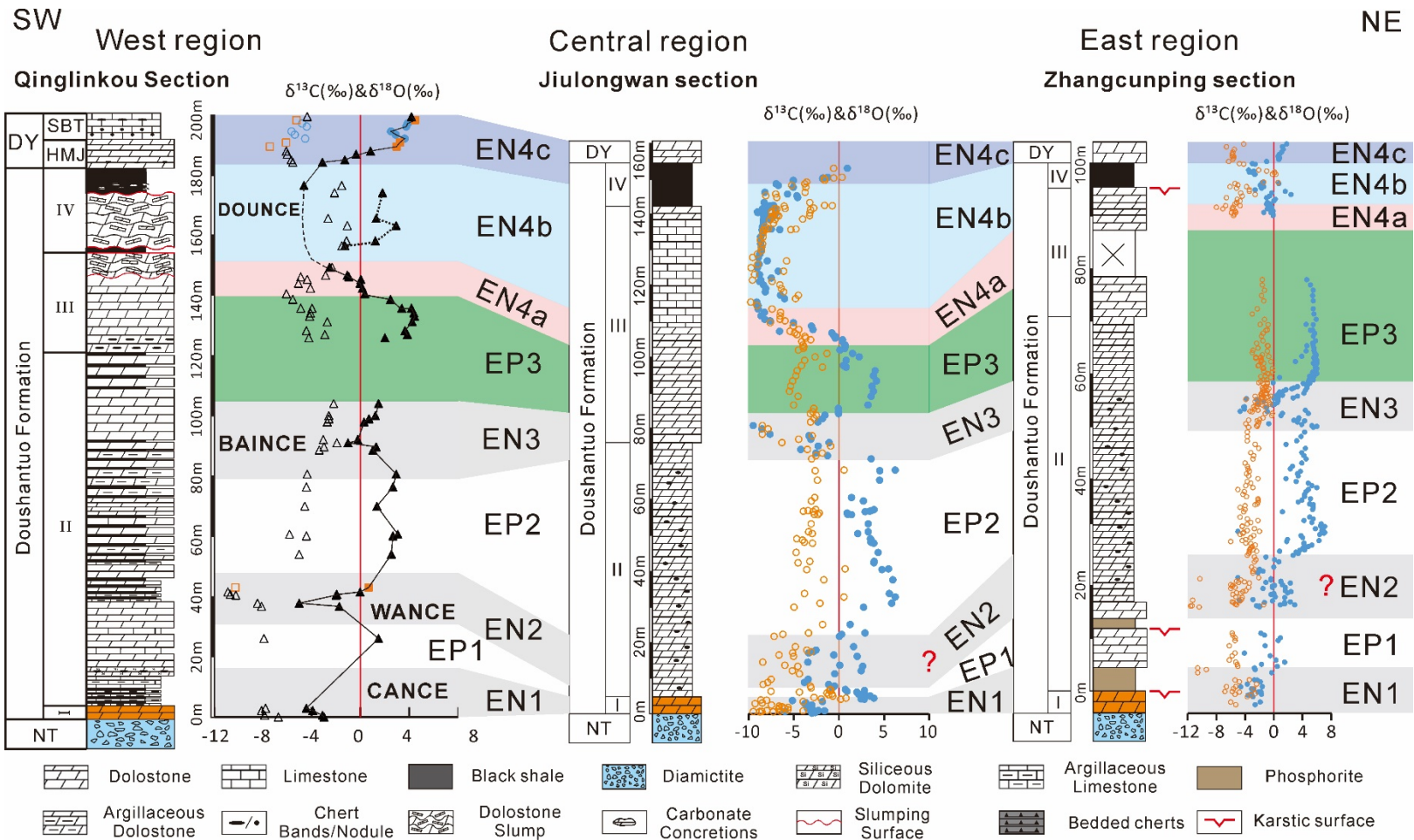


Fig. 3. 14 Lithostratigraphic and chemostratigraphic correlation of the Doushantuo Formation in the Huangling Anticline area. Data from the Qinglinkou section is from this study after the diagenetic screening. Data from the Jiulongwan section is from (Jiang et al., 2007; McFadden et al., 2008). Zhangcunping section data is from (Wang et al., 2017b; Ouyang et al., 2019). Shaded symbols represent the carbon isotope values, and unshaded symbols represent the oxygen isotope values.

3.5.3.3 Elemental Correlation

The Lianghong and Sishang sections were added to better constrain and correlate the late Ediacaran chemostratigraphic framework in South China (Fig. 3.8, 3.9).

In a previous study, Lu et al. (2013) assigned the middle part (36.5-75.4m) of the Sishang section to the Doushantuo Formation and the upper part (91.5-124m) to the Dengying Formation (Fig. 3.9). However, according to the carbon isotope profile, elemental data and correlation with the other two sections, the constantly high $\delta^{13}\text{C}_{\text{carb}}$ (average 1.04‰) value is more likely to imply affinity with the Dengying Formation instead. Moreover, the Sishang section is a condensed carbonate section (with no recognizable Doushantuo Member IV), and so is not likely to have the DOUNCE/Shuram aftermath recorded in nearly 40m thick Doushantuo carbonate. The drop of $\delta^{13}\text{C}_{\text{carb}}$ to 0.24‰ at level 91.5m of the Sishang section can be correlated with the negative carbon isotope excursion (BACE) around the Ediacaran-Cambrian boundary (Wang et al., 2016; Zhu and Li, 2017). Moreover, samples from level 91.5-124m at the Sishang section generate a constantly low Sr (ppm) and Sr/(Ca+Mg) ratio (69 ppm and 0.00022 respectively), which cannot be correlated to the Dengying Formation at the Lianghong and Qinglinkou sections.

In this study, except for carbon isotope $\delta^{13}\text{C}_{\text{carb}}$ chemostratigraphic correlation, I also use the Sr concentration and Sr/(Ca+Mg) ratio as an aid to do stratigraphic correlation, especially for the Dengying Formation limestone samples. In all three sections, Lianghong, Sishang, and Qinglinkou sections, the Sr concentrations and Sr/(Ca+Mg) ratios are consistently low (average 197 ppm, 0.00061; 309 ppm and 0.00092; and 57 ppm, 0.00019 respectively) during EN4a and EN4b. However, Sr (ppm) and Sr/(Ca+Mg) start to increase during EN4c and reach the highest plateau during EP4 (average 2366 ppm, 0.0074, 2958 ppm, and 0.0046 and 1161ppm, 0.0031, respectively).

3.6 Conclusions

Detailed fieldwork, structural measurement, stratigraphic and chemostratigraphic study of the Ediacaran succession in the Qinglinkou area indicate that the middle dolostone unit between two black shale layers in the western region of the Huangling Anticline area exhibits an unconformable contact with overlying and underlying layers. The middle carbonate could be correlated to the Dengying Hamajing Member dolostone. This means that the middle carbonate positive excursion should be excluded from the DOUNCE when correlating sections using the carbon isotope profile. My data clearly shows 4 negative carbon isotope $\delta^{13}\text{C}_{\text{carb}}$ excursions recorded in the Ediacaran strata in South China. The late Ediacaran Dengying Shibantan Member and the equivalent rock unit in South China is characterized by consistently high carbon isotope values and high Sr concentration and Sr/(Ca+Mg) ratio (~2000 ppm, ~0.005 respectively).

Chapter 4 Large-scale Slumping in the Western Region of the Huangling Anticline Area, South China

Abstract

The stratigraphic correlation of the Ediacaran sections from the western region of the Huangling Anticline area has puzzled many scientists for a long time. Comparing the sections from the western, central, and eastern regions of the Huangling Anticline area indicate large-scale regional mass slumping has changed the stratigraphy of the upper Doushantuo and lower Dengying formations. I give two new possible evolutionary models to explain the forming of the middle carbonate unit and new stratigraphic correlation to the other sections in South China.

Author Contributions: This chapter benefitted from discussions with Graham Shields and Ying Zhou.

4.1 Introduction

In recent decades, the Huangling Anticline area has been one of the most intensively studied areas for Ediacaran strata in South China. However, in the western region of the Huangling Anticline area, the consistent appearance of the middle carbonate in between two black shale layers overlying Member III has become a great challenge for building the Ediacaran stratigraphic framework and doing chemostratigraphic correlations for many scientists.

Alongside traditional stratigraphic and biostratigraphic correlations, carbon isotopes represent a powerful tool for global chemostratigraphic correlation (Ishikawa et al., 2008; Hoefs, 2015; Shields, 2017). Most examples of the DOUNCE excursions in South China start with a gradual decline from the Doushantuo Member III, followed by a relatively stable period through the Doushantuo Member III and IV, and finally a sharp increase to positive values from the upper Doushantuo Member IV to the Dengying Hamajing Member (Grotzinger et al., 2011).

However, C isotope data of the middle carbonate shows a strange positive excursion, which separates the DOUNCE excursion into two parts. Moreover, the dramatic shift of C isotope profiles in different sections and the lack of a reliable fossil record makes the correlation even harder. Alternative correlations include 1. These three units are in situ and their relative ages are in normal superposition (Zhou et al., 2017b). 2. The middle carbonate is an olistostrome block, which means that these two negative excursions represent the same DOUNCE/Shuram excursion (Lu et al., 2013; Zhu et al., 2013). 3. The lower black shale I is Member IV, which means only the lower negative excursion can be correlated to the DOUNCE/Shuram excursion and the upper black shale II is equivalent to the Dengying Shibantan Member (An et al., 2015). Except for these uncertainties, only a few studies can provide a possible evolutionary history of this phenomenon. After detailed fieldwork, geochemical analysis of the Qinglinkou section, and comparison with other sections around the Huangling Anticline area, my study may help to better understand the problematic stratigraphic correlations of the upper Doushantuo Formation in South China.

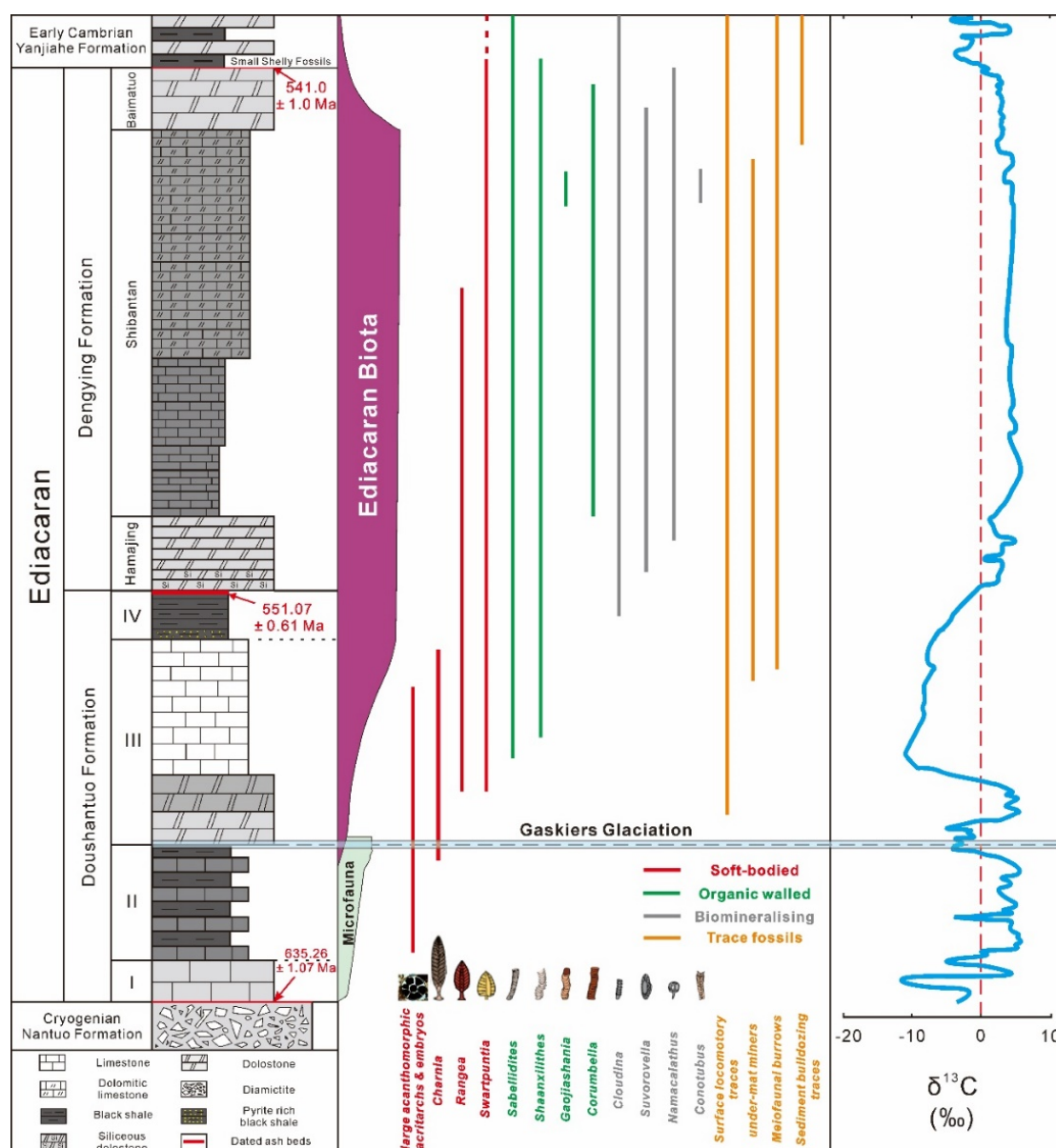


Fig. 4. 1 Generalized lithostratigraphic column, TOC vs carbonate proportion column, biostratigraphic column, and carbonate carbon isotope chemostratigraphic column in the Yangtze Gorges area. Fossil records were modified from (Zhu and Li, 2017; Wood et al., 2019). Carbon isotope data from (Wei et al., 2018b).

4.2 Geological Background

The Huangling Anticline area is located in between the southern margins of the Jiangnan intracontinental orogenic belt and the northern margins of the Qinling-Dabie orogenic belt (Wang et al., 2019b). The Jiulongwan section exhibits the most continues succession in this region and is likely not affected by slumping. At the Jiulongwan section, the classic Ediacaran succession of the central region of the Huangling Anticline area, can be divided into the Doushantuo Formation and the Dengying Formation (Fig.

4.1). The Doushantuo Formation (c. 635.26 – c. 551.01 Ma) there consists of four lithologic Members (Hawkins et al., 2017): Member I is cap carbonate. Member II is thin-medium bedded carbonate interbedded with black shale layers and chert bands. Member III is medium bedded dolostone. Member IV or Miaohe Member is black shale with carbonate concretions. The Dengying Formation consists of three Members: the Hamajing Member is medium-thick bedded siliceous dolostone with siliceous concretions; the Shibantan Member is thin-medium bedded dark limestone; the Baimatuo Member contains light grey dolostone (An et al., 2015).

4.3 Stratigraphic Correlation of the Surrounding Sections

The Huangling Anticline area is commonly divided into three regions, western region, central region, and eastern region. In this study, based on my 3D stratigraphic correlation (Fig. 4.2), I further subdivided the central region into the western central and eastern central regions. The western central region includes the Jiulongwan, Xiangerwan and Zhengjiatang sections. The eastern central region includes the Tianjiayuanzi and Baiguoyuan sections. This figure shows that the middle carbonate layer only exists in the western region where it is only absent in the Zhimaping and Liaojiagou sections.

In Chapter 3, I found that the middle carbonate unit might be equivalent to the Hamajing Member. Interestingly, from the Qinglinkou section and published sections in the west region of the Huangling Anticline area (Lu et al., 2013; An et al., 2015; Zhou et al., 2017b), it is apparent that the thickness of this middle carbonate layer is about double that of the Hamajing Member. In the Qinglinkou section, the middle dolostone is ~18.1m thick, and the Hamajing Member is 7.8m thick. The thickness of the middle dolostone layer and the Hamajing Member at the Jiuqunao section is ~10m and ~4.4m, respectively. For the Miaohe section, the thickness is ~9.8m and ~4.2m, respectively. For the Gaolan section, the thickness is ~15m and ~7.6m, respectively.

From W to E (Fig. 4.2), the thickness of the pink layers (upper Doushantuo Member III) increases at the Jiulongwan-Zhengjiatang section in the western central region and is thinner at the Tianjiayuanzi section in the eastern central region. Then thicker again

at the Niuping section from the Eastern region. A similar trend can be found in the thickness of the Hamajing Member.

However, the thickness of the shale layer (Doushantuo Member IV) shows the opposite trend. For example, in the western region, the thickness of the shale layer at the Jiuqunao section and Miaohe section is ~24 and ~15 m, respectively. In the western central region, the average thickness of the shale layer is 5.2 m. The shale layer becomes thick again in the eastern central region. At the Baiguoyuan and Tianjiayuanzi sections, the shale layer is 20 m thick and 21 m thick, respectively. This shale layer is absent from the Niuping section in the Eastern region.

4.4 The Existence of the ‘Mirror plane’ at the Qinglinkou Section

From the data I presented in Chapter 3, I noticed that the carbon isotope data shows the highest value 2.97‰ in the middle part of this dolomite layer (Fig. 4.3). The $\delta^{13}\text{C}_{\text{carb}}$ profile also shows the middle dolostone layer has no transitional values from the 1.81‰ to -4.6‰. There seems to be a gap between the top of this middle carbonate layer and the carbonate concretions from the shale II layer. A similar trend can be found in the Mg/Ca, Mn/Sr, Sr/Ca, Mn/Ca, and Fe/Ca ratios. They all show that the sample from level 164.9m either has the highest or the lowest value of nearly all the elemental ratios. The wide occurrence of the ‘Z’ shape folds (especially in the soft sediments in the Doushantuo Member II, Appendix A), the doubled thickness of the middle carbonate unit compared with the upper Hamajing Member in nearly all the sections in the western region inspired me to make a hypothesis that these middle carbonate layers might be a folded slumping layer, and that the mirror plane is the axial plane. Moreover, the petrographic correlation of the middle carbonate unit in Chapter 3 also indicates that the middle carbonate unit might be overturned due to slumping. With this hypothesis, this ‘mirror plane’ might also exist in other sections in the western region of the Huangling Anticline area.

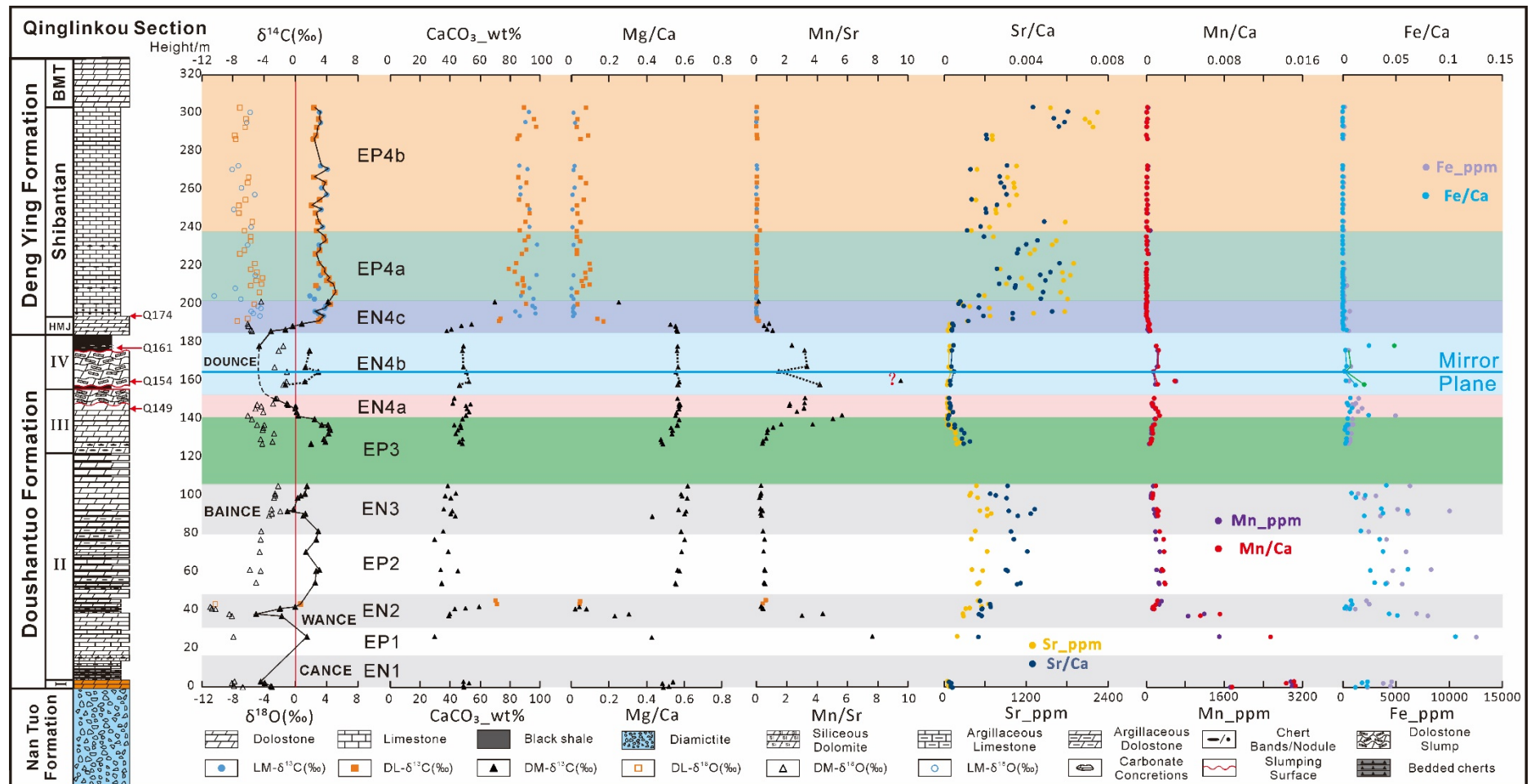


Fig. 4. 3 Lithostratigraphy, $\delta^{13}C_{\text{carb}}$, $\delta^{18}O_{\text{carb}}$, and elemental profiles of the Doushantuo Formation at the Qinglinkou section. Gray shades identify four negative carbon isotope excursions. The blue line represents the 'mirror plane'. HMJ, Hamajing Member; BMT, Baimatuo Member.

4.5 Chemostratigraphic Correlation

Based on this hypothesis, I want to determine whether the ‘mirror plane’ exists in other sections in the western region of the Huangling Anticline area. So, I made a correlation of the lithostratigraphy and $\delta^{13}\text{C}_{\text{carb}}$ profiles of different sections in the surrounding Huangling Anticline area (Fig. 4.4, 4.5).

Almost all the upper part of the Doushantuo Formation in the western region contains a middle carbonate unit between two black shale layers. I noticed that the middle carbonate from nearly all the sections from the western region is not in conformable contact with the surrounding layers. As can be seen from the Jijiawan (Jiuqunao) section, the base of this middle carbonate layer represents the slumped surface (Lu et al., 2013). Miaohe section also shows that the upper surface and the base of the middle carbonate layer represent the slumping surface (Lu et al., 2013). The middle carbonate unit from the Gaolan section is not bedded and seems not in conformable contact with other layers (Zhou et al., 2017b). At the Liaojiagou section, it seems that the dolostone (Hamajing Member) layer is missing above the Doushantuo shale layer (Zhou et al., 2017b) (Fig. 4.4).

From the chemostratigraphic correlation below, I found that the $\delta^{13}\text{C}_{\text{carb}}$ value of the middle carbonate layer can be correlated back to the Hamajing Member. The dashed blue line represents the mirror plane, from which the middle carbonate layer can be divided into two Hamajing layers. The $\delta^{13}\text{C}_{\text{carb}}$ value of either side can represent the typical Hamajing Member.

In the central and eastern regions (Fig. 4.5), the stratigraphic succession is much simpler than in the western region. Briefly, the upper Doushantuo Formation in the eastern region mainly comprises dolostone with a thin black shale unit (<1m). Only one shale layer can be observed in the central region at the upper Doushantuo Formation, and sections from this region can easily be correlated with other sections in South China.

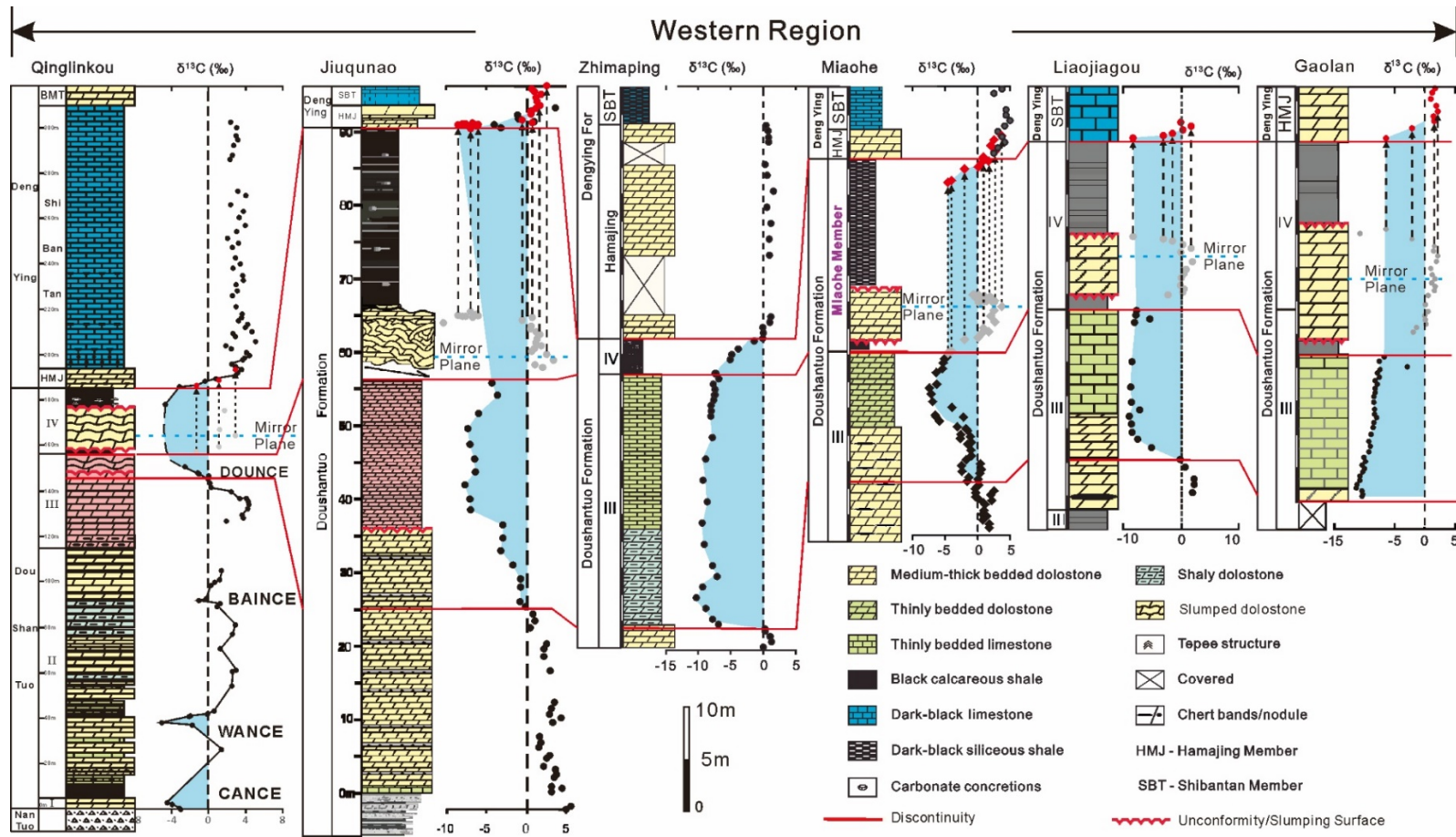


Fig. 4. 4 Lithostratigraphy and $\delta^{13}\text{C}_{\text{carb}}$ profiles of Ediacaran successions in the western region of the Huangling Anticline area. The red lines represent the stratigraphic correlations. The shaded blue area represents the negative carbon isotope excursion. The grey circles represent the data from the middle carbonate unit and could be recovered to the red circles based on my mirror plane hypothesis. The data of the Qinglinkou section are from this study. $\delta^{13}\text{C}_{\text{carb}}$ profiles of the Jiuqunao and Miaohe section are from (Lu et al., 2013), Zhimaping section is from (An et al., 2015), Liaojiagou and Gaolan section are from (Zhou et al., 2017b).

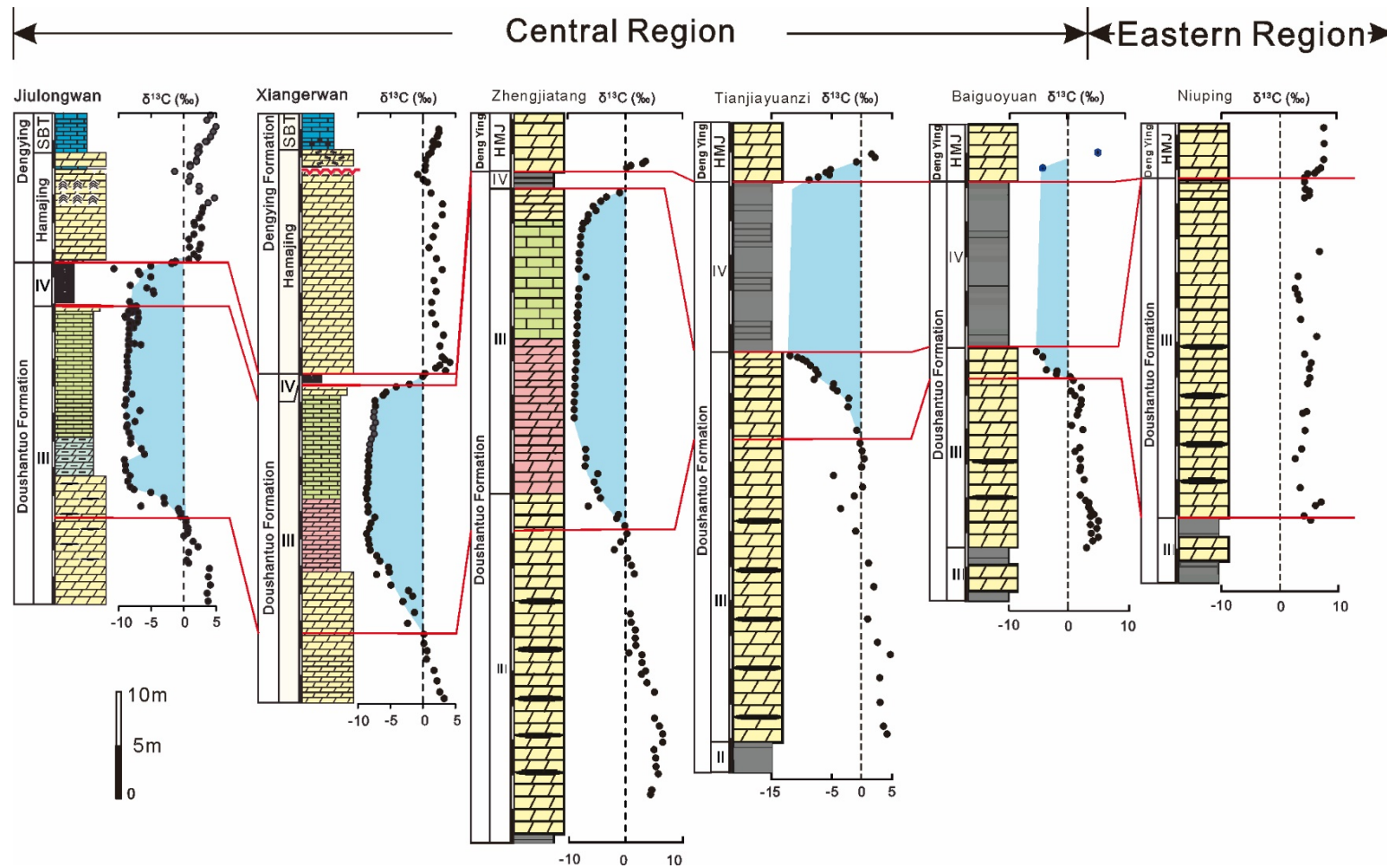


Fig. 4. 5 Lithostratigraphy and $\delta^{13}\text{C}_{\text{carb}}$ profiles of the Ediacaran successions in the central and eastern region of the Huangling Anticline area. $\delta^{13}\text{C}_{\text{carb}}$ profile of the Jiulongwan section is from (Jiang et al., 2007), Xiangerwan section is from (An et al., 2015), Zhengjiatang section is from (Zhou et al., 2017b), Tianjiayuanzi section is from (Zhou et al., 2012), Baiguoyuan section is from (Zhu et al., 2007), Niuping section is from (Liu et al., 2013).

4.6 Slide Dimensions and Paleogeographic Recovery

Wang et al. (2019b) made a paleogeographic reconstruction of the Doushantuo Formation around the Yichang area based on drill core data. They divided the lithofacies into the lower slope-deepwater basin, upper slope facies, platform margin facies, and platform facies from west to east. I made a cross-section from W to E based on their reconstruction and my 3D stratigraphic correlation (Fig. 4.6). From the figure, in the middle east and eastern region, sections are forming below the fair-weather wave base and above the storm wave base in the platform environment (Wang et al., 2019b). In the middle west region, sections mainly form in platform margin or upper slope with thinner shale layer and relatively stable and continuous stratigraphic successions. In the western region, except for the Liaojiagou and Zhimaping sections, most sections form in the lower slope-deep water basin with thick shale layers and unusual middle carbonate slump.

The estimated distribution of the dolostone slump is colored in orange in Fig. 4.6-A. The Liaojiagou and Zhimaping sections are two sections with possibly absent of the dolostone Hamajing Member and could be considered as the forming source of the slumped unit. If considering the Liaojiagou section as the forming source of this large-scale slump and the slump developed basinward (NEE to SWW) to the Miaohe section, the estimated shortest slide displacement distance is around 5km. If we consider the Zhimaping section as the forming source, the estimated longest slide displacement distance is around 12km.

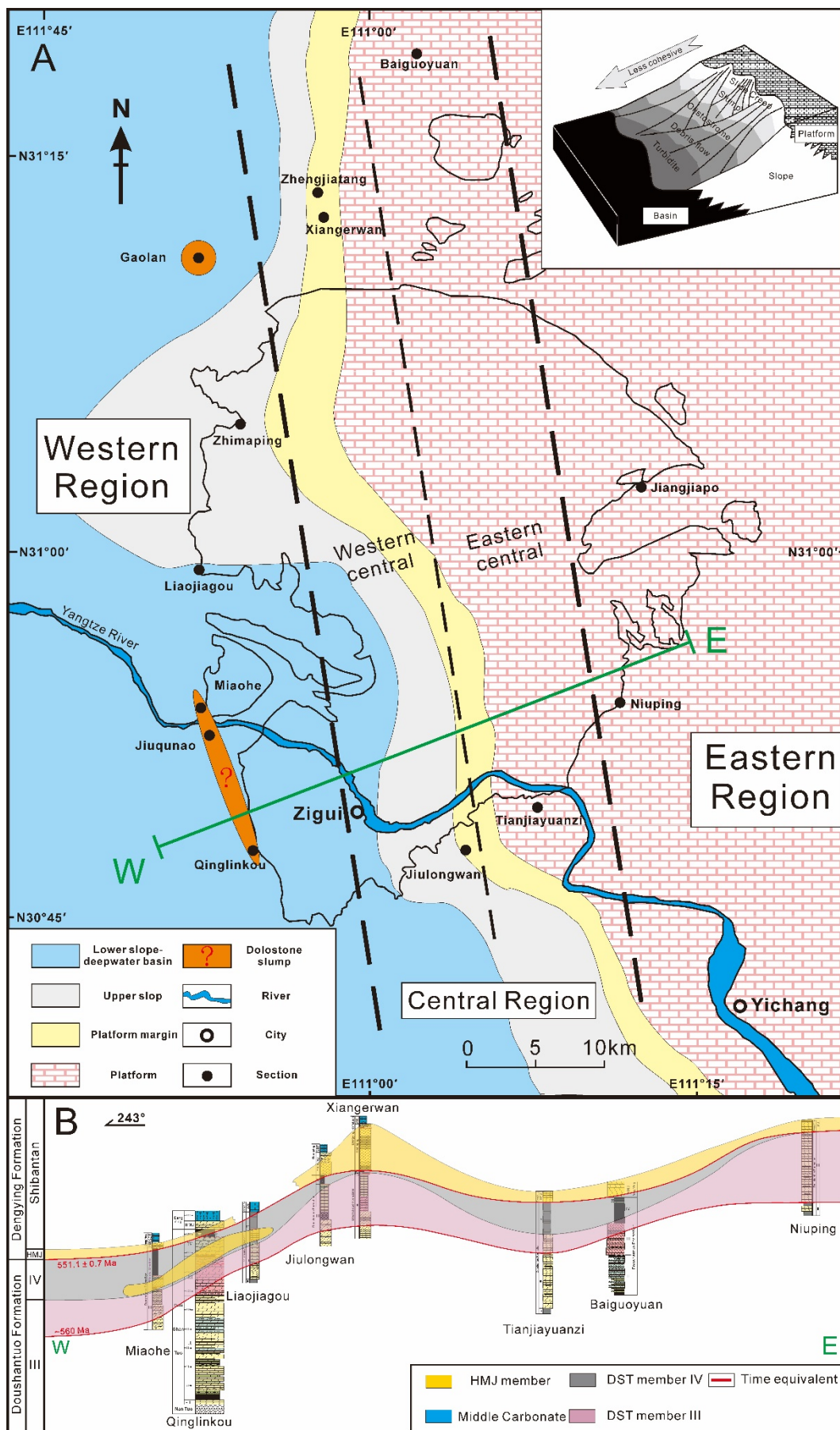


Fig. 4. A: Paleogeographic recovery of the Huangling Anticline area. Modified from (Wang et al., 2019b). B: Cross-section from W to E.

4.7 Possible Evolution History

Two possible explanations might be able to explain the formation of the middle carbonate unit in the western region of the Huangling Anticline area.

The first one might be caused by sequential slumping along the slope (Fig. 4.7). This hypothesis includes four stages: Stage A represents the slump cutting through all the bedded upper Doushantuo III, shale layers, and Hamajing Member to create a basin for later slumps to fill. In Stages B and C, after the deposition of the lower Hamajing member, this rock unit first slumped down (Slump I) into the basin, followed by the underling Shale II layers, which caused the overturned layer sequence. The final step happened after the deposition of the upper Hamajing layer. In Stage D, the upper Hamajing Member slumped down (Slump II) to the basin on top of the Shale II layers, causing these sandwiched layers. In this hypothesis, the middle carbonate is older than the Hamajing Member at the Qinglinkou section and can be correlated with the lower Hamajing Member in the central region. The first main slump happened in between the deposition of the lower Hamajing Member and upper Hamajing Member. And the second slump happened after the deposition of the upper Hamajing Member.

This evolution model is characterized by two sequential slumping. Slump I happened after the deposition of lower Hamajing Member and Slump II happened after the deposition of the upper Hamajing Member. However, the shale II layer should show extensive disruptions due to slumping. But my field observations show that the shale II layer is laminated with carbonate concretions also laminated, which indicates that this explanation might also not be true. Except for this, if the sequential slumping hypothesis is correct, then the upper slumping unit should always show similar moving direction compared to the lower slumped layers at the Qinglinkou section. However, only the upper shale II shows a backthrust relationship with the middle carbonate unit, but the other slumped units show a downward moving direction compared to the underlying layers (Fig. 4.10-A). Moreover, although the Hamajing Member at the central region shows a first increase then decrease trend of the carbon isotope values. The decreasing magnitude of the $\delta^{13}\text{C}_{\text{carb}}$ is very minor compared with the middle carbonate unit (Table 4.1). This indicates that the middle carbonate unit from the western region of the Huangling Anticline area might not be able to directly correlate with the lower Hamajing Member from the central region.

Table 4. 1 Comparison between the decreasing magnitude of the $\delta^{13}\text{C}_{\text{carb}}$ from the middle carbonate unit and the Hamajing Member.

Middle Carbonate Unit $\delta^{13}\text{C}_{\text{carb}}$			Hamajing Member $\delta^{13}\text{C}_{\text{carb}}$		
Location	Sections	The lowest value during the decreasing period	Location	Sections	The lowest value during the decreasing period
Western region	This study Qinglinkou section	1.29‰	Central region	Xiangdangping section (Zhu et al., 2013)	-0.51‰
	Jiuqunao/Jijiawan section (Lu et al., 2013; An et al., 2015)	-10.3‰		Jiulongwan section (An et al., 2015)	-1.29‰
	Miaohe section (Lu et al., 2013)	-12.83‰		Xiang'erwan section (An et al., 2015)	-0.77‰
	Liaojiagou section (Zhou et al., 2017b)	-8.3‰		Tianjiayuanzi section (Zhou et al., 2012)	-3.5‰
	Gaolan section (Zhou et al., 2017b)	-10.4‰			

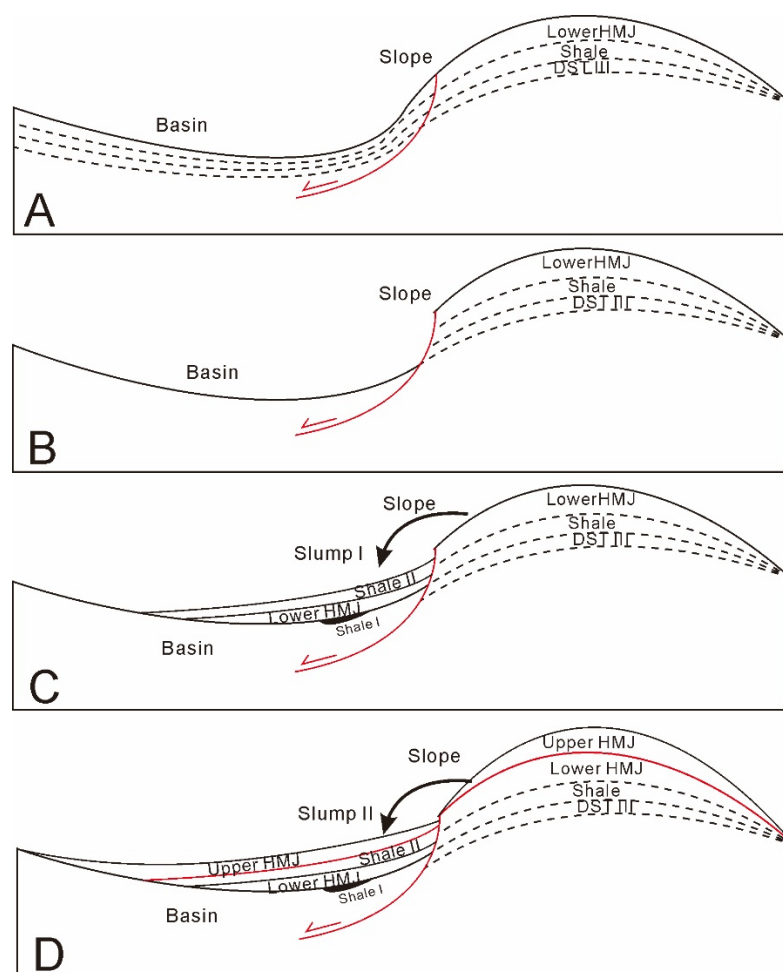


Fig. 4. 7 The first possible evolution history of the middle carbonate unit. In this hypothesis, slumping occurs after the deposition of the lower HMJ Member. The lower HMJ has been slumped down into the basin, followed by the shale layers. After the deposition of the upper HMJ, which also slumped down and resulted in the sandwiched layers.

Slumping is the movement en masse of sedimentary deposits by gravity (Lewis, 1971). In modern submarine settings, slumping layers commonly occur on slopes (Lewis, 1971). During slumping, compression occurs at the toe of a slump and tension at the head of a slump, resulting in folding of the slumped layers. This reminds me to think about the possibility of the folded Hamajing Member slump hypothesis. Based on my observation, chemical analysis, and correlations, I put forward a second explanation for the formation of this middle dolostone layer and possible evolutionary history.

The second possible evolution history can be divided into four stages (Fig. 4.8). Stage A represents the deposition of the Doushantuo Member III (Carbonate layer), Member IV (shale layer), and Hamajing Member (Dolostone layer). Following that, within the slope area in the western region, the uplift and/or significant regressions may have initiated this large-scale sliding (Stage B). The presence of a thick shale layer at the base of the Hamajing dolostone layer may have facilitated this displacement as the ‘lubricant’ surface of slip. At stage C, the Hamajing layer slides along the shale layer and forms a Z-shape close fold. As the slide continues, the Hamajing layer breaks up into two parts, and the upper part backthrust on top of the lower part at stage D. In this hypothesis, slumping occurred after the deposition of the Hamajing Member and before the deposition of the Shibantan Member.

An example photo of this hypothesis is shown in Fig. 4.9. Fig. 4.9 shows that the slumping unit is a tight-folded carbonate unit, which slips on top of the horizontal detachment surface (Khan et al., 2020). The slumped unit is truncated by a northeast dipping backthrust fault. Moreover, the slumped unit also show folding and thicker than the left side. My field observation at the Qinglinkou section shows the relative moving direction between the upper shale II and the middle carbonate unit supporting this hypothesis (Fig. 4.10).

This evolution model is characterized by only one large-scale slumping that happened after the deposition of the Hamajing Member, and the middle carbonate unit is the slumped folded block coming from the slope area Hamajing dolostone unit. Firstly, this model clearly explained why two shale layers seem to exist and a dolostone layer in between. Secondly, this model also explains that the Hamajing Member dolostone might be the source of this middle dolostone layer and that no layer can be correlated with it from the underlying layers. As the Hamajing layer possibly has been folded and doubled in this middle dolostone layer, this model also

answers why it shows a mirrored trend in the carbon isotope and elemental profiles in this middle dolostone layer. From the sections in the western region, this model also answers why the middle dolostone has a nearly doubled thickness compared to the Hamajing layer.

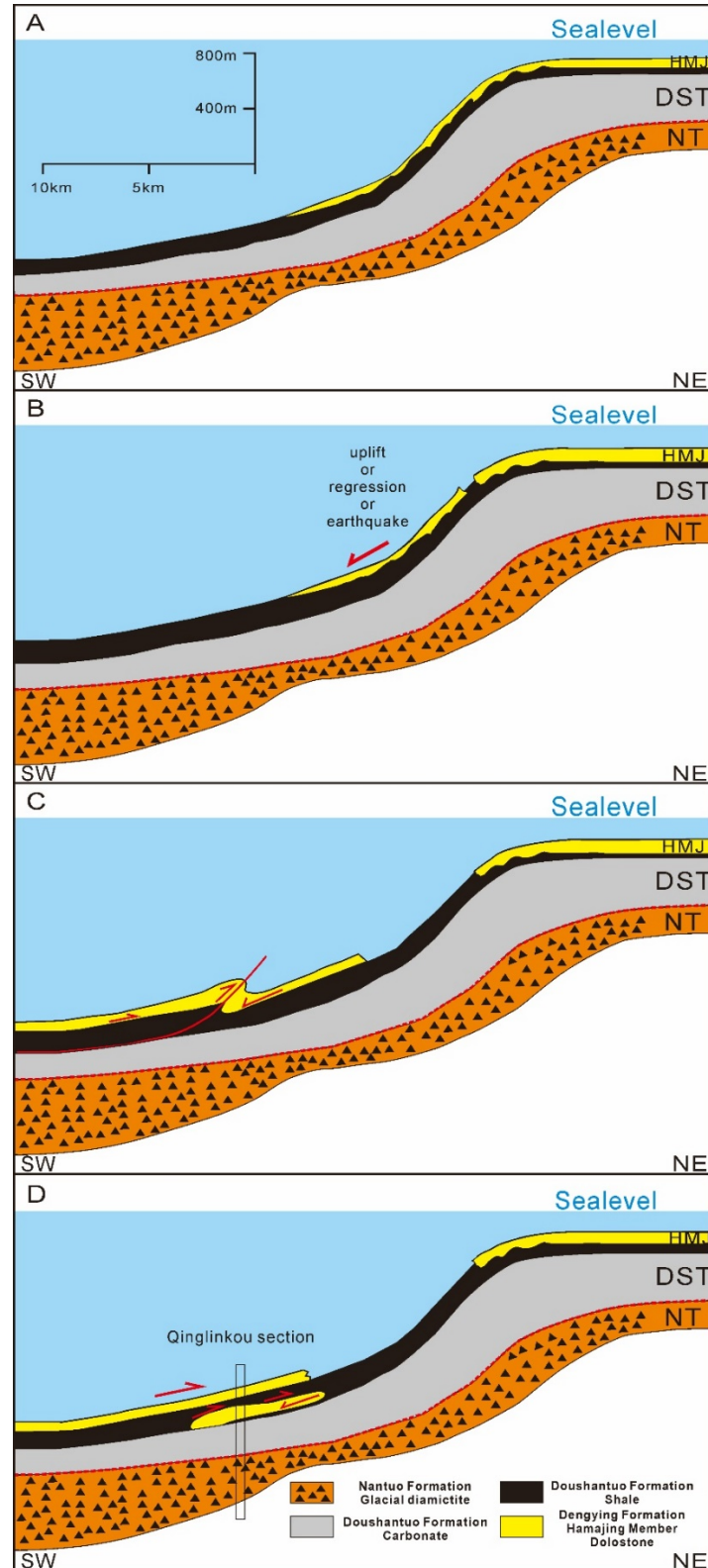


Fig. 4. 8 The second possible evolution history of the middle carbonate unit (Shelf-to-basin transect). The red arrows represent the relative moving direction. Modified from (Jiang et al., 2011).

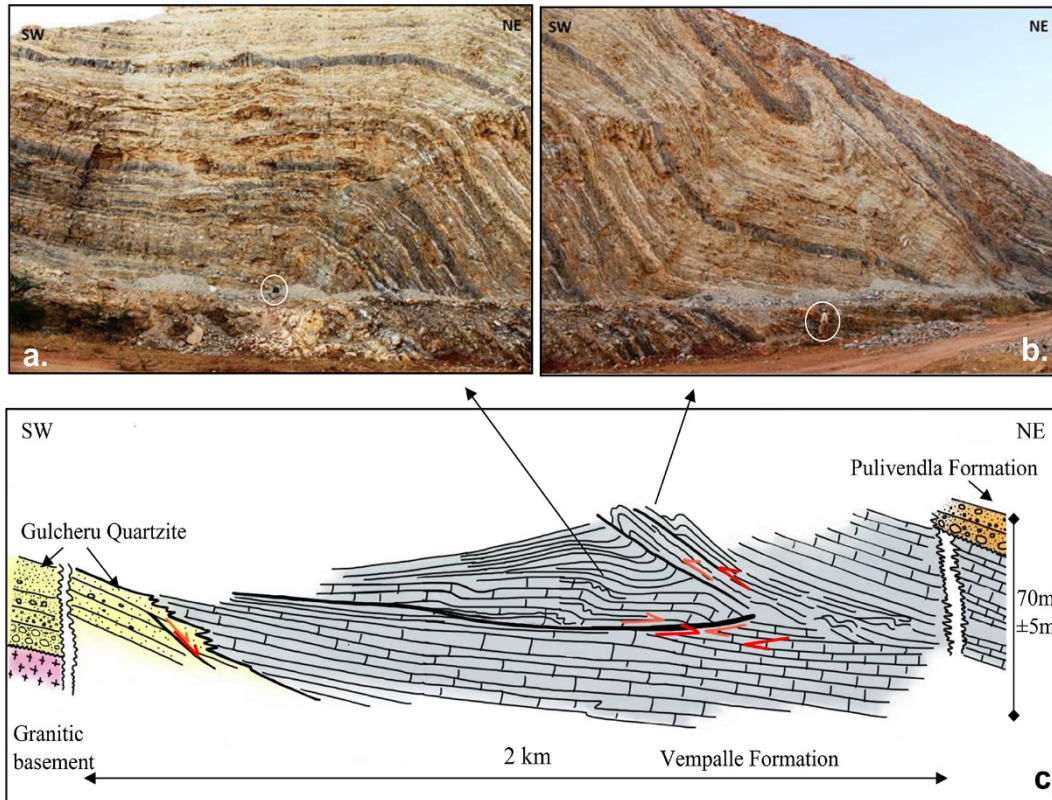


Fig. 4. 9 An example field photo and sketch showing the deformed carbonate unit slumping along the horizontal detachment surface and the NE-dipping Pulivendla Formation backthrust on top of the folded carbonate slumping unit. Figure from (Khan et al., 2020).

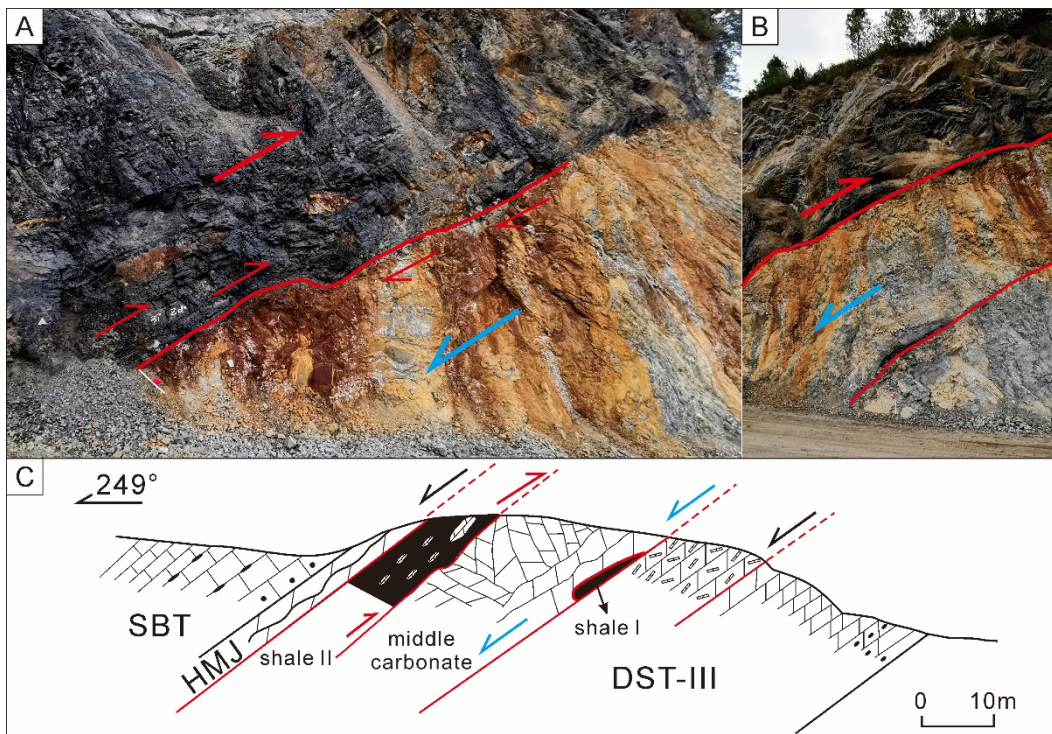


Fig. 4. 10 A: Field photograph of the 'Z' shape contact surface between the upper shale II and the middle carbonate unit. B: Field photograph showing the uncontinuous lower shale I layer. C: Schematic sketch showing the lateral occurrence of different lithounits and the controlling structures. The arrows in the figures represent the relative moving directions of the upper shale II layers (red arrows) and the middle carbonate unit (blue arrows).

4.8 Future Plans for Developing the Models

Although the second model seems plausible, we still lack direct evidence to support opinions of the folded middle carbonate layers and mirror plan hypothesis. Because of the time limitations and the COVID-19 pandemic, it became impossible for me to revisit those sections during my PhD. The next step is to go back and visit the other sections in the Western region of the Huangling Anticline area to look into details of the direct field evidence to support my hypothesis.

4.9 Conclusions

My work documents the large-scale slumping developed in the western region of the Huangling Anticline area during the Ediacaran, and the estimated slide distance is ~5-12 km. The middle carbonate layer is likely to be a slumped unit coming from the Hamajing Member around the upper slope area. I put forward two possible explanations to explain the forming of the middle carbonate unit. Among them, the second evolution model clearly explains the forming history of the large-scale slumping and shows the existence of a ‘mirror plane’ as the middle carbonate has been folded and doubled. The uplift and/or significant regressions might initiate this slump. By comparing and correlating with other sections, I have recovered the chemostratigraphic profiles from the western region of the Huangling Anticline area. The recovered chemostratigraphic profile is relatively consistent and fits the original data. More sections should be added if we want to better understand the slide dimension in the future.

Chapter 5 Experimental Comparisons of Carbonate-associated Sulfate Extraction Methods

Abstract

Carbonate-associated sulfate (CAS) refers to trace amounts of sulfate incorporated into carbonate minerals during precipitation. CAS has been the most commonly used approach to recover the paleo-seawater sulfate sulfur isotope composition ($\delta^{34}\text{S}_{\text{sw}}$) as carbonate rocks or fossils are more common and occur in less restricted marine environments than alternative sulfate-bearing minerals (such as gypsum and barite). However, uncertainties remain about the reliability of preparation techniques due to the inadvertent inclusion of contaminant sulfurous species. This study applied three new oxidative pre-leaching CAS extraction methods and compared their final CAS $\delta^{34}\text{S}_{\text{CAS}}$ values with those following repeated pre-leaching in 10% NaCl (aq). The final CAS sulfur isotope values ($\delta^{34}\text{S}_{\text{CAS}}$) after sequential pre-leaching by a combined 12% NaOCl, 1% H_2O_2 , and 10% NaCl approach were systematically higher by between 0.65‰ and 0.9‰ than rival methods. My experiments demonstrate that non-CAS contamination, organic sulfur, and especially pyrite sulfur can affect the measured CAS sulfur isotope ratio even with short reaction times (<30 min) and that a single pre-leach with standard oxidizing reagents is insufficient to eliminate such contamination. I recommend that $\delta^{34}\text{S}_{\text{CAS}}$ and $\delta^{18}\text{O}_{\text{CAS}}$ studies apply sequential pre-leaching when handling organic and pyrite-rich limestone samples.

Author Contributions: The new methods and experiments were designed and tested by the author ZHEYU TIAN. Dr. Aubrey Zerkle helps me extract inorganic sulfides at the University of St Andrews. Dr. Tianchen He (Leeds) and Dr. Wei Shi (CUG Wuhan) gave me helpful suggestions, and Gary Tarbuck offered technical support. This chapter benefitted from discussions with Graham Shields and Ying Zhou.

5.1 Introduction

Carbonate-associated sulfate (CAS) refers to trace sulfate that was incorporated into carbonate minerals during precipitation (Burdett et al., 1989). CAS has been used as a reliable proxy archive for tracing paleo-seawater isotopic composition since the 1980s (Burdett et al., 1989; Staudt and Schoonen, 1995; Kampschulte and Strauss, 2004; Bottrell and Newton, 2006; Tostevin et al., 2017). Compared with sulfate minerals (barite and sulfate evaporites), which generally precipitate from derived seawater, CAS co-precipitates with normal marine carbonate minerals and so $\delta^{34}\text{S}_{\text{CAS}}$ can serve as a more reliable tracer of the isotopic evolution of seawater sulfate ($\delta^{34}\text{S}_{\text{SW}}$) and may even be used for chemostratigraphic correlation (Kampschulte and Strauss, 1998; Tostevin et al., 2017; Shi et al., 2018; Edwards et al., 2019; He et al., 2019). Moreover, carbonate deposits occur more widely and in less restricted marine environments than other sulfate minerals, further underlining the potential of CAS to better understand the long-term global sulfur cycle (Marenco et al., 2008b).

Despite such promise, $\delta^{34}\text{S}_{\text{CAS}}$ might still deviate from $\delta^{34}\text{S}_{\text{SW}}$ due to post-depositional alteration during meteoric water-rock interaction and recrystallization (Present et al., 2015). Such issues can generally be resolved after careful petrological (grain size, mineral assemblages) and geochemical screening. For example, recrystallized carbonate mineral grains are usually larger ($>50\mu\text{m}$) with lower $\delta^{18}\text{O}$ values (Al-Aasm and Clarke, 2004; Zhang et al., 2020c) and higher Mn/Sr ratios (Kaufman and Knoll, 1995; Bartley et al., 1998; Lan et al., 2019). Cross-plots of $\delta^{34}\text{S}_{\text{CAS}}$ against traditional indicators of diagenetic alteration, CAS concentration, Mn/Sr, Mg/Ca and $\delta^{18}\text{O}_{\text{carb}}$, are therefore widely used to evaluate carbonate diagenesis and the fidelity of the CAS sulfur isotopic composition (Veizer, 1983; Derry et al., 1994; Goldberg et al., 2005b; Guo et al., 2015; He et al., 2019). However, it seems unlikely that such alteration proxies can reliably identify deviation from open ocean $\delta^{34}\text{S}_{\text{SW}}$ values due to mineral precipitation from porewaters affected by early diagenetic microbial sulfate reduction (MSR) (Rennie and Turchyn, 2014; Fike et al., 2015). MSR results in ^{34}S -enrichment in the residual sulfate reservoir, while sulfide oxidation may conversely release ^{34}S -depleted sulfate into porewaters. Although these effects are difficult to assess in individual samples, and may lead to uncertainty over the contemporaneous $\delta^{34}\text{S}_{\text{SW}}$ value, systematic trends and similar

correlative $\delta^{34}\text{S}_{\text{CAS}}$ values are unlikely to result from such localized isotopic fractionation. The thorniest problem surrounding $\delta^{34}\text{S}_{\text{CAS}}$ studies pertains to the inadvertent extraction of sulfate from the non-carbonate matrix of bulk carbonate rocks, including secondary atmospheric sulfate (SAS), organic-bound sulfur, and disseminated pyrite, with $\delta^{34}\text{S}$ values down to -50‰ (Canfield, 2001a; Sim et al., 2011; Hoefs, 2015). It has been demonstrated, in particular, that pyrite oxidation can occur in both strong and weak acids during the CAS extraction process (Marenco et al., 2008b). Such contamination can significantly affect the measured CAS sulfur isotope value during CAS extraction, resulting in lowered $\delta^{34}\text{S}_{\text{CAS}}$ values (Lomans et al., 2002; Marenco et al., 2008a; Peng et al., 2014). In addition to inadvertent signal contamination, analytical protocols can also affect final sulfur isotope values (Wotte et al., 2012a; Fichtner et al., 2017). Even working with well-preserved carbonate samples, generating a reliable CAS signal without incorporating non-CAS contaminants is still a key consideration when using the CAS approach.

To produce reliable CAS sulfur isotope signals, two different approaches have been proposed for CAS extraction. The first of these techniques (Aim-I) aims to eliminate soluble salts, SAS, and hinder further pyrite oxidation and was first used to isolate structurally substituted sulfate from sedimentary phosphate minerals (Wotte et al., 2012a; Theiling and Coleman, 2015; He et al., 2019). The second approach (Aim-II) aims to eliminate organic sulfur and disseminated pyrite by adding oxidants such as NaOCl or H_2O_2 (Burdett et al., 1989; Hurtgen et al., 2002; Marenco et al., 2008a; Guo et al., 2015). Various comparative experimental studies have been carried out. For example, Wotte et al. (2012a) compared a range of pre-leaching techniques: Aim-I: 1) 10% NaCl (aq); 2) pure water only (aq); and Aim-II: 1) 10% NaOCl (aq) only; 2) 10% NaCl (aq) followed by 10% NaOCl (aq); 3) 10% NaCl (aq) followed by 10% H_2O_2 (aq). The authors noted that pre-leaching with those oxidizing agents was insufficient to remove all non-CAS contamination from even finely ground, bulk carbonate rock powder, while residual oxidants proved difficult to eradicate fully. As a consequence, they recommended a single reagent NaCl pre-leaching method (Aim-I), commenting further that the addition of oxidizing agents (NaOCl and H_2O_2) as the last pre-leaching step could potentially oxidize surviving sulfide minerals in the residue, thus contaminating the extracted CAS sulfate.

Other Aim-I trials to prevent sulfide oxidation have included using N_2 carrier

gas in a closed system to prevent the oxidization of acid volatile sulfides and pyrite (Wei et al., 2020b). Other Aim-II trials to use oxidants to remove reduced sulfur included adding 30% H₂O₂ for 48 h to 30-100g sample powder before or after rinse with 10% NaCl solution and deionized water (Shen et al., 2011; Xiao et al., 2012). Such high concentrations of H₂O₂ (aq) are unlikely to be stable and might dissolve carbonate portions of the samples. However, addition of oxidant before salt solution rinses have the potential to guarantee effective removal of both oxidized sulfide and oxidizing reagent.

In this study, I designed and compared three new methods trying to eliminate all non-CAS sulfur-bearing phases using oxidizing agents. My new methods do not add contaminant ions and could completely remove those oxidants before the final CAS extraction steps. (1) 10% H₂O₂ (aq) followed by 10% NaCl (aq); (2) 12% NaOCl (aq) followed by 10% NaCl (aq); (3) Combined NaOCl then H₂O₂ followed by 10% NaCl (aq). I compared these three methods against a refined single reagent 10% NaCl (aq) leaching method (He et al., 2019) in order to identify contaminant sulfur sources and the influence on the measured CAS sulfur isotope values. Here I present the results of those experiments in order to establish a more effective CAS extraction protocol for dealing with problematic pyrite- and/or organic-rich carbonate rocks.

5.2 Sample Selection, Pre-treatment, and Analytical Methodology

Four representative samples from South China have been chosen to test the new methods. Basic descriptions of these samples are given in Table 5.1, while more detailed descriptions can be found in the Supplementary Materials. The samples are selected based on three criteria: 1) the most common carbonate rock types; 2) a wide range of CAS concentrations and $\delta^{34}\text{S}_{\text{CAS}}$ values; 3) a wide range of pyrite and TOC contents (Table 5.1).

Hand specimens of these rock samples were cleaned with water and cut into small blocks in order to remove weathered surfaces before being heated in an oven at 60°C for 48 hours to dry them out thoroughly. One of the dried blocks was used for making thin sections at University College London (UCL) and studied petrographically. The other blocks were first broken into small pieces, and only the pieces without veins were chosen to be ground into powder in a tungsten carbide

Tema mill and crushed again by hand with an agate mortar to maximize its surface area and expose interstitial pyrite. After the crushing process, the machine was cleaned carefully with water and acetone to prevent contamination between samples.

For the elemental test, including Ca, Mg, Mn, Sr, Al, K, Fe, 20mg rock powder was dissolved in 10ml 2% HNO₃ overnight and centrifuged before being measured using a *Varian®* 720 ICP-OES at the London Geochemistry and Isotope Centre (LOGIC) at UCL. The analytical precisions were better than 5%.

Pyrite density was estimated using a petrographic microscope at UCL. Pyrite crystals were counted within a 1×1 mm² area. For each sample, five representative 1×1 mm² areas were chosen to estimate the pyrite density of the sample. The pyrite crystal sizes are relatively homogeneous and range from 7-16µm (See supplementary). The final pyrite density is the average number of pyrite crystals within a 1×1 mm² area in each thin section. Samples with pyrite density < 10/mm² were labelled as low pyrite density, 10/mm² < pyrite density < 100/mm² labelled as medium pyrite density, and pyrite density > 100/mm² labelled as high pyrite density.

Solid inorganic sulfides, operationally defined as acid volatile sulfur (AVS) and chromium reducible sulfur (CRS), were extracted in the Geobiology Laboratory at the University of St Andrews using the chromium reduction method, as previously described (Izon et al., 2015). Briefly, 5-10 g of rock powder was placed in a tri-neck flask and sequentially refluxed with 6M HCl to release AVS, followed by acidified 1M CrCl₂ to release CRS. The resulting H₂S gas was carried on a stream of oxygen-free N₂ into a solution of AgNO₃ and captured as silver sulfide (Ag₂S) for sulfur isotope analyses.

The detail of the CAS extraction procedures will be discussed later. After CAS extraction, sulfate was collected as barium sulfate using excess BaCl₂ (aq). BaSO₄ and Ag₂S precipitates were analyzed for S isotope values and purity by EA-IRMS in the *ISO-Analytical lab* on dried residues of > 0.05mg. The reference material used for analysis was IA-R061 (barium sulfate, δ³⁴S_{CDT} = +20.33‰). IA-R025 (barium sulphate, δ³⁴S_{V-CDT} = +8.53‰), IA-R026 (silver sulphide, δ³⁴S_{V-CDT} = +3.96‰). S isotope values are reported in the δ notation against V-CDT. Along with the sulfur isotope values, we also obtained %S contents that were then used to calculate the purity of the BaSO₄. The analytical precisions were better than 0.06‰ (1SD).

Total organic carbon (TOC) content was analyzed using a *Leco® CS-200* carbon analyzer at UCL. About 1g of sample powders was weighed and reacted with

excess 10% HCl to eliminate carbonate, followed by repeated rinsing with Milli-Q water to remove contamination. The residual was dried at 40°C for 48 hours for the TOC test. Analytical precisions within 1%.

Table 5. 1 Selected carbonate samples. Age estimation is based on its stratigraphic height and geological unit. QLKS = Qinglinkou section, CC = Zhimaping section, LH = Lianghong section.

Sample	Geological unit & estimated age	Lithology	CaCO ₃ wt%	[CAS] ppm	Pyrite Density	$\delta^{34}\text{S}_{\text{CAS}}$ ‰ NaCl rinse
QLKS18	Shibantan Member, Dengying Formation (~546Ma)	Dolostone with calcite veins	50.36	21.734	3.7/mm ² Low	35.84
QLKS6	Shibantan Member, Dengying Formation (~548Ma)	Dark grey thinly laminated limestone with calcite veins	91.63	27.29	22.5/mm ² Medium	46.00
CC3	Shibantan Member, Dengying Formation (~550Ma)	Dark limestone	76.63	111.53	236.1/mm ² High	36.52
LHA6.5	Member III, Doushantuo Formation (~555Ma)	Grey-orange fine-grain limestone	84.92	78.84	17.9/mm ² Medium	20.21

5.3 Refined NaCl Leaching Method (method 1)

Using smaller and more finely ground samples can significantly decrease the risk of contamination by non-CAS components in bulk carbonate powders. In this regard, the NaCl leaching method (Wotte et al., 2012) (see Fig. 5.1-A) has been applied increasingly to smaller samples, now 8-10g (Tostevin et al., 2017; He et al., 2019) compared with the more commonly larger 30-100g samples (Xiao et al., 2012; Shi et al., 2018; Toyama et al., 2020).

It has been shown by (He et al., 2019; He et al., 2020) that the sulfur concentration in the NaCl-leachates declines dramatically through sequential leaching, reaching near blank levels after the fifth leach. In my study, rock powder was leached five times in an actively mixed 10% NaCl solution over 24 hours, followed each time by centrifugation to remove the supernatant. Between each leach, the residue was rinsed three times with deionized water. After the final leach with NaCl solution, the residue was rinsed five times with deionized water, followed by immediate CAS extraction using 6 M HCl (aq).

After the pre-leaching, I used excess 6 M HCl (aq) for the final dissolution step (8-10g samples) for all tested CAS extraction methods (Fig. 5.1-D). Reaction times

were kept to no more than 30 minutes to minimize the potential for pyrite oxidation (He et al., 2019). The solution was then filtered using a polyethylene syringe and a 0.2µm polypropylene membrane filter. 1.5 ml 200g/L BaCl₂ (aq) was added to the filtrate and left for 3-4 days in order to precipitate released trace sulfate. After centrifugation and supernatant removal, the residue was rinsed with 6M HCl and deionized water to remove soluble components, such as BaCl₂ and BaCO₃, and dried at 60°C for three days.

Previous studies used saturated BaCl₂ solution (312g/L) to precipitate barium sulfate (Li et al., 2017, Tostevin et al., 2017, He et al., 2019). However, this study found that adding saturated BaCl₂ (aq) into the decarbonated HCl solution may cause BaCl₂ to precipitate instead of barite. After several tests, I found that adding 1.5 ml 200g/L BaCl₂ (aq) improved the purity of the yield (Fig. 5.1-D).

This method is easy to handle and can remove most water-soluble sulfate and SAS in the carbonate powder. However, the method cannot eliminate AVS, CRS, and organic sulfur, which could undergo partial oxidation during CAS extraction. Therefore, this method could potentially generate a different, most likely lower $\delta^{34}\text{S}_{\text{CAS}}$ value compared with the actual carbonate value, which should approximate the $\delta^{34}\text{S}_{\text{sw}}$ value of contemporaneous seawater.

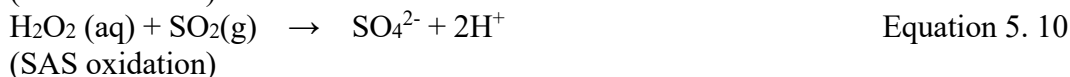
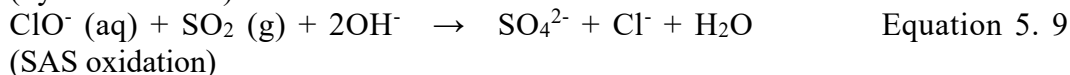
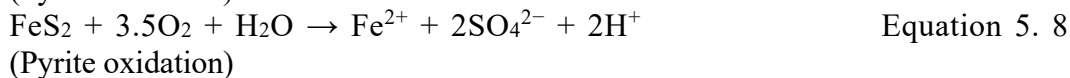
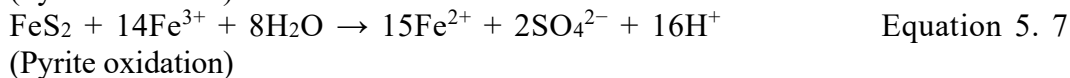
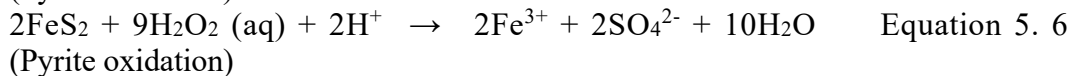
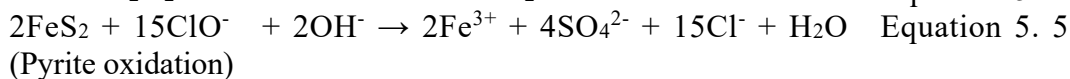
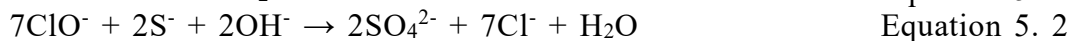
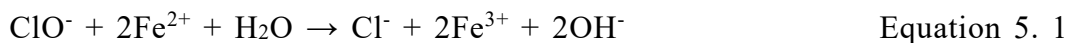
5.4 Three Newly Designed Methods

5.4.1 H₂O₂ and NaOCl Leaching (methods 2a and 2b)

These two methods were developed from a combined NaCl-NaOCl leach method, as applied by (Gill et al., 2011a; Gill et al., 2011b), in which 10% NaCl solution is first added to the samples for 24h. Subsequently, the samples are rinsed twice with deionized water and then in 4% NaOCl solution for 48h in order to oxidize the non-CAS sulfur. Two additional rinses with deionized H₂O follow this step. (Wotte et al., 2012a) argued that this method has the following drawbacks: 1) It cannot ensure the elimination of pyrite; and 2) It cannot totally remove the oxidants before CAS extraction. Consequently, if the powder is not sufficiently fine, interstitial pyrite might be oxidized in the subsequent extraction process by a combination of Fe (III) and any oxidants that remain in the slurry (Equation 5.5-5.8).

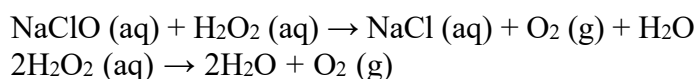
In my revised single oxidative methods (Fig. 5.1-B), samples were leached firstly with 10% H₂O₂ (aq) solution (method 2a) or 12% NaOCl (aq) solution

(method 2b) for 24 h in order to remove the SAS, organic sulfur and pyrite (equations 5.5-5.10). The anticipated reaction in the slurry is shown in equations 5.1-5.10. These oxidants have been widely used by, for example (Ohkouchi et al., 1999; Hurtgen et al., 2002; Newton et al., 2004; Shen et al., 2011; Loyd et al., 2012; Xiao et al., 2012). The leaching procedure was repeated three times for 24 h each. In order to disintegrate the powder further and maximize pyrite surface area, an ultrasonic bath was used between vigorous shaking using a rotator. The residue was rinsed three times with deionized water between each leach to remove the oxidized sulfur in the slurry. Nearly no barium sulfate precipitate was observed after the third leach, after which the residue was washed repeatedly using the refined 10% NaCl (aq) leaching method (Fig. 5.1-A) to remove remaining sulfate, SAS, and oxidant in the slurry.



5.4.2 Combined NaOCl-H₂O₂ Leaching (method 3)

According to the study by (Wotte et al., 2012a), it is hard to eliminate oxidants in the slurry totally. The new combined oxidative method (method 3) in this study was designed to solve this issue (Fig. 5.1-C). After final leaching with NaOCl and water in method 2b, 1% H₂O₂ (aq) was added to the slurry in order to remove the NaOCl (Equation 5.11). The absence of bubbles shows whether the NaOCl was successfully removed from the slurry. Importantly, the addition of hydrogen peroxide will not add further contaminant ions to the slurry, while being unstable, it can be easily removed by heating at 90°C (Equation 5.12), followed by the refined 10% NaCl (aq) leaching method, as shown in Fig. 5.1-A.



Equation 5. 11

Equation 5. 12

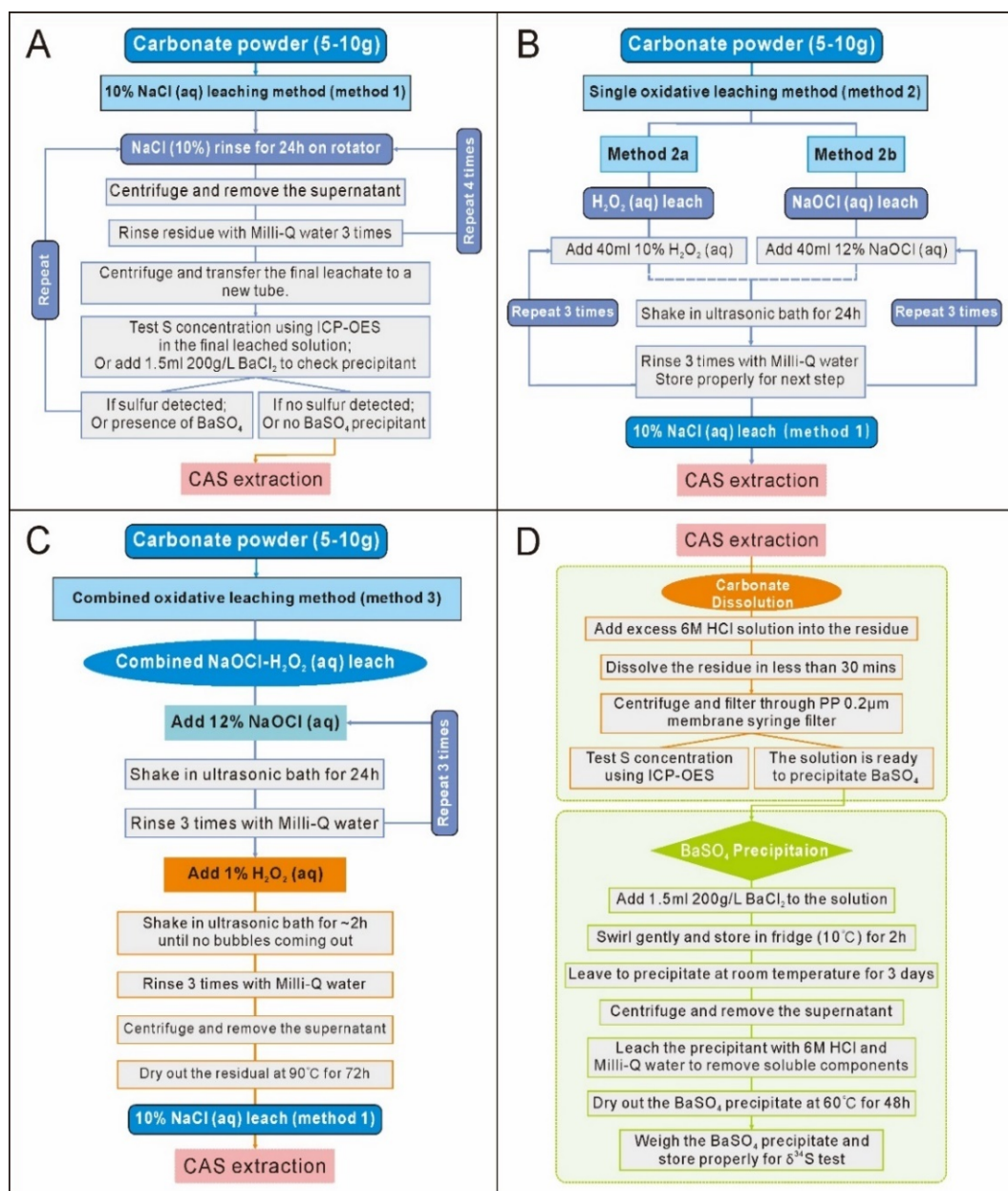


Fig. 5. 1 New designed and tested carbonate-associated sulfate (CAS) pre-leaching and extraction protocols in this study. A: Refined 10% NaCl (aq) pre-leaching method (method 1). B: Single oxidative-NaCl pre-leaching methods: 10% H₂O₂ (aq) leach (method 2a) and 12% NaOCl leach (aq) (method 2b). C: Combined NaOCl-H₂O₂-NaCl pre-leaching method (method 3). D: Refined CAS extraction protocols.

5.5 Results

Leachate precipitate weights, sulfur isotope values, and final CAS sulfur isotope values are shown in Table 5.2. Because precipitates are rarely pure barium sulfate, I back-calculated barium sulfate weights based on the purity data. The leachate precipitate sulfur isotope values are shown as $\delta^{34}\text{S}_{\text{SL}}$, and the final CAS

sulfur isotope values are shown as $\delta^{34}\text{S}_{\text{CAS}}$. For method 2a, as H_2O_2 (aq) is a weak dibasic acid, it will cause partial dissolution of samples. Moreover, it is not stable and might cause accidents if not handled properly, so I have not tested the leachate sulfur isotope value of all samples using method 2a. As QLKS18 is a dolostone sample with a very low sulfate concentration (Table 5.1), I failed to get the final CAS sulfur isotope data. All the elemental data are shown in (Table 5.3).

Extracted AVS and CRS concentrations were also back-calculated based on the purity data. As LHA6.5 is a pure limestone with very low pyrite and TOC content, I failed to obtain AVS and CRS sulfur isotope values from this sample.

Table 5. 2 Leachate precipitate weight, sulfur isotope composition, and final CAS sulfur isotope values from different pre-leaching methods together with the TOC content, AVS, CRS concentration, and its sulfur isotope values of the samples. “--” means too low to get a reliable value. SL = solution. S isotope values are reported in the δ notation against V-CDT.

Sample	Method	Powder weight (g)	Rinse Times	BaSO ₄ Corrected (mg)	Leachate $\delta^{34}\text{S}_{\text{SL}}$ (‰)	CAS $\delta^{34}\text{S}_{\text{CAS}}$ (‰)	Method I $\delta^{34}\text{S}_{\text{CAS}}$ (‰)	AVS S(ppm)	$\delta^{34}\text{S}_{\text{AVS}}$ (‰)	CRS S(ppm)	$\delta^{34}\text{S}_{\text{CRS}}$ (‰)	TOC(wt%)
QLKS18	2a	7.59	1	1.39	--							
			2	1.84	--							
			3	1.09	--							
	2b	8	1	0.08	20.65	--	35.84	4.00	--	9.75	30.47	0.022
			2	0.63	--							
			3	0.33	--							
QLKS6	2a	7.5	1	0.12	31.82		46.00	1.41	--	90.50	37.16	0.14
			2	0.15	20.28	46.37						
			3	0.05	--							
	3	8	1	0.12	--	46.79						
			2	0.77	--	--						
			3	0.17								
CC3	2a	7.52	1	133.37								
			2	2.42	--	--						
			3	0.16								
	2b	8	1	134.24	24.15		36.52	16.05	24.26	1769.16	22.19	2.53
			2	0.84	20.45	36.91						
			3	0.04	18.88							
LHA6.5	2a	7.51	1	0.13								
			2	1.09		--						
			3	0.29								
	2b	8	1	0.08	--		20.21	1.37	--	13.77	--	0.013
			2	0.33		20.72						
			3	0.11								
	3	8	1	0.08		20.86						
			2	0.08								

Table 5. 3 Elemental concentrations of the acid-soluble fractions of the samples measured by ICP-OES. Carbonate content (%): weight percentages of acid-leachable content ($\text{CaCO}_3 + \text{MgCO}_3$).

Sam ple	Ca, (%)	Mg (ppm)	Al (ppm)	K (ppm)	Fe (ppm)	Mn (ppm)	Sr (ppm)	Mn/ Sr	Mg/ Ca	Sr/ Ca	Fe/ Ca	Carbo nate conte nt, %
QLK S18	20.1 4	12230 1	154.3 7	43.42	38.59	155.81	43.42	3.59	0.61	0.00 022	0.00 019	93.16
QLK S6	36.6 5	11917 .94	47.71	23.85	4.77	32.92	1125. 95	0.02 9	0.03 3	0.00 31	0.00 0013	95.80
CC3	30.6 5	8433. 85	121.6 0	325.8 8	525.2 9	14.11	3706. 23	0.00 39	0.02 8	0.01 2	0.00 17	79.57
LHA 6.5	33.9 7	3398. 95	130.1 9	91.19	1940. 90	333.85	207.0 6	1.61	0.01 0	0.00 061	0.00 57	86.11

5.6 Discussion

5.6.1 Diagenetic Evaluation

Samples with calcium carbonate content $>70\%$ and Mg/Ca ratio <0.025 are shown in Fig. 5.2-A as limestones (LM), calcium carbonate content $>70\%$ and Mg/Ca ratio >0.025 are dolomitic limestones (DL), and calcium carbonate content $<70\%$ are dolostones (DM). On this basis, Fig. 5.2-A shows that sample QLKS18 is near stoichiometric dolomite, while the others are limestones.

Cross-plots of Mn/Sr, Mg/Ca, Sr/Ca, and Fe/Ca ratios are commonly used to evaluate the extent of diagenetic alteration, as dissolution and recrystallization can raise Mn, Fe, and Zn contents and lower Sr, Na contents (Kaufman and Knoll, 1995; Bartley et al., 1998; Lan et al., 2019). Mn/Sr ratios lower than 2, Sr/Ca ratios higher than 0.001, Mg/Ca ratios lower than 0.257 and Fe/Ca ratios lower than 0.01 indicate that the limestone samples in this study have undergone limited diagenetic alteration (Fig. 5.2). The low CAS yield from sample QLKS18 is perhaps unsurprising due to dolomitization, which typically occurs under sulfate-reducing conditions (Staudt and Schoonen, 1995; Swart, 2015; Fichtner et al., 2017); however, I noted that several published studies report dolomite CAS isotopic data, implying that carbonate-associated sulfate can withstand burial diagenesis and potentially record the paleo seawater $\delta^{34}\text{S}_{\text{CAS}}$ signature (Wotte et al., 2012b; Guo et al., 2015; Fichtner et al., 2017; Tostevin et al., 2017; Shi et al., 2018). Although I tried several times with sample QLKS18, I failed to get enough BaSO_4 precipitate for isotopic analysis.

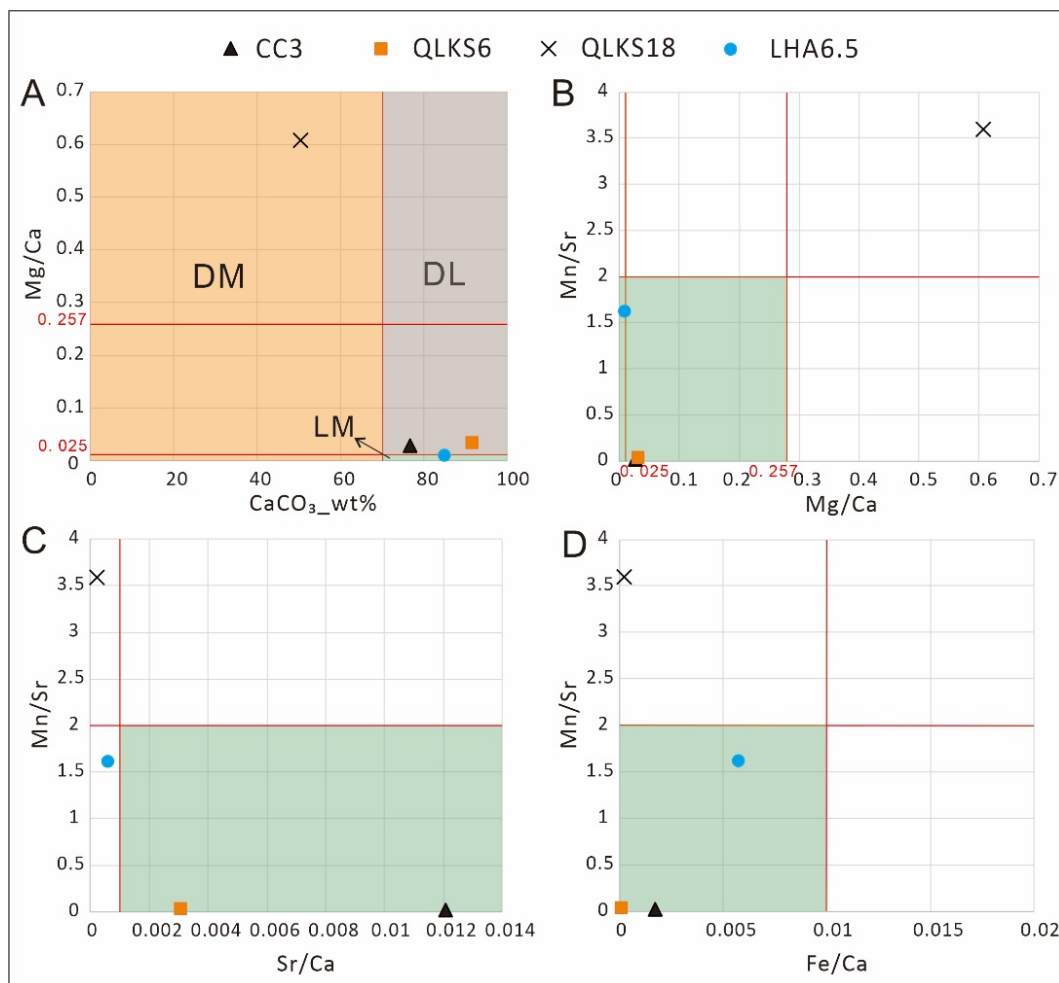


Fig. 5. 2 Cross-plot of the selected samples. DM: dolomite (calcium carbonate content < 70%); DL: dolomitic limestone (calcium carbonate content > 70%; Mg/Ca > 0.025); LM: limestone (calcium carbonate content > 70%; Mg/Ca < 0.025). Thresholds for the green shaded area (best-preserved samples) are Mn/Sr < 2, Sr/Ca > 0.001, Mg/Ca < 0.257 and Fe/Ca < 0.01.

5.6.2 Evaluation of the Three New Methods

NaOCl leachates with pink to brown color shows how after adding oxidants to the slurry, iron, likely in the form of pyrite, has been oxidized (Fig. 5.3). Fig. 5.4-A, B shows that the final barite precipitate (back-calculated) weight from the leached solutions using all these three tested methods shows a similar trend towards zero after the third leach. Only sample CC3, which is dark limestone with the highest pyrite density and TOC content, shows a continuously decreasing trend of the precipitate weight (grey line). The other samples show that the second leachate has the most sulfate. The third and fourth leachates have similar precipitate weights almost below the lower limit for S isotope analysis (Fig. 5.4-C), confirming that nearly all the contaminant S has been removed during leach steps 3 and/or 4.

All leachates have significantly lower sulfur isotope $\delta^{34}\text{S}_{\text{SL}}$ values compared

with the final $\delta^{34}\text{S}_{\text{CAS}}$ values ($\sim 13\text{--}26\text{‰}$ lower) (Table 5.2), indicating that the leaching process removes contaminant sulfur-bearing species (atmospheric sulfate or SAS, organic sulfur, and pyrite) rather than CAS. The first leachates from samples QLKS6, CC3, and QLKS18, all from the Shibantan Member of the Dengying Formation, have the highest sulfur isotope values with $\delta^{34}\text{S}_{\text{SL}}$ of 31.82‰, 24.15‰, and 20.65‰ respectively, whereas second and third leachates of those samples have consistent $\delta^{34}\text{S}_{\text{SL}}$ values around 20‰.

Fig. 5.4-D shows the final $\delta^{34}\text{S}_{\text{CAS}}$ value using different methods. Comparing with the single NaCl (aq) leaching method, the methods 2b and 3 show incrementally higher final $\delta^{34}\text{S}_{\text{CAS}}$ values for the same sample. For samples LHA6.5, QLKS6, and CC3, there is a systematic difference of 0.65‰, 0.79‰, and 0.90‰, respectively, between the single NaCl leaching method and the combined oxidative method 3. These relative differences mirror the samples' estimated pyrite density (17.9, 22.5, and 236.1) and measured AVS + CRS contents, respectively (Table 5.2). My test reveals method 3 to be the superior method in the sense that it will more likely result in pristine CAS sulfur isotope values for pyrite-rich samples. However, the differences, although systematic in direction, are relatively minor.

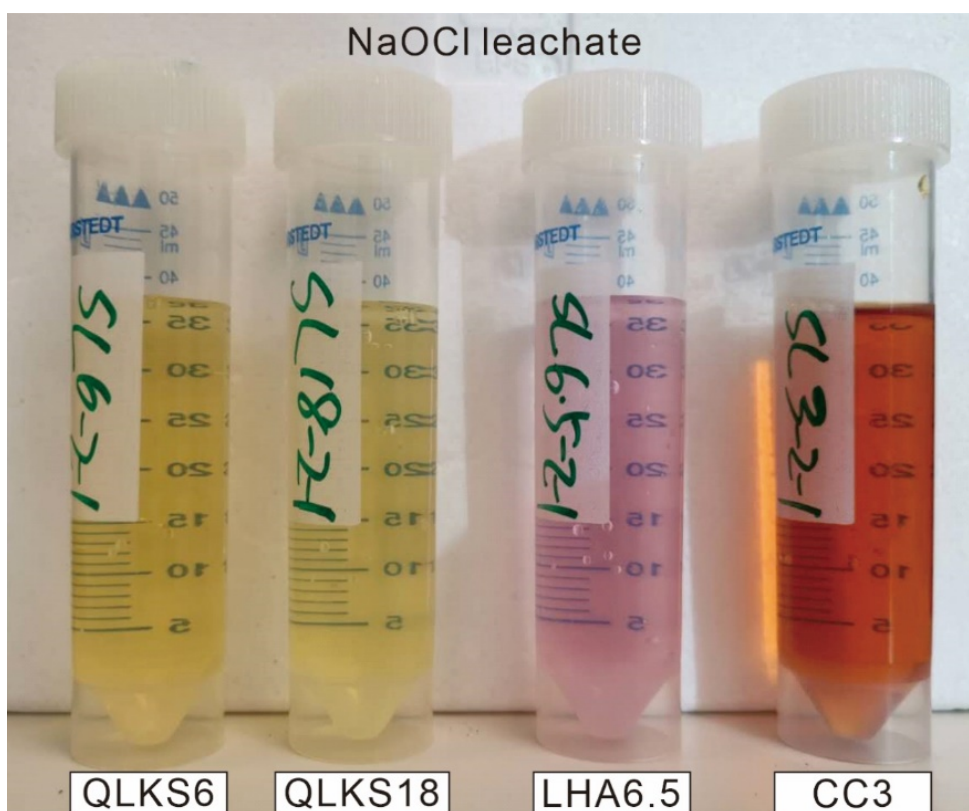
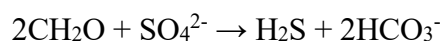


Fig. 5. 3 NaOCl leachates with pink/brown color showing the pyrite has been oxidized.

5.6.3 Contaminant Sulfur Evaluation

Compared to pyrite sulfur and organic sulfur, atmospheric SO₂ can potentially influence final CAS sulfur isotope values but is relatively hard to evaluate (Peng et al., 2014). Moreover, SAS sulfur is likely to be sorbed onto the surfaces of carbonate crystals (Edwards et al., 2019) and so can be leached out with continued NaCl rinses. So, in this study, I mainly tested the S isotope values of AVS and CRS (pyrite) in each sample and the TOC content to evaluate the potential influence of those sulfur-bearing contaminants on the final CAS sulfur isotope values. The results show that TOC content and/or pyrite content could significantly influence the CAS values (Fig. 5.4-E). Sample CC3, which has the most pyrite and TOC content, exhibits the greatest difference between CAS sulfur isotope values. Although LHA6.5 and QLKS6 have similar TOC contents, sample QLKS6, which has more CRS, shows the greater change in final CAS value.

Fig. 5.4-F shows that except for sample CC3, all the other leachates have much lower $\delta^{34}\text{S}$ than CRS. As pyrite sulfur and organic sulfur compounds (OSC) are the two main sulfur sources in TOC-rich carbonate samples (Werne et al., 2003; Siedenberg et al., 2018), I consider that OSC might causes the lowered leachate sulfur isotope values. The origin and composition of the organic sulfur compounds are still not fully understood, but it has been reported that organic sulfur isotope values are at least 8‰ lower than ambient seawater sulfate (Siedenberg et al., 2018), while kerogen sulfur was reported to range widely between -32.6‰ and 30.3‰ in Archean stromatolite samples (Bontognali et al., 2012). Although the first leachate precipitate weight of sample CC3 is ~100 times higher than the highest values from the other samples, the AVS + CRS concentration of this sample is only 20 times higher than the other samples. This further indicates that I oxidized the OSC and that the difference between the leachate and CRS sulfur isotope values was caused by oxidizing the OSC. It is generally believed that negligible sulfur isotope fraction is associated with the formation of pyrite and organic sulfur compounds (OSC) from sulfide or sulfur intermediates (Werne et al., 2003), which means the CRS and OSC sulfur isotope values indicate their source and pathways. Both pyrite and organic sulfur can be formed or incorporated as the result of MSR by the generalized reaction (Berner, 1984):



Equation 5. 13

However, pyrite can also be formed directly by the presence of Fe^{2+} and $\text{H}_2\text{S}(\text{aq})$ in hydrothermal systems Graham and Ohmoto (1994). Moreover, Cui et al. (2018) show that pyrite of hydrothermal origin can be isotopically heavier due to thermochemical sulfate reduction (TSR). Their different forming pathways might cause different sulfur isotope values.

I also noticed that the leachate sulfur isotope values show a decreasing trend and leachates 2 and 3 have relatively stable isotope values of around 20‰. It seems that the first leachate is more complex, whereby the first leachate of sample CC3 has nearly the same sulfur isotope value as AVS: 24.15‰ and 24.26‰, respectively. As pyrite is more easily oxidized by oxidant (NaOCl) than OSC, while SAS might have only a negligible influence on the leachate sulfur isotope values, the first leachate is more likely to represent the combination of both AVS and CRS. However, leachate 2, and especially leachate 3 might indicate the organic sulfur isotope composition.

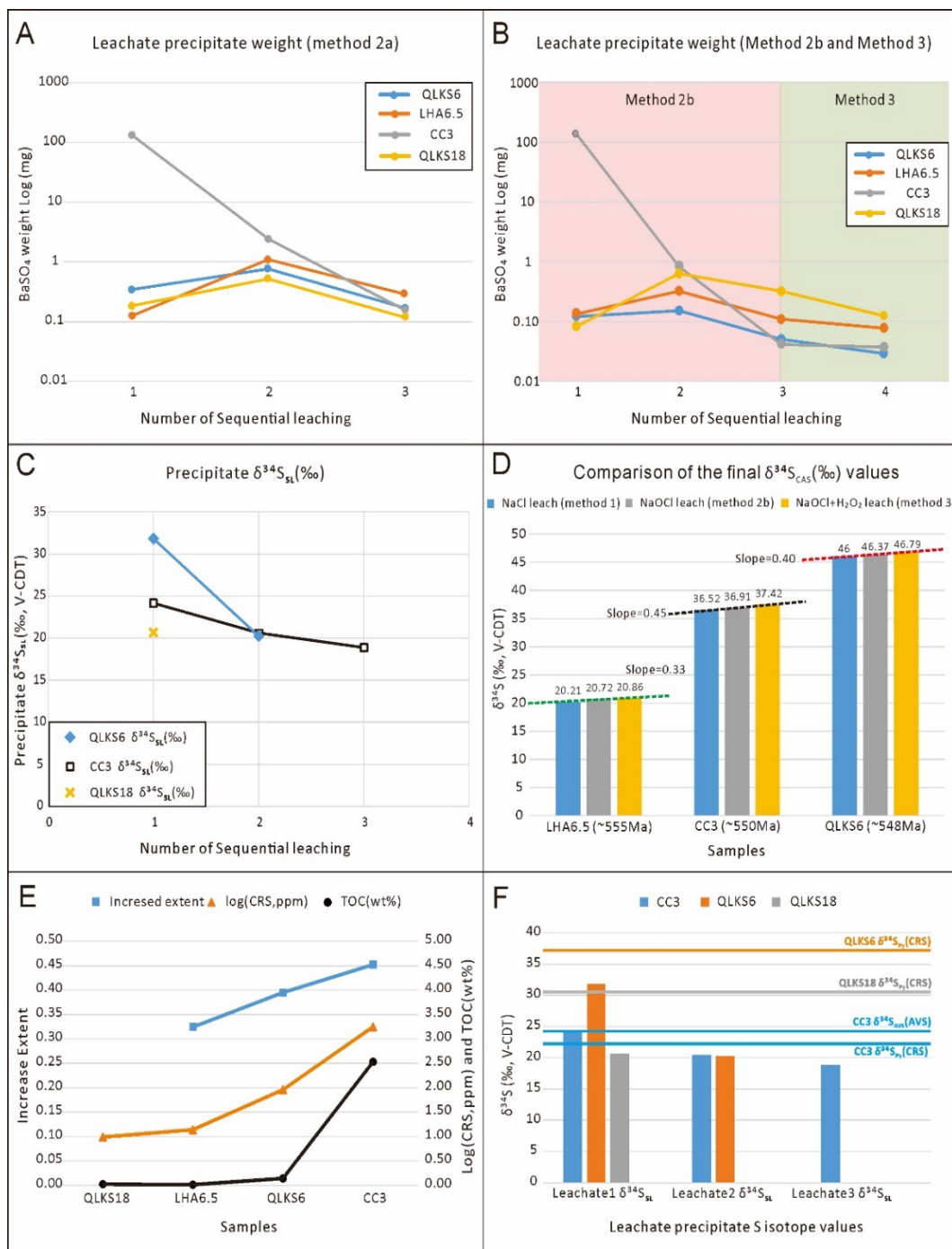


Fig. 5. 4 Comparison and evaluation of four methods results in this study. A: Barite precipitate weight from 3 leachates using method 2a. B: Barite precipitate weight from 3-4 leachates using method 2b (shaded in pink) and 3 (shaded in green). C: Leachate sulfate sulfur isotope values $\delta^{34}\text{S}_{\text{SL}}$. D: Comparison of the final CAS sulfur isotope value $\delta^{34}\text{S}_{\text{CAS}}$ using three different methods (NaCl only, methods 2b, and method 3). E: Comparison between the gradient of CAS $\delta^{34}\text{S}_{\text{CAS}}$ increase from NaCl pre-leaching to method 3 and samples' CRS concentration and TOC content. F: Comparison of the leachate precipitate S isotope value with pyrite S isotope value showing the leachate S isotope values are consistently lower than the coeval pyrite S isotope values. Sample CC3 (dark limestone with the highest pyrite density and AVS + CRS concentration, ~550Ma) has the highest increase of the final $\delta^{34}\text{S}_{\text{CAS}}$ value (and greatest slope), then QLKS6 (dark grey limestone, ~548Ma), then LHA6.5 (grey limestone, ~555Ma).

5.6.4 Comparing the New Data with Published CAS Data

This study chose three samples from the Shibantan Member, Dengying Formation (CC3, QLKS6, QLKS18) and one sample from Doushantuo Member III (LHA6.5). In the Yangtze Gorges area, the Dengying Formation is subdivided into three Members, which from bottom to top are the siliceous dolostone Hamajing Member, dark banded limestone Shibantan Member, and light grey dolostone Baimatuo Member. These three Members can be correlated with the Algal Dolomite, Gaojiashan, and Beiwan Members, respectively, in the southern Shaanxi Gaojiashan area (Chen et al., 2015; Cui et al., 2016a). The Dengying Formation can also be correlated to the Nama Group in Namibia (Tostevin et al., 2017). For sample LHA6.5, with the carbon isotope value -8.1‰ (Lu et al., 2013), it can be correlated with the upper Doushantuo Member III in the Jiulongwan section (Shi et al., 2018).

The CAS sulfur isotope data and $\Delta\delta^{34}\text{S}$ data from this study and published equivalent samples' data are summarized in Table 5.4. By comparison, the results using method 3 could generate higher CAS sulfur isotope values (Fig. 5.5). The average $\delta^{34}\text{S}_{\text{CAS}}$ using method 3 is 40.02‰, which is comparable with stratigraphically equivalent samples from the Gaojiashan Member, Gaojiashan section (42.40‰) (Cui et al., 2016a) but higher than values from the Gaojiashan Member, Lianghekou section (36.1‰) (Chen et al., 2015) and the Nama group (34.13‰) (Tostevin et al., 2017). Although I only tested three samples from the Shibantan Member for this study, one sample tested with the new method generated a CAS sulfur isotope composition of 46.8‰, which is 1‰ higher than the highest published values from either the Gaojiashan Member or the Nama Group. Furthermore, the value from Doushantuo Member III in this study is 0.2-0.7‰ higher than the average CAS sulfur isotope composition (the balance state period) from the Jiulongwan section (McFadden et al., 2008; Shi et al., 2018). These suggest that the improved method here could significantly prevent the inclusion of contaminant sulfur (up to 15.2‰ lower than resultant CAS, Table 5.2) and generate more reliable CAS data. Moreover, by oxidizing the contaminant sulfur, my new method 3 could prevent the incorporation of contaminant O from the water H_2O or the dissolved oxygen O_2 (Equation 5.7, 5.8), which could potentially generate more reliable CAS $\delta^{18}\text{O}_{\text{CAS}}$ too.

In summary, my experiments outlined here demonstrate that method 3 is a

potentially superior method for handling pyrite-rich and organic-rich (high TOC content) limestone samples. However, If the sample is pure limestone with low pyrite density and TOC content, repeated pre-leaching with 10% NaCl is still shown to be both straightforward and relatively reliable.

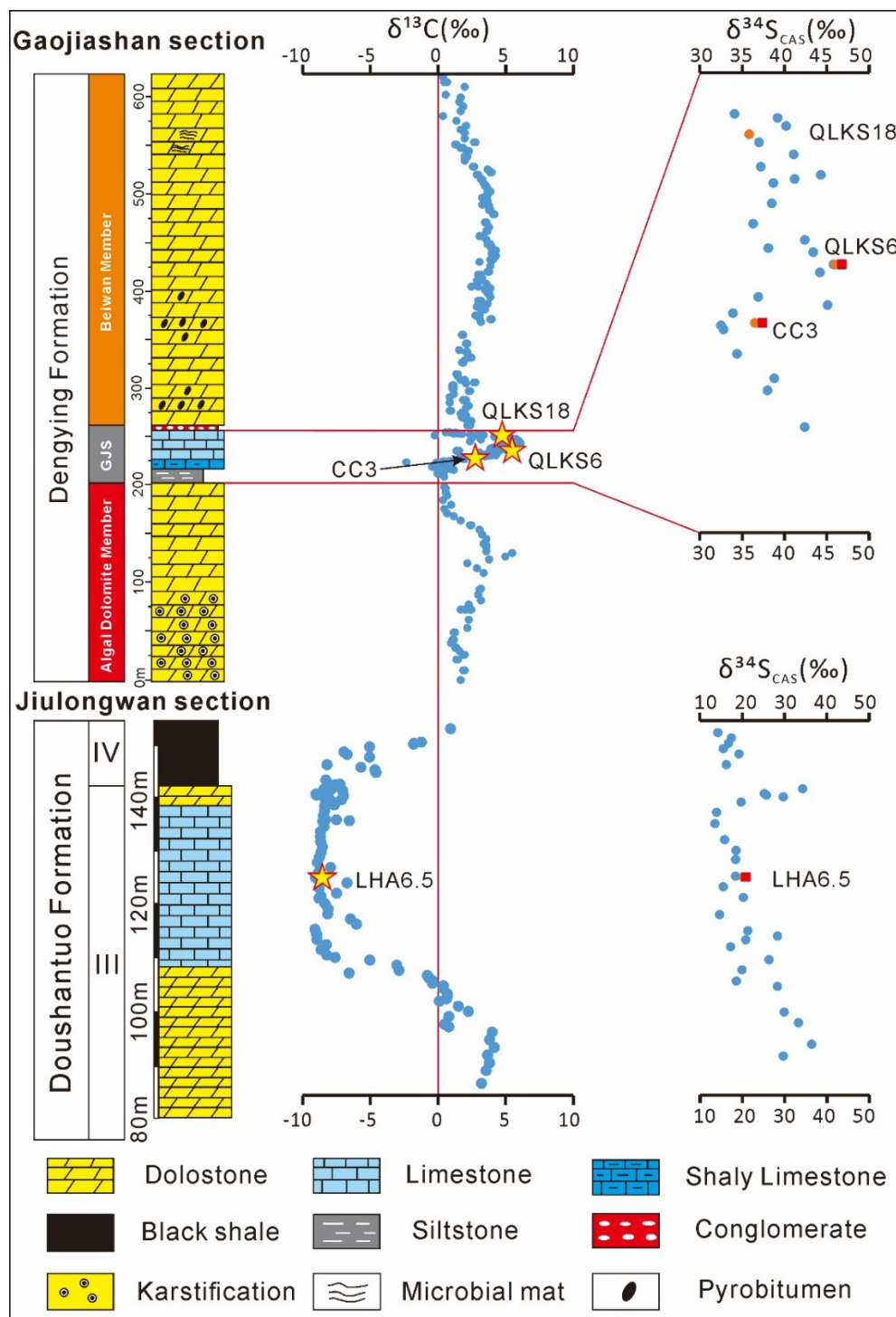


Fig. 5.5 Comparison of the published $\delta^{34}\text{S}_{\text{CAS}} (\text{‰})$ and the data from this study using method 1 (orange circles) and method 3 (red square). The relative stratigraphic heights of the samples are based on age estimations and carbon isotope values. Sample LHA6.5 is from the Lianghong section. Sample CC3 is from the Zhimaping section. Sample QLKS6 and QLKS18 are from the Qinglinkou section. The blue dots are published data from (Cui et al., 2016a; Shi et al., 2018). GJS = Gaojiashan Member.

5.6.5 Rethinking the ‘Superheavy Pyrite’

The phenomenon of high sulfide sulfur isotope values (higher than contemporaneous sulfate sulfur isotope value) has been referred to as the ‘superheavy pyrite’ problem (Ries et al., 2009a). However, sedimentary pyrite sulfur $\delta^{34}\text{S}_{\text{PY}}$ can generally never be isotopically heavier than its ambient sulfate reservoir $\delta^{34}\text{S}_{\text{sulfate}}$, which has puzzled geochemists for decades (Canfield, 2001a; Fike et al., 2015; Cui et al., 2018).

The result from Tostevin et al. (2017) indicated the average $\Delta\delta^{34}\text{S}_{\text{CAS-PY}}$ of only less than 1‰ difference ($-0.72 \pm 5.68\text{‰}$, Table 5.4, Fig. 5.6-A) and only two samples have higher pyrite sulfur $\delta^{34}\text{S}_{\text{PY}}$ than the $\delta^{34}\text{S}_{\text{CAS}}$. Moreover, a recent study by (Wang et al., 2019a) reports new data from the Sturtian Nanhua Basin. The $\Delta\delta^{34}\text{S}_{\text{CAS-PY}}$ values in that study range from -6.5‰ to $+8.0\text{‰}$, with a mean of $+0.7\text{‰}$ (Fig. 5.6-B). However, this slight difference might have resulted from the CAS extraction method, potentially being contaminated and lowering the CAS sulfur isotope values. In this regard, it may be significant that $\delta^{34}\text{S}_{\text{CRS}}$ values from my study, although high, up to 37.2‰ , are consistently lower than $\delta^{34}\text{S}_{\text{CAS}}$ values from the same sample. Therefore, it can still be argued that ‘superheavy pyrite’ might just be ‘heavy pyrite’, which can be achieved in a low sulfate environment via Rayleigh distillation (Chen et al., 2008; Ries et al., 2009a; Wood et al., 2015). Cui et al. (2018) proposed that post-depositional TSR might generate high pyrite sulfur $\delta^{34}\text{S}_{\text{PY}}$. However, hydrothermal activity is a local process, and not all isotopically heavy pyrite has been subject to hydrothermal influence (Wang et al., 2019a). Moreover, isotopically heavy pyrite might also form in shallow, high sedimentation rate environments, which involves partial oxidation of the sulfide during frequent sedimentary reworking (Fike et al., 2015). Until more reliable isotopic data come out, the origins or even existence of ‘superheavy pyrite’ will likely remain obscure.

Table 5. 4 Comparisons between CAS sulfur isotope values $\delta^{34}\text{S}_{\text{CAS}}$ and $\Delta\delta^{34}\text{S}_{\text{CAS-PY}}$ from this study and published data. ‘n’ indicates the sample number. Errors are one standard deviation.

Age	Samples	$\delta^{34}\text{S}_{\text{CAS}}$ highest	$\delta^{34}\text{S}_{\text{CAS}}$ lowest	$\delta^{34}\text{S}_{\text{CAS}}$ mean	$\Delta\delta^{34}\text{S}_{\text{CAS-PY}}$
Middle Dengying Formation	This study Shibantan Member Qinglinkou section (method 3)	46.79‰	35.84‰	$40.02 \pm 5.92\text{‰}$ (n=3)	$10.08 \pm 4.95\text{‰}$ (n=3)
	Cui et al. (2016a) Gaojiashan Member Gaojiashan section	45.8‰	32.5‰	$42.40 \pm 3.74\text{‰}$ (n=42)	$34.65 \pm 9.61\text{‰}$ (n=26)

	Chen et al. (2015) Gaojiashan Member Lianghekou section	37.8‰	33.1‰	$36.1 \pm 2.17‰$ (n=4)	--
	Tostevin et al. (2017) Nama Group Namibia	45.43‰	21.87‰	$34.13 \pm 5.34‰$ (n=51)	$-0.72 \pm 5.68‰$ (n=11)
Doushantuo Member III	This study Doushantuo III Lianghong section (method 3)	20.9‰	20.9‰	20.9‰	--
	McFadden et al. (2008) Upper Doushantuo Jiulongwan section	43.5‰	6.9‰	$20.7 \pm 8.6‰$ (n=50)	$22.8 \pm 10.0‰$ (n=18)
	Shi et al. (2018) Upper Doushantuo Jiulongwan section	34.3‰	13.5‰	$20.2 \pm 6.3‰$ (n=14)	$24.8 \pm 11.8‰$ (n=13)

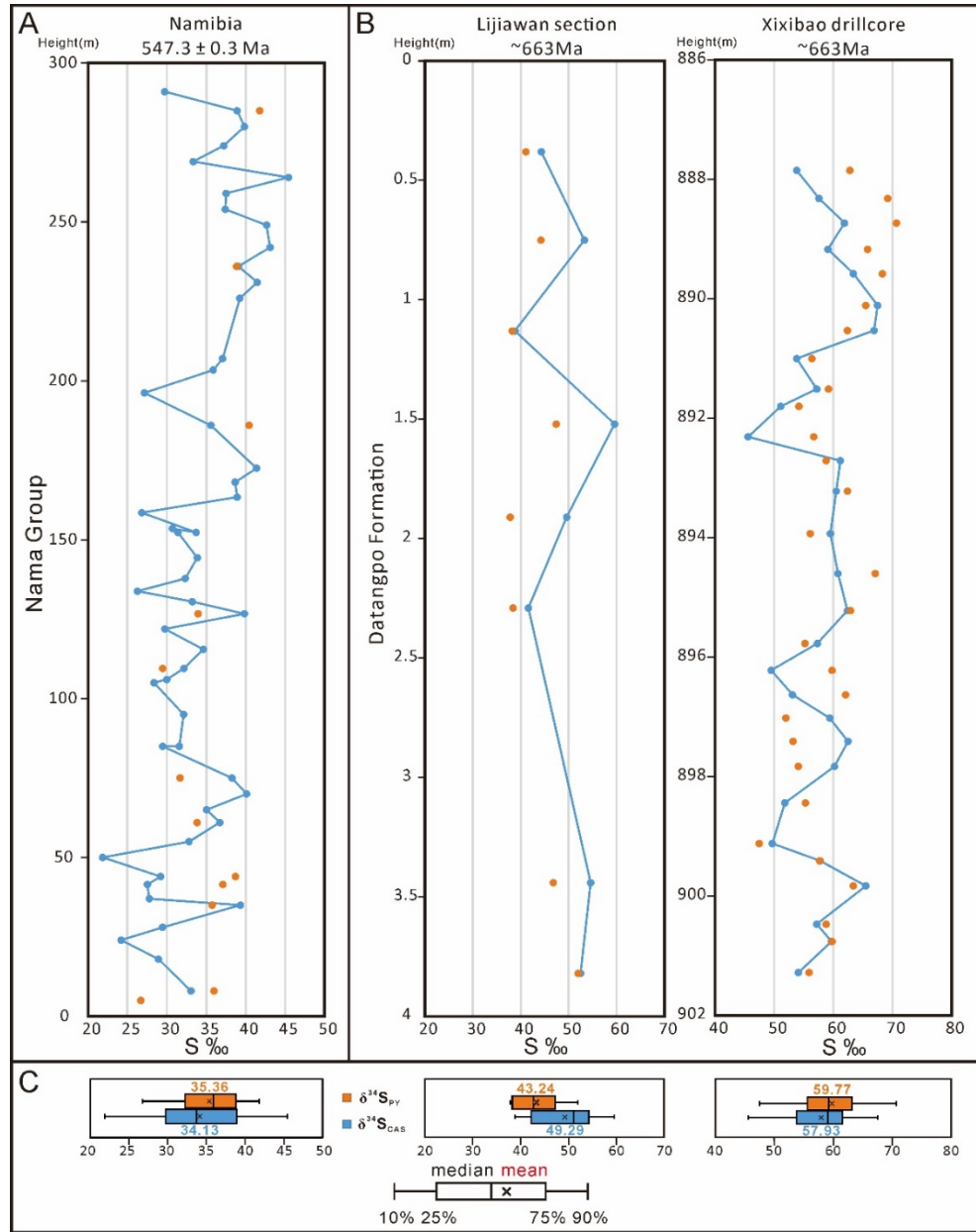


Fig. 5. 6 A-B: Comparison of published $\delta^{34}\text{S}_{\text{CAS}}$ (blue color) and $\delta^{34}\text{S}_{\text{PY}}$ (orange color) data measured from ‘superheavy pyrite’ sections. A: Nama Group data from (Tostevin et al., 2017). B: Datangpo Formation data from (Wang et al., 2019a). C: Box plots of corresponding data. The black line and cross symbols in each box show the median and mean values, respectively.

5.7 Conclusions

In this study, I designed and compared three oxidative CAS leaching methods with the refined NaCl leaching method in order to establish a robust protocol for CAS extraction. My experiments demonstrate that:

- (1) The combined oxidizing method '12% NaOCl + 1% H₂O₂ followed by repeated 10% NaCl leaching' is, by comparison, the most suitable method to handle samples with high pyrite and organic contents. If the sample is pure limestone with low pyrite density, repeated pre-leaching with 10% NaCl is more straightforward and relatively reliable. Adding 1% H₂O₂ after NaOCl leaches not only eliminates NaOCl from the solution but also has the potential to remove some late-stage carbonate cement.
- (2) My new method 3 could prevent the incorporation of contaminant O from the water H₂O and/or dissolved oxygen O₂, which could potentially generate more reliable CAS $\delta^{18}\text{O}_{\text{CAS}}$.
- (3) The final CAS sulfur $\delta^{34}\text{S}_{\text{CAS}}$ using the combined 12% NaOCl + 1% H₂O₂ method were between 0.65‰ and 0.9‰ higher than rival methods.
- (4) Even after restricted time used (<30 min) to extract CAS, non-CAS contaminants, organic sulfur, and especially pyrite sulfur could lower final CAS sulfur isotope compositions $\delta^{34}\text{S}_{\text{CAS}}$.
- (5) My experiment confirms that a single leaching step with oxidizing reagents is not enough to remove all contaminants.
- (6) Based on the data, I successfully oxidized pyrite and OSC. The first leachate likely represents the combination of both AVS and CRS. However, leachates 2 and 3 are more likely to represent the organic sulfur isotope values $\delta^{34}\text{S}_{\text{OSC}}$.
- (7) My study suggests that organic sulfur isotope values $\delta^{34}\text{S}_{\text{OSC}}$ can be significantly different from, and in this case, lower than the coeval pyrite sulfur isotope value $\delta^{34}\text{S}_{\text{PY}}$.
- (8) My data fit well with published data from South China and Namibia but showing higher $\delta^{34}\text{S}_{\text{CAS}}$ values.
- (9) With only ~0.7‰ difference between CAS sulfur and pyrite sulfur isotope values $\Delta\delta^{34}\text{S}_{\text{CAS-PY}}$ from those 'superheavy pyrite' samples, it is worthwhile to revisit such cases with improved CAS extraction methods in future studies.

Chapter 6 Reconstructing the Late Ediacaran Sulfur Cycle

Using New Data from South China

Abstract

The carbon and sulfur cycles play an important role in governing and regulating oxygen, climate and environmental shifts of the Earth's surface system, with implications for the evolution of life. The South China Craton (SCC) has provided a relatively complete and intensely researched rock record of the Ediacaran Period, which makes it an ideal place to understand redox coupling between the C and S cycles during that interval. Previous studies on the SCC revealed multiple Ocean Oxygenation Events (OOE) after the Marinoan glaciation. To study the best known OOE, which is associated with the late Ediacaran DOUNCE/Shuram carbon isotope excursion and radiation of aerobic biota into the deep marine realm, this study looks into carbon and CAS sulfur isotope data from three sections (Lianghong, Sishang, and Qinglinkou). Sulfate sulfur isotope values show a coupled decreasing trend with the carbonate carbon isotope values ($\sim -10\text{‰}$), reaching near modern levels ($\sim +21\text{‰}$) during the DOUNCE/Shuram. Moreover, the $\Delta\delta^{34}\text{S}_{\text{sulfate-sulfide}}$ and the estimated seawater sulfate concentration show similar values to modern levels. However, after the DOUNCE/Shuram, the sulfate reservoir shrank back to pre-excursion levels and influenced the S cycling pathways, which resulted in a decoupled C-S trend and ocean deoxygenation. The rises and falls of the estimated seawater sulfate concentration show a coupled shift with Sr isotope values, suggesting that the DOUNCE/Shuram was likely to be tectonically controlled, possibly via weathering-derived nutrient input. Global correlation indicates that the CAS sulfur isotope profile can be used as a chemostratigraphic correlation tool at times when sulfate concentration was relatively high ($>3\text{ mM}$).

Author Contributions: The CAS sulfur was extracted by the author ZHEYU TIAN at UCL and tested by EA-IRMS in the ISO-Analytical lab. This chapter benefitted from discussions with Graham Shields and Ying Zhou. I thank Dr. Huan Cui, Dr. Weiqi Yao, Dr. Tianchen He, Dr. Wei Shi, and Dr. Fred Bowyer for offering help.

6.1 Introduction

In the marine system, sulfur and carbon cycles are closely linked with each other via their redox-sensitive reservoirs and fluxes (Bottrell and Newton, 2006; Fike et al., 2015; He et al., 2019). Their marine sulfate and inorganic carbon reservoir have the isotope composition controlled by MSR and microbial photosynthesis. The residual is depleted with light isotope with preferential uptake of light sulfur and carbon by the microbe. Moreover, this process can only be settled with the help of pyrite burial and organic carbon burial. The riverine input and MSR reduction are two key fluxes that regulate the seawater sulfate concentrations because the pyrite oxidation and MSR both depend on the oxygen levels, which means the increasing of sulfate concentration is probably linked with an oxygenation event (Fike et al., 2006).

During the late Ediacaran (~580 - 541 Ma), the DOUNCE/Shuram carbonate carbon isotope excursion was the most pronounced negative excursion ($< -5\text{‰}$ and lasted for ~10 Ma) in Earth history. The origin of the DOUNCE/Shuram has been studied by many scientists with two main hypotheses: the altered origin (diagenetic or meteoric water altered) (Derry, 2010; Schrag et al., 2013; Cui et al., 2017); and the oxidation of a huge oceanic dissolved organic matter (DOM) pool (Fike et al., 2006; McFadden et al., 2008; Li et al., 2017; Shields, 2017). However, considering the low paleo oxygen level (0.01-1% PAL) (Lyons et al., 2014), the oxygen could be quickly exhausted by oxidation of the DOM estimated by the numerical model (Bristow and Kennedy, 2008). Shields et al. (2019) pointed out that surplus oxidant (sulfate) is needed to maintain such long-lasting negative excursion. It is reasonable to expect that the dramatic seawater sulfate sulfur isotope composition change will also be recorded during this period.

The CAS sulfur isotope values showing the sulfur isotope composition decrease from 39‰ to as low as 14.2‰ during the DOUNCE/Shuram in South China (Shi et al., 2018) and 29.2‰ to 20.8‰ in Oman (Fike et al., 2006). $\Delta\delta^{34}\text{S}$ increases to 47.9‰ in South China and ~35‰ in Oman, indicating an increase of the seawater sulfate concentration $> 200 \mu\text{M}$ (Gomes and Hurtgen, 2015). Shi et al. (2018) indicated that the

seawater sulfate concentration increased to 8.7mM during the DOUNCE/Shuram. However, no sulfate gradient should exist considering the long residence time of sulfate (~ 20Ma) and high sulfate concentration during the DOUNCE/Shuram. To better investigate this, in this study, I carried out a high-resolution CAS sulfur isotope ($\delta^{34}\text{S}_{\text{CAS}}$) study together with paired carbonate carbon ($\delta^{13}\text{C}$) and oxygen isotope ($\delta^{18}\text{O}$) data of the late Ediacaran sections in the western part of SCC Lianghong section, north-facing northwestern part of SCC Sishang section, and the Qinglinkou sections around the Yangtze Gorges area in South China to understand the C and S cycling during that period.

This chapter provides improved, high-resolution, high-fidelity CAS sulfur isotope records that could be compared with published data from South China and worldwide. Stable isotope and elemental data indicate that these three successions are relatively well preserved and, by correlation, confirm that the Ediacaran Period experienced episodic redox oscillations throughout the Ediacaran-Cambrian transition. Here I present biogeochemical and conceptual models to explain seawater sulfate sulfur isotope compositions and illuminate their connection to regional-to-global ocean redox variability and biological evolutions.

6.2 Methods

As all samples from the three sections are relatively pure carbonate, based on petrographic observation and elemental data shown in former chapters, a more conventional NaCl and DI water CAS extraction method was applied in this study. Another reason is time limitation because of the COVID-19 pandemic. The powder usage for extracting the CAS from carbonate samples is around 7g. Detail methods and analytical methodology can be found in Chapter 5.

6.3 Results

6.3.1 CAS Concentration-[CAS]

Based on carbon isotope chemostratigraphy, the late Ediacaran DOUNCE/Shuram and its aftermath have been divided into five episodes (see Chapter 3: EN4a, EN4b, EN4c, EP4a, EP4b; EN = Ediacaran Negative excursion, EP = Ediacaran Positive excursion).

The CAS concentrations from the limestone sections (e.g., Lianghong and Sishang section) show synchronous variations throughout the late Ediacaran (Fig. 6.1). The [CAS] increases from low values ~22 ppm to ~200 ppm during the onset period of the DOUNCE/Shuram (EN4a). During the DOUNCE/Shuram (EN4b), the CAS concentration shows some fluctuations but remains relatively high at Lianghong (average 111.9 ppm) and Sishang sections (average 102.1 ppm). The [CAS] decreases again to pre-excursion levels during the recovery period of the DOUNCE/Shuram (EN4c) and remains at this low concentration at Lianghong (average 23.8 ppm) and Sishang section (average 49.2 ppm) during the DOUNCE/Shuram aftermath (EP4a and EP4b). The Cambrian strata at the Sishang section show a decreasing trend of the [CAS] value from 202.1 ppm to 31.2 ppm.

Unlike these two sections, it is interesting to note that the Qinglinkou section (mainly dolostone samples) shows an opposite trend to the [CAS] during the DOUNCE/Shuram. However, the limestone samples from the Dengying Formation show a similar decreasing trend as the other two sections from (164 ppm) to relatively low values (average 48.9 ppm) during EP4a and EP4b.

6.3.2 CAS Sulfur Isotope Values ($\delta^{34}\text{S}_{\text{CAS}}$)

The CAS sulfur isotope values from these three sections show a consistent pattern (Fig. 6.1). From lower to top, EP3 represents a relatively steady state for S isotope values

(average 36.3‰ at the Qinglinkou section). Unfortunately, I do not have any data from the onset period of the DOUNCE/Shuram (EN4a) at the Lianghong section due to the samples' low [CAS] concentration. However, the CAS sulfur isotope values $\delta^{34}\text{S}_{\text{CAS}}$ from the other two sections show a decreasing trend from 37.4‰ to 22.8‰ and 40.6‰ to 33.6‰ at the Sishang and Qinglinkou section respectively. During the EN4b interval, $\delta^{34}\text{S}_{\text{CAS}}$ displays a constantly low value with an average of 21.0‰, 20.3‰, and 30.7‰ at the Lianghong, Sishang, and Qinglinkou section respectively. The $\delta^{34}\text{S}_{\text{CAS}}$ values increase again from 16.3‰ to 23.8‰, 20.7‰ to 28.9‰ and 30.7‰ to 49.1‰ during the recovery period of the DOUNCE/Shuram (EN4c) at the Lianghong, Sishang, and Qinglinkou sections, respectively.

During the DOUNCE/Shuram aftermath (EP4a), the $\delta^{34}\text{S}_{\text{CAS}}$ show a first increase trend from 23.8‰ to 32.3‰, 25.0‰ to 33.6‰ and 43.9‰ to 56.2‰ at the Lianghong, Sishang, and Qinglinkou section respectively. Then followed a decreasing trend back to 25.1‰ at the Sishang section and 40.0‰ at the Qinglinkou section. The $\delta^{34}\text{S}_{\text{CAS}}$ value recovers again to 35.3‰ and 49.9‰ during the EP4b at the Sishang and Qinglinkou sections, respectively.

6.3.3 Correlation with Carbon Isotope Data

The CAS sulfur isotope $\delta^{34}\text{S}_{\text{CAS}}$ data shows a coupled change with the carbon isotope shift range from 18.5‰ to 25.0‰, 18.8‰ to 28.9‰, and 30.7‰ to 49.1‰ during the DOUNCE/Shuram at the Lianghong, Sishang, and Qinglinkou section respectively (Fig. 6.1). The average magnitude of the shift $\Delta\delta^{34}\text{S}_{\text{CAS}}$ is 11.7‰. EP4a also shows coupled C-S changes. However, EP4b is characterized by the decoupled trend of the carbon isotope record with the sulfur isotope record. In this period, carbon isotope value is relatively stable (average $1.2\text{‰} \pm 0.3\text{‰}$ at Sishang section and $3.1\text{‰} \pm 0.4\text{‰}$ at Qinglinkou section), but sulfur isotope shifts dramatically.

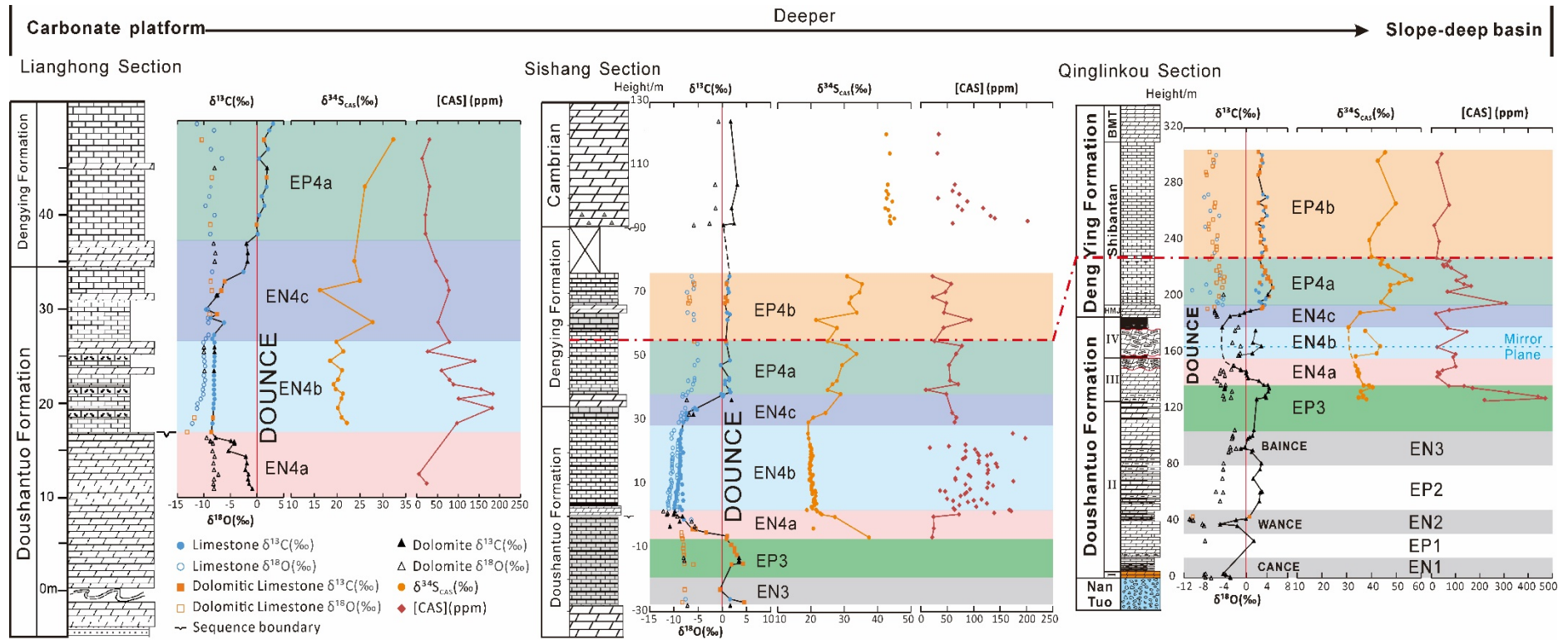


Fig. 6. 1 Late Ediacaran $\delta^{13}C_{carb}$, $\delta^{18}O_{carb}$, and $\delta^{34}S_{CAS}$ profiles of three sections in South China. According to the petrology and elemental test (Chapter 3), I separate the carbonate samples into limestone (blue circle), dolomitic limestone (orange square), and dolomite (black triangle) samples (shown in the $\delta^{13}C_{carb}$ profiles). The entire DOUNCE/Shuram excursion is divided into three stages (EN4a, 4b, 4c). The blue dashed line represents the ‘mirror plane’ at the Qinglinkou sections. HMJ-Hamajing Member; BMT-Baimatuo Member; EN-Ediacaran negative excursion; EP-Ediacaran positive excursion. DOUNCE=Doushantuo negative carbon isotope excursion. BAINCE=Baiguoyuan negative carbon isotope excursion. WANCE=Weng’an negative carbon isotope excursion. CANCE=Cap carbonate negative carbon isotope excursion.

6.3.4 Diagenetic Evaluation

During diagenesis, carbonates are prone to alteration and recrystallization, which might have the potential to alter the CAS concentration-[CAS] (ppm) and $\delta^{34}\text{SCAS}$ (‰) values (Staudt and Schoonen, 1995; Swart, 2015; Fichtner et al., 2017).

It has been reported that dissolution and recrystallization can cause a simultaneously low $\delta^{13}\text{C}_{\text{carb}}$ and $\delta^{18}\text{O}_{\text{carb}}$ (Banner and Hanson, 1990; Lu et al., 2013). Fig. 6.2-a shows that most samples exhibit weak to minor correlations between $\delta^{13}\text{C}_{\text{carb}}$ and $\delta^{18}\text{O}_{\text{carb}}$, which might indicate that most samples have undergone minor diagenetic overprinting. However, samples from Lianghong Doushantuo Formation and Sishang Cambrian exhibit moderate correlations between $\delta^{13}\text{C}_{\text{carb}}$ and $\delta^{18}\text{O}_{\text{carb}}$ ($R^2 = 0.49$ and 0.57 respectively), indicating some degree of diagenesis imprints. However, the cross-plot of $\delta^{34}\text{SCAS}$ (‰) - $\delta^{18}\text{O}_{\text{carb}}$ (‰) of the samples from the Lianghong Doushantuo Formation show low correlation ($R^2 = 0.0028$), which proves the $\delta^{34}\text{SCAS}$ values from those samples might not be influenced by diagenesis. A similar high correlation trend between $\delta^{34}\text{SCAS}$ and $\delta^{18}\text{O}_{\text{carb}}$ can be observed from the Sishang Cambrian samples ($R^2 = 0.83$) (Fig. 6.2-b). Thus, I could say those samples' $\delta^{34}\text{SCAS}$ values might be altered. The relatively high correlation between $\delta^{34}\text{SCAS}$ and $\delta^{18}\text{O}_{\text{carb}}$ ($R^2 = 0.99$), $\delta^{34}\text{SCAS}$ (‰) and Carbonate (%) ($R^2 = 0.41$), $\delta^{34}\text{SCAS}$ (‰)-Mg/Ca (w/w) ($R^2 = 0.47$), $\delta^{34}\text{SCAS}$ (‰)-[CAS] (ppm) ($R^2 = 0.50$) of the Lianghong Dengying samples might be a result of the very small numbers of the samples. As discussed in Chapter 3, these samples from the Lianghong section are well-preserved limestone samples. Moreover, the $\delta^{13}\text{C}_{\text{carb}}$ and $\delta^{34}\text{SCAS}$ records from the Lianghong section, as shown in Fig. 6.1, exhibit a consistent and gradual curve, which is also comparable with the other sections globally (Zhu et al., 2013; Li et al., 2017; Tostevin et al., 2017; Shi et al., 2018). Besides, the systematics of the $\delta^{13}\text{C}_{\text{carb}}$ and $\delta^{18}\text{O}_{\text{carb}}$ can result from non-diagenetic covariations (Shields et al., 2003). Therefore, the Lianghong section is not likely to be the result of diagenesis imprint.

Elemental concentrations (Ca, Mg, Fe, Mn, Sr) have been widely used to approximate the post-depositional alteration (Brand and Veizer, 1980; Veizer, 1983; Tostevin et al., 2017). Mn and Fe are tended to be enriched in diagenetic carbonates, while Sr is depleted (Brand and Veizer, 1980). Even though it has been reported that CAS concentration has a negative linear correlation with progressing burial diagenesis, $\delta^{34}\text{SCAS}$ tends to be more robust to the changes (Fichtner et al., 2017).

This study still uses Mn/Sr or Fe/Sr ratio and [CAS] (ppm) to test the diagenetic grade of these samples. Except for those samples mentioned above (e.g., Lianghong Dengying samples and Sishang Cambrian samples), all the other samples almost show no correlation between $\delta^{34}\text{S}_{\text{CAS}}$ (‰)-Carbonate (%) (Fig. 6.2-c) ($R^2 < 0.097$), $\delta^{34}\text{S}_{\text{CAS}}$ (‰)-Mg/Ca (w/w) (Fig. 6.2-d) ($R^2 < 0.18$), $\delta^{34}\text{S}_{\text{CAS}}$ (‰)-[CAS] (ppm) (Fig. 6.2-e) ($R^2 < 0.16$), $\delta^{34}\text{S}_{\text{CAS}}$ (‰)-Mn/Sr (w/w) (Fig. 6.2-f) ($R^2 < 0.20$), which indicates that those samples might recorded the original $\delta^{34}\text{S}_{\text{CAS}}$ values.

The samples from the Qinglinkou Doushantuo Formation are mostly dolomite and/or dolomitic limestone (see Chapter 3, Fig. 3.7, 3.10, 3.12). The correlation between [CAS] (ppm) and Mg/Ca (w/w) of the Qinglinkou Doushantuo samples is strongly negative ($R^2 = 0.78$) (Fig. 6.2-g), weak between [CAS] (ppm) and Mn/Sr (w/w) ($R^2 = 0.21$) (Fig. 6.2-h). This might mean that dolomitization could influence the CAS sulfur concentration. Therefore, the measured [CAS] (ppm) from the Qinglinkou Doushantuo samples are likely to have been lowered during dolomitization.

In summary, most of the $\delta^{34}\text{S}_{\text{CAS}}$ values of the three sections are likely to represent primary signatures of the late Ediacaran seawater sulfate. However, Cambrian-aged samples from the Sishang section might be influenced by diagenesis. The [CAS] (ppm) values of the Lianghong and Sishang sections are likely to be original signals. However, the Qinglinkou section samples, especially the Doushantuo Formation samples, are likely to have been lowered due to dolomitization.

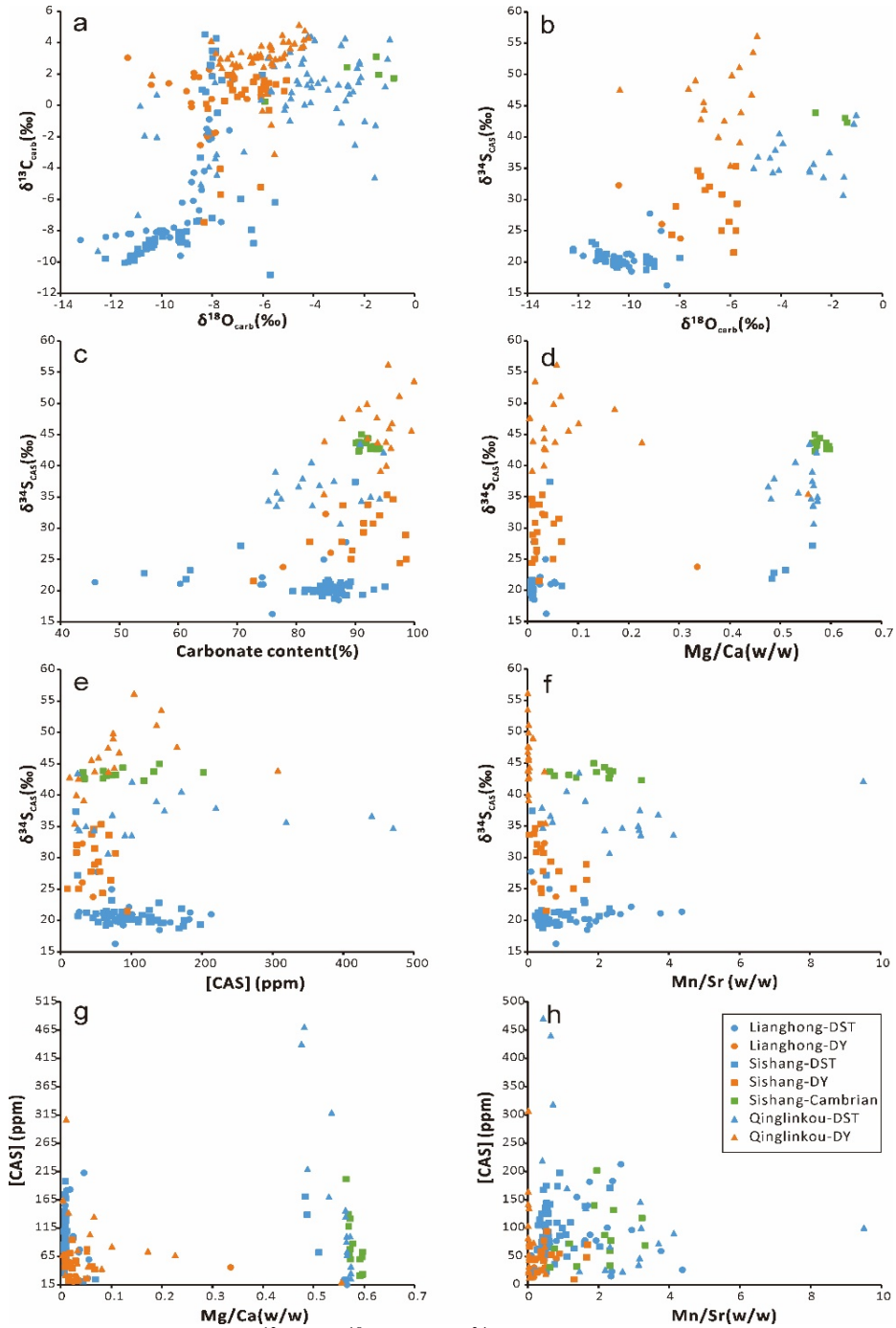


Fig. 6. 2 Cross-plots of the $\delta^{13}\text{C}_{\text{carb}}$, $\delta^{18}\text{O}_{\text{carb}}$ and $\delta^{34}\text{S}_{\text{CAS}}$ and elemental ratios of the Lianghong, Sishang and Qinglinkou sections. a. $\delta^{13}\text{C}_{\text{carb}}$ (‰)- $\delta^{18}\text{O}_{\text{carb}}$ (‰) (Lianghong-DST, DY R² = 0.49, 0.19; Sishang-DST, DY, Cambrian R² = 0.34, 0.2, 0.57; Qinglinkou-DST, DY R² = 0.33, 0.059). b. $\delta^{34}\text{S}_{\text{CAS}}$ (‰)- $\delta^{18}\text{O}_{\text{carb}}$ (‰) (Lianghong-DST, DY R² = 0.0028, 0.99; Sishang-DST, DY, Cambrian R² = 0.20, 0.013, 0.83; Qinglinkou-DST, DY R² = 0.014, 0.013). c. $\delta^{34}\text{S}_{\text{CAS}}$ (‰)-carbonate content (%) (Lianghong-DST, DY R² = 0.0025, 0.41; Sishang-DST, DY, Cambrian R² = 0.028, 0.171, 0.14; Qinglinkou-DST, DY R² = 0.046, 0.097). d. $\delta^{34}\text{S}_{\text{CAS}}$ (‰)-Mg/Ca (w/w) (Lianghong-DST, DY R² = 0.0019, 0.47; Sishang-DST, DY, Cambrian R² = 0.13, <0.0001, 0.23; Qinglinkou-DST, DY R² = 0.0074, 0.18). e. $\delta^{34}\text{S}_{\text{CAS}}$ (‰)-[CAS] (ppm) (Lianghong-DST, DY R² = 0.064, 0.50; Sishang-DST, DY, Cambrian R² = 0.15, 0.016, 0.15; Qinglinkou-DST, DY R² = <0.0001, 0.16). f. $\delta^{34}\text{S}_{\text{CAS}}$ (‰)-Mn/Sr (w/w) (Lianghong-DST, DY R² = 0.035, 0.082; Sishang-DST, DY, Cambrian R² = <0.0001, 0.20, 0.018; Qinglinkou-DST, DY R² = 0.030, 0.19). g. [CAS] (ppm)-Mg/Ca (w/w) (Lianghong-DST, DY R² = 0.26, 0.67; Sishang-DST, DY, Cambrian R² = 0.0003, 0.0031, 0.5654; Qinglinkou-DST, DY R² = 0.78, 0.074). h. [CAS] (ppm)-Mn/Sr (w/w) (Lianghong-DST, DY R² = 0.0093, 0.76; Sishang-DST, DY, Cambrian R² = 0.029, 0.0003, 0.073; Qinglinkou-DST, DY R² = 0.21, 0.057). Carbonate content (%): weight percentages of HCl-leachable CaCO_3 and $\text{CaMg}(\text{CO}_3)_2$.

6.4 Discussion

6.4.1 Estimation of Seawater Sulfate Concentration-‘Rate method’ Model

Seawater sulfate concentration is an important proxy for understanding the Earth’s surface oxidation state (Algeo et al., 2015). Attempts have been made to estimate the paleo-seawater sulfate concentrations. This includes the sulfur isotope fractionation $\Delta^{34}\text{S}_{\text{CAS-PY}}$ method (using logarithmic equation Fig. 6.3, $\delta^{34}\text{S} = 7.03\ln([\text{SO}_4^{2-}]) + 21.22$) (Gomes and Hurtgen, 2015) and ‘The rate method’ (Algeo et al., 2015). The ‘rate method’ could provide us with an upper estimation of the marine sulfate reservoir size (Algeo et al., 2015). This study uses ‘the rate method’ to estimate the seawater sulfate concentration and the fractionation method as an evaluation tool.

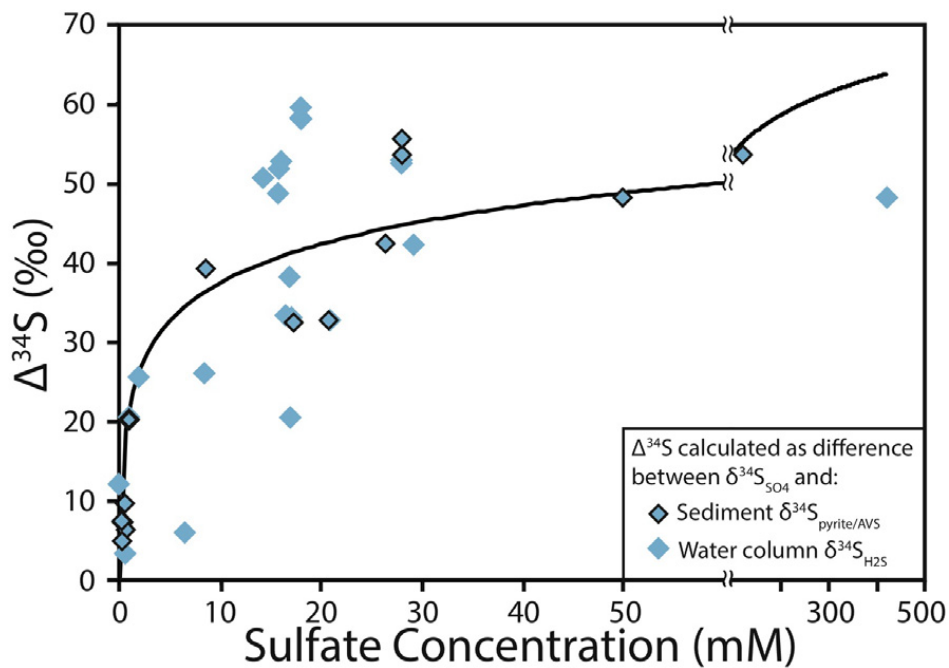


Fig. 6. 3 The compilation of $\Delta^{34}\text{S}$ values versus sulfate concentration in the euxinic system. From (Gomes and Hurtgen, 2015)

In the ‘rate method’, the estimated seawater sulfate concentration $[\text{SO}_4^{2-}]_{\text{sw}}$ is based on two parameters: the sulfur isotope difference between the sulfate and sulfide ($\Delta^{34}\text{S}_{\text{CAS-PY}}$); and the observed rate of change of seawater sulfate sulfur isotopes. In the simplified sulfur cycle (Fig. 6.4), the oceanic sulfate concentration and the sulfur isotope composition are controlled by the weathering and burial flux.

The seawater sulfate sulfur isotope value is mainly influenced by the burial of pyrite ($\sim -20\text{‰}$) and input flux ($\sim 3\text{‰}$), which means the rates of change of the seawater sulfate sulfur isotope values ($\partial^{34}\text{S}_{\text{CAS}}/\partial t$) can be deduced by Equation 6.1 and the seawater sulfate concentration by Equation 6.2.

$$\partial^{34}\text{S}_{\text{CAS}}/\partial t = [(F_{\text{in}} \times \Delta^{34}\text{S}_{\text{in-CAS}}) + (F_{\text{PY}} \times \Delta^{34}\text{S}_{\text{CAS-PY}})] / M_{\text{sw}} \quad \text{Equation 6.1}$$

$$[\text{SO}_4^{2-}]_{\text{sw}} = k_1 \times k_2 \times M_{\text{sw}} \quad \text{Equation 6.2}$$

In Equation 6.1, F_{in} is the input flux, $\Delta^{34}\text{S}_{\text{in-CAS}}$ is the difference in the isotopic compositions of the input source and seawater, F_{PY} is the pyrite burial flux, $\Delta^{34}\text{S}_{\text{CAS-PY}}$ is the sulfur isotopic difference between sulfate and pyrite. In the Equation 6.2, M_{sw} is the mass of seawater sulfate, conversion constants $k_1 = 10^6$, $k_2 = 2.22 \times 10^{-20}$ mM/g. We can calculate the seawater sulfate concentration with Equation 6.3. When the source flux goes to zero ($F_{\text{in}} \times \Delta^{34}\text{S}_{\text{in-CAS}} = 0$), the estimated seawater sulfate concentration is the maximum (Equation 6.4).

$$[\text{SO}_4^{2-}]_{\text{sw}} = k_1 \times k_2 \times [(F_{\text{in}} \times \Delta^{34}\text{S}_{\text{in-CAS}}) + (F_{\text{PY}} \times \Delta^{34}\text{S}_{\text{CAS-PY}})] / \partial^{34}\text{S}_{\text{CAS}}/\partial t \quad \text{Equation 6.3}$$

$$[\text{SO}_4^{2-}]_{\text{sw}}(\text{max}) = k_1 \times k_2 \times F_{\text{PY}} \times \Delta^{34}\text{S}_{\text{CAS-PY}} / \partial^{34}\text{S}_{\text{CAS}}/\partial t \quad \text{Equation 6.4}$$

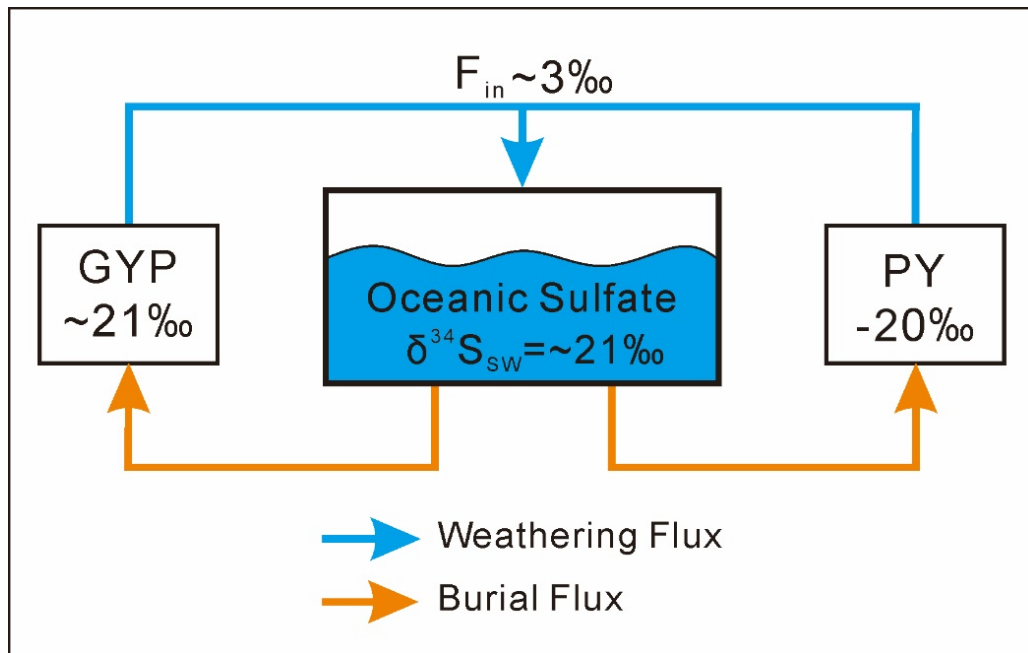


Fig. 6. 4 The simplified box model of the sulfur cycle. GYP = gypsum and PY = pyrite. The sulfur isotope composition for each parameter is from (Fike et al., 2015).

6.4.2 Underestimated Seawater Sulfate Concentration in the Late Ediacaran

The ‘rate method’ model uses CAS and pyrite S isotope value to constrain the ancient paleo-seawater sulfate concentration $[\text{SO}_4^{2-}]$ (mM). Previous studies reported bulk rock $\delta^{34}\text{S}_{\text{Py}}$ values of Doushantuo Member III with a large range from -16.2‰ to 30.2‰ and an average $\sim 5.9\text{‰}$ (Wang et al., 2017a; Shi et al., 2018). However, the bulk pyrite is a mixture of euhedral to subhedral pyrite and framboidal pyrite. Framboidal pyrite is commonly formed in the water column or within marine sediments, which mirrors the isotopic composition of seawater H_2S and is the most reliable record of reduced sulfur isotope value through microbial sulfate reduction (MSR) (Wang et al., 2012a; Cui et al., 2018; Lang et al., 2018; Wang et al., 2021). However, the euhedral to subhedral pyrite with the size $> 50\mu\text{m}$ might form from pore waters, and the late-stage diagenesis or flux alteration, which could easily influence its sulfur isotope value (Berner, 1984). Some of the late Ediacaran samples clearly show recrystallization (Chapter 3, Fig. 3.7, 3.12) and/or have larger pyrite crystals (Chapter 3, Fig. 3.6). The bulk pyrite sulfur isotope value might reflect the pore water value rather than the water column. This is also evidenced by other late Ediacaran sections in South China (Wang et al., 2012a). A recent study that used *in situ* nanoSIMS by Wang et al. (2021) shows that the framboidal pyrite average value of the upper Doushantuo Formation samples ($-11.5 \pm 5.2\text{‰}$) is much lower than the bulk rock $\delta^{34}\text{S}_{\text{Py}}$ value ($4.5 \pm 20.5\text{‰}$) (Fig. 6.5), which means that the average $\Delta^{34}\text{S}_{\text{CAS-Py}}$ value ($\sim 23.2\text{‰}$) and the estimation of the maximum seawater sulfate concentration using the ‘rate method’ of late Ediacaran is likely underestimated (Equation 6.4).

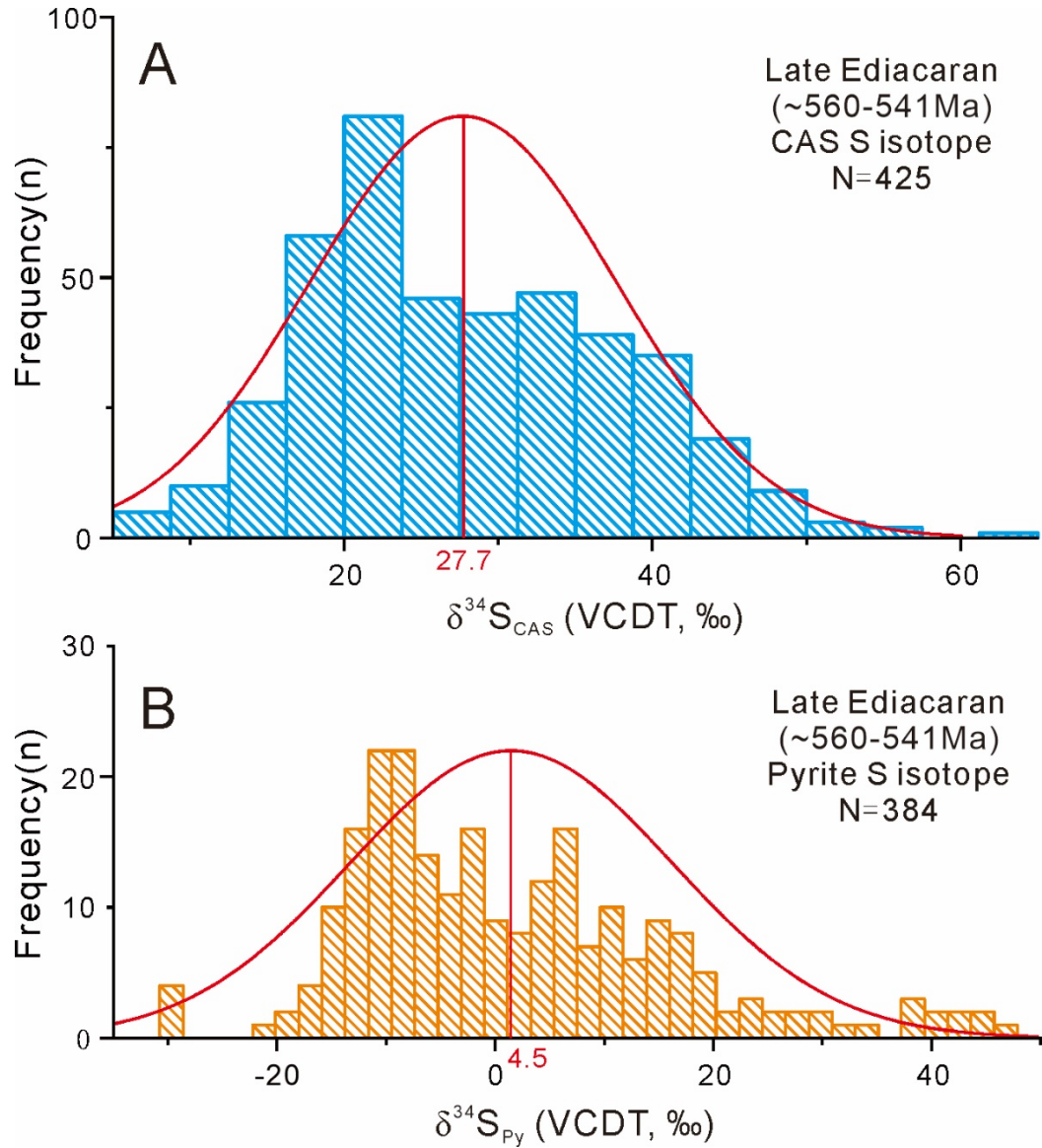


Fig. 6. 5 Comparisons of bulk rock CAS and pyrite S isotope value of the late Ediacaran (~560-541Ma) samples from different sections around the world. A: The histogram shows $\delta^{34}\text{S}_{\text{CAS}}$ during late Ediacaran has an average value of $27.7 \pm 10.0\%$; B: The histogram shows $\delta^{34}\text{S}_{\text{Py}}$ during late Ediacaran has an average value of $4.5 \pm 20.5\%$. The CAS and pyrite data compiled here including this study and data from (Hurtgen et al., 2005; Fike et al., 2006; Fike and Grotzinger, 2008; McFadden et al., 2008; Ries et al., 2009b; Wu et al., 2015; Cui et al., 2016a; Wang et al., 2017a; Shi et al., 2018; Wang et al., 2020).

The models of the seawater sulfate concentrations are based on the point-to-point $\delta^{34}\text{S}_{\text{CAS}}$ changing rate between samples. However, an unavoidable bias is that estimations of the maximum seawater sulfate concentration between two points could be under- or overestimated. However, the lowest estimated seawater sulfate concentration value was generated with the maximum $\delta^{34}\text{S}_{\text{CAS}}$ changing rate (Equation 6.3) and could provide a more reasonable estimation (shaded area in Fig. 6.6). The data presented here were smoothed, and Akima spline interpolated with the time grid of 0.2Ma and 0.4Ma. Although the age difference between each sample

is below 0.1 Ma, the 0.2Ma and 0.4Ma time grids were used to avoid the uncertainty $\delta^{34}\text{S}_{\text{CAS}}$ data due to sample quality.

Another bias is that no faithful constraints on the pyrite S isotope values from the Dengying Formation. The existence of ‘heavy’ and/or ‘superheavy’ pyrite during the DOUNCE/Shuram aftermath has been reported by many scientists (Table 6.1). For example, in South China, bulk rock pyrite sulfur isotope values can be as high as 37.2‰, 17.7‰, and 24.7‰ from the Qinglinkou section, Gaojiashan section, and Meishuxia section, respectively. Moreover, reported ‘superheavy’ pyrite S isotope values from the Nama Group in Namibia can be as high as 80.2‰ (Ries et al., 2009b). Although the work by Tostevin et al. (2017) using an improved method pointed out that ‘superheavy’ pyrite may not be widespread in the Nama group, their pyrite S isotope values are still relatively high (max = 41.8‰). Meanwhile, the $\Delta\delta^{34}\text{S}_{\text{CAS-Py}}$ values seem to have a wide range from $-0.72 \pm 5.7\text{‰}$ to $44.2 \pm 6.5\text{‰}$ between sections, which proves spatial heterogeneity in pyrite sulfur isotope composition between sections. This is also why I use three different sections to reconstruct the paleo seawater sulfate concentration during that time interval.

Except for those explanations mentioned in Chapter 5, another possible explanation is that the bulk rock pyrite sulfur isotope values have been contaminated by late-stage subhedral to euhedral pyrites. More work is needed by using *in situ* nanoSIMS to constrain pyrite S isotope values during the DOUNCE/Shuram aftermath. In this study, although the pyrite sulfur isotope values seem increased and $\Delta\delta^{34}\text{S}_{\text{CAS-Py}}$ values lowered during that period, I still use the average framboidal pyrite S isotope values of the upper Doushantuo Formation samples as constraints for building the ‘rate method’ model during the DOUNCE/Shuram aftermath. Moreover, the $\Delta\delta^{34}\text{S}_{\text{CAS-Py}}$ value from the Gaojiashan Member is relatively high (Table 6.1). A possible consequence is that the estimated sulfate concentration during the DOUNCE/Shuram aftermath might be exaggerated by 2-3 times higher than the actual values. This means that the result is a maximum constraint on seawater sulfate concentration during the late Ediacaran. However, if the estimated maximum sulfate concentration is still quite low during this period, the real sulfate concentration could only be much lower than my estimation.

Table 6. 1 Comparison between pyrite sulfur isotope values $\delta^{34}\text{S}_{\text{Py}}$ and $\Delta\delta^{34}\text{S}_{\text{CAS-PY}}$ from this study and published data during the DOUNCE/Shuram aftermath. Errors are one standard deviation.

Location	Samples	$\delta^{34}\text{S}_{\text{Py}}$ highest	$\delta^{34}\text{S}_{\text{Py}}$ lowest	$\delta^{34}\text{S}_{\text{Py}}$ mean	$\Delta\delta^{34}\text{S}_{\text{CAS-PY}}$
South China	This study Shibantan Member Qinglinkou section	37.2‰	22.2‰	$29.9 \pm 7.5\text{‰}$ (n=3)	$10.1 \pm 5.0\text{‰}$ (n=3)
	Cui et al. (2016a) Gaojiashan Member Gaojiashan section	17.7‰	-30‰	$-1.4 \pm 15.3\text{‰}$ (n=30)	$34.7 \pm 9.6\text{‰}$ (n=26)
	Wang et al. (2020) Doushantuo Formation Meishuxia section	24.7‰	-7.3‰	$11.2 \pm 9.8\text{‰}$ (n=15)	$13.8 \pm 6.8\text{‰}$ (n=12)
Global	Tostevin et al. (2017) Nama Group Namibia	41.8‰	26.7‰	$36.2 \pm 4.5\text{‰}$ (n=12)	$-0.72 \pm 5.7\text{‰}$ (n=11)
	Ries et al. (2009b) Nama Group Namibia	80.2‰	22.7‰	$37.3 \pm 12.0\text{‰}$ (n=54)	$-4.5 \pm 11.1\text{‰}$ (n=44)
	Fike et al. (2006) Upper Buah Formation Oman	-6.7‰	-25.9‰	$-19.1 \pm 6.3\text{‰}$ (n=19)	$44.2 \pm 6.5\text{‰}$ (n=19)

The estimation of the maximum seawater sulfate concentration $[\text{SO}_4^{2-}]_{\text{max}}$ shows an apparent coincidence with the DOUNCE/Shuram from all three sections in South China. The trends of the three sections are quite similar. Unfortunately, I do not have the data from the EN4a at the Lianghong section. However, the [CAS] value gives us a possible trend, representing an increase in the seawater sulfate concentration. Before the DOUNCE/Shuram (EP3), the $[\text{SO}_4^{2-}]_{\text{max}}$ value in South China was as low as ~2.5 - 4.5 mM (Fig. 6.6-c) but increased dramatically to ~4.1 - 6.7 mM during the onset of the DOUNCE/Shuram (EN4a) (Fig. 6.6-b). The seawater sulfate concentration continued increasing to the highest plateau by the early stage of EN4b with the highest value of ~10 mM at the Lianghong section and a higher than modern value (29 mM) at the Sishang and Qinglinkou sections. Limited data points might cause the lowered estimation of the seawater reservoir during this time interval at the Lianghong section (Fig. 6.6-a). This high sulfate ocean lasted for at least 4Myr, followed by a sharp decline during the late EN4b and EN4c to ~0.6-3.0 mM. The DOUNCE/Shuram aftermath, especially EP4a, is a gradual recovery of the seawater sulfate level, which increased to the highest value (~8-10 mM) at the Ediacaran-Cambrian boundary.

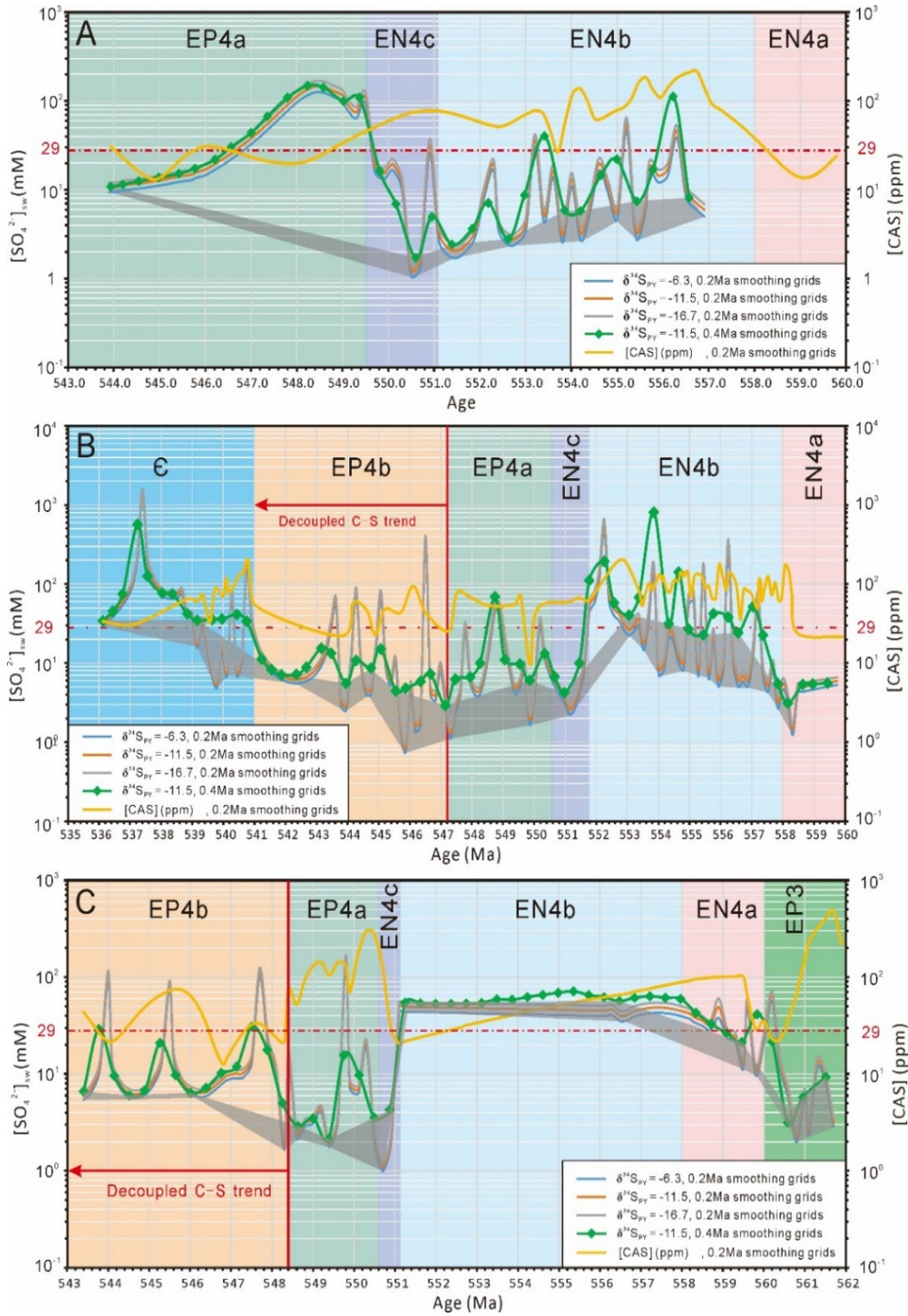


Fig. 6 'Rate method' model of maximum seawater sulfate concentration in late Ediacaran (~560-541 Ma). A: Lianghong section B: Sishang section. C: Qinglinkou section. The blue, orange and grey curves represent the estimated seawater sulfate concentration with 0.2Ma smoothing grids when $\delta^{34}S_{PY} = -6.3$ ‰, -11.5 ‰, and -16.7 ‰, respectively. The green pointed curve represents the estimated sulfate concentration with 0.4Ma smoothing grids and $\delta^{34}S_{PY} = -11.5$ ‰. The yellow curve represents the CAS concentration curve of the samples. The grey shaded area connects the baseline of the model lines and represents the best estimation of the seawater sulfate concentration.

6.4.3 Tectonic Controls on the DOUNCE/Shuram

To further constrain the causes of increased seawater sulfate concentration during the DOUNCE/Shuram, I compiled the carbonate carbon isotope $\delta^{13}\text{C}_{\text{carb}}$, CAS sulfur isotope $\delta^{34}\text{S}_{\text{CAS}}$ from this study together with the global seawater $^{87}\text{Sr}/^{86}\text{Sr}$ trend (Fig. 6.7).

The carbon and sulfur cycle are closely linked and quite similar. They both have a large oceanic reservoir and input flux. The burial of oxidized flux mirrors the seawater values, and reduced flux (organic carbon and pyrite) is microbially fractionated. When the oceanic reservoirs of oxidized carbon and sulfate are large, a coupled trend of the carbonate carbon and sulfate sulfur isotope could result.

The coupled C-S isotope data from this study show a strong correlation with the published Sr-isotope data with the highest $^{87}\text{Sr}/^{86}\text{Sr}$ ratios up to 0.7090 (Fig. 6.7), which possibly indicates an increasing weathering rate during the DOUNCE/Shuram interval (Cui et al., 2015; Li et al., 2017). This increased weathering flux might have been caused by the collisional formation of Gondwanaland (completed by 530 Ma) (Brasier and Lindsay, 2000; Bradley, 2011; Shields, 2017), which provided additional sulfate into the seawater and possibly caused the increase of the seawater sulfate reservoir during the DOUNCE/Shuram. The decrease of the $^{87}\text{Sr}/^{86}\text{Sr}$ ratios from 0.7090 to 0.7084 during EN4c is also coincident with the dramatic drop of the seawater sulfate concentration during that period (Fig. 6.6). Thus, it is possible that the increased oxygen level (Wei et al., 2019; Zhang et al., 2019) together with the increased riverine sulfate flux provided the oxidants to oxidize the large DOM pool stored in the pre-Cambrian ocean that led to the coupled negative $\delta^{13}\text{C}_{\text{carb}}$ and $\delta^{34}\text{S}_{\text{CAS}}$ excursions during the DOUNCE/Shuram.

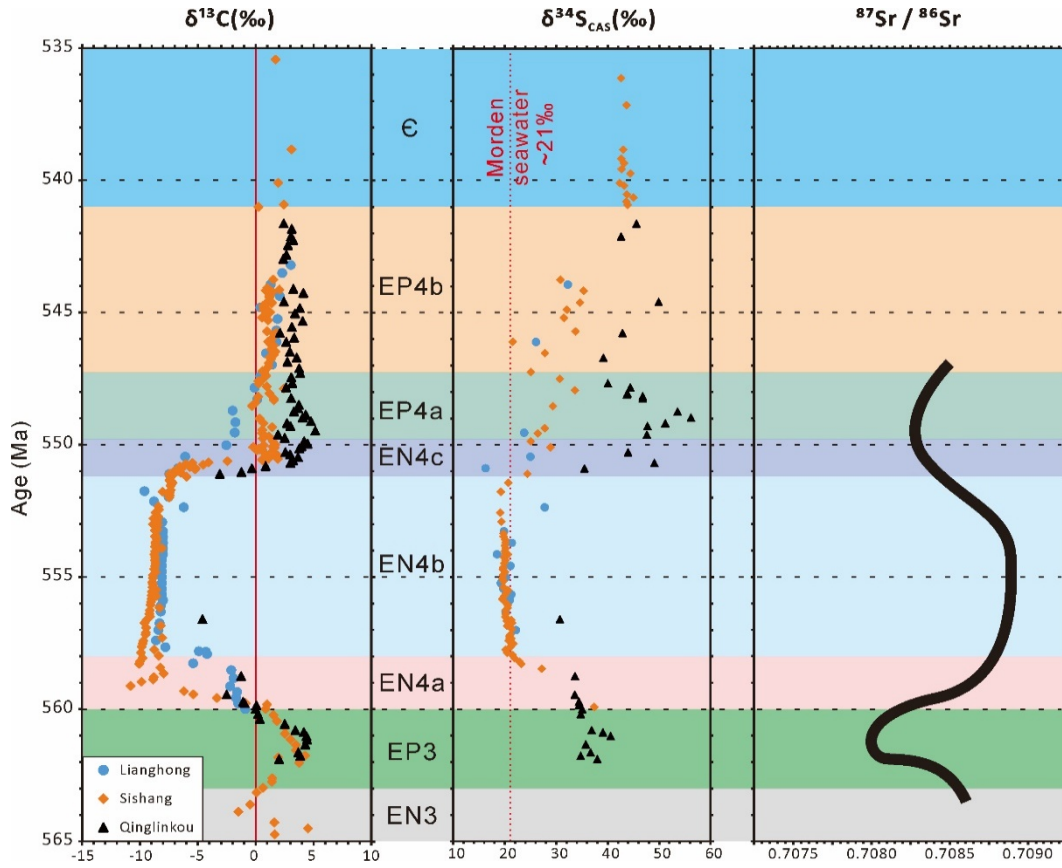


Fig. 6.7 Summary of carbonate carbon isotope $\delta^{13}\text{C}_{\text{carb}}$, CAS sulfur isotope $\delta^{34}\text{S}_{\text{CAS}}$ from the Lianghong, Sishang, Qinglinkou section and compiled $^{87}\text{Sr}/^{86}\text{Sr}$ ratios profile (Li et al., 2017) during the late Ediacaran (~565- 541 Ma).

6.4.4 Carbon and Sulfur Cycling before and during the DOUNCE/Shuram

As mentioned previously, in general, the negative DOUNCE/Shuram $\delta^{13}\text{C}_{\text{carb}}$ excursion can be attributed to the dominance of organic carbon oxidation over burial, which represents a global oxygenation event (Hoefs, 2015; Tostevin, 2015; Shields, 2017). The hydrothermal origin and diagenesis origin have been abandoned because no obvious evidence indicates that the samples in this study have been influenced by hydrothermal fluids or undergone heavy diagenetic overprint.

Before the DOUNCE/Shuram, Fig. 6.8 shows the $\Delta\delta^{34}\text{S}_{\text{CAS-PY}}$ lower than the values during the DOUNCE/Shuram, which proves the low sulfate concentration during that period (around 0.98mM based on logarithmic equation in Fig. 6.3). This is similar to my 'rate method' estimated maximum seawater concentration 2mM before the DOUNC/Shuram.

Fig. 6.8 shows that the CAS sulfur isotope values from the shallow area Lianghong section and the deeper Sishang sections fit well with the global values.

However, significantly higher CAS sulfur isotope values (constantly $\sim 10\text{‰}$ higher than the global value) from the slope-deep basin Qinglinkou section seem to show a marine sulfur isotope gradient during and after the DOUNCE/Shuram excursion.

Four explanations may be able to account for this result. First, the existence of a marine sulfate gradient during the DOUNCE/Shuram (Li et al., 2010; Shi et al., 2018), which means the seawater sulfate availability declined from shallow to the deep area during that period. Shi et al. (2018) hypothesis a seawater sulfate concentration gradient between the shallow and deep sections. However, in all three sections, my model (Fig. 6.6) indicates that the seawater sulfate concentration was quite high, even higher or similar to modern levels ($\sim 29 \text{ mM}$). No obvious gradient was noted between sections. Shi et al. (2018) also propose that low concentration of sulfate and increased riverine sulfate fluxes could have decreased the residence time of seawater sulfate during that period, causing the sulfate gradient. However, the high estimated seawater sulfate concentration during the DOUNCE/Shuram does not support their hypothesis. Moreover, the higher weathering rate (Fig. 6.7) (Li et al., 2017; Zhou et al., 2020) and tectonic movements (Gondwanaland assembly) (Li and Powell, 2001; Shields, 2017) would possibly have increased the circulation rate of seawater and shorten the oceanic mixing time. In summary, a possible longer residence time for seawater sulfate and shorter oceanic mixing time during the DOUNCE/Shuram do not support this hypothesis.

Another possibility is that the Qinglinkou section has been influenced by diagenesis, which means that the CAS trapped in the carbonate lattice was forming from the pore water through MSR rather than from the water column. The Rayleigh distillation in a closed system could result in elevated CAS sulfur isotope values (Cui et al., 2018) at the Qinglinkou section. However, the pyrite sulfur isotope values from the upper Doushantuo Formation do not support the coincidence of high pyrite sulfur isotope values and lower $\Delta\delta^{34}\text{S}$. Second, suppose the diagenesis plays an essential role in controlling the CAS sulfur isotope values from the Qinglinkou section. In that case, the lithology shift between the Doushantuo Formation (mainly dolostone) and Dengying Formation (mainly limestone) could result in a dramatic difference between the CAS sulfur isotope values. However, Fig. 6.8 shows that the Dengying Formation limestone samples still have higher CAS sulfur isotope values than the global ones.

The third possibility is that the base of the Hamajing Member at the Qinglinkou

section is not the same age as the base of the Dengying Formation at the Sishang and Lianghong sections. This hypothesis is based on the sequential slumping evolution hypothesis mentioned in Chapter 4. However, if this hypothesis is true, which means the lower Dengying Formation is missing at the Qinglinkou section and most sections at the western region of the Huangling Anticline area. According to the newest time constraints on the DOUNCE/Shuram, which ends at ~565 Ma (Yang et al., 2021), there will have to have been a >10 Ma gap between the base of the Hamajing Member at the Qinglinkou section and the base of the Dengying Formation at the other two sections. However, my data seems not to support this hypothesis as the CAS sulfur profile fits well both in the trend (first increase then decrease and finally increase again in the Dengying Formation) and the magnitude (changing around 10 ‰) of the variations between these three sections. This problem could be solved only when more reliable dating results come out.

The fourth possibility is that the Qinglinkou section forms in a semi-restricted basin with access to the open ocean (Jiang et al., 2011; Xiao et al., 2012). The high CAS sulfur isotope values can be met with limited accessibility of the sulfate in the Yangtze Gorges area and persistent high activity of MSR due to increased nutrient input and deep water euxinic conditions (Wang et al., 2012a; Cui et al., 2015) during the DOUNCE/Shuram. This hypothesis is also supported by a positive shift of the cerium anomaly (0.67 to 0.89) (Wei et al., 2018b) and $Fe_{HR}/Fe_T > 0.46$, $Fe_{py}/Fe_{HR} > 0.7$ in the Doushantuo III and IV shale layers (Li et al., 2015; Ostrander et al., 2019; Bridger et al., 2021).

6.4.5 Carbon and Sulfur Cycling after the DOUNCE/Shuram

A notable biogeochemical shift during the DOUNCE/Shuram aftermath (EP4) is the lower $\Delta\delta^{34}S$, with some samples even below zero ('Superheavy' pyrite) (Fig. 6.8). According to the 'rate method' model, the estimated seawater sulfate concentration after the DOUNCE/Shuram dropped dramatically from ~29mM to < 1mM. Although the sulfate concentration gradually increases during this period, the reservoir is still quite small (<10 mM). As the sulfate concentration decreases globally, the special heterogeneity of the CAS sulfur and pyrite sulfur could be met because the low sulfate ocean is more sensitive to the geochemical oscillations on a global scale and/or local shifts and sulfate have a shorter residence time. Moreover,

the low sulfate ocean during the DOUNCE/Shuram aftermath could result in a lower $\Delta\delta^{34}\text{S}$ but higher $\delta^{34}\text{S}_{\text{sulfate}}$ and $\delta^{34}\text{S}_{\text{sulfide}}$ (Canfield, 2001a; Fike et al., 2015; Cui et al., 2018). However, whether the ‘superheavy’ pyrite does exist is still questionable, as mentioned in Chapter 5.

The shrinking of the sulfate reservoir during the DOUNCE/Shuram aftermath coincides with the drop of the weathering rate (Sr-isotope values). The cut-off of the high riverine flux might be the terminator of the DOUNCE/Shuram. Moreover, this surprisingly low sulfate concentration during EP4 means the microbial sulfate reduction (MSR) has been suppressed (Equation 6.5), and methanogenesis (Equation 6.6, 6.7) dominated the organic carbon remineralization and controlling the atmospheric greenhouse gases (Newton et al., 2011; Gomes and Hurtgen, 2015; He et al., 2020). This will result in a greater flux of methane release and a decrease in bottom-water oxygen levels (Equation 6.8), which is proved from extremely low U isotope values ($\sim -0.8\text{‰}$) (Wei et al., 2018a; Zhang et al., 2018; Tostevin et al., 2019). Elevated methane production may promote methane escape to the atmosphere and cause global warming during that time interval, as evidenced by the wide occurrence of gypsum deposits (Cui et al., 2016a; Shields et al., 2019). The S cycling pathways change due to low sulfate concentration might be the fundamental reason for the decoupled C-S trend during EP4b and control the ocean redox state and climate changes.



While some others proposed that the occurrence of the bioturbation, as evidenced by trace fossils in the Dengying Formation (Wood et al., 2019), ended the DOUNCE/Shuram excursion (Canfield and Farquhar, 2009). However, the influence of bioturbation on sulfur cycling might still have been very limited until the Cambrian (Meysman et al., 2006). Moreover, the earliest widespread occurrence of trace fossils (Wood et al., 2019) is at least around 4 million years later than the end of the DOUNCE/Shuram anomaly. So, this hypothesis might not be true.

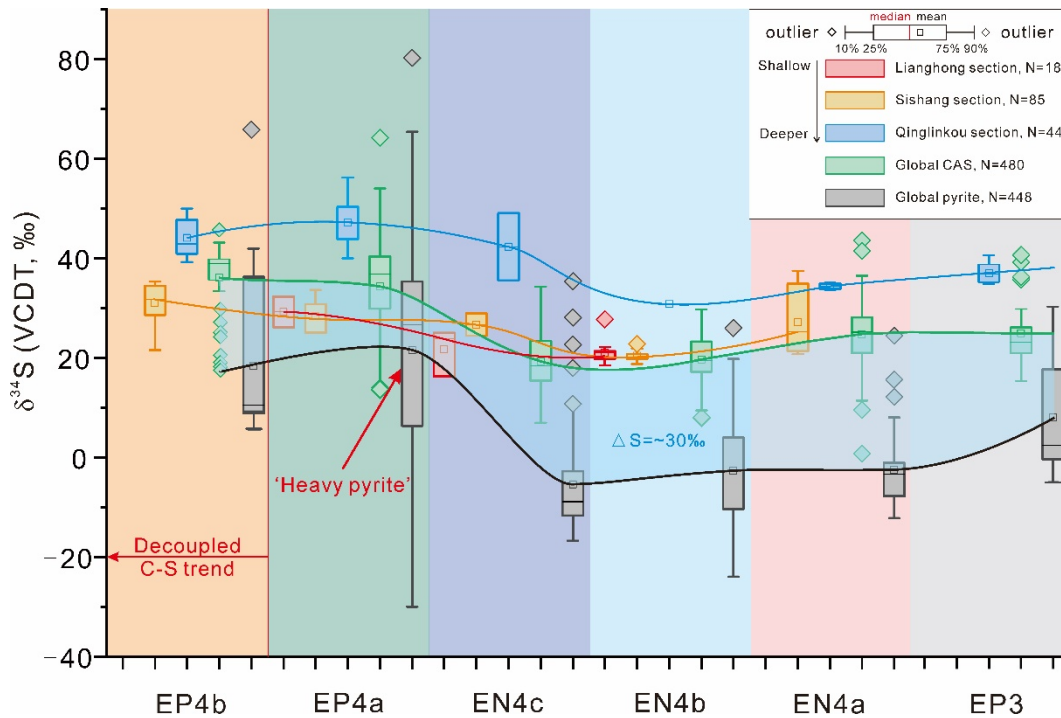


Fig. 6.8 Box plots of bulk rock CAS $\delta^{34}\text{S}_{\text{CAS}}$ and pyrite S isotope $\delta^{34}\text{S}_{\text{PY}}$ values of the late Ediacaran (~570-541 Ma) samples from this study and around the world. The red, orange, and blue lines represent the CAS sulfur isotope curves (mean values) of the Lianghong, Sishang, and Qinglinkou section samples, respectively. The green and black lines represent the global CAS sulfur and pyrite sulfur isotope profiles, respectively. The blue and red shaded areas represent the difference between the CAS sulfur and pyrite sulfur isotope values $\Delta\delta^{34}\text{S}_{\text{CAS-PY}}$. The data compiled here include the data from this study and data from (Hurtgen et al., 2005; Fike et al., 2006; Fike and Grotzinger, 2008; McFadden et al., 2008; Ries et al., 2009b; Wu et al., 2015; Cui et al., 2016a; Wang et al., 2017a; Shi et al., 2018; Wang et al., 2020).

6.4.6 Global Correlation and S Isotope Chemostratigraphy

The CAS sulfur isotope composition from all three sections shows similarities and shifts coincident with other geochemical, biological changes, and/or stratigraphic boundaries (Fig. 6.1). In general, changes in biomass and the oceanic chemical composition can be reflected in sulfur cycling. For example, the limited availability of organic matter will slow the MSR rate and reduce the burial of pyrite. Moreover, the weathering rate could also change the availability of the sulfate in the ocean and nutrient supply to the ocean, which can change the sedimentation rate, rock type and influence the MSR rate (Wortmann and Chernyavsky, 2007; Canfield and Farquhar, 2009). As a result, sulfur isotopes could be used as a chemostratigraphic tool to correlate with other sections and identify age intervals and/or faunal changes.

Here in this chapter (Fig. 6.8), I present a new compilation of the carbonate C, sulfate S (including barite, evaporite, CAS, and other mineral-bound sulfate), and

sulfide S (pyrite) isotope data from Cryogenian to middle Cambrian times (700-500Ma). My compilation identifies four negative carbon isotope excursions in the Ediacaran, and my data fit well with the compiled data from South China and other global sections (Fig. 6.8-A). The estimated time and extent of these four excursions could be used to correlate sections in future studies.

The seawater $\delta^{34}\text{S}_{\text{sulfate}}$ record (Fig. 6.8-B) during the Cryogenian Period (range from +10.0‰ to +51.5‰) is limited due to two big ‘snowball earth’ events, i.e., the Sturtian glaciation (~720-660 Ma) and Marinoan glaciation (~650-635 Ma) (Hoffman et al., 2017). However, the compiled data seems to show a coupled positive shift before the Marinoan, followed by a negative shift between carbonate C and sulfate S isotope composition during the Marinoan, which shows a similar trend to the DOUNCE/Shuram excursion. During the early Ediacaran, the seawater sulfate sulfur $\delta^{34}\text{S}_{\text{sulfate}}$ record shows a narrower range (18.8‰ – 53.7‰) compared with the Cryogenian, which supports an increase in the seawater sulfate concentration and more resistance to chemical changes as a larger sulfate reservoir could buffer the influence caused by input and output fluxes (Kah et al., 2004). The seawater sulfur concentration did not change substantially (1-5mM) (Shi et al., 2018) during the early Ediacaran until the DOUNCE/Shuram event, during which the sulfate sulfur isotope $\delta^{34}\text{S}_{\text{sulfate}}$ composition (average $20.5 \pm 1.3\text{‰}$ at the Lianghong and Sishang sections, and $33.8 \pm 1.5\text{‰}$ at the Qinglinkou Section). The difference between sulfate sulfur and sulfide sulfur isotope values $\Delta\delta^{34}\text{S}_{\text{sulfate-sulfide}}$ (21.5‰ - 52‰), and estimated seawater sulfate concentration (~29mM) all shows similar values to the modern levels. After the DOUNCE/Shuram anomaly, the sulfate reservoir shrank dramatically to pre-excursion levels or even lower. This huge shift influenced the S cycling pathways and caused the decoupled C-S trend.

I also noticed that the middle carbonate unit at the Qinglinkou section shows a mirrored trend of the CAS sulfur isotope values (first increase from ~30‰ to 40‰, then decrease again, Fig. 6.1), which further supports the ‘mirror plane’ hypothesis (see chapter 4) and indicates that sulfur isotopes could be used as a robust chemostratigraphic correlation tool.

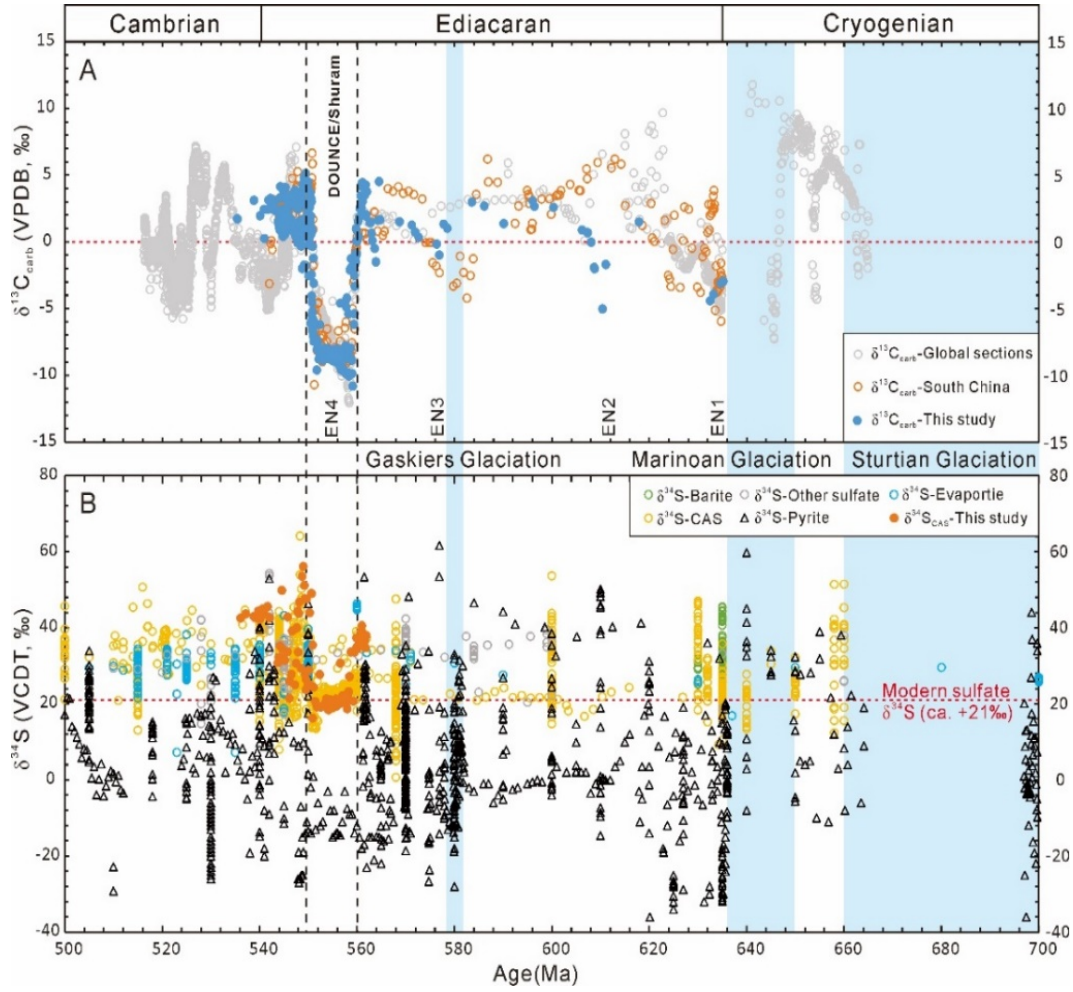


Fig. 6. 9 Compilation of the carbonate carbon isotope $\delta^{13}\text{C}_{\text{carb}}$, barite sulfur $\delta^{34}\text{S}_{\text{barite}}$, evaporite sulfur $\delta^{34}\text{S}_{\text{evaporite}}$, other mineral bound sulfate $\delta^{34}\text{S}_{\text{other}}$, CAS sulfur $\delta^{34}\text{S}_{\text{CAS}}$, and pyrite sulfur $\delta^{34}\text{S}_{\text{py}}$ isotope composition from published papers and this study from Cryogenian to middle Cambrian. Carbonate carbon isotope data from global sections are from (Cox et al., 2016; Bowyer et al., 2017; Wood et al., 2019). South China data from (Jiang et al., 2011; Wang et al., 2012b; Gamper et al., 2015). Barite data from (Misi and Veizer, 1998; Peng et al., 2011; Crockford et al., 2016). Evaporite data from (Gorjan et al., 2000; Strauss et al., 2001; Peryt et al., 2010; Crockford et al., 2019). CAS data from (Fike and Grotzinger, 2008; Hurtgen et al., 2009; Ries et al., 2009b; Bao et al., 2012; Wu et al., 2015; Cui et al., 2016a; Tostevin et al., 2017; Shi et al., 2018). Other mineral bound sulfate data from (Shields et al., 1999; Walter et al., 2000; Shields et al., 2004; Goldberg et al., 2005a; Hough et al., 2006). Pyrite sulfur data from (Sahoo et al., 2012; Tostevin et al., 2017; Shi et al., 2018; Wang et al., 2021). The red dashed line in figure B represents the modern seawater sulfate S isotope value ($\sim 21\text{‰}$) (Tostevin et al., 2014; Cui et al., 2016a). The compiled data set can be accessed by contacting the author.

6.5 Conclusions

This chapter presents high-resolution, high-fidelity carbon and CAS sulfur isotopic data from the three South China sections (Lianghong, Sishang, and Qinglinkou). In brief summary, my work reveals that:

- 1) Diagenesis can potentially influence the CAS sulfur concentration of carbonate samples, evidenced by the significant negative correlation between [CAS] (ppm) versus Mg/Ca (w/w) and [CAS] (ppm) versus Mn/Sr (w/w).
- 2) During the DOUNCE/Shuram excursion interval, the estimated maximum seawater sulfate concentration increased dramatically from (~2.5-4.5 mM) to near modern levels (~29 mM) for at least 4 million years. After the DOUNCE/Shuram excursion, the seawater reservoir shrank back to pre-excursion levels (~0.6-3.0 mM) and then increased gradually again to a peak (~8-10 mM) by the Ediacaran-Cambrian boundary.
- 3) The $^{87}\text{Sr}/^{86}\text{Sr}$ ratio profile shows a clear pulse (up to 0.7090) coincident with the DOUNCE/Shuram excursion and a dramatic increase of the estimated seawater sulfate concentration.
- 4) The high CAS sulfur isotope values at the Qinglinkou section might indicate that the Yangtze Gorges area was a semi-restricted basin and that deeper waters remained euxinic during the DOUNCE/Shuram interval.
- 5) After the DOUNCE/Shuram excursion, a decrease in the weathering rate ($^{87}\text{Sr}/^{86}\text{Sr}$ ratio decrease from 0.7090 to 0.7082) might have ended the DOUNCE/Shuram anomaly, resulting in a shrinking of the seawater sulfate reservoir during that period.
- 6) During the DOUNCE/Shuram aftermath, the low sulfate ocean changed S cycling pathways and resulted in an expansion of deep-water anoxia and a decoupled C-S trend.
- 7) Global correlation indicates that the DOUNCE excursion can be correlated with the global Shuram-Wonoka excursion. The CAS sulfur isotope profile can be used as a potential global chemostratigraphic correlation tool when seawater sulfate concentration is relatively high (~>3 mM).
- 8) The CAS S profile of the middle carbonate unit at the Qinglinkou section further supports the existence of the ‘mirror plane’ at the western region of the Huangling Anticline Area.

Chapter 7 Marine Redox Oscillations during the Late Ediacaran

Abstract

Oxygen has long been viewed as an important control on life evolution and mass extinction. The rise of Ediacaran biota has been attributed to the rise of oxygen levels during the NOE, especially during the DOUNCE/Shuram anomaly interval. However, oceanic dissolved O₂ levels during and after the DOUNCE/Shuram excursion are still equivocal. Here, I use a combination of multi-proxies, RSTE (Mo, U, V trace elements), and uranium isotopes in carbonate samples to examine the late Ediacaran seawater redox evolutions temporally in South China. From the three representative carbonate sections (Lianghong, Sishang, and Qinglinkou sections), my data indicate that the DOUNCE/Shuram interval is not a simple oxygenation event. The $\delta^{238}\text{U}$ data of these three sections show there are two possible transient oxygenations during the onset (increase from -0.82‰ to -0.12‰) and recovery periods (increase from -0.45‰ to -0.20‰) of the DOUNCE/Shuram. However, in between, the ocean floor turned back to largely anoxic (possibly euxinia) during most of the DOUNCE/Shuram interval (decrease to $-0.41 \pm 0.09\text{‰}$). After the DOUNCE/Shuram, also identified by previous publications, U isotope data from the studied sections firstly show evidence for an expansion of anoxia seawater (decrease to -0.82‰, -0.99‰, and -1.22‰ at the Lianghong, Sishang, and the Qinglinkou section respectively). This deoxygenation event was followed by a gradual recovery of the oxygen level (increase to -0.46‰, -0.35‰, and -1.02‰ at three sections, respectively) close to the Ediacaran-Cambrian boundary. The trend of U isotope evolution during the late Ediacaran is supported by the RSTE data from this study. The appearance and radiation of benthic Ediacaran biota also offer evidence for the existence of oxygen on the ocean floor during the terminal Ediacaran period.

Author Contributions: The sample pretreatment and test were conducted by the author ZHEYU TIAN and helped by Gary Tarbuck (UCL) and Anirban Basu, Alexander Dickson (The University of Royal Holloway). This chapter benefitted from discussions with Graham Shields, Ying Zhou, and Anirban Basu.

7.1 Introduction

The Ediacaran biota (c. ~574 - 541 Ma) is a special and lonely taxonomic classification in Earth history and famous for the tubular, frondose, flat-bodied organisms and the first appearance of complex multicellular organisms (Grotzinger et al., 1995; Bobrovskiy et al., 2018; Wood et al., 2019). Ediacaran benthos first appeared around 574 Ma, and burrowing animals appeared only after 560 Ma and ceased coincident with the Cambrian Explosion of skeletal animals (~541 Ma) (Saylor et al., 1995; Narbonne and Gehling, 2003; Canfield et al., 2007; Pu et al., 2016; Sial et al., 2018). The rises and falls of this unique Ediacaran biota have been attributed to ocean redox evolution by many scientists (Sahoo et al., 2016; Zhang et al., 2018; Tostevin et al., 2019; Wei et al., 2021b).

All metazoans only survive in oxic conditions, though the oxygen level might influence the diversity, size, and evolution of these animals. For example, more complex and motile animals (evidenced by trace fossils) indicate higher oxygen levels at the terminal Ediacaran (Wood et al., 2019). Previous studies on the Ediacaran period show evidence for oxygenation events, termed as the “Neoproterozoic Oxygenation Event (NOE)” (Shields-Zhou and Och, 2011; Och and Shields-Zhou, 2012). During the late Ediacaran (~580 – 541 Ma), the most severe negative carbon isotope excursion in Earth history (the DOUNCE/Shuram Excursion) is commonly interpreted to represent the oxidation of the large DOM pool, which imply the deep ocean at least mildly oxygenated (Fike et al., 2006; Och and Shields-Zhou, 2012). In South China, the DOUNCE/Shuram is recorded in the upper Doushantuo Formation and lower Dengying Formation or equivalent strata (details please see Chapter 3).

Many scientists have made attempts to reveal the scenarios, magnitude, and spatial evolution history of oceanic oxygen levels during and after the DOUNCE/Shuram (Zhang et al., 2018; Tostevin et al., 2019; Zhang et al., 2019; Li et al., 2020), which might be the final step to drive our planet’s oceanic oxygen level to near modern stage. However, their results seem to show a conflicting picture. For example, carbonate-associated uranium isotope data (averagely a ca. 0.5‰ increase and close to the modern Bahama carbonate (0.27 ± 0.14 ‰ heavier than modern seawater) (Zhang et al., 2019)) point to a near-modern level of ocean oxygenation during the DOUNCE/Shuram interval (Zhang et al., 2019), followed by an

expansion of anoxia (decrease to $-0.95 \pm 0.10\%$, $-0.97 \pm 0.09\%$, and $-0.81 \pm 0.06\%$ for Gaojiashan, Wuhe sections, and Nama Group respectively) after the DOUNCE/Shuram (Zhang et al., 2018; Tostevin et al., 2019). A prominent increase of the I/(Ca+Mg) ratios (from ~ 0.2 $\mu\text{mol/mol}$ to 4.5 $\mu\text{mol/mol}$ from the Daotuo drillcore section) during the DOUNCE/Shuram suggests a significant rise of O_2 (Wei et al., 2019). However, iron speciation data from the upper Doushantuo Formation black shale samples ($\text{Fe}_{\text{py}}/\text{Fe}_{\text{HR}} > 0.7$ from the Wuhe and Miaohu section) indicate persistently euxinic local environments during the DOUNCE/Shuram (Li et al., 2010; Sahoo et al., 2016; Bridger et al., 2021). Similarly, a positive shift of the Doushantuo Member III Ce anomaly from 0.67 to 0.89 indicates that the DOUNCE/Shuram represents a possible increase in local anoxia (Wei et al., 2018b).

Moreover, the increasing concentrations of the RSTE in shale samples of the Doushantuo Member IV suggest the presence of large RSTE reservoirs and a widely oxygenated ocean (Sahoo et al., 2016). However, this idea is based on the principles that the global marine redox evolution controls the size of the dissolved oceanic RSTE reservoir and the RSTE enrichments in anoxic shales reflect the size of the oceanic RSTE reservoir (Emerson and Huested, 1991; Sahoo et al., 2016). But the changing of the oceanic RSTE concentration could also be controlled by changing the riverine input (as evidenced by the increased $^{87}\text{Sr}/^{86}\text{Sr}$ ratio during the DOUNCE/Shuram (Li et al., 2017)) rather than the marine redox state. To address this bias, comparing RSTE concentration in shale samples and contemporaneous carbonate samples might shed some light on the real oxygenation history during that time interval.

In this study, I present new data of the late Ediacaran carbonate RSTE concentration together with the carbonate-associated uranium isotope values from the three sections (Lianghong, Sishang, and Qinglinkou sections) in South China. The new data further support and improve the stepwise paleo-ocean oxygenation scenarios during the late Ediacaran. I also present an updated uranium isotope and RSTE concentration compilation from Cryogenian to Cambrian based on different rock types (e.g., carbonate and shale/organic-rich mudstone). The updated data compilation suggests multiple transient oceanic oxygenation events happened during the late Ediacaran.

7.2 Redox Proxies Background

The background of the uranium isotopes proxy and RSTE proxy can be found from Chapter 1.

7.3 Methods

7.3.1 Trace Elements

For trace elements, 7 g of sample powder was weighed, washed with 10% NaCl and Milli-Q water 5 times to remove the exchangeable elements. After dried, 20mg sample powder was dissolved with 10ml 6M HCl for 24h (same solution for CAS extraction). Then 1ml solution was dried and redissolved using 2% HNO₃ and tested with Varian 720 ICP-OES for Ca concentration first. And then, the solution was diluted to 10ppm Ca and tested trace elements using Agilent 7900 ICP-MS at UCL. For the data set presented in Appendix C, drift correction has already been applied to the RSTE (U, Mo, V). The test precision was better than 5%. According to the data set of this study, the trace elements were normalized to Sc not only because it is associated with non-carbonate components but also because it has a smaller RSD than Ti. In this study, the enrichment factors of RSTE (U, Mo, V) were calculated as: $EF_x = ([X]/Sc_{sample})/([X]/Sc_{AUCC})$. Average Upper Continental Crust (AUCC) RSTE concentrations were obtained from (McLennan, 2001). For the compiled data, the enrichment factors of RSTE in shale samples were normalized to Al concentration of the Post-Archean average Australian Shale (PAAS, Tribovillard et al. (2006)) and in carbonate samples were compared to AUCC. An enrichment factor index ($\sum EF$) is used for comparing the different sections (Bodin et al., 2007). The $\sum EF = U_{EF} + V_{EF} + Mo_{EF}$.

7.3.2 Uranium Isotopes

Half to one gram of carbonate powder of each sample was weighed and dissolved with 15ml 0.2M acetic acid for 24h at the University of Royal Holloway. After centrifuge, the supernatant was separated into two parts. Around 0.5ml of each supernatant was tested U, Ca concentration on ICP-OES and ICP-MS at UCL. The rest was used for U column chemistry and isotope measurements. An appropriate

amount of double spike ($^{236}\text{U} - ^{233}\text{U}$) was added to each sample to correct for instrumental and procedural mass-dependent fractionation (Basu et al., 2014; Zhang et al., 2020a). Uranium was purified using the UTEVA resin method to remove matrix ions before the isotope analysis (e.g., Na, Ca, Pu, Th, Np) (Horwitz et al., 1992; Basu et al., 2014; Zhang et al., 2020a). U isotope measurements were carried out using a Nu Plasma HR MC-ICP-MS at the University of Royal Holloway. All the data present here have uncertainty values (2σ) below 0.11‰.

7.3.3 The LOWESS Fit

Using LOWESS fit can tell a general trend of my uranium isotope profile. But it is unavoidable that some of the data will be smoothed. The LOWESS (Locally-Weighted regression Scatterplot Smoother) Fit was developed by (Cleveland, 1979; Cleveland et al., 1992) and has been used widely in reconstructing the marine Sr-Isotope curve (Smalley et al., 1994; McArthur et al., 2001). Detailed method procedure is given in (Howarth and McArthur, 1997). LOWESS fit provides a better way to generate the best-fit geochemical curves fitted as a quadratic function of numerical age using weighted least squares regression (McArthur et al., 2001). Briefly, the average geochemical value 'X' at a certain time 't' is determined by:

$$X_i = \sum (1 / (1 + ((t - t_i) / a)^2) \times X_i) / \sum (1 / (1 + ((t - t_i) / a)^2)) \quad \text{Equation 7.1}$$

In this equation, 'X_i' represents the geochemical value $\delta^{238}\text{U}$ at the time 't_i'. 't_i' is the age of each sample, 'i' represent the samples number range from 1 to n (the total sample number). 'a' is the time interval chosen to smooth the data. In this study, the time interval is 0.2 Ma.

7.4 Results

7.4.1 Redox Sensitive Trace Elements (RSTE)

Lianghong section: The RSTE (U, Mo, V) concentration and their normalized ratio (U/Sc, Mo/Sc, V/Sc) show covariation (Fig. 7.1). There are four redox scenarios during the DOUNCE/Shuram and its aftermath. The onset period EN4a is characterized by high U, Mo, V enrichments (Fig. 7.1). High U/Sc, Mo/Sc, V/Sc

occur during the onset of the DOUNCE/Shuram (EN4a) with the range of 0.40-1.37, 0.26-0.65, 35.45-63.84, respectively. During EN4b, these three values decrease dramatically to the nadir 0.13-0.30, 0.053-0.30, 3.50-7.20, respectively. The recovery period of the DOUNCE/Shuram (mainly EN4c) shows a sudden increase in the RSTE enrichments and is followed by a gradual decrease trend (U/Sc: 0.57-5.4, Mo/Sc: 0.24-4.58, V/Sc: 10.40-14.98). After the DOUNCE/Shuram, the RSTE concentrations are relatively stable with the U/Sc, Mo/Sc, V/Sc ratios ranging from 1.1-2.0, 0.34-0.90, and 10.16-17.46, respectively.

Sishang section: The RSTE concentration and their normalized ratio show a similar pattern with the Lianghong section. EP3 is characterized with constantly low U, Mo, V enrichments (average value of U/Sc, Mo/Sc, V/Sc are 0.089, 0.20, 2.89 respectively) (Fig. 7.2). A sudden increase of U/Sc, Mo/Sc, V/Sc occurred during the EN4a and was followed by a decreasing trend. The highest values of U/Sc, Mo/Sc, and V/Sc reach 1.04, 1.74, and 12.00. During EN4b, these three values remain constantly low 0.025-0.23, 0.024-0.57, 2.89-5.05, respectively. The recovery period of the DOUNCE/Shuram (mainly EN4c) shows a similar trend with the EN4a (the highest value of U/Sc, Mo/Sc, V/Sc are 1.23, 1.06, 8.03, respectively). After the DOUNCE/Shuram (EP4), the RSTE concentrations are relatively low with the U/Sc, Mo/Sc, V/Sc ratios range 0.30-0.45, 0.079-1.16, 2.83-4.18, respectively.

Qinglinkou section: The RSTE concentration before the DOUNCE/Shuram (~635-560 Ma) is constantly low (average value of U/Sc, Mo/Sc, V/Sc are 0.081, 0.12, 3.29 respectively) (Fig. 7.3). A similar trend of the RSTE concentration during and after the DOUNCE/Shuram was also observed at the Qinglinkou section. Two pulses occurred during EN4a and EN4c with the highest values of U/Sc (0.35 and 0.75 respectively), Mo/Sc (1.46 and 0.78 respectively), V/Sc (17.17 and 10.49 respectively).

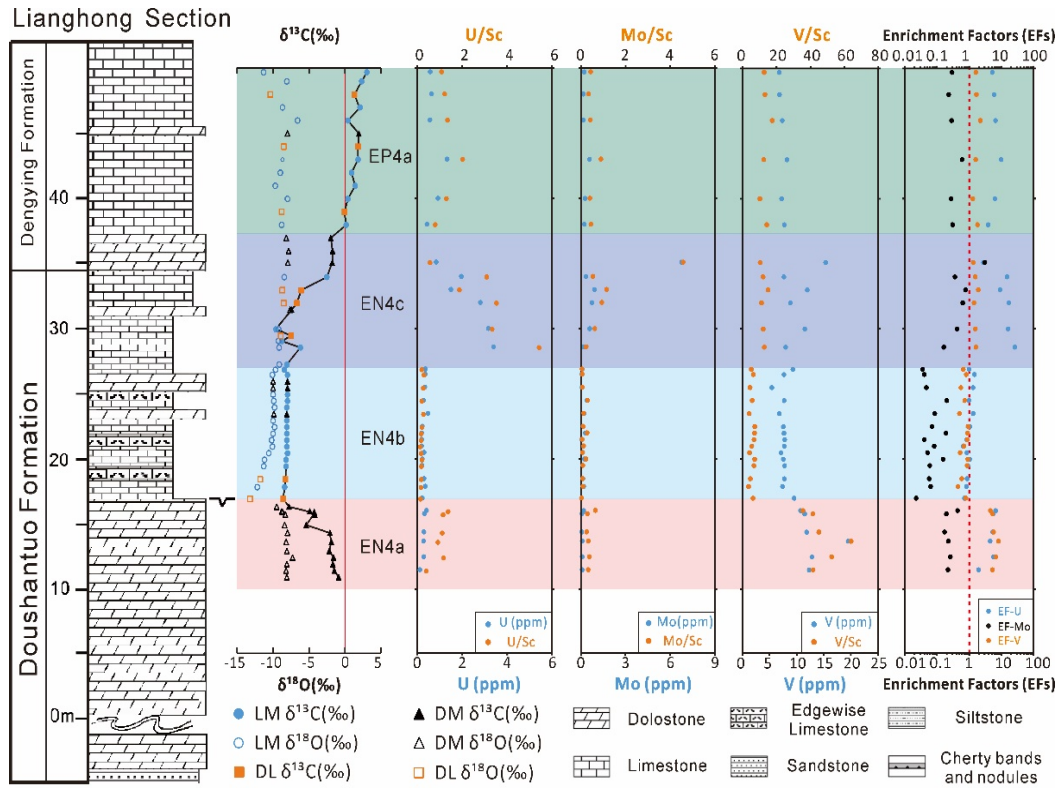


Fig. 7. 1 The geochemical profiles of the redox-sensitive trace elements across the DOUNCE/Shuram at the Lianghong section.

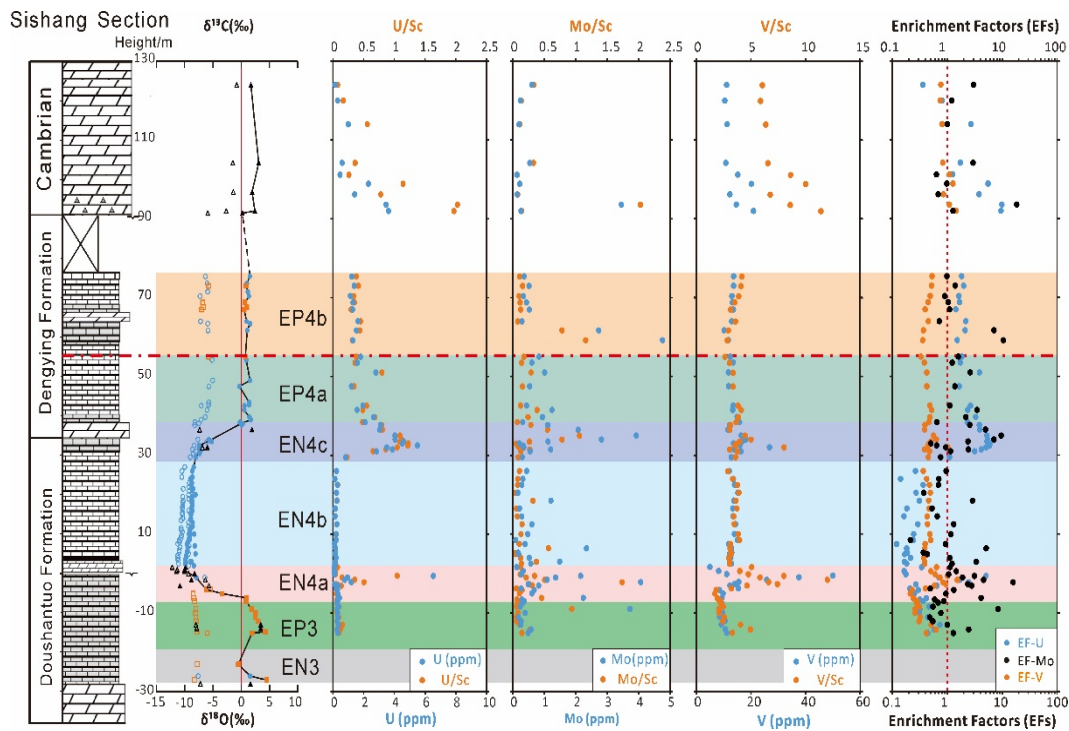


Fig. 7. 2. The geochemical profiles of the redox-sensitive trace elements across the DOUNCE/Shuram at the Sishang section.

Qinglinkou Section

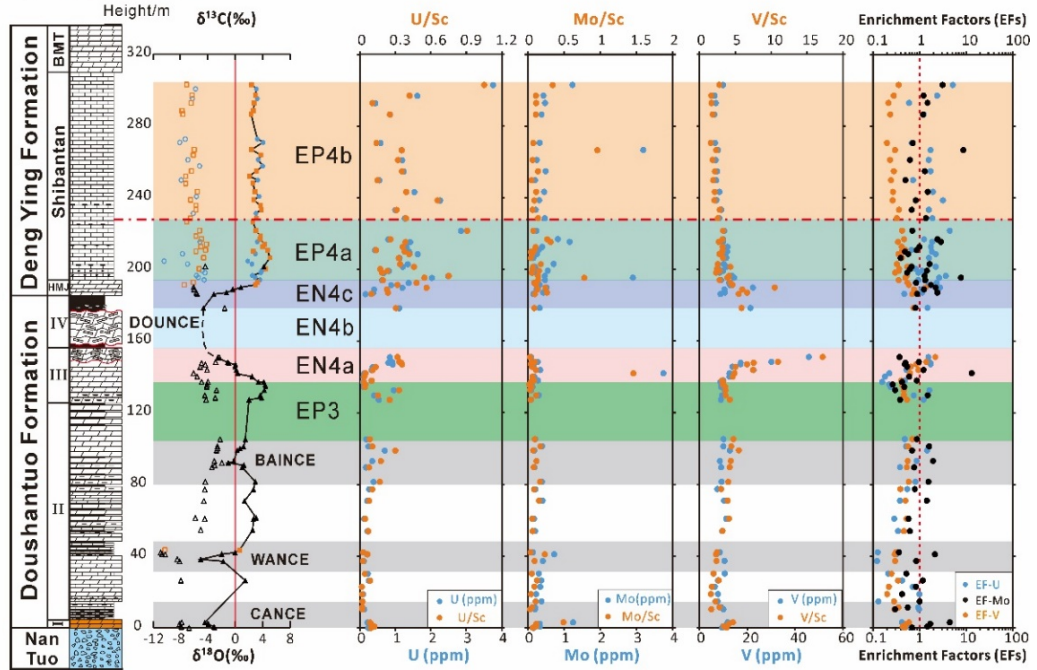


Fig. 7.3 The geochemical profiles of the redox-sensitive trace elements across the Ediacaran Period at the Qinglinkou section.

7.4.2 Uranium Isotopes

The $\delta^{238}\text{U}$ profiles (Fig. 7.4) from the three sections in this study display a similar trend. During the onset period of the DOUNCE/Shuram, the $\delta^{238}\text{U}$ value increased from -0.5‰ to -0.22‰ (EN4a) at the Lianghong section, -0.82‰ to -0.12‰ (EP3 and EN4a) at the Sishang section, and -1.04‰ to -0.6‰ (EN4a) at the Qinglinkou section. EN4b is characterized as constantly high, near modern level ($-0.392 \pm 0.005\text{‰}$), $\delta^{238}\text{U}$ values with an average of $-0.41 \pm 0.09\text{‰}$ at the Lianghong and Sishang sections. No uranium data are available for this period at the Qinglinkou section. The recovery period of the DOUNCE/Shuram (EN4c) shows a transient increasing trend from -0.45‰ to -0.34‰ at the Lianghong section and -0.45‰ to -0.20‰ at the Sishang section, followed by a decreasing trend to -0.63‰ , -0.79‰ , and -1.15‰ at the Lianghong, Sishang, and Qinglinkou sections, respectively.

During the DOUNCE/Shuram aftermath, $\delta^{238}\text{U}$ values decreased to the lowest during EP4a (-0.82‰ at the Lianghong section, -0.99‰ at the Sishang section, and -1.22‰ at the Qinglinkou section). EP4b shows an increasing trend to -0.46‰ at the Lianghong section, -0.35‰ at the Sishang section, and -1.02‰ at the Qinglinkou section. It seems that during the end of EP4b, the $\delta^{238}\text{U}$ decreased again to -1.0‰ at the Sishang section.

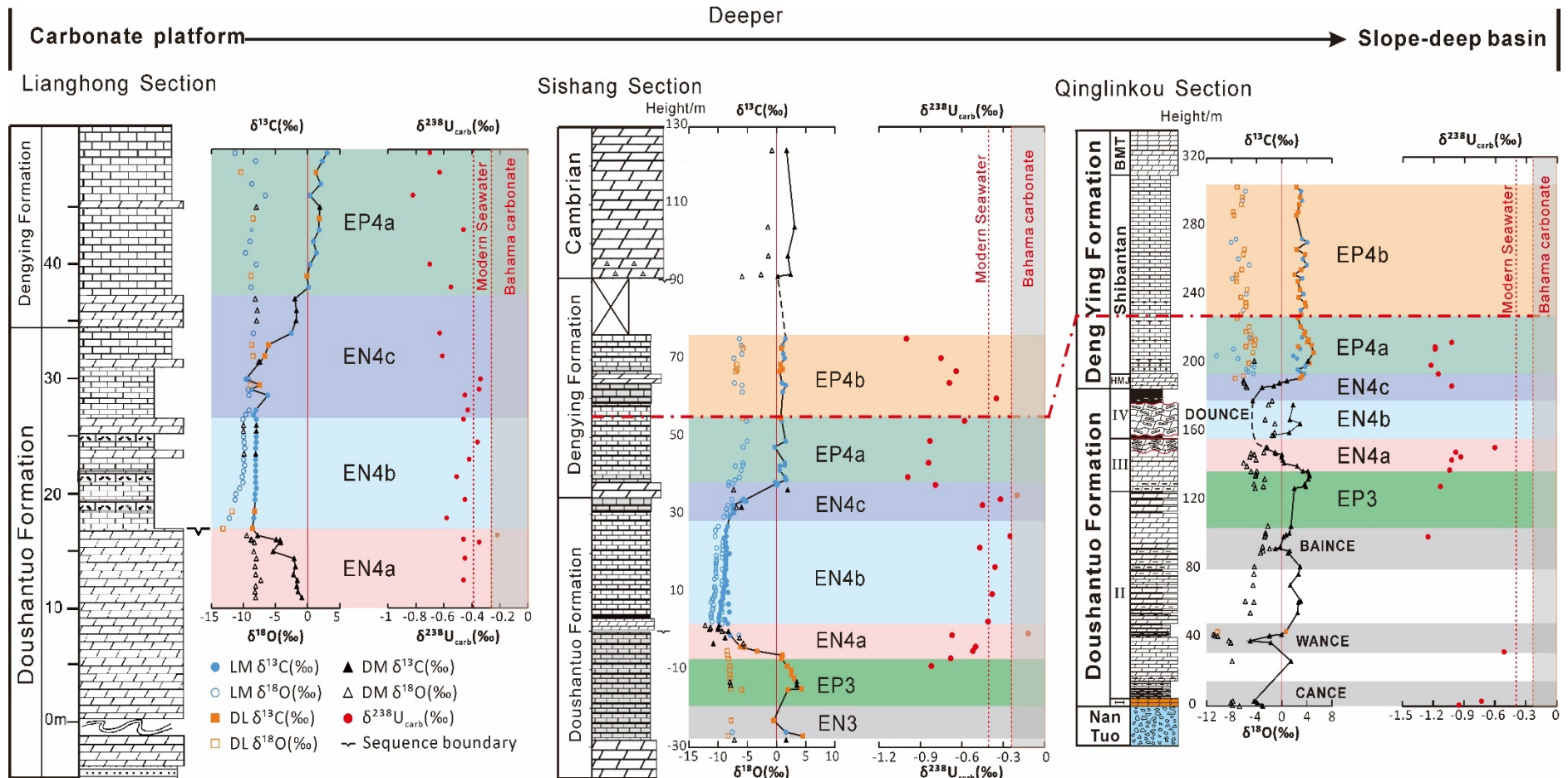


Fig. 7. 4. Ediacaran $\delta^{13}\text{C}_{\text{carb}}$, $\delta^{18}\text{O}_{\text{carb}}$, and $\delta^{238}\text{U}$ profiles of the carbonate samples of the studied sections from this study. The red-dashed line represents the modern seawater $\delta^{238}\text{U}$ value $-0.392 \pm 0.005\text{‰}$. The red-dashed shaded area represents the modern Bahama carbonate ($0.27 \pm 0.14\text{‰}$ heavier than modern seawater) (Tissot and Dauphas, 2015; Chen et al., 2018).

7.5 Discussion

7.5.1 Diagenetic Evaluation

It has been reported that $\delta^{238}\text{U}$ values are more robust against rock-fluid interactions than $\delta^{18}\text{O}_{\text{carb}}$ and Sr isotope values (Lau et al., 2017; Chen et al., 2018; Zhang et al., 2019). In this chapter, besides the evaluations shown in earlier chapters, I still compared my U isotope data with traditional carbonate diagenetic indicators O isotope and other elemental ratios, such as Mn/Sr, Mg/Ca (Fig. 7.5).

Dissolution and recrystallization can lower $\delta^{18}\text{O}_{\text{carb}}$ (Banner and Hanson, 1990; Lu et al., 2013). The samples' cross-plot of $\delta^{238}\text{U}$ - $\delta^{18}\text{O}_{\text{carb}}$ (Fig. 7.5-a) show minor correlation (Lianghong section $R^2 = 0.016$, Sishang section $R^2 = 0.22$, Qinglinkou section $R^2 = 0.002$), which indicates that the $\delta^{238}\text{U}$ might not be diagenetically altered. Mn/Sr ratios have been used to indicate post-depositional alteration by many scientists (Kaufman and Knoll, 1995; Zhang et al., 2020a). The cross-plot of the $\delta^{238}\text{U}$ -Mn/Sr (Fig. 7.5-b) show moderate to minor correlation (Lianghong section $R^2 = 0.38$, Sishang section $R^2 = 0.0002$, Qinglinkou section $R^2 = 0.294$). Moreover, all the selected samples have the Mn/Sr ratios <10 , indicating that those samples are well preserved.

The influence of the lithology changes or dolomitization has been examined by the cross-plot of $\delta^{238}\text{U}$ -carbonate content and $\delta^{238}\text{U}$ -Mg/Ca. The results show that all the samples have a very limited correlation ($R^2 < 0.09$) between $\delta^{238}\text{U}$ -carbonate content (Fig. 7.5-c) and $\delta^{238}\text{U}$ -Mg/Ca (Fig. 7.5-d) at Lianghong and Sishang sections. In the Qinglinkou section, the lithology changes from dolostone to limestone between Doushantuo and Dengying Formations, which might cause the moderate correlation between the $\delta^{238}\text{U}$ -carbonate content ($R^2 = 0.365$) and $\delta^{238}\text{U}$ -Mg/Ca ($R^2 = 0.211$). However, that does not mean the U isotope values have been changed due to the dolomitization. Therefore, I infer that the dolomitization is unlikely to influence the $\delta^{238}\text{U}$ record of my samples significantly.

I further investigated the correlations of $\delta^{238}\text{U}$ -U/Sc and $\delta^{238}\text{U}$ -Al for all studied samples. No obvious correlations between these indicators ($R^2 < 0.218$) are evident in any of these three sections. I used 0.2M acetic acid to extract the uranium, which will minimize the dissolution of non-carbonate minerals (e.g., clay minerals and silicates). Moreover, my samples have U/Al ratios much higher than (10 to 100 times

higher) the crustal value (~ 0.33 ppm/wt.%) (Fig. 7.5-f), which might suggest that the $\delta^{238}\text{U}$ present in this study is more likely to be authigenic rather than influenced by detrital contaminations.

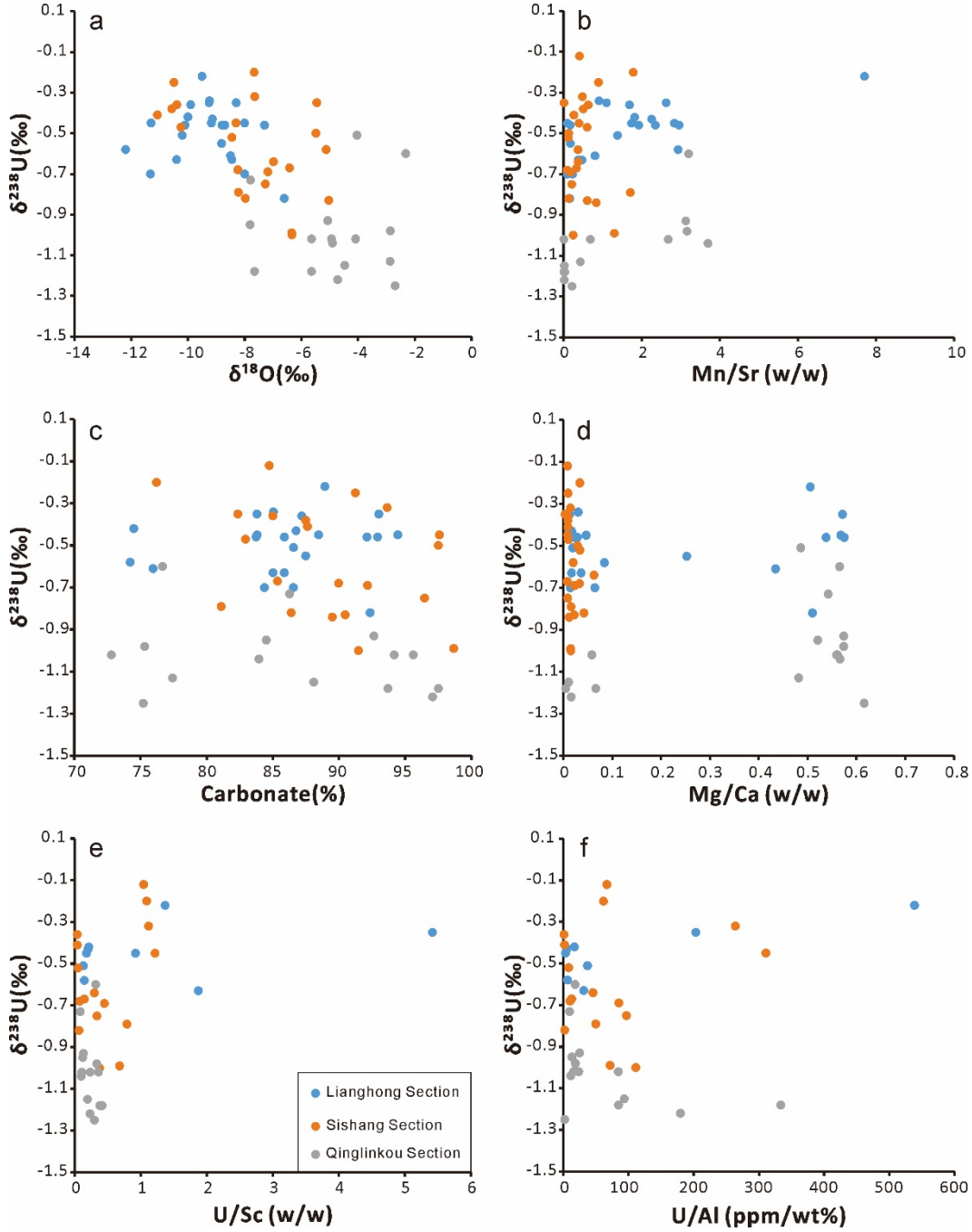


Fig. 7.5 Cross-plots of the $\delta^{238}\text{U}$, $\delta^{18}\text{O}_{\text{carb}}$ and elemental ratios of the Lianghong, Sishang and Qinglinkou sections. a. $\delta^{238}\text{U}$ (‰)- $\delta^{18}\text{O}_{\text{carb}}$ (‰) (Lianghong $R^2 = 0.016$; Sishang $R^2 = 0.22$; Qinglinkou $R^2 = 0.002$); b. $\delta^{238}\text{U}$ (‰)-Mn/Sr (Lianghong $R^2 = 0.38$; Sishang $R^2 = 0.0002$; Qinglinkou $R^2 = 0.294$); c. $\delta^{238}\text{U}$ (‰)-Carbonate content (%) (Lianghong $R^2 = 0.012$; Sishang $R^2 = 0.087$; Qinglinkou $R^2 = 0.365$); d. $\delta^{238}\text{U}$ (‰)-Mg/Ca (Lianghong $R^2 = 0.0032$; Sishang $R^2 = 0.040$; Qinglinkou $R^2 = 0.211$); e. $\delta^{238}\text{U}$ (‰)-U/Sc (Lianghong $R^2 = 0.088$; Sishang $R^2 = 0.15$; Qinglinkou $R^2 = 0.086$); f. $\delta^{238}\text{U}$ (‰)-U/Al (Lianghong $R^2 = 0.070$; Sishang $R^2 = 0.11$; Qinglinkou $R^2 = 0.218$);

7.5.2 Ocean Redox Oscillations during the DOUNCE/Shuram

The concentrations and normalized ratios of RSTE are indicators of local redox conditions (Tribovillard et al., 2006; Chang et al., 2012; Och and Shields-Zhou, 2012). The seafloor oxygenation changes will influence the seawater RSTE reservoir and, in return, influence the abundance of RSTE incorporated into marine carbonates (Brennecke et al., 2011; Elrick et al., 2017; Smrzka et al., 2019). The fundamental assumption is that those RSTE were incorporated into the carbonate minerals in a known or predictable ratio (Webb and Kamber, 2000; Smrzka et al., 2019). For example, the decrease of RSTE concentrations in the seawater and their normalized ratios reflect enhanced removal rates of the RSTE to the sediment, presumably, expanded anoxia of the seafloor (Lau et al., 2017; Smrzka et al., 2019; Ansari et al., 2020). The uptake of authigenic U occurs at the Fe(III) to Fe(II) redox boundary (suboxic conditions) (Zheng et al., 2002). And in sulfidic environments (exist of H_2S), Mo sinks more efficiently than U, which might result in very low Mo/U ratios in the water column (Algeo and Tribovillard, 2009; Sahoo et al., 2016; Yano et al., 2020). In modern ocean, Mo has longer residence time than U and is more enriched in the seawater (Chapter 1, Table 1.1). The trend of $\text{Mo}_{\text{EF}} < \text{U}_{\text{EF}}$ in the carbonate samples and $\text{Mo}_{\text{EF}} > \text{U}_{\text{EF}}$ in the contemporaneous shale samples might indicate the occurrence of locally euxinic bottom water.

Although the Doushantuo Formation at the Qinglinkou section is mainly dolostone, the general trends of the RSTE concentration are similar in timing and magnitude to those limestone samples at the Lianghong and Sishang section. Moreover, the diagenesis evaluation shows no correlation between the RSTE concentration and lithofacies. Thus, the Qinglinkou section likely records the primary seawater trends. However, the Yangtze Gorges area likely remained partially restricted (lagoonal settings) during the DOUNCE/Shuram (Jiang et al., 2011; Och et al., 2016; Bridger et al., 2021), which might be the main reason for the extremely low $\delta^{238}\text{U}$ values (-1.38‰) after the DOUNCE/Shuram compared to the other two sections ($\sim -0.99\text{‰}$). The highest RSTE concentration and $\delta^{238}\text{U}$ occur coincidentally during the EN4a and EN4c, representing transient whole ocean oxygenation. The detailed late Ediacaran oxygenation history can be divided into six scenarios.

Before the DOUNCE/Shuram, the RSTE concentration and their normalized

ratios are constantly low with minor fluctuations at the Qinglinkou section (we only have pre-DOUNCE value from this section, Fig. 7.3), likely representing the seafloor remain anoxia.

A dramatic increase of the RSTE levels (Fig. 7.6-A, B) occurs during the onset of the DOUNCE/Shuram (**EN4a**) coincidence with the rise of the $\delta^{238}\text{U}$ (Fig. 7.6-C: -0.5‰ to -0.22‰ at the Lianghong section, -0.82‰ to -0.12‰ at the Sishang section, and -1.04‰ to -0.6‰ at the Qinglinkou section), which might represent a dramatic expansion of oceanic oxygenation. Many previous scientists reported $\delta^{238}\text{U}$ isotope studies from different sections similar to my result (Zhang et al., 2019; Li et al., 2020), which might indicate that deep-water oxygenation is a global event during this interval. However, the rise of the RSTE and U isotope composition might just represent the transient result of increased weathering flux ($^{87}\text{Sr}/^{86}\text{Sr}$ ratios increase from 0.7080 to 0.7090, Fig. 6.7).

In the modern Earth system, the riverine flux of $\delta^{238}\text{U}$ is close to the crust value, which is slightly lighter (0.1‰) than the seawater composition (Fig. 1.8). Increased weathering flux might bring enormous light $\delta^{238}\text{U}$ and RSTE into the ocean and cause this pulse increase of the RSTE and $\delta^{238}\text{U}$. However, the increasing magnitude of the Uranium isotope is around 0.3-0.7‰, which is much larger than the difference between the riverine input and seawater values. This means the increased riverine flux might not play a critical role in controlling the seawater U isotope composition. Moreover, a recent study reported a prominent increase of the $\text{I}/(\text{Ca} + \text{Mg})$ value increase from ($\sim 0.2\mu\text{mol/mol}$ to $4.5\mu\text{mol/mol}$ and $0.07\mu\text{mol/mol}$ to $0.48\mu\text{mol/mol}$) coincident with the negative shift (**EN4a**) of the $\delta^{13}\text{C}$ in the Daotuo drillcore section and Siduping section respectively (Hardisty et al., 2017; Wei et al., 2019). This evidence supports the transient oxygenation theory during the onset period of the DOUNCE/Shuram.

During the DOUNCE/Shuram (**EN4b**), $\delta^{238}\text{U}$ values decreased but still maintained constant high values ($-0.41 \pm 0.09\text{‰}$) near the modern level, but the RSTE enrichments (Fig. 7.6-A, B) decreased to pre-excursion level. Two opposite explanations have been put forward to address the redox state during this period.

Based on the steady-state isotopic mass balance model, Zhang et al. (2019) proposed that seawater reached near modern level oxygenation during the DOUNCE/Shuram with a dramatic expansion of seafloor oxic area. However, the shrinking of the anoxic area represents a decrease of the RSTE sink, which will cause

an increase of the RSTE concentrations. Moreover, the increased weathering rate during the DOUNCE/Shuram ($^{87}\text{Sr}/^{86}\text{Sr}$ ratios up to 0.7090, Chapter 6) brings more RSTE into the ocean. The decrease of RSTE during EN4b cannot be met with this hypothesis.

The increased riverine input of RSTE needs to have an even larger sink during the EN4b to drive the decreasing trend in the RSTE concentrations. I propose that the increased MSR activity and oxidizing of the ocean DOM pool is the driving force for the decreasing trend of RSTE. The increased MSR (evidenced from CAS data in Chapter 6) is not likely to represent a near-modern level of seawater oxygenation. On the contrary, it indicates an expansion of deepwater euxinia coincides with an increase of the O_2 levels in the water column and atmosphere. Moreover, the increase of local euxinia is also evidenced by a positive shift in Ce/Ce^* (Zhou et al., 2012; Cui et al., 2015; Wei et al., 2018b), increased RSTE enrichment in the Doushantuo IV shale layers (Bridger et al., 2021) and $\text{Fe}_{\text{HR}}/\text{Fe}_{\text{T}} > 0.46$, $\text{Fe}_{\text{py}}/\text{Fe}_{\text{HR}} > 0.7$ (Fig. 7.6-D) in the Doushantuo III and IV shale layers (Li et al., 2015; Ostrander et al., 2019; Bridger et al., 2021). The existence of a large DOM pool stored in the late Ediacaran ocean is the main barrier for the whole ocean to be oxygenated.

During the recovery period from the DOUNCE/Shuram anomaly (**EN4c**), a shrink of the riverine input ($^{87}\text{Sr}/^{86}\text{Sr}$ ratios decrease from 0.7090 to 0.7084, Fig. 6.7) of sulfate and RSTE caused the decrease of the sulfate concentration and the decrease of the MSR activity correspond to a decrease in deepwater euxinia (Fig. 4.6-D). In return, the RSTE concentration increase again ($U_{\text{EF}} = 0.6$ to 5.8 ; $Mo_{\text{EF}} = 0.8$ to 2.2 ; $V_{\text{EF}} = 0.6$ to 0.9) during this period (Fig. 7.6-A) together with a transient increase of $\delta^{238}\text{U}$ (Fig. 7.6-C: -0.41‰ to -0.20‰). This transient oxygenation period is also supported with the iron speciation data (Fig. 7.6-D), the enhanced primary production (Canadas et al., 2022), and enriched pyrite burial in the shale layers (Chapter 3, Fig. 3.7). Without enough oxidant supply (O_2 and sulfate), the global seawater oxygen level decrease, resulting in the decrease of $\delta^{238}\text{U}$ back to pre-excursion level or even lower, and the RSTE concentration also decrease simultaneously.

In summary, the pre-DOUNCE/Shuram interval is characterized by anoxic paleo-seawater. During the onset and recovery period, the ocean experienced transient oxygenation (<1.6 Ma). During DOUNCE/Shuram (EN4b), the whole seawater oxygen level increased, but the deepwater remained euxinic.

7.5.3 Ocean Redox Oscillations after the DOUNCE/Shuram

After the DOUNCE/Shuram, marine sulfate concentration reached the lowest values (< 1 mM) (Chapter 6, Fig. 6.6), resulting in increased methanogenesis and methane release at the seafloor, which causes the expansion of anoxic conditions as evidenced by the decrease of RSTE enrichments and $\delta^{238}\text{U}$ during **EP4a** (Fig. 7.6). Evidence also includes the decreasing trend of $\delta^{238}\text{U}$ reaching $-0.81 \pm 0.06\text{‰}$ from the Nama Group (550-547Ma), Wuhe section (-1.2‰) and Gaojiashan section (-1.18‰) (Zhang et al., 2018; Tostevin et al., 2019); the positive shift of Ce/Ce* from 0.69 to 0.92 of the Donglongtan Member at the Xiaotan section (Wei et al., 2018a; Wei et al., 2020c).

EP4b is an increasing period of the marine sulfate concentration, RSTE enrichments, and $\delta^{238}\text{U}$ values, representing a gradual whole ocean oxygenation event. The negative shift of Ce/Ce* values from 0.92 to 0.42 at the Xiaotan section (Wei et al., 2018a; Wei et al., 2020c), from 0.58 to 0.29 at the Gaojiashi-Yanjiahe section (Wei et al., 2018a), and from 0.92 to 0.30 in the Yangtze Gorges area (Wei et al., 2018b) also indicate pervasive oxygenation of the seawater. This oxygenation period provides a perfect window for raising benthic Shibantan/Gaojiashan biota, evidenced by the wide occurrence of trace fossils (Wood et al., 2019; Xiao et al., 2021). Sulfate concentration shows a consistent trend with the RSTE concentration and $\delta^{238}\text{U}$ values during the DOUNCE/Shuram aftermath, proving that the sulfur cycle plays an essential role in controlling oxygen, climate perturbations, and environmental shift of the Earth surface system.

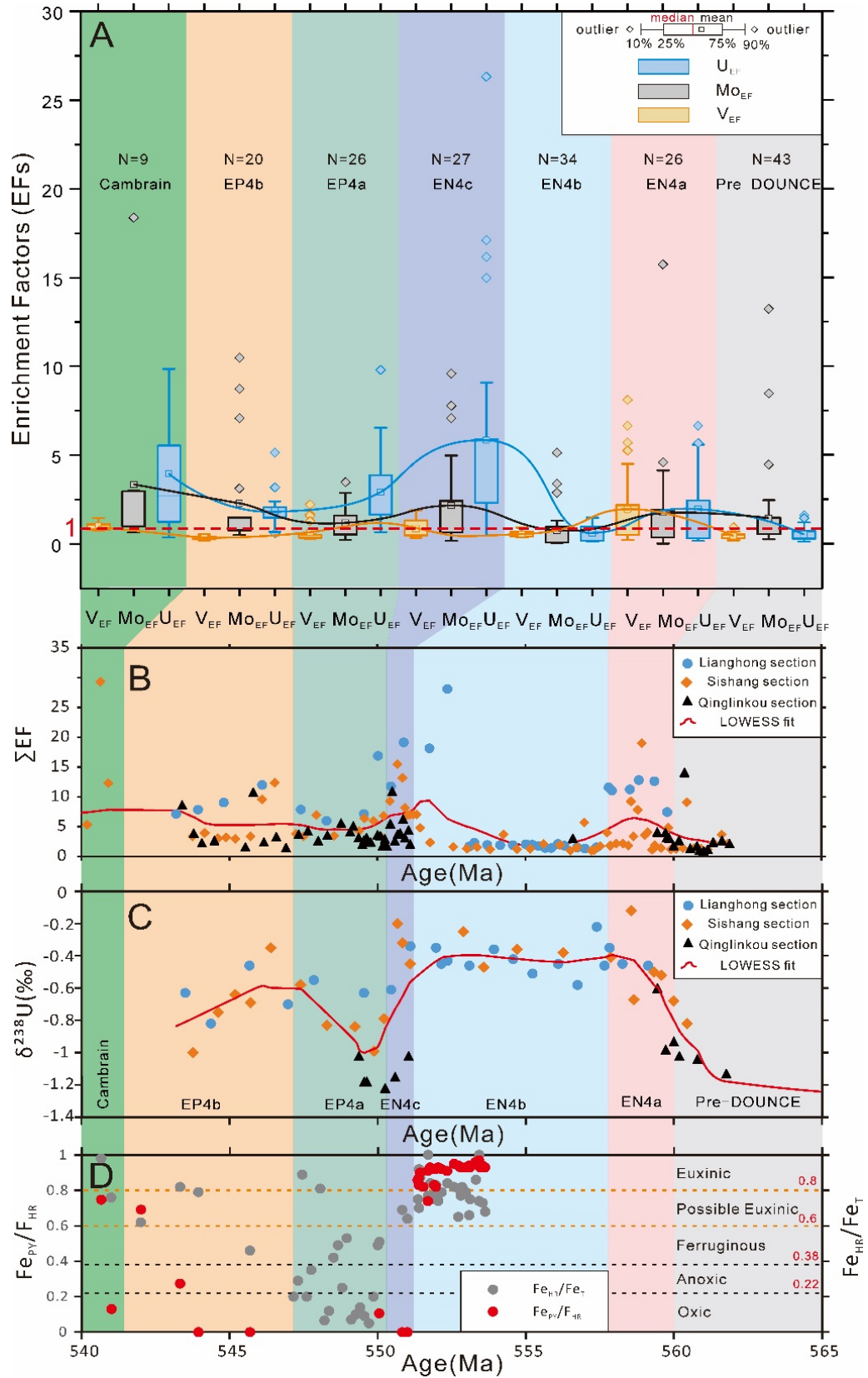


Fig. 7. 6 A: Boxplots of Enrichment Factors (U_{EF} , Mo_{EF} , and V_{EF}) of the carbonate samples from each period during pre-DOUNCE to early Cambrian. N = number of samples. The blue, black, and orange curve lines represent the average U_{EF} , Mo_{EF} , and V_{EF} values, respectively. B: The enrichment factor index (ΣEF) profile of each section. C: Uranium isotope $\delta^{238}U$ profile of the studied sections (Lianghong, Sishang, and Qinglinkou section). D: Iron speciation data from Yanjia section, Daotuo drillcore, Jiulongwan section, and Three Gorges Core ($Fe_{HR}/Fe_T > 0.38$; $Fe_{PY}/Fe_{HR} > 0.8$ indicate euxinic water-column). The red curves are LOWESS smoothed profiles.

7.5.4 Global Ocean Paleo-redox Shifts and Life Evolutions

The $\delta^{238}\text{U}$, U_{EF} , and Mo_{EF} values of this study show consistency with the published global data (Fig. 7.7). As the Cryogenian is out of the scope of this thesis, even though the compiled data stretch back to the interval after the Sturtian glaciation, I would not try to describe or interpret the data.

During the early Ediacaran, the ocean oxygen levels remained relatively low until the DOUNCE/Shuram. The DOUNCE/Shuram is characterized as a two-pulse increase of the carbonate $\delta^{238}\text{U}$, U_{EF} , and Mo_{EF} values during the onset and recovery periods, representing two global ocean oxygenation events. During the DOUNCE/Shuram, the carbonate U_{EF} and Mo_{EF} values drop dramatically with an increase of the shale U_{EF} and Mo_{EF} values ($Mo_{\text{EF}} > U_{\text{EF}}$). However, the carbonate $\delta^{238}\text{U}$ values remain relatively high (near modern seawater), likely representing an expansion of the deepwater euxinic realm, while the ocean oxygen level as a whole increased. It has been reported that the marine carbonate rocks have slightly heavier $\delta^{238}\text{U}$ values (0.2‰ - 0.4‰) compared to ambient seawater values (Lau et al., 2019). If we back-calculate this difference, during the DOUNCE/Shuram anomaly, carbonate $\delta^{238}\text{U}$ is shown to be slightly lower than modern seawater values, suggesting that the near-modern levels of ocean oxygenation hypothesis (Zhang et al., 2019) might not be correct. The oxygenation of seawater during the DOUNCE/Shuram is coincident with the increased diversification and taxonomic disparity of the ‘Ediacaran macrobiota’ (~560 Ma) (Wood et al., 2019). A possible interpretation is that the increasing of the oxygen in the seawater stimulates and supports the evolution of more complex life.

After the DOUNCE/Shuram, the ocean oxygen level drops dramatically, as evidenced by a consistent decreasing trend of carbonate $\delta^{238}\text{U}$, U_{EF} , and Mo_{EF} . This anoxia event is closely linked with the reduced diversity of non-bilaterian metazoans and the first appearance of biomineralized taxa (~551 Ma, Fig. 7.7-E) (Wood et al., 2019). The latest Ediacaran period is marked by the gradual recovery of the ocean oxygen level and occurrence of the bilaterian stem-group faunas and re-flourish of the non-bilaterian stem-group faunas (Fig. 7.7-E). The trace fossils are also widespread during this period, recorded in the middle to upper Dengying Formation (Xiao et al., 2021).

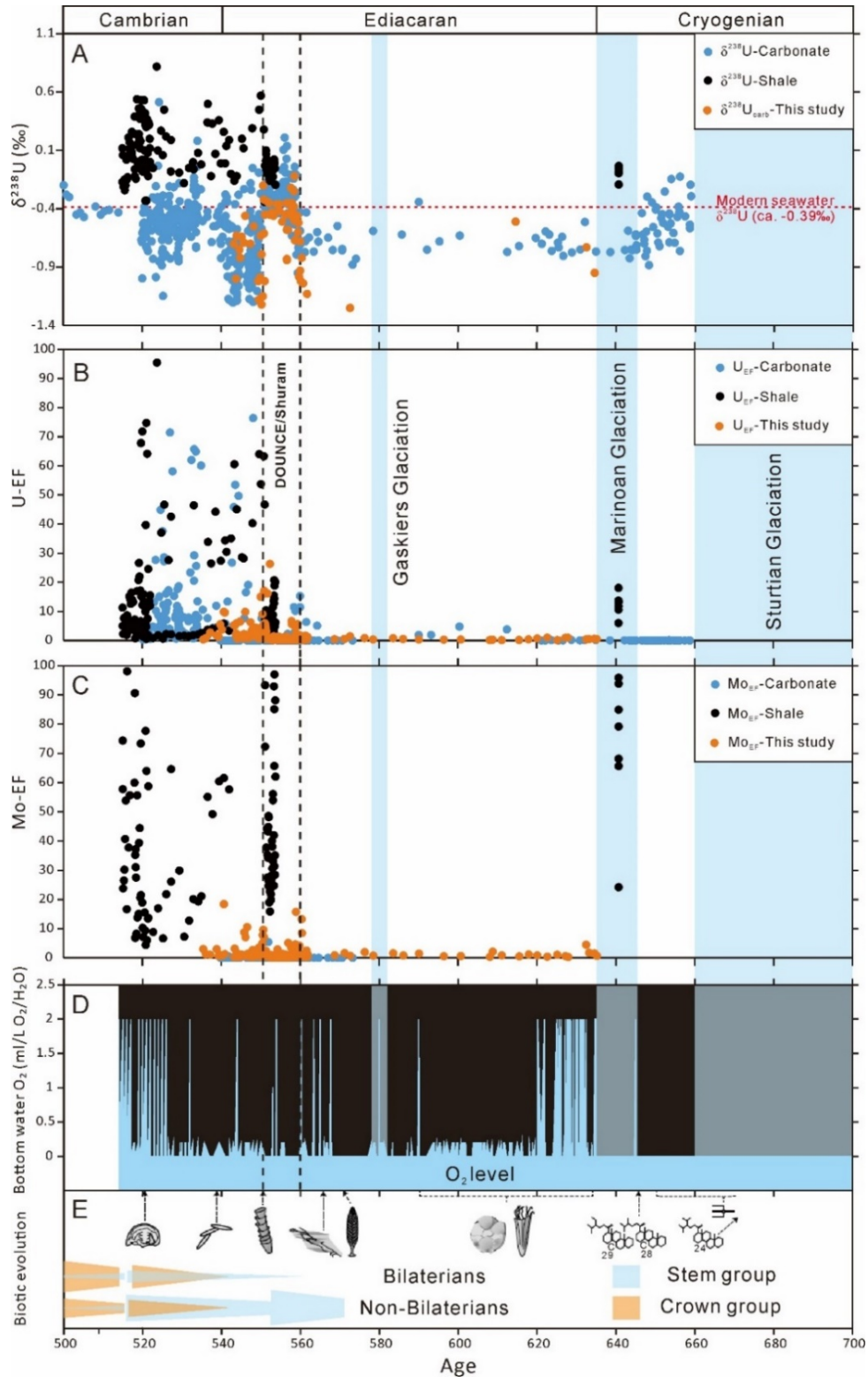


Fig. 7. 7 Compilation of the $\delta^{238}\text{U}$ (A), U_{EF} (B), and Mo_{EF} (C) from carbonate samples and shale samples from published papers and this study. (D) Estimated bottom water oxygen levels based on published iron speciation data. (E) Biotic evolution records cross Cryogenian-Cambrian, modified from (Wood et al., 2019). Oxidic condition $[\text{O}_2] > 2 \text{ ml/l (O}_2/\text{H}_2\text{O)}$; Suboxic condition $0.2 < [\text{O}_2] < 2 \text{ ml/l (O}_2/\text{H}_2\text{O)}$; Anoxic condition $[\text{O}_2] < 0.2 \text{ ml/l (O}_2/\text{H}_2\text{O)}$; Ferruginous condition $[\text{O}_2] < 0.1 \text{ ml/l (O}_2/\text{H}_2\text{O)}$; Euxinic $[\text{O}_2] = 0 \text{ ml/l (O}_2/\text{H}_2\text{O)}$ (Tyson and Pearson, 1991; Tribouillard et al., 2006). Compiled data includes (Dahl et al., 2014; Azmy et al., 2015; Kendall et al., 2015; Lau et al., 2017; Wei et al., 2018a; Zhang et al., 2018; Dahl et al., 2019; Tostevin et al., 2019; Zhang et al., 2019; Cheng et al., 2020; Li et al., 2020; Wei et al., 2020a; Wei et al., 2021a). The compiled data set can be accessed by contacting the author.

7.6 Conclusions

This study provides uranium isotope and Redox-Sensitive Trace Element (RSTE) profiles across the entire DOUNCE/Shuram Excursion and its aftermath. By correlating with the published global data, I propose that:

- 1) Based on published data and data from this study, the late Ediacaran period might have experienced stepwise oxygenation events.
- 2) The DOUNCE/Shuram excursion might not be a simple oxygenation event.
- 3) The DOUNCE/Shuram is characterized by two possible transient global oceanic oxygenations during the onset and recovery periods and in between, possibly an expansion of anoxic (possibly euxinia) the sea floor.
- 4) After the DOUNCE/Shuram anomaly, the ocean experienced the last major expansion of anoxia of the Precambrian, after which oxygen levels gradually recovered near the Ediacaran-Cambrian boundary.
- 5) This study offers further proof that oxygen levels in seawater played a vital role in the biological evolution at the terminal Ediacaran.

Chapter 8 Towards a Conceptual Model of Ocean Evolution through the DOUNCE/Shuram Interval

As mentioned in previous chapters, the late Ediacaran period witnessed dramatic ocean redox, weathering, and climate changes. My results indicate a stepwise ocean oxygenation history during the late Ediacaran. Below I divide the late Ediacaran into six stages, whereby the duration of each stage is estimated based on the age model presented in Chapter 2.

8.1 Pre-DOUNCE/Shuram Period (EP3)

The pre-DOUNCE/Shuram period (EP3) witnessed a relatively stable state with positive carbon isotope $\delta^{13}\text{C}_{\text{carb}}$ (Average: 2.89‰, 3.04‰ at the Sishang and Qinglinkou section) and relatively high sulfate sulfur isotope $\delta^{34}\text{S}_{\text{sulfate}}$ (> 34‰) values, which likely corresponded to elevated rates of primary production and organic carbon and pyrite burial. A huge DOM pool and sedimentary pyrite pool might have accumulated slowly during this period.

During EP3, the dominant creatures in the oceans were microfauna (possibly Weng'an biota: *large acanthomorphic acritarchs & soft-bodied discoidal Aspidella*) (Zhu and Li, 2017; Wood et al., 2019). The primary producers' carbon fixation rate is stable due to relatively stable nutrient supply (stable weathering flux). The result is a relatively stable amount of O_2 released and a balanced state of the oxygen level in the seawater and atmosphere.

In this figure (Fig. 8.1), there are two sources (riverine and hydrothermal) of dissolved iron and sulfate. The dominant source is the riverine input. Continental pyrite has been oxidized to trivalent iron (Fe^{3+}), which has been washed into the ocean and changed to bivalent iron (Fe^{2+}) beneath the chemocline. Together with SO_4^{2-} , which is weathered from continental pyrite sources or gypsum deposits, reached the pyrite formation zone (PFZ, shaded in yellow). With the help of microbial sulfate reduction, pyrite has been formed and released oxygen to the exogenic system (Garrels and Lerman, 1984; Shields et al., 2019). The escaped O_2 might increase the O_2 level in the atmosphere, and conversely, the CO_2 level falls, triggering climate cooling. However, a negative feedback linking cooling to decreasing chemical weathering buffers this influence and causes a relatively steady

state. In this period, the SOL (sulfate pool) in the ocean accumulates slowly or remains constantly low.

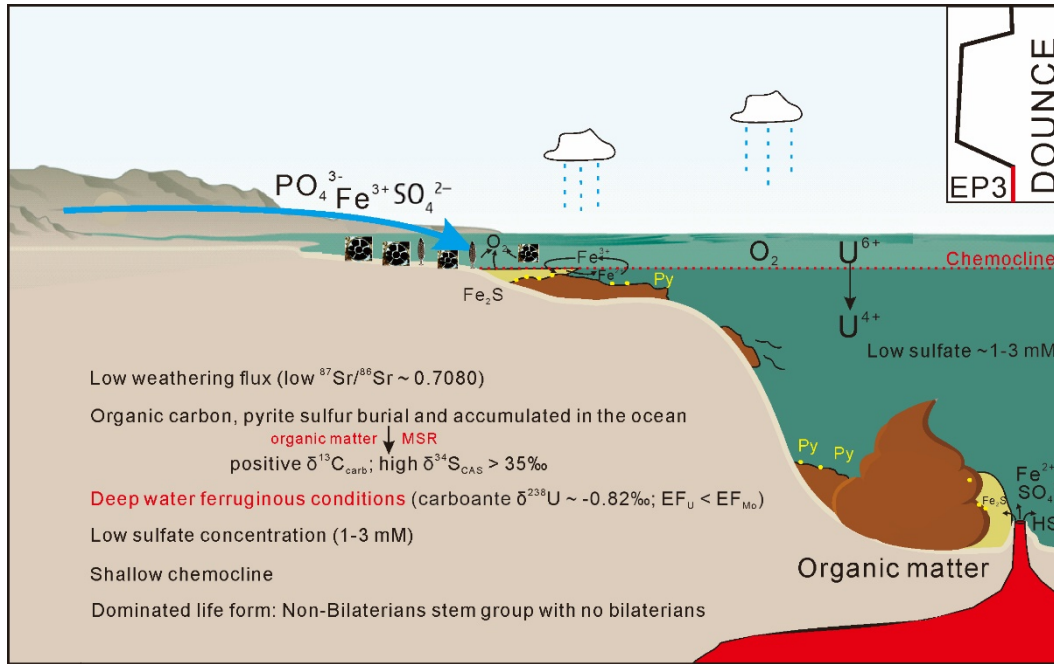


Fig. 8. 1 Conceptual model showing the seawater oxygenation state during the pre-excursion period (EP3). The pyrite formation zone (PFZ) is shaded in yellow.

8.2 Onset Period of the DOUNCE/Shuram (EN4a)

The onset of the DOUNCE/Shuram (EN4a) is the first non-steady-state period during the late Ediacaran. The $\delta^{13}\text{C}_{\text{carb}}$ column in Fig. 8.2 is marked by the dramatic coupled negative shift in carbon isotopes ($\delta^{13}\text{C}_{\text{carb}}$ values decrease to $\sim -10\text{‰}$) and sulfate sulfur isotopes ($\delta^{34}\text{S}_{\text{sulfate}}$ values decrease from $\sim 34\text{‰}$ to 21‰), which is mainly caused by the oxygenation of the huge DOM pool accumulated during EP3 and earlier.

This period lasts around 1.6 Ma and represents a transient whole ocean oxygenation event. The driving force is likely to be the collisional forming of Gondwanaland, which causes two main changes. The first change is the increasing weathering flux (physical and chemical, $^{87}\text{Sr}/^{86}\text{Sr}$ increases from 0.7080 to 0.7090). The increasing riverine input brings enormous nutrients (PO_4^{2-}), iron (Fe^{3+}), sulfate (SO_4^{2-}) into the ocean, resulting in the increase of primary productivity, oxygen release via photosynthesis and pyrite burial, which in turn causes a fall in the chemocline, the oxygenation and shrinking of the DOM pool both in shallow and deep ocean realms. The second one is the increasing degassing rate with high

volcanic activities (Rossetti et al., 2015; Williams et al., 2019). Both the oxygenation of the DOM pool and the increased degassing will cause the total CO₂ in the atmosphere to increase, resulting in a rise in temperature, which in turn increases the chemical weathering rate. However, although increased chemical weathering of silicate rocks draws down CO₂, thus buffering the CO₂ increase, non-steady-state oxidation of the DOM reservoir means that levels did not fall substantially. The increasing O₂ availability in the paleo seawater and the higher ocean temperatures might stimulate the flourishing of Ediacaran biota.

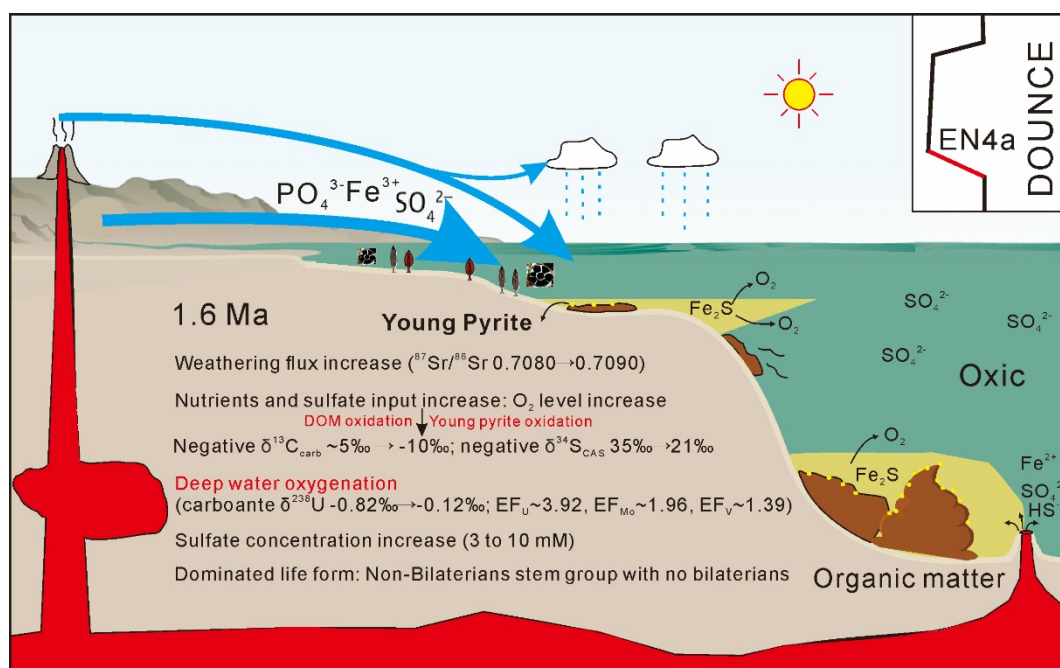


Fig. 8. 2 Conceptual model showing the seawater oxygenation state during the onset period of the DOUNCE/Shuram (EN4a). The pyrite formation zone (PFZ, euxinic) is shaded in yellow. This period lasted around 1.6 Ma in South China.

8.3 During the DOUNCE/Shuram (EN4b)

The EN4b is a steady-state period lasting around 7.3 Ma in South China (Fig. 8.3). During the EN4b, the weathering rate remains constantly high, evidenced by the Sr isotope record ($^{87}\text{Sr}/^{86}\text{Sr}$ ~ 0.7090). The weathering consumption of the CO₂ has reached a balanced state with the increasing CO₂ release through DOM oxidation and degassing, shown by the constant low carbon isotope values. The CO₂ level in the atmosphere possibly reaches a peak, which means that temperatures also reach their highest levels.

The DOM pool stored in the ocean is continuously shrinking during this period. However, compared to EN4a, the increasing of the sulfate concentration in the

seawater increases the MSR activity in deep water and causes an expansion of the deepwater euxinia.

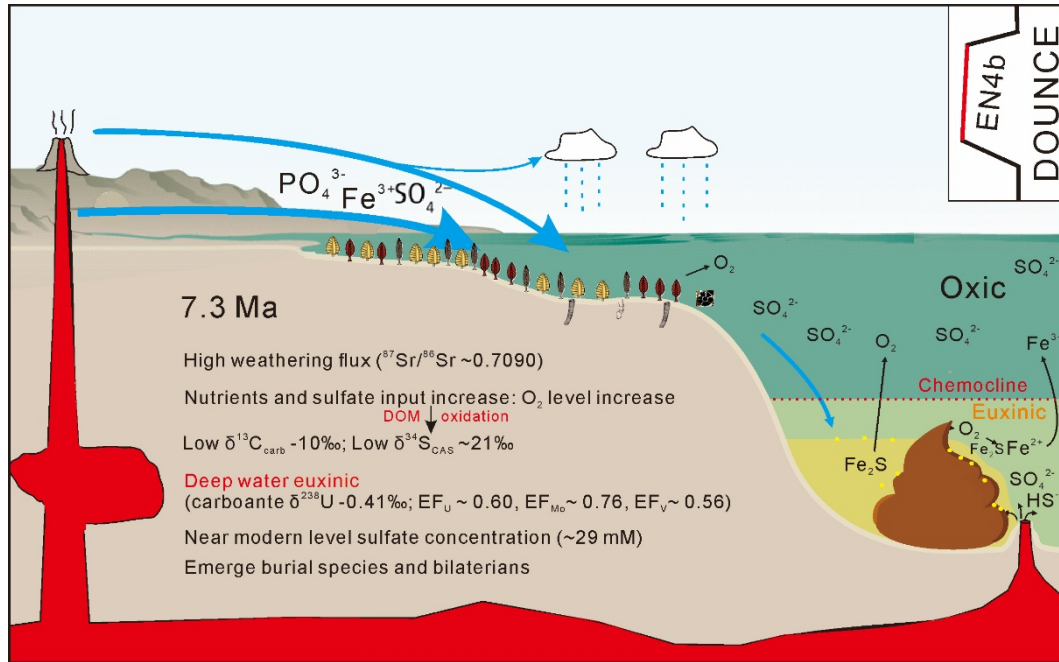


Fig. 8.3 Conceptual model showing the seawater oxygenation state during the DOUNCE/Shuram (EN4b). This period lasted around 7.3 Ma in South China.

8.4 The Recovery Period of the DOUNCE/Shuram (EN4c)

The recovery period of the DOUNCE/Shuram is another non-steady-state period that lasts around 1.1 Ma in South China (Fig. 8.4). The recovery of the carbon isotope values may be driven by decreasing weathering rates, which cut off the nutrient and sulfate supply to the ocean, resulting in a decline in seawater sulfate concentration. The MSR activity in the deep oceans has been suppressed due to low sulfate concentration ($< 3\text{ mM}$). Moreover, most of the DOM in the seawater has nearly been oxidized, which clears the way for the second transient whole ocean oxygenation event together with the recovery of the carbon isotope values and sulfate sulfur isotope values.

The decreasing DOM oxidation, increasing atmospheric oxygen level, and high CO_2 consumption through chemical weathering cause the temperature to decrease during this period, as evidenced by the decrease of CIA values (Chen et al., 2020).

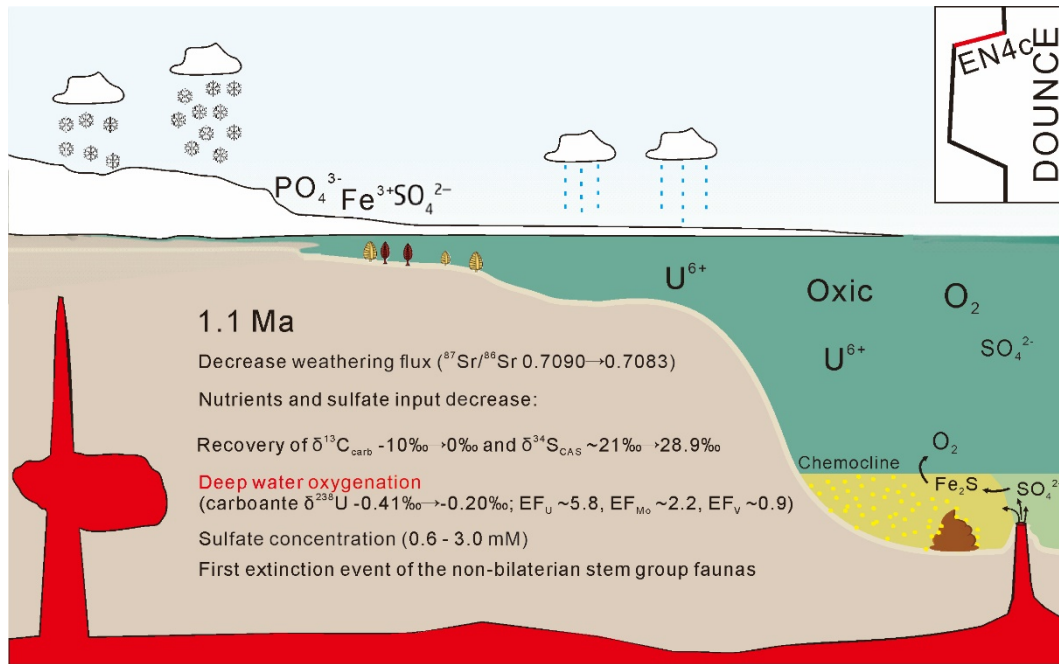


Fig. 8. 4 Conceptual model showing the seawater oxygenation state during the recovery period of the DOUNCE/Shuram (EN4c). This period lasted around 1.1 Ma in South China.

8.5 The DOUNCE/Shuram Aftermath (EP4a)

The carbon isotope value is relatively stable during the DOUNCE/Shuram aftermath (EP4a) (Fig. 8.5). Low sulfate concentration results in increased methanogenesis and methane release on the seafloor (Newton et al., 2011; He et al., 2020), which causes an expansion of anoxic conditions in the seawater and this period lasts for around 3.1 Ma in South China. During this period, the methane that escaped to the atmosphere might have buffered the climate towards higher temperatures.

8.6 The DOUNCE/Shuram Aftermath (EP4b)

This period is characterized by the decoupled C-S trend and lasts for around 3.7 Ma in South China (Fig. 8.6). During the EP4b period, the marine sulfate concentration, RSTE enrichments, and $\delta^{238}U$ values increase, representing the last transient ocean oxygenation event before the Cambrian.

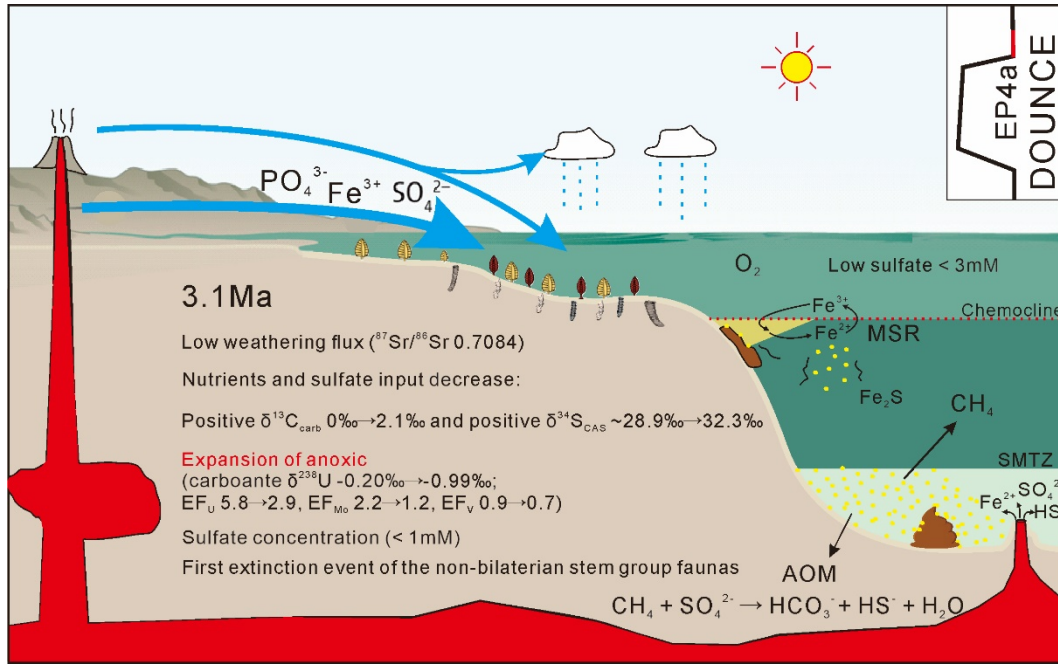


Fig. 8. 5 Conceptual model showing the seawater oxygenation state during the DOUNCE/Shuram aftermath (EP4a). This period lasts around 3.1 Ma in South China and is characterized by coupled C-S trend.

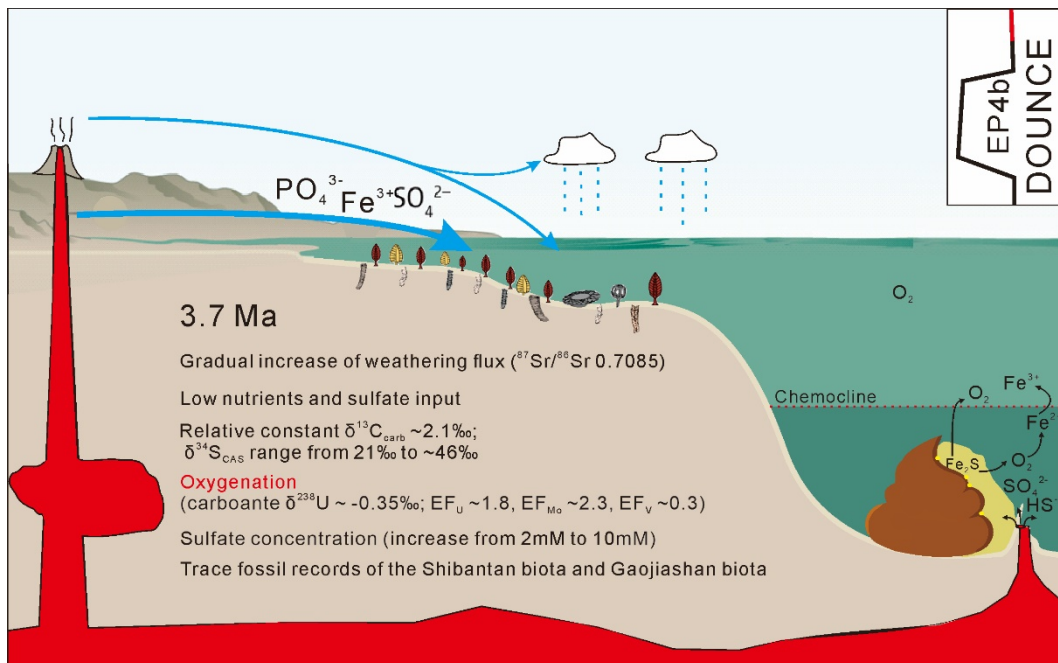


Fig. 8. 6 Conceptual model showing the seawater oxygenation state during the DOUNCE/Shuram aftermath (EP4b). This period lasts around 3.7 Ma in South China and is characterized by the decoupled C-S trend.

Chapter 9 Conclusions and Future Work

9.1 Conclusions

This study presents detailed lithological, stratigraphic, and geochemical (C-S-U) research on three representative carbonate sections covering the late Ediacaran period (~580-541 Ma) in South China. My work reveals a stepwise oxygenation history and further updates our understanding of the relationship between continental weathering history, marine environmental changes, and life evolution during the late Ediacaran. In **Chapter 1**, I put forward several research aims. They are:

- **This study aimed to improve global stratigraphic and chemostratigraphic correlation through the key interval (the DOUNCE/Shuram excursion) of Earth history.**

The field observations and measurements at the Qinglinkou section in the western Huangling Anticline area provide a perfect window to better understand the stratigraphic and chemostratigraphic correlation of the late Ediacaran sections in South China. In **Chapter 3**, my work suggests that the middle carbonate unit between two black shale layers of the upper Doushantuo Formation in the western region of the Huangling Anticline area is a slumped unit that likely derives from the overlying Hamajing Member of the lower Dengying Formation.

In **Chapter 4**, I compared and correlated most sections around the Huangling Anticline area to further address the slide distance and correlation with other sections. I documented that the large-scale slumping is well developed in the western region of the Huangling Anticline area and that the estimated slide distance is ~5-12 km. This study put forward and compared two evolution models of this middle carbonate unit and recovered the chemostratigraphic profiles from other sections in this region. The age framework is presented by comparing the published ages in South China and other global sections.

- **This study also aimed to identify possible global isotopic events and trends through the late Ediacaran.**

In **Chapter 3**, the carbonate carbon isotope profile at the Qinglinkou section further supports the existence of four major negative carbon isotope excursions during the Ediacaran Period. From bottom to top, they are CANCE (down to -4.4‰), WANCE (reached -5.0‰), BAINCE (-0.2‰), and DOUNCE (lowest value is -4.6‰), the last of which is equivalent to the Shuram-Wonoka excursion on a global scale. The DOUNCE in South China shows a gradual decrease to the lowest value in around 1.6 Ma (EN4a). Following that is a relatively steady-state period that lasts around 7.3 Ma (EN4b). The DOUNCE (EN4c) recovery period lasts 1.1 Ma in South China and shows a sharp increase in carbon isotope compositions.

In **Chapter 6**, the CAS sulfur isotope profile shows consistent patterns between the three studied sections. Before the DOUNCE/Shuram (EP3), CAS sulfur isotope values are relatively stable with an average value of 36.3‰. During the onset period of the DOUNCE/Shuram (EN4a), the CAS sulfur $\delta^{34}\text{S}_{\text{CAS}}$ shows a decreasing trend to near modern values (average 21.0‰). The DOUNCE/Shuram recovery period (EN4c) is characterized as a gradually increasing trend of the $\delta^{34}\text{S}_{\text{CAS}}$ to as high as 49.1‰ at the Qinglinkou section. After the DOUNCE/Shuram, $\delta^{34}\text{S}_{\text{CAS}}$ values display an increasing trend during EP4a, followed by a decreasing trend during EP4b. The constantly high CAS sulfur isotope values at the Qinglinkou section (5-10 ‰ higher than the other two sections) might indicate that the Yangtze Gorges area was a semi-restricted basin and that deepwater remained euxinic during the DOUNCE/Shuram interval

- **To improve the existing CAS extraction method and establish a robust protocol for CAS extraction.**

Carbon-associated sulfate is a robust proxy for reconstructing the paleo-seawater sulfate sulfur isotope values. However, contaminations (such as pyrite, organic sulfur, SAS) might overprint the original signal and lower the CAS sulfur isotope values during the extraction process. To eliminate inadvertent contamination and establish a robust protocol for CAS extraction, in **Chapter 5**, I

designed and compared three oxidative CAS leaching methods. My experiments demonstrate that the non-CAS sulfur can lower the measured $\delta^{34}\text{S}_{\text{CAS}}$ value, and a single leach with oxidizing reagents is not enough to remove all the contaminants. Organically bound sulfur can have a significantly different $\delta^{34}\text{S}$ value from coeval pyrite. I recommend that the new sequential NaOCl, H_2O_2 , and NaCl pre-leaching method is better suited to handling pyrite- and organic-rich samples.

- **The fourth and fifth goals were to better our understanding of the carbon and sulfur cycles and the weathering history during the DOUNCE/Shuram Excursion and its aftermath.**

The sulfur and carbon cycles are tightly linked in the marine system. The riverine input and output of carbon and sulfur flux are redox-sensitive, allowing us to trace the paleo-oceanic redox history. In **Chapter 6**, using the refined CAS extraction method, this study provides high-resolution, high-fidelity carbon and CAS sulfur isotopic data from three representative carbonate sections in South China (Lianghong, Sishang, and Qinglinkou sections). The CAS sulfur isotope values from the three selected sections show a coupled trend with the carbon isotope profile during the DOUNCE/Shuram and reached a near modern level ($\sim +21\text{‰}$). After the DOUNCE/Shuram, the CAS sulfur and carbonate carbon isotope show a decoupled trend likely due to a shrinking of the seawater sulfate reservoir. My work reveals the fluctuations of the seawater sulfate concentrations during the late Ediacaran, and the rises and falls of the sulfate concentration are coincidental with the $^{87}\text{Sr}/^{86}\text{Sr}$ ratios profile indicates highly tectonic controls. The estimated sulfate concentration during the DOUNCE/Shuram reaches almost the modern levels ($\sim 29\text{ mM}$) and lasts for at least 4 Ma. After the DOUNCE/Shuram, the decrease of seawater sulfate concentration might end the DOUNCE/Shuram and change the S cycling pathways during the DOUNCE/Shuram aftermath and result in an expansion of deep-water anoxia and decoupled C-S trend. By comparing with other global sections, the DOUNCE CAS sulfur isotope values from South China can be correlated with the Shuram-Wonoka excursion, indicating that the CAS sulfur profile can be used as a chemostratigraphic correlation tool for future studies.

- **Another aim of this thesis is to better our understanding of the oxygenation history during the DOUNCE/Shuram Excursion and its aftermath.**

In our Earth system, oxygen plays an important role in controlling life evolution and mass extinction. The late Ediacaran is remarkable for the extinction of the Ediacaran biota and the beginning of the Cambrian explosion/radiation, which offers a perfect window to understanding the relationship between redox oscillations and life evaluations. In **Chapter 7**, I use combined RSTE (Mo, U, V trace elements) and Uranium isotopes proxies to reveal the ocean oxygenation history during the late Ediacaran. I identified two global ocean oxygenation events during the onset EN4a) and recovery (EN4c) periods of the DOUNCE/Shuram. However, during the DOUNCE/Shuram (EN4b), the ocean oxygen level increased together with an expansion of deepwater euxinic. After the DOUNCE/Shuram, an expansion of anoxia of the deep seawater was followed by a gradual recovery of the oxygen level until the Ediacaran-Cambrian boundary. My work indicates that the further evolution of energetic (muscular) animals was likely delayed due to low oxygen levels before the DOUNCE/Shuram. The oxygenation of large storage of the DOM pool in the ocean causes the coupled negative C-S trend during the DOUNCE/Shuram and buffers the increased extent of the oxygen levels in the ocean. My work further suggests that the global oxygen level of the seawater played a vital role in regulating life evolution.

- **The final goal of this research is to build a conceptual model of paleoenvironmental changes during the DOUNCE/Shuram Excursion and its aftermath, incorporating their relationship with the evolution of life.**

In **Chapter 8**, I presented a conceptual model of the late Ediacaran redox shifts, weathering changes, and geochemical condition changes. I divided the late Ediacaran period into six scenarios, which indicates a stepwise ocean oxygenation history.

9.2 Future Studies

This study has generated a lot of high-quality data. However, due to time limitations and COVID-19 lockdown for nearly one year, I have not had the chance to do modeling as envisaged using the ‘forward’ COPSE model (Bergman et al., 2004; Lenton et al., 2018; Tostevin and Mills, 2020). The next step is to do the biogeochemical models to support my conceptual models and illuminate the connection between seawater sulfate isotope and concentration trends, regional-to-global ocean redox variability, and biological evolution.

I also noticed that there are few reliable constraints on the pyrite S isotope values from the Dengying Formation. With the help of *in situ* nanoSIMS for Dengying framboidal pyrites, we might be able to have better constraints on the sulfur cycling during the DOUNCE/Shuram aftermath and further our understanding of the ‘superheavy pyrite’ problem.

REFERENCES

- Al-Aasm, I.S. and Clarke, J.D., 2004. The effect of hydrothermal fluid flow on early diagenetic dolomitization: an example from the Devonian Slave Point Formation, northwest Alberta, Canada.
- Algeo, T.J., Luo, G.M., Song, H.Y., Lyons, T.W. and Canfield, D.E., 2015. Reconstruction of secular variation in seawater sulfate concentrations. *Biogeosciences*, 12(7): 2131-2151.
- Algeo, T.J. and Tribouillard, N., 2009. Environmental analysis of paleoceanographic systems based on molybdenum–uranium covariation. *Chemical Geology*, 268(3-4): 211-225.
- An, Z., Jiang, G., Tong, J., Tian, L., Ye, Q., Song, H. and Song, H., 2015. Stratigraphic position of the Ediacaran Miaohe biota and its constraints on the age of the upper Doushantuo $\delta^{13}\text{C}$ anomaly in the Yangtze Gorges area, South China. *Precambrian Research*, 271: 243-253.
- Andersen, M.B., Romaniello, S., Vance, D., Little, S.H., Herdman, R. and Lyons, T.W., 2014. A modern framework for the interpretation of $^{238}\text{U}/^{235}\text{U}$ in studies of ancient ocean redox. *Earth and Planetary Science Letters*, 400: 184-194.
- Andersen, M.B., Vance, D., Morford, J.L., Bura-Nakic, E., Breitenbach, S.F.M. and Och, L., 2016. Closing in on the marine U- $^{238}\text{U}/^{235}\text{U}$ budget. *Chemical Geology*, 420: 11-22.
- Ansari, A.H., Pandey, S.K., Kumar, K., Agrawal, S., Ahmad, S. and Shekhar, M., 2020. Palaeoredox link with the late Neoproterozoic–early Cambrian Bilara carbonate deposition, Marwar Supergroup, India. *Carbonates and Evaporites*, 35(2).
- Azmy, K., Kendall, B., Brand, U., Stouge, S. and Gordon, G.W., 2015. Redox conditions across the Cambrian–Ordovician boundary: Elemental and isotopic signatures retained in the GSSP carbonates. *Palaeogeography, Palaeoclimatology, Palaeoecology*, 440: 440-454.
- Banner, J.L. and Hanson, G.N., 1990. Calculation of Simultaneous Isotopic and Trace-Element Variations during Water–Rock Interaction with Applications to Carbonate Diagenesis. *Geochimica Et Cosmochimica Acta*, 54(11): 3123-3137.
- Bao, H., Chen, Z.-Q. and Zhou, C., 2012. An ^{17}O record of late Neoproterozoic glaciation in the Kimberley region, Western Australia. *Precambrian Research*, 216-219: 152-161.
- Bartley, J.K. and Kah, L.C., 2004. Marine carbon reservoir, Corg–Ccarb coupling, and the evolution of the Proterozoic carbon cycle. *Geology*, 32(2).
- Bartley, J.K., Pope, M., Knoll, A.H., Semikhatov, M.A. and Petrov, P., 1998. A Vendian–Cambrian boundary succession from the northwestern margin of the Siberian Platform: stratigraphy, palaeontology, chemostratigraphy and correlation. *Geol Mag*, 135(4): 473-94.
- Basu, A., Sanford, R.A., Johnson, T.M., Lundstrom, C.C. and Löffler, F.E., 2014. Uranium isotopic fractionation factors during U(VI) reduction by bacterial isolates. *Geochimica et Cosmochimica Acta*, 136: 100-113.
- Bergman, N.M., Lenton, T.M. and Watson, A.J., 2004. COPSE: A new model of

- biogeochemical cycling over Phanerozoic time. *American Journal of Science*, 304(5): 397-437.
- Bergmann, K.D., Zentmyer, R.A. and Fischer, W.W., 2011. The stratigraphic expression of a large negative carbon isotope excursion from the Ediacaran Johnnie Formation, Death Valley. *Precambrian Research*, 188(1-4): 45-56.
- Berner, R.A., 1984. Sedimentary Pyrite Formation - an Update. *Geochimica Et Cosmochimica Acta*, 48(4): 605-615.
- Berner, R.A., 1999. A new look at the long-term carbon cycle. *Gsa Today*, 9(11): 1-6.
- Berner, R.A., 2003. The long-term carbon cycle, fossil fuels and atmospheric composition. *Nature*, 426(6964): 323-326.
- Bigeleisen, J., 1996. Nuclear size and shape effects in chemical reactions. Isotope chemistry of the heavy elements. *Journal of the American Chemical Society*, 118(15): 3676-3680.
- Bobrovskiy, I., Hope, J.M., Ivantsov, A., Nettersheim, B.J., Hallmann, C. and Brocks, J.J., 2018. Ancient steroids establish the Ediacaran fossil Dickinsonia as one of the earliest animals. *Science*, 361(6408): 1246-1249.
- Bodin, S., Godet, A., Matera, V., Steinmann, P., Vermeulen, J., Gardin, S., Adatte, T., Coccioni, R. and Föllmi, K.B., 2007. Enrichment of redox-sensitive trace metals (U, V, Mo, As) associated with the late Hauterivian Faraoni oceanic anoxic event. *International Journal of Earth Sciences*, 96(2): 327-341.
- Bontognali, T.R., Sessions, A.L., Allwood, A.C., Fischer, W.W., Grotzinger, J.P., Summons, R.E. and Eiler, J.M., 2012. Sulfur isotopes of organic matter preserved in 3.45-billion-year-old stromatolites reveal microbial metabolism. *Proc Natl Acad Sci U S A*, 109(38): 15146-51.
- Böttcher, M.E., Brumsack, H.J. and Dürselen, C.D., 2007. The isotopic composition of modern seawater sulfate: I. Coastal waters with special regard to the North Sea. *Journal of Marine Systems*, 67(1-2): 73-82.
- Bottrell, S.H. and Newton, R.J., 2006. Reconstruction of changes in global sulfur cycling from marine sulfate isotopes. *Earth-Science Reviews*, 75(1-4): 59-83.
- Bowring, S.A., Grotzinger, J.P., Condon, D.J., Ramezani, J., Newall, M.J. and Allen, P.A., 2007. Geochronologic constraints on the chronostratigraphic framework of the neoproterozoic Huqf Supergroup, Sultanate of Oman. *American Journal of Science*, 307(10): 1097-1145.
- Bowyer, F., Wood, R.A. and Poulton, S.W., 2017. Controls on the evolution of Ediacaran metazoan ecosystems: A redox perspective. *Geobiology*, 15(4): 516-551.
- Bradley, D.C., 2011. Secular trends in the geologic record and the supercontinent cycle. *Earth-Science Reviews*, 108(1-2): 16-33.
- Brand, U. and Veizer, J., 1980. Chemical Diagenesis of a Multicomponent Carbonate System .1. Trace-Elements. *Journal of Sedimentary Petrology*, 50(4): 1219-1236.
- Brasier, M. and Lindsay, J., 1998. A billion years of environmental stability and the emergence of eukaryotes: New data from northern Australia. *Geology*, 26(6): 555-558.
- Brasier, M.D. and Lindsay, J.F., 2000. 4. Did Supercontinental Amalgamation Trigger the "Cambrian Explosion"? The ecology of the Cambrian radiation.

- Columbia University Press, pp. 69-89.
- Brennecke, G.A., Herrmann, A.D., Algeo, T.J. and Anbar, A.D., 2011. Rapid expansion of oceanic anoxia immediately before the end-Permian mass extinction. *Proc Natl Acad Sci U S A*, 108(43): 17631-4.
- Bridger, P., Poulton, S.W., Zhou, Y., Li, C., Zhang, K. and Shields, G.A., 2021. The Ediacaran 'Miaohe Member' of South China: new insights from palaeoredox proxies and stable isotope data. *Geological Magazine*: 1-15.
- Bristow, T.F. and Kennedy, M.J., 2008. Carbon isotope excursions and the oxidant budget of the Ediacaran atmosphere and ocean. *Geology*, 36(11): 863-866.
- Brocks, J.J., Love, G.D., Summons, R.E., Knoll, A.H., Logan, G.A. and Bowden, S.A., 2005. Biomarker evidence for green and purple sulphur bacteria in a stratified Palaeoproterozoic sea. *Nature*, 437(7060): 866-70.
- Brown, S.T., Basu, A., Ding, X., Christensen, J.N. and DePaolo, D.J., 2018. Uranium isotope fractionation by abiotic reductive precipitation. *Proc Natl Acad Sci U S A*, 115(35): 8688-8693.
- Burdett, J.W., Arthur, M.A. and Richardson, M., 1989. A Neogene Seawater Sulfur Isotope Age Curve from Calcareous Pelagic Microfossils. *Earth and Planetary Science Letters*, 94(3-4): 189-198.
- Burnett, W.C., Aggarwal, P.K., Aureli, A., Bokuniewicz, H., Cable, J.E., Charette, M.A., Kontar, E., Krupa, S., Kulkarni, K.M., Loveless, A., Moore, W.S., Oberdorfer, J.A., Oliveira, J., Ozyurt, N., Povinec, P., Privitera, A.M., Rajar, R., Ramessur, R.T., Scholten, J., Stieglitz, T., Taniguchi, M. and Turner, J.V., 2006. Quantifying submarine groundwater discharge in the coastal zone via multiple methods. *Sci Total Environ*, 367(2-3): 498-543.
- Burns, S. and Matter, A., 1993. Carbon isotopic record of the latest Proterozoic from Oman. *Eclogae Geologicae Helvetiae*, 86(2): 595-607.
- Butterfield, N.J., 2007. Macroevolution and macroecology through deep time. *Palaeontology*, 50(1): 41-55.
- Calver, C.R., 2000. Isotope stratigraphy of the Ediacarian (Neoproterozoic III) of the Adelaide Rift Complex, Australia, and the overprint of water column stratification. *Precambrian Research*, 100(1-3): 121-150.
- Canadas, F., Papineau, D., Leng, M.J. and Li, C., 2022. Extensive primary production promoted the recovery of the Ediacaran Shuram excursion. *Nat Commun*, 13(1): 148.
- Canfield, D.E., 2001a. Biogeochemistry of sulfur isotopes. *Stable Isotope Geochemistry*, 43(1): 607-636.
- Canfield, D.E., 2001b. Isotope fractionation by natural populations of sulfate-reducing bacteria. *Geochimica Et Cosmochimica Acta*, 65(7): 1117-1124.
- Canfield, D.E., 2004. The evolution of the Earth surface sulfur reservoir. *American Journal of Science*, 304(10): 839-861.
- Canfield, D.E., 2005. THE EARLY HISTORY OF ATMOSPHERIC OXYGEN: Homage to Robert M. Garrels. *Annual Review of Earth and Planetary Sciences*, 33(1): 1-36.
- Canfield, D.E. and Farquhar, J., 2009. Animal evolution, bioturbation, and the sulfate concentration of the oceans. *Proc Natl Acad Sci U S A*, 106(20): 8123-7.
- Canfield, D.E., Knoll, A.H., Poulton, S.W., Narbonne, G.M. and Dunning, G.R., 2020.

- Carbon isotopes in clastic rocks and the Neoproterozoic carbon cycle. *American Journal of Science*, 320(2): 97-124.
- Canfield, D.E., Poulton, S.W. and Narbonne, G.M., 2007. Late-Neoproterozoic deep-ocean oxygenation and the rise of animal life. *Science*, 315(5808): 92-5.
- Canfield, D.E. and Thamdrup, B., 1994. The production of ^{34}S -depleted sulfide during bacterial disproportionation of elemental sulfur. *Science*, 266(5193): 1973-5.
- Chang, H.-J., Chu, X.-L., Feng, L.-J. and Huang, J., 2012. Progressive oxidation of anoxic and ferruginous deep-water during deposition of the terminal Ediacaran Laobao Formation in South China. *Palaeogeography, Palaeoclimatology, Palaeoecology*, 321-322: 80-87.
- Chen, C. and Feng, Q.L., 2019. Carbonate carbon isotope chemostratigraphy and U-Pb zircon geochronology of the Liuchapo Formation in South China: Constraints on the Ediacaran-Cambrian boundary in deep-water sequences. *Palaeogeography Palaeoclimatology Palaeoecology*, 535.
- Chen, C., Wang, J.S., Wang, Z., Peng, Y.B., Chen, X.H., Ma, X.C., Cen, Y., Zhao, J. and Zhou, P., 2020. Variation of chemical index of alteration (CIA) in the Ediacaran Doushantuo Formation and its environmental implications. *Precambrian Research*, 347.
- Chen, X., Li, D., Ling, H.F. and Jiang, S.Y., 2008. Carbon and sulfur isotopic compositions of basal Datangpo Formation, northeastern Guizhou, South China: Implications for depositional environment. *Progress in Natural Science-Materials International*, 18(4): 421-429.
- Chen, X., Romaniello, S.J., Herrmann, A.D., Hardisty, D., Gill, B.C. and Anbar, A.D., 2018. Diagenetic effects on uranium isotope fractionation in carbonate sediments from the Bahamas. *Geochimica et Cosmochimica Acta*, 237: 294-311.
- Chen, Y.L., Chu, X.L., Zhang, X.L. and Zhai, M.G., 2015. Carbon isotopes, sulfur isotopes, and trace elements of the dolomites from the Dengying Formation in Zhenba area, southern Shaanxi: Implications for shallow water redox conditions during the terminal Ediacaran. *Science China-Earth Sciences*, 58(7): 1107-1122.
- Chen, Z., Zhou, C., Xiao, S., Wang, W., Guan, C., Hua, H. and Yuan, X., 2014. New Ediacara fossils preserved in marine limestone and their ecological implications. *Sci Rep*, 4: 4180.
- Cheng, M., Li, C., Jin, C., Wang, H., Algeo, T.J., Lyons, T.W., Zhang, F. and Anbar, A., 2020. Evidence for high organic carbon export to the early Cambrian seafloor. *Geochimica et Cosmochimica Acta*, 287: 125-140.
- Claypool, G.E., Holser, W.T., Kaplan, I.R., Sakai, H. and Zak, I., 1980. The age curves of sulfur and oxygen isotopes in marine sulfate and their mutual interpretation. *Chemical geology*, 28: 199-260.
- Cleveland, W., Grosse, E. and Shyu, W., 1992. Local regression models In: Chambers S. Hastie JM, Wadsworth TJ (eds.).
- Cleveland, W.S., 1979. Robust locally weighted regression and smoothing scatterplots. *Journal of the American statistical association*, 74(368): 829-836.

- Condon, D., Zhu, M., Bowring, S., Wang, W., Yang, A. and Jin, Y., 2005. U-Pb ages from the neoproterozoic Doushantuo Formation, China. *Science*, 308(5718): 95-8.
- Cox, G.M., Halverson, G.P., Stevenson, R.K., Vokaty, M., Poirier, A., Kunzmann, M., Li, Z.X., Denyszyn, S.W., Strauss, J.V. and Macdonald, F.A., 2016. Continental flood basalt weathering as a trigger for Neoproterozoic Snowball Earth. *Earth and Planetary Science Letters*, 446: 89-99.
- Crockford, P.W., Cowie, B.R., Johnston, D.T., Hoffman, P.F., Sugiyama, I., Pellerin, A., Bui, T.H., Hayles, J., Halverson, G.P., Macdonald, F.A. and Wing, B.A., 2016. Triple oxygen and multiple sulfur isotope constraints on the evolution of the post-Marinoan sulfur cycle. *Earth and Planetary Science Letters*, 435: 74-83.
- Crockford, P.W., Kunzmann, M., Bekker, A., Hayles, J., Bao, H., Halverson, G.P., Peng, Y., Bui, T.H., Cox, G.M., Gibson, T.M., Wörndle, S., Rainbird, R., Lepland, A., Swanson-Hysell, N.L., Master, S., Sreenivas, B., Kuznetsov, A., Krupenik, V. and Wing, B.A., 2019. Claypool continued: Extending the isotopic record of sedimentary sulfate. *Chemical Geology*, 513: 200-225.
- Cui, H., Kaufman, A.J., Xiao, S., Peek, S., Cao, H., Min, X., Cai, Y., Siegel, Z., Liu, X.M., Peng, Y., Schiffbauer, J.D. and Martin, A.J., 2016a. Environmental context for the terminal Ediacaran biomineralization of animals. *Geobiology*, 14(4): 344-63.
- Cui, H., Kaufman, A.J., Xiao, S., Zhou, C. and Liu, X.-M., 2017. Was the Ediacaran Shuram Excursion a globally synchronized early diagenetic event? Insights from methane-derived authigenic carbonates in the uppermost Doushantuo Formation, South China. *Chemical Geology*, 450: 59-80.
- Cui, H., Kaufman, A.J., Xiao, S., Zhu, M., Zhou, C. and Liu, X.-M., 2015. Redox architecture of an Ediacaran ocean margin: Integrated chemostratigraphic ($\delta^{13}\text{C}$ - $\delta^{34}\text{S}$ - $87\text{Sr}/86\text{Sr}$ - Ce/Ce^*) correlation of the Doushantuo Formation, South China. *Chemical Geology*, 405: 48-62.
- Cui, H., Kitajima, K., Spicuzza, M.J., Fournelle, J.H., Denny, A., Ishida, A., Zhang, F.F. and Valley, J.W., 2018. Questioning the biogenicity of Neoproterozoic superheavy pyrite by SIMS. *American Mineralogist*, 103(9): 1362-1400.
- Cui, H., Xiao, S.H., Zhou, C.M., Peng, Y.B., Kaufman, A.J. and Plummer, R.E., 2016b. Phosphogenesis associated with the Shuram Excursion: Petrographic and geochemical observations from the Ediacaran Doushantuo Formation of South China. *Sedimentary Geology*, 341: 134-146.
- Cunningham, J.A., Vargas, K., Yin, Z.J., Bengtson, S. and Donoghue, P.C.J., 2017. The Weng'an Biota (Doushantuo Formation): an Ediacaran window on soft-bodied and multicellular microorganisms. *Journal of the Geological Society*, 174(5): 793-802.
- Dahl, T.W., Boyle, R.A., Canfield, D.E., Connelly, J.N., Gill, B.C., Lenton, T.M. and Bizzarro, M., 2014. Uranium isotopes distinguish two geochemically distinct stages during the later Cambrian SPICE event. *Earth Planet Sci Lett*, 401: 313-326.
- Dahl, T.W., Connelly, J.N., Li, D., Kouchinsky, A., Gill, B.C., Porter, S., Maloof, A.C. and Bizzarro, M., 2019. Atmosphere-ocean oxygen and productivity dynamics during early animal radiations. *Proc Natl Acad Sci U S A*, 116(39): 19352-

19361.

- Derry, L., Brasier, M., Corfield, R.e.a., Rozanov, A.Y. and Zhuravlev, A.Y., 1994. Sr and C isotopes in Lower Cambrian carbonates from the Siberian craton: a paleoenvironmental record during the 'Cambrian explosion'. *Earth and Planetary Science Letters*, 128(3-4): 671-681.
- Derry, L.A., 2010. A burial diagenesis origin for the Ediacaran Shuram-Wonoka carbon isotope anomaly. *Earth and Planetary Science Letters*, 294(1-2): 152-162.
- Donnadieu, Y., Godd  ris, Y., Ramstein, G., N  d  lec, A. and Meert, J., 2004. A 'snowball Earth' climate triggered by continental break-up through changes in runoff. *Nature*, 428(6980): 303-306.
- Duda, J.P., Blumenberg, M., Thiel, V., Simon, K., Zhu, M.Y. and Reitner, J., 2014. Geobiology of a palaeoecosystem with Ediacara-type fossils: The Shibantan Member (Dengying Formation, South China). *Precambrian Research*, 255: 48-62.
- Edwards, C.T., Fike, D.A. and Saltzman, M.R., 2019. Testing carbonate-associated sulfate (CAS) extraction methods for sulfur isotope stratigraphy: A case study of a Lower-Middle Ordovician carbonate succession, Shingle Pass, Nevada, USA. *Chemical Geology*, 529.
- Elrick, M., Polyak, V., Algeo, T.J., Romaniello, S., Asmerom, Y., Herrmann, A.D., Anbar, A.D., Zhao, L. and Chen, Z.-Q., 2017. Global-ocean redox variation during the middle-late Permian through Early Triassic based on uranium isotope and Th/U trends of marine carbonates. *Geology*, 45(2): 163-166.
- Emerson, S.R. and Huested, S.S., 1991. Ocean anoxia and the concentrations of molybdenum and vanadium in seawater. *Marine Chemistry*, 34(3-4): 177-196.
- Farquhar, G.D., Ehleringer, J.R. and Hubick, K.T., 1989. Carbon isotope discrimination and photosynthesis. *Annual review of plant biology*, 40(1): 503-537.
- Fichtner, V., Strauss, H., Immenhauser, A., Buhl, D., Neuser, R.D. and Niedermayr, A., 2017. Diagenesis of carbonate associated sulfate. *Chemical Geology*, 463: 61-75.
- Fike, D.A., Bradley, A.S. and Rose, C.V., 2015. Rethinking the Ancient Sulfur Cycle. *Annual Review of Earth and Planetary Sciences*, Vol 43, 43(1): 593-622.
- Fike, D.A. and Grotzinger, J.P., 2008. A paired sulfate-pyrite $\delta^{34}\text{S}$ approach to understanding the evolution of the Ediacaran-Cambrian sulfur cycle. *Geochimica et Cosmochimica Acta*, 72(11): 2636-2648.
- Fike, D.A., Grotzinger, J.P., Pratt, L.M. and Summons, R.E., 2006. Oxidation of the Ediacaran ocean. *Nature*, 444(7120): 744-7.
- Gamper, A., Struck, U., Ohnem  ller, F., Heubeck, C. and Hohl, S., 2015. Chemo- and biostratigraphy of the Gaojiashan section (northern Yangtze platform, South China): a new Pc-C boundary section. *Fossil Record*, 18(2): 105-117.
- Garrels, R.M. and Lerman, A., 1984. Coupling of the Sedimentary Sulfur and Carbon Cycles - an Improved Model. *American Journal of Science*, 284(9): 989-1007.
- Gernon, T.M., Hincks, T.K., Tyrrell, T., Rohling, E.J. and Palmer, M.R., 2016. Snowball Earth ocean chemistry driven by extensive ridge volcanism during Rodinia

- breakup. *Nature Geoscience*, 9(3): 242-U83.
- Gill, B.C., Lyons, T.W. and Jenkyns, H.C., 2011a. A global perturbation to the sulfur cycle during the Toarcian Oceanic Anoxic Event. *Earth and Planetary Science Letters*, 312(3-4): 484-496.
- Gill, B.C., Lyons, T.W., Young, S.A., Kump, L.R., Knoll, A.H. and Saltzman, M.R., 2011b. Geochemical evidence for widespread euxinia in the later Cambrian ocean. *Nature*, 469(7328): 80-3.
- Glaessner, M.F., 1985. *The dawn of animal life: a biohistorical study*. CUP Archive.
- Goldberg, T., Poulton, S. and Strauss, H., 2005a. Sulphur and oxygen isotope signatures of late Neoproterozoic to early Cambrian sulphate, Yangtze Platform, China: Diagenetic constraints and seawater evolution. *Precambrian Research*, 137(3-4): 223-241.
- Goldberg, T., Poulton, S.W. and Strauss, H., 2005b. Sulphur and oxygen isotope signatures of late Neoproterozoic to early Cambrian sulphate, Yangtze Platform, China: diagenetic constraints and seawater evolution. *Precambrian Research*, 137(3-4): 223-241.
- Gomes, M.L. and Hurtgen, M.T., 2015. Sulfur isotope fractionation in modern euxinic systems: Implications for paleoenvironmental reconstructions of paired sulfate-sulfide isotope records. *Geochimica Et Cosmochimica Acta*, 157: 39-55.
- Gómez-Peral, L.E., Arrouy, M.J., Poiré, D.G. and Cavarozzi, C.E., 2019. Redox-sensitive trace element distribution in the Loma Negra Formation in Argentina: The record of an Ediacaran oxygenation event. *Precambrian Research*, 332.
- Gong, Z., Kodama, K.P. and Li, Y.X., 2017. Rock magnetic cyclostratigraphy of the Doushantuo Formation, South China and its implications for the duration of the Shuram carbon isotope excursion. *Precambrian Research*, 289: 62-74.
- Gorjan, P., Veevers, J. and Walter, M., 2000. Neoproterozoic sulfur-isotope variation in Australia and global implications. *Precambrian Research*, 100(1-3): 151-179.
- Graham, U.M. and Ohmoto, H., 1994. Experimental-Study of Formation Mechanisms of Hydrothermal Pyrite. *Geochimica Et Cosmochimica Acta*, 58(10): 2187-2202.
- Grotzinger, J.P., Bowring, S.A., Saylor, B.Z. and Kaufman, A.J., 1995. Biostratigraphic and geochronologic constraints on early animal evolution. *Science*, 270(5236): 598-604.
- Grotzinger, J.P., Fike, D.A. and Fischer, W.W., 2011. Enigmatic origin of the largest-known carbon isotope excursion in Earth's history. *Nature Geoscience*, 4(5): 285-292.
- Guo, H., Du, Y.S., Kah, L.C., Hu, C.Y., Huang, J.H., Huang, H., Yu, W.C. and Song, H.Y., 2015. Sulfur isotope composition of carbonate-associated sulfate from the Mesoproterozoic Jixian Group, North China: Implications for the marine sulfur cycle. *Precambrian Research*, 266: 319-336.
- Guo, Q.J., Strauss, H., Zhu, M.Y., Zhang, J.M., Yang, X.L., Lu, M. and Zhao, F.C., 2013. High resolution organic carbon isotope stratigraphy from a slope to basinal setting on the Yangtze Platform, South China: Implications for the

- Ediacaran-Cambrian transition. *Precambrian Research*, 225: 209-217.
- Hardisty, D.S., Lu, Z., Bekker, A., Diamond, C.W., Gill, B.C., Jiang, G., Kah, L.C., Knoll, A.H., Loyd, S.J., Osburn, M.R., Planavsky, N.J., Wang, C., Zhou, X. and Lyons, T.W., 2017. Perspectives on Proterozoic surface ocean redox from iodine contents in ancient and recent carbonate. *Earth and Planetary Science Letters*, 463: 159-170.
- Hawkins, A.D., Xiao, S.H., Jiang, G., Wang, X.Q. and Shi, X.Y., 2017. New biostratigraphic and chemostratigraphic data from the Ediacaran Doushantuo Formation in intra-shelf and upper slope facies of the Yangtze platform: Implications for biozonation of acanthomorphic acritarchs in South China. *Precambrian Research*, 300: 28-39.
- He, T., Dal Corso, J., Newton, R.J., Wignall, P.B., Mills, B.J.W., Todaro, S., Di Stefano, P., Turner, E.C., Jamieson, R.A., Randazzo, V., Rigo, M., Jones, R.E. and Dunhill, A.M., 2020. An enormous sulfur isotope excursion indicates marine anoxia during the end-Triassic mass extinction. *Sci Adv*, 6(37): eabb6704.
- He, T., Zhu, M., Mills, B.J.W., Wynn, P.M., Zhuravlev, A.Y., Tostevin, R., Pogge von Strandmann, P.A.E., Yang, A., Poulton, S.W. and Shields, G.A., 2019. Possible links between extreme oxygen perturbations and the Cambrian radiation of animals. *Nat Geosci*, 12(6): 468-474.
- Hoefs, J., 2015. *Stable Isotope Geochemistry*. Springer.
- Hoffman, P.F., Abbot, D.S., Ashkenazy, Y., Benn, D.I., Brocks, J.J., Cohen, P.A., Cox, G.M., Creveling, J.R., Donnadieu, Y., Erwin, D.H., Fairchild, I.J., Ferreira, D., Goodman, J.C., Halverson, G.P., Jansen, M.F., Le Hir, G., Love, G.D., Macdonald, F.A., Maloof, A.C., Partin, C.A., Ramstein, G., Rose, B.E.J., Rose, C.V., Sadler, P.M., Tziperman, E., Voigt, A. and Warren, S.G., 2017. Snowball Earth climate dynamics and Cryogenian geology-geobiology. *Sci Adv*, 3(11): e1600983.
- Hohl, S.V., Becker, H., Herzlieb, S. and Guo, Q.J., 2015. Multiproxy constraints on alteration and primary compositions of Ediacaran deep-water carbonate rocks, Yangtze Platform, South China. *Geochimica Et Cosmochimica Acta*, 163: 262-278.
- Holland, H.D., 2002. Volcanic gases, black smokers, and the Great Oxidation Event. *Geochimica et Cosmochimica Acta*, 66(21): 3811-3826.
- Holland, H.D., 2006. The oxygenation of the atmosphere and oceans. *Philos Trans R Soc Lond B Biol Sci*, 361(1470): 903-15.
- Horwitz, E.P., Dietz, M.L., Chiarizia, R., Diamond, H., Essling, A.M. and Graczyk, D., 1992. Separation and preconcentration of uranium from acidic media by extraction chromatography. *Analytica Chimica Acta*, 266(1): 25-37.
- Hough, M., Shields, G., Evins, L., Strauss, H., Henderson, R. and Mackenzie, S., 2006. A major sulphur isotope event at c. 510 Ma: a possible anoxia-extinction-volcanism connection during the Early-Middle Cambrian transition? *Terra Nova*, 18(4): 257-263.
- Howarth, R.J. and McArthur, J.M., 1997. Statistics for strontium isotope stratigraphy: a robust LOWESS fit to the marine Sr-isotope curve for 0 to 206 Ma, with look-up table for derivation of numeric age. *The Journal of Geology*, 105(4): 441-456.

- Huang, T., Chen, D., Ding, Y., Zhou, X. and Zhang, G., 2020. SIMS U-Pb zircon geochronological and carbon isotope chemostratigraphic constraints on the Ediacaran-Cambrian boundary succession in the Three Gorges Area, South China. *Journal of Earth Science*, 31(1): 69-78.
- Hulston, J. and Thode, H., 1965. Variations in the S33, S34, and S36 contents of meteorites and their relation to chemical and nuclear effects. *Journal of Geophysical Research*, 70(14): 3475-3484.
- Hurtgen, M.T., Arthur, M.A. and Halverson, G.P., 2005. Neoproterozoic sulfur isotopes, the evolution of microbial sulfur species, and the burial efficiency of sulfide as sedimentary pyrite. *Geology*, 33(1).
- Hurtgen, M.T., Arthur, M.A., Suits, N.S. and Kaufman, A.J., 2002. The sulfur isotopic composition of Neoproterozoic seawater sulfate: implications for a snowball Earth? *Earth and Planetary Science Letters*, 203(1): 413-429(1): 413-429.
- Hurtgen, M.T., Pruss, S.B. and Knoll, A.H., 2009. Evaluating the relationship between the carbon and sulfur cycles in the later Cambrian ocean: An example from the Port au Port Group, western Newfoundland, Canada. *Earth and Planetary Science Letters*, 281(3-4): 288-297.
- Ireland, T.R., Flottmann, T., Fanning, C.M., Gibson, G.M. and Preiss, W.V., 1998. Development of the early Paleozoic Pacific margin of Gondwana from detrital-zircon ages across the Delamerian orogen. *Geology*, 26(3): 243-246.
- Ishikawa, T., Ueno, Y., Komiya, T., Sawaki, Y., Han, J., Shu, D.G., Li, Y., Maruyama, S. and Yoshida, N., 2008. Carbon isotope chemostratigraphy of a Precambrian/Cambrian boundary section in the Three Gorge area, South China: Prominent global-scale isotope excursions just before the Cambrian Explosion. *Gondwana Research*, 14(1-2): 193-208.
- Izon, G., Zerkle, A.L., Zhelezinskaia, I., Farquhar, J., Newton, R.J., Poulton, S.W., Eigenbrode, J.L. and Claire, M.W., 2015. Multiple oscillations in Neoproterozoic atmospheric chemistry. *Earth and Planetary Science Letters*, 431: 264-273.
- Jansyn, J., 1990. Strato-tectonic evolution of a large subsidence structure associated with the late Proterozoic Wonoka Formation at Wilpena Pound, central Flinders Ranges, South Australia.
- Jiang, G., Kaufman, A.J., Christie-Blick, N., Zhang, S. and Wu, H., 2007. Carbon isotope variability across the Ediacaran Yangtze platform in South China: Implications for a large surface-to-deep ocean $\delta^{13}\text{C}$ gradient. *Earth and Planetary Science Letters*, 261(1-2): 303-320.
- Jiang, G., Kennedy, M.J. and Christie-Blick, N., 2003. Stable isotopic evidence for methane seeps in Neoproterozoic postglacial cap carbonates. *Nature*, 426(6968): 822-6.
- Jiang, G., Shi, X., Zhang, S., Wang, Y. and Xiao, S., 2011. Stratigraphy and paleogeography of the Ediacaran Doushantuo Formation (ca. 635–551Ma) in South China. *Gondwana Research*, 19(4): 831-849.
- Kah, L.C., Lyons, T.W. and Frank, T.D., 2004. Low marine sulphate and protracted oxygenation of the Proterozoic biosphere. *Nature*, 431(7010): 834-8.
- Kampschulte, A. and Strauss, H., 1998. The isotopic composition of trace sulphates in Paleozoic biogenic carbonates: implications for coeval seawater and geochemical cycles. *Mineralogical Magazine*, 62(2): 744-745.

- Kampschulte, A. and Strauss, H., 2004. The sulfur isotopic evolution of Phanerozoic seawater based on the analysis of structurally substituted sulfate in carbonates. *Chemical Geology*, 204(3-4): 255-286.
- Kaufman, A.J., Corsetti, F.A. and Varni, M.A., 2007. The effect of rising atmospheric oxygen on carbon and sulfur isotope anomalies in the Neoproterozoic Johnnie Formation, Death Valley, USA. *Chemical Geology*, 237(1-2): 47-63.
- Kaufman, A.J. and Knoll, A.H., 1995. Neoproterozoic variations in the C-isotopic composition of seawater: stratigraphic and biogeochemical implications. *Precambrian Res*, 73(1-4): 27-49.
- Keith, M. and Weber, J., 1964. Carbon and oxygen isotopic composition of selected limestones and fossils. 28(10-11): 1787-1816.
- Kendall, B., Komiya, T., Lyons, T.W., Bates, S.M., Gordon, G.W., Romaniello, S.J., Jiang, G.Q., Creaser, R.A., Xiao, S.H., McFadden, K., Sawaki, Y., Tahata, M., Shu, D.G., Han, J., Li, Y., Chu, X.L. and Anbar, A.D., 2015. Uranium and molybdenum isotope evidence for an episode of widespread ocean oxygenation during the late Ediacaran Period. *Geochimica Et Cosmochimica Acta*, 156: 173-193.
- Kendall, C. and Caldwell, E.A., 1998. Fundamentals of isotope geochemistry, Isotope tracers in catchment hydrology. Elsevier, pp. 51-86.
- Khan, S., Majumder, T., Patranabis-Deb, S. and Saha, D., 2020. Deformation Structures in a Large Slump Horizon, Paleoproterozoic Vempalle Formation, Cuddapah Basin, Southern India. *The Journal of Geology*, 128(6): 517-534.
- Knoll, A., Hayes, J., Kaufman, A., Swett, K. and Lambert, I., 1986. Secular variation in carbon isotope ratios from Upper Proterozoic successions of Svalbard and East Greenland. *Nature*, 321(6073): 832-838.
- Knoll, A.H., 2003. The geological consequences of evolution. *Geobiology*, 1(1): 3-14.
- Kump, L.R. and Arthur, M.A., 1999. Interpreting carbon-isotope excursions: carbonates and organic matter. *Chemical Geology*, 161(1-3): 181-198.
- Kurzweil, F., Claire, M., Thomazo, C., Peters, M., Hannington, M. and Strauss, H., 2013. Atmospheric sulfur rearrangement 2.7 billion years ago: Evidence for oxygenic photosynthesis. *Earth and Planetary Science Letters*, 366: 17-26.
- Lan, Z., Sano, Y., Yahagi, T., Tanaka, K., Shirai, K., Papineau, D., Sawaki, Y., Ohno, T., Abe, M., Yang, H., Liu, H., Jiang, T. and Wang, T., 2019. An integrated chemostratigraphic ($\delta^{13}\text{C}$ - $\delta^{18}\text{O}$ - $^{87}\text{Sr}/^{86}\text{Sr}$ - $\delta^{15}\text{N}$) study of the Doushantuo Formation in western Hubei Province, South China. *Precambrian Research*, 320: 232-252.
- Lang, X., Shen, B., Peng, Y., Xiao, S., Zhou, C., Bao, H., Kaufman, A.J., Huang, K., Crockford, P.W., Liu, Y., Tang, W. and Ma, H., 2018. Transient marine euxinia at the end of the terminal Cryogenian glaciation. *Nat Commun*, 9(1): 3019.
- Lau, K.V., Macdonald, F.A., Maher, K. and Payne, J.L., 2017. Uranium isotope evidence for temporary ocean oxygenation in the aftermath of the Sturtian Snowball Earth. *Earth and Planetary Science Letters*, 458: 282-292.
- Lau, K.V., Maher, K., Altiner, D., Kelley, B.M., Kump, L.R., Lehrmann, D.J., Silva-Tamayo, J.C., Weaver, K.L., Yu, M. and Payne, J.L., 2016. Marine anoxia and delayed Earth system recovery after the end-Permian extinction. *Proc Natl Acad Sci U S A*, 113(9): 2360-5.
- Lau, K.V., Romaniello, S.J. and Zhang, F., 2019. The Uranium Isotope Paleoredox

Proxy.

- Le Guerroue, E., 2006. Sedimentology and Chemostratigraphy of the Ediacaran Shuram Formation, Nafun Group, Oman, Eidgenössische Technische Hochschule Zürich (ETHZ).
- Lee, C., Love, G.D., Fischer, W.W., Grotzinger, J.P. and Halverson, G.P., 2015. Marine organic matter cycling during the Ediacaran Shuram excursion. *Geology*, 43(12): 1103-1106.
- Lenton, T.M., Boyle, R.A., Poulton, S.W., Shields-Zhou, G.A. and Butterfield, N.J., 2014. Co-evolution of eukaryotes and ocean oxygenation in the Neoproterozoic era. *Nature Geoscience*, 7(4): 257-265.
- Lenton, T.M., Daine, S.J. and Mills, B.J.W., 2018. COPSE reloaded: An improved model of biogeochemical cycling over Phanerozoic time. *Earth-Science Reviews*, 178: 1-28.
- Lewis, K., 1971. Slumping on a continental slope inclined at 1–4. *Sedimentology*, 16(1-2): 97-110.
- Li, C., Hardisty, D.S., Luo, G., Huang, J., Algeo, T.J., Cheng, M., Shi, W., An, Z., Tong, J., Xie, S., Jiao, N. and Lyons, T.W., 2017. Uncovering the spatial heterogeneity of Ediacaran carbon cycling. *Geobiology*, 15(2): 211-224.
- Li, C., Love, G.D., Lyons, T.W., Fike, D.A., Sessions, A.L. and Chu, X., 2010. A stratified redox model for the Ediacaran ocean. *Science*, 328(5974): 80-3.
- Li, C., Planavsky, N.J., Shi, W., Zhang, Z., Zhou, C., Cheng, M., Tarhan, L.G., Luo, G. and Xie, S., 2015. Ediacaran Marine Redox Heterogeneity and Early Animal Ecosystems. *Sci Rep*, 5: 17097.
- Li, D., Ling, H.F., Shields-Zhou, G.A., Chen, X., Cremonese, L., Och, L., Thirlwall, M. and Manning, C.J., 2013a. Carbon and strontium isotope evolution of seawater across the Ediacaran-Cambrian transition: Evidence from the Xiaotan section, NE Yunnan, South China. *Precambrian Research*, 225: 128-147.
- Li, Z., Cao, M., Loyd, S.J., Algeo, T.J., Zhao, H., Wang, X., Zhao, L. and Chen, Z.-Q., 2020. Transient and stepwise ocean oxygenation during the late Ediacaran Shuram Excursion: Insights from carbonate $\delta^{238}\text{U}$ of northwestern Mexico. *Precambrian Research*, 344.
- Li, Z.X., Bogdanova, S.V., Collins, A.S., Davidson, A., De Waele, B., Ernst, R.E., Fitzsimons, I.C.W., Fuck, R.A., Gladkochub, D.P., Jacobs, J., Karlstrom, K.E., Lu, S., Natapov, L.M., Pease, V., Pisarevsky, S.A., Thrane, K. and Vernikovskiy, V., 2008. Assembly, configuration, and break-up history of Rodinia: A synthesis. *Precambrian Research*, 160(1-2): 179-210.
- Li, Z.X., Evans, D.A.D. and Halverson, G.P., 2013b. Neoproterozoic glaciations in a revised global palaeogeography from the breakup of Rodinia to the assembly of Gondwanaland. *Sedimentary Geology*, 294: 219-232.
- Li, Z.X., Evans, D.A.D. and Zhang, S., 2004. A 90° spin on Rodinia: possible causal links between the Neoproterozoic supercontinent, superplume, true polar wander and low-latitude glaciation. *Earth and Planetary Science Letters*, 220(3-4): 409-421.
- Li, Z.X. and Powell, C.M., 2001. An outline of the palaeogeographic evolution of the Australasian region since the beginning of the Neoproterozoic. *Earth-*

- Science Reviews, 53(3-4): 237-277.
- Ling, H.F., Chen, X., Li, D., Wang, D., Shields-Zhou, G.A. and Zhu, M.Y., 2013. Cerium anomaly variations in Ediacaran-earliest Cambrian carbonates from the Yangtze Gorges area, South China: Implications for oxygenation of coeval shallow seawater. *Precambrian Research*, 225: 110-127.
- Linnemann, U., Ovtcharova, M., Schaltegger, U., Gartner, A., Hautmann, M., Geyer, G., Vickers-Rich, P., Rich, T., Plessen, B., Hofmann, M., Zieger, J., Krause, R., Kriesfeld, L. and Smith, J., 2019. New high-resolution age data from the Ediacaran-Cambrian boundary indicate rapid, ecologically driven onset of the Cambrian explosion. *Terra Nova*, 31(1): 49-58.
- Liu, P.J., Yin, C.Y., Chen, S.M., Tang, F. and Gao, L.Z., 2013. The biostratigraphic succession of acanthomorphic acritarchs of the Ediacaran Doushantuo Formation in the Yangtze Gorges area, South China and its biostratigraphic correlation with Australia. *Precambrian Research*, 225: 29-43.
- Lomans, B., Van der Drift, C., Pol, A. and Den Camp, H.O., 2002. Microbial cycling of volatile organic sulfur compounds. *Cellular and Molecular Life Sciences CMLS*, 59(4): 575-588.
- Loyd, S.J., Berelson, W.M., Lyons, T.W., Hammond, D.E. and Corsetti, F.A., 2012. Constraining pathways of microbial mediation for carbonate concretions of the Miocene Monterey Formation using carbonate-associated sulfate. *Geochimica Et Cosmochimica Acta*, 78: 77-98.
- Lu, M., Zhu, M.Y., Zhang, J.M., Shields-Zhou, G., Li, G.X., Zhao, F.C., Zhao, X. and Zhao, M.J., 2013. The DOUNCE event at the top of the Ediacaran Doushantuo Formation, South China: Broad stratigraphic occurrence and non-diagenetic origin. *Precambrian Research*, 225: 86-109.
- Lyons, T.W., Reinhard, C.T. and Planavsky, N.J., 2014. The rise of oxygen in Earth's early ocean and atmosphere. *Nature*, 506(7488): 307-15.
- Lyu, Z.Y., Zhang, L., Algeo, T.J., Zhao, L.S., Chen, Z.Q., Li, C., Ma, B.A. and Ye, F.H., 2019. Global-ocean circulation changes during the Smithian-Spathian transition inferred from carbon-sulfur cycle records. *Earth-Science Reviews*, 195: 114-132.
- Macdonald, F.A., Pruss, S.B. and Strauss, J.V., 2015. Trace Fossils with Spreiten from the Late Ediacaran Nama Group, Namibia: Complex Feeding Patterns Five Million Years Before the Precambrian-Cambrian Boundary. *Journal of Paleontology*, 88(2): 299-308.
- Machel, H.G., 2001. Bacterial and thermochemical sulfate reduction in diagenetic settings—old and new insights. *Sedimentary Geology*, 140(1-2): 143-175.
- Machel, H.G. and Buschkuehle, B.E., 2008. Diagenesis of the Devonian Southesk-Cairn Carbonate Complex, Alberta, Canada: marine cementation, burial dolomitization, thermochemical sulfate reduction, anhydritization, and squeegee fluid flow. *Journal of Sedimentary Research*, 78(5): 366-389.
- Marenco, P.J., Corsetti, F.A., Hammond, D.E., Kaufman, A.J. and Bottjer, D.J., 2008a. Oxidation of pyrite during extraction of carbonate associated sulfate. *Chemical Geology*, 247(1-2): 124-132.
- Marenco, P.J., Corsetti, F.A., Kaufman, A.J. and Bottjer, D.J., 2008b. Environmental and diagenetic variations in carbonate associated sulfate: An investigation of

- CAS in the Lower Triassic of the western USA. *Geochimica Et Cosmochimica Acta*, 72(6): 1570-1582.
- Martin, M.W., Grazhdankin, D.V., Bowring, S.A., Evans, D.A., Fedonkin, M.A. and Kirschvink, J.L., 2000. Age of Neoproterozoic bilaterian body and trace fossils, White Sea, Russia: implications for metazoan evolution. *Science*, 288(5467): 841-5.
- Matthews, J.J., Liu, A.G., Yang, C., McIlroy, D., Levell, B. and Condon, D.J., 2020. A Chronostratigraphic Framework for the Rise of the Ediacaran Macrobiota: New Constraints from Mistaken Point Ecological Reserve, Newfoundland. *GSA Bulletin*, 133(3-4): 612-624.
- McArthur, J.M., Howarth, R. and Bailey, T., 2001. Strontium isotope stratigraphy: LOWESS version 3: best fit to the marine Sr-isotope curve for 0–509 Ma and accompanying look-up table for deriving numerical age. *The Journal of Geology*, 109(2): 155-170.
- McFadden, K.A., Huang, J., Chu, X., Jiang, G., Kaufman, A.J., Zhou, C., Yuan, X. and Xiao, S., 2008. Pulsed oxidation and biological evolution in the Ediacaran Doushantuo Formation. *Proc Natl Acad Sci U S A*, 105(9): 3197-202.
- McLennan, S.M., 2001. Relationships between the trace element composition of sedimentary rocks and upper continental crust. *Geochemistry, Geophysics, Geosystems*, 2(4).
- Meysman, F.J., Middelburg, J.J. and Heip, C.H., 2006. Bioturbation: a fresh look at Darwin's last idea. *Trends in Ecology & Evolution*, 21(12): 688-695.
- Minguez, D. and Kodama, K.P., 2017. Rock magnetic chronostratigraphy of the Shuram carbon isotope excursion: Wonoka Formation, Australia. *Geology*, 45(6): 567-570.
- Minguez, D., Kodama, K.P. and Hillhouse, J.W., 2015. Paleomagnetic and cyclostratigraphic constraints on the synchronicity and duration of the Shuram carbon isotope excursion, Johnnie Formation, Death Valley Region, CA. *Precambrian Research*, 266: 395-408.
- Misi, A. and Veizer, J., 1998. Neoproterozoic carbonate sequences of the Una Group, Irecê Basin, Brazil: chemostratigraphy, age and correlations. *Precambrian Research*, 89(1-2): 87-100.
- Mukherjee, I., Large, R.R., Corkrey, R. and Danyushevsky, L.V., 2018. The Boring Billion, a slingshot for Complex Life on Earth. *Sci Rep*, 8(1): 4432.
- Narbonne, G.M., 2011. EVOLUTIONARY BIOLOGY When life got big. *Nature*, 470(7334): 339-340.
- Narbonne, G.M. and Gehling, J.G., 2003. Life after snowball: The oldest complex Ediacaran fossils. *Geology*, 31(1): 27-30.
- Newton, R.J., Pevitt, E.L., Wignall, P.B. and Bottrell, S.H., 2004. Large shifts in the isotopic composition of seawater sulphate across the Permo-Triassic boundary in northern Italy. *Earth and Planetary Science Letters*, 218(3-4): 331-345.
- Newton, R.J., Reeves, E.P., Kafousia, N., Wignall, P.B., Bottrell, S.H. and Sha, J.-G., 2011. Low marine sulfate concentrations and the isolation of the European epicontinental sea during the Early Jurassic. *Geology*, 39(1): 7-10.
- O'Connor, A.E., Lueck, J.L., McIntosh, H. and Beck, A.J., 2015. Geochemistry of redox-

- sensitive trace elements in a shallow subterranean estuary. *Marine Chemistry*, 172: 70-81.
- O'Leary, M.H., 1981. Carbon isotope fractionation in plants. *Phytochemistry*, 20(4): 553-567.
- Och, L.M., 2011. Biogeochemical cycling through the Neoproterozoic-Cambrian transition in China: an integrated study of redox-sensitive elements, UCL (University College London).
- Och, L.M., Cremonese, L., Shields-Zhou, G.A., Poulton, S.W., Struck, U., Ling, H., Li, D., Chen, X., Manning, C., Thirlwall, M., Strauss, H., Zhu, M. and Fairchild, I., 2016. Palaeoceanographic controls on spatial redox distribution over the Yangtze Platform during the Ediacaran-Cambrian transition. *Sedimentology*, 63(2): 378-410.
- Och, L.M. and Shields-Zhou, G.A., 2012. The Neoproterozoic oxygenation event: Environmental perturbations and biogeochemical cycling. *Earth-Science Reviews*, 110(1-4): 26-57.
- Oehlert, A.M. and Swart, P.K., 2014. Interpreting carbonate and organic carbon isotope covariance in the sedimentary record. *Nat Commun*, 5: 4672.
- Ohkouchi, N., Kawamura, K., Kajiura, Y., Wada, E., Okada, M., Kanamatsu, T. and Taira, A., 1999. Sulfur isotope records around Livello Bonarelli (northern Apennines, Italy) black shale at the Cenomanian-Turonian boundary. *Geology*, 27(6): 535-538.
- Ohmoto, H., 1997. Sulfur and carbon isotopes. *Geochemistry of Hydrothermal Ore Deposit*.
- Olanipekun, B.J. and Azmy, K., 2018. In situ geochemical characterization of pyrite crystals in burial dolomites of St. George Group carbonates. *Canadian Journal of Earth Sciences*, 55(5): 536-544.
- Ono, S., Whitehill, A.R. and Lyons, J.R., 2013. Contribution of isotopologue self-shielding to sulfur mass-independent fractionation during sulfur dioxide photolysis. *Journal of Geophysical Research: Atmospheres*, 118(5): 2444-2454.
- Ostrander, C.M., Sahoo, S.K., Kendall, B., Jiang, G.Q., Planavsky, N.J., Lyons, T.W., Nielsen, S.G., Owens, J.D., Gordon, G.W., Romaniello, S.J. and Anbar, A.D., 2019. Multiple negative molybdenum isotope excursions in the Doushantuo Formation (South China) fingerprint complex redox-related processes in the Ediacaran Nanhua Basin. *Geochimica Et Cosmochimica Acta*, 261: 191-209.
- Ouyang, Q., Zhou, C.M., Xiao, S.H., Chen, Z. and Shao, Y.F., 2019. Acanthomorphic acritarchs from the Ediacaran Doushantuo Formation at Zhangcunping in South China, with implications for the evolution of early Ediacaran eukaryotes. *Precambrian Research*, 320: 171-192.
- Partin, C.A., Bekker, A., Planavsky, N.J., Scott, C.T., Gill, B.C., Li, C., Podkovyrov, V., Maslov, A., Konhauser, K.O., Lalonde, S.V., Love, G.D., Poulton, S.W. and Lyons, T.W., 2013. Large-scale fluctuations in Precambrian atmospheric and oceanic oxygen levels from the record of U in shales. *Earth and Planetary Science Letters*, 369-370: 284-293.
- Paula-Santos, G.M., Campanha, G.A.d.C., Faleiros, F.M., Hollanda, M.H.B.M. and Rodrigues, S.W.d.O., 2021. Carbon isotope variations of high magnitude

- recorded in carbonate rocks from the Stenian-Tonian Lajeado Group, Southeast Brazil. *Journal of South American Earth Sciences*, 109.
- Pavlov, A. and Kasting, J., 2002. Mass-independent fractionation of sulfur isotopes in Archean sediments: strong evidence for an anoxic Archean atmosphere. *Astrobiology*, 2(1): 27-41.
- Paytan, A., Kastner, M., Campbell, D. and Thiemens, M.H., 1998. Sulfur isotopic composition of cenozoic seawater sulfate. *Science*, 282(5393): 1459-62.
- Paytan, A., Kastner, M., Campbell, D. and Thiemens, M.H., 2004. Seawater sulfur isotope fluctuations in the Cretaceous. *Science*, 304(5677): 1663-5.
- Pell, S., McKirdy, D., Jansyn, J. and Jenkins, R., 1993. Ediacaran carbon isotope stratigraphy of South Australia—an initial study. *Transactions of the Royal Society of South Australia*, 117(3-4): 153-161.
- Peng, Y., Bao, H., Zhou, C. and Yuan, X., 2011. ^{17}O -depleted barite from two Marinoan cap dolostone sections, South China. *Earth and Planetary Science Letters*, 305(1-2): 21-31.
- Peng, Y.B., Bao, H.M., Pratt, L.M., Kaufman, A.J., Jiang, G.Q., Boyd, D., Wang, Q.X., Zhou, C.M., Yuan, X.L., Xiao, S.H. and Loyd, S., 2014. Widespread contamination of carbonate-associated sulfate by present-day secondary atmospheric sulfate: Evidence from triple oxygen isotopes. *Geology*, 42(9): 815-818.
- Peryt, T.M., Halas, S. and Petrivna Hryniv, S., 2010. Sulphur and oxygen isotope signatures of late Permian Zechstein anhydrites, West Poland: seawater evolution and diagenetic constraints. *Geological Quarterly*, 54: 387-400.
- Planavsky, N.J., Asael, D., Hofmann, A., Reinhard, C.T., Lalonde, S.V., Knudsen, A., Wang, X., Ossa Ossa, F., Pecoits, E., Smith, A.J.B., Beukes, N.J., Bekker, A., Johnson, T.M., Konhauser, K.O., Lyons, T.W. and Rouxel, O.J., 2014. Evidence for oxygenic photosynthesis half a billion years before the Great Oxidation Event. *Nature Geoscience*, 7(4): 283-286.
- Porter, S.M. and Knoll, A.H., 2000. Testate amoebae in the Neoproterozoic Era: evidence from vase-shaped microfossils in the Chuar Group, Grand Canyon. *Paleobiology*, 26(3): 360-385.
- Poulton, S.W., Bekker, A., Cumming, V.M., Zerkle, A.L., Canfield, D.E. and Johnston, D.T., 2021. A 200-million-year delay in permanent atmospheric oxygenation. *Nature*, 592(7853): 232-236.
- Present, T.M., Paris, G., Burke, A., Fischer, W.W. and Adkins, J.F., 2015. Large Carbonate Associated Sulfate isotopic variability between brachiopods, micrite, and other sedimentary components in Late Ordovician strata. *Earth and Planetary Science Letters*, 432: 187-198.
- Pu, J.P., Bowring, S.A., Ramezani, J., Myrow, P., Raub, T.D., Landing, E., Mills, A., Hodgin, E. and Macdonald, F.A., 2016. Dodging snowballs: Geochronology of the Gaskiers glaciation and the first appearance of the Ediacaran biota. *Geology*, 44(11): 955-958.
- Rees, C., Jenkins, W. and Monster, J., 1978. The sulphur isotopic composition of ocean water sulphate. *Geochimica et Cosmochimica Acta*, 42(4): 377-381.
- Rennie, V.C. and Turchyn, A.V., 2014. The preservation of δSSO_{434} and δOSO_{418} in carbonate-associated sulfate during marine diagenesis: A 25 Myr test case

- using marine sediments. 395: 13-23.
- Ries, J.B., Fike, D.A., Grotzinger, J.P., Pratt, L.M. and Lyons, T.W., 2009a. Superheavy pyrite ($\delta^{34}\text{S}_{\text{pyr}} > \delta^{34}\text{S}_{\text{SCAS}}$) in the terminal Proterozoic Nama Group, southern Namibia: A consequence of low seawater sulfate at the dawn of animal life. *Geology*, 37(8): 743-746.
- Ries, J.B., Fike, D.A., Pratt, L.M., Lyons, T.W. and Grotzinger, J.P., 2009b. Superheavy pyrite ($\delta^{34}\text{S}_{\text{pyr}} > \delta^{34}\text{S}_{\text{SCAS}}$) in the terminal Proterozoic Nama Group, southern Namibia: A consequence of low seawater sulfate at the dawn of animal life. *Geology*, 37(8): 743-746.
- Romaniello, S.J., Herrmann, A.D. and Anbar, A.D., 2013. Uranium concentrations and $^{238}\text{U}/^{235}\text{U}$ isotope ratios in modern carbonates from the Bahamas: Assessing a novel paleoredox proxy. *Chemical Geology*, 362: 305-316.
- Rooney, A.D., Cantine, M.D., Bergmann, K.D., Gomez-Perez, I., Al Baloushi, B., Boag, T.H., Busch, J.F., Sperling, E.A. and Strauss, J.V., 2020. Calibrating the coevolution of Ediacaran life and environment. *Proc Natl Acad Sci U S A*, 117(29): 16824-16830.
- Rooney, A.D., Macdonald, F.A., Strauss, J.V., Dudas, F.O., Hallmann, C. and Selby, D., 2014. Re-Os geochronology and coupled Os-Sr isotope constraints on the Sturtian snowball Earth. *Proc Natl Acad Sci U S A*, 111(1): 51-6.
- Rosman, K. and Taylor, P., 1998. Isotopic compositions of the elements 1997 (Technical Report). *Pure and Applied Chemistry*, 70(1): 217-235.
- Rossetti, F., Nozaem, R., Lucci, F., Vignaroli, G., Gerdes, A., Nasrabadi, M. and Theye, T., 2015. Tectonic setting and geochronology of the Cadomian (Ediacaran-Cambrian) magmatism in Central Iran, Kuh-e-Sarhangi region (NW Lut Block). *Journal of Asian Earth Sciences*, 102: 24-44.
- Rothman, D.H., Hayes, J.M. and Summons, R.E., 2003. Dynamics of the Neoproterozoic carbon cycle. *Proceedings of the National Academy of Sciences*, 100(14): 8124-8129.
- Sahoo, S.K., Planavsky, N.J., Jiang, G., Kendall, B., Owens, J.D., Wang, X., Shi, X., Anbar, A.D. and Lyons, T.W., 2016. Oceanic oxygenation events in the anoxic Ediacaran ocean. *Geobiology*, 14(5): 457-68.
- Sahoo, S.K., Planavsky, N.J., Kendall, B., Wang, X., Shi, X., Scott, C., Anbar, A.D., Lyons, T.W. and Jiang, G., 2012. Ocean oxygenation in the wake of the Marinoan glaciation. *Nature*, 489(7417): 546-9.
- Sawaki, Y., Ohno, T., Tahata, M., Komiya, T., Hirata, T., Maruyama, S., Windley, B.F., Han, J., Shu, D.G. and Li, Y., 2010. The Ediacaran radiogenic Sr isotope excursion in the Doushantuo Formation in the Three Gorges area, South China. *Precambrian Research*, 176(1-4): 46-64.
- Saylor, B.Z., Grotzinger, J.P. and Germs, G.J.B., 1995. Sequence Stratigraphy and Sedimentology of the Neoproterozoic Kuibis and Schwarzrand Subgroups (Nama Group), Southwestern Namibia. *Precambrian Research*, 73(1-4): 153-171.
- Schrag, D.P., Higgins, J.A., Macdonald, F.A. and Johnston, D.T., 2013. Authigenic carbonate and the history of the global carbon cycle. *science*, 339(6119): 540-543.
- Schroder, S. and Grotzinger, J.P., 2007. Evidence for anoxia at the Ediacaran-

- Cambrian boundary: the record of redox-sensitive trace elements and rare earth elements in Oman. *Journal of the Geological Society*, 164(1): 175-187.
- Scott, C., Lyons, T.W., Bekker, A., Shen, Y., Poulton, S.W., Chu, X. and Anbar, A.D., 2008. Tracing the stepwise oxygenation of the Proterozoic ocean. *Nature*, 452(7186): 456-9.
- Seal, R.R., 2006. Sulfur isotope geochemistry of sulfide minerals. *Reviews in mineralogy and geochemistry*, 61(1): 633-677.
- Seilacher, A., Grazhdankin, D. and Legouta, A., 2003. Ediacaran biota: The dawn of animal life in the shadow of giant protists. 7(1): 43-54.
- Shen, B., Xiao, S.H., Bao, H.M., Kaufman, A.J., Zhou, C.M. and Yuan, X.L., 2011. Carbon, sulfur, and oxygen isotope evidence for a strong depth gradient and oceanic oxidation after the Ediacaran Hankschough glaciation. *Geochimica Et Cosmochimica Acta*, 75(5): 1357-1373.
- Shi, W., Li, C., Luo, G.M., Huang, J.H., Algeo, T.J., Jin, C.S., Zhang, Z.H. and Cheng, M., 2018. Sulfur isotope evidence for transient marine-shelf oxidation during the Ediacaran Shuram Excursion. *Geology*, 46(3): 267-270.
- Shields-Zhou, G. and Och, L., 2011. The case for a Neoproterozoic Oxygenation Event: Geochemical evidence and biological consequences. *GSA Today*, 21(3): 4-11.
- Shields, G., Kimura, H., Yang, J. and Gammon, P., 2004. Sulphur isotopic evolution of Neoproterozoic-Cambrian seawater: new francolite-bound sulphate $\delta^{34}\text{S}$ data and a critical appraisal of the existing record. *Chemical Geology*, 204(1-2): 163-182.
- Shields, G.A., 2017. Earth system transition during the Tonian-Cambrian interval of biological innovation: nutrients, climate, oxygen and the marine organic carbon capacitor. *Earth System Evolution and Early Life: A Celebration of the Work of Martin Brasier*, 448(1): 161-177.
- Shields, G.A., 2018. Carbon and carbon isotope mass balance in the Neoproterozoic Earth system. *Emerg Top Life Sci*, 2(2): 257-265.
- Shields, G.A., Carden, G.A.F., Veizer, J., Meidla, T., Rong, J.Y. and Li, R.Y., 2003. Sr, C, and O isotope geochemistry of Ordovician brachiopods: A major isotopic event around the Middle-Late Ordovician transition. *Geochimica Et Cosmochimica Acta*, 67(11): 2005-2025.
- Shields, G.A., Mills, B.J.W., Zhu, M.Y., Raub, T.D., Daines, S.J. and Lenton, T.M., 2019. Unique Neoproterozoic carbon isotope excursions sustained by coupled evaporite dissolution and pyrite burial. *Nature Geoscience*, 12(10): 823-+.
- Shields, G.A., Strauss, H., Howe, S.S. and Siegmund, H., 1999. Sulphur isotope compositions of sedimentary phosphorites from the basal Cambrian of China: implications for Neoproterozoic-Cambrian biogeochemical cycling. *Journal of the Geological Society*, 156(5): 943-955.
- Sial, A.N., Gaucher, C., Ramkumar, M. and Ferreira, V.P., 2018. *Chemostratigraphy Across Major Chronological Boundaries*, 240. John Wiley & Sons.
- Siedenberg, K., Strauss, H., Podlaha, O. and van den Boorn, S., 2018. Multiple sulfur isotopes ($\delta^{34}\text{S}$, $\Delta^{33}\text{S}$) of organic sulfur and pyrite from Late Cretaceous to Early Eocene oil shales in Jordan. *Organic Geochemistry*, 125: 29-40.
- Sim, M.S., Bosak, T. and Ono, S., 2011. Large sulfur isotope fractionation does not

- require disproportionation. *Science*, 333(6038): 74-77.
- Smalley, P., Higgins, A., Howarth, R., Nicholson, H., Jones, C., Swinburne, N. and Bessa, J., 1994. Seawater Sr isotope variations through time: A procedure for constructing a reference curve to date and correlate marine sedimentary rocks. *Geology*, 22(5): 431-434.
- Smrzka, D., Zwicker, J., Bach, W., Feng, D., Himmler, T., Chen, D. and Peckmann, J., 2019. The behavior of trace elements in seawater, sedimentary pore water, and their incorporation into carbonate minerals: a review. *Facies*, 65(4).
- Song, H.Y., Tong, J.N., Algeo, T.J., Song, H.J., Qiu, H.O., Zhu, Y.Y., Tian, L., Bates, S., Lyons, T.W., Luo, G.M. and Kump, L.R., 2014. Early Triassic seawater sulfate drawdown. *Geochimica Et Cosmochimica Acta*, 128: 95-113.
- Staudt, W.J. and Schoonen, M.A., 1995. Sulfate incorporation into sedimentary carbonates. ACS Publications.
- Strauss, H., Banerjee, D.M. and Kumar, V., 2001. The sulfur isotopic composition of Neoproterozoic to early Cambrian seawater—evidence from the cyclic Hanseran evaporites, NW India. *Chemical Geology*, 175(1-2): 17-28.
- Swart, P.K., 2015. The geochemistry of carbonate diagenesis: The past, present and future. *Sedimentology*, 62(5): 1233-1304.
- Theiling, B.P. and Coleman, M., 2015. Refining the extraction methodology of carbonate associated sulfate: Evidence from synthetic and natural carbonate samples. *Chemical Geology*, 411: 36-48.
- Tissot, F.L.H. and Dauphas, N., 2015. Uranium isotopic compositions of the crust and ocean: Age corrections, U budget and global extent of modern anoxia. *Geochimica et Cosmochimica Acta*, 167: 113-143.
- Tostevin, R., 2015. Developing proxies to constrain redox gradients in terminal Ediacaran oceans, UCL (University College London).
- Tostevin, R., Clarkson, M.O., Gangl, S., Shields, G.A., Wood, R.A., Bowyer, F., Penny, A.M. and Stirling, C.H., 2019. Uranium isotope evidence for an expansion of anoxia in terminal Ediacaran oceans. *Earth and Planetary Science Letters*, 506: 104-112.
- Tostevin, R., He, T.C., Turchyn, A.V., Wood, R.A., Penny, A.M., Bowyer, F., Antler, G. and Shields, G.A., 2017. Constraints on the late Ediacaran sulfur cycle from carbonate associated sulfate. *Precambrian Research*, 290: 113-125.
- Tostevin, R. and Mills, B.J.W., 2020. Reconciling proxy records and models of Earth's oxygenation during the Neoproterozoic and Palaeozoic. *Interface Focus*, 10(4): 20190137.
- Tostevin, R., Turchyn, A.V., Farquhar, J., Johnston, D.T., Eldridge, D.L., Bishop, J.K.B. and McIlvin, M., 2014. Multiple sulfur isotope constraints on the modern sulfur cycle. *Earth and Planetary Science Letters*, 396: 14-21.
- Toyama, K., Paytan, A., Sawada, K. and Hasegawa, T., 2020. Sulfur isotope ratios in co-occurring barite and carbonate from Eocene sediments: A comparison study. *Chemical Geology*, 535.
- Tribovillard, N., Algeo, T.J., Lyons, T. and Riboulleau, A., 2006. Trace metals as paleoredox and paleoproductivity proxies: An update. *Chemical Geology*, 232(1-2): 12-32.
- Tyson, R.V. and Pearson, T.H., 1991. Modern and ancient continental shelf anoxia:

- an overview. Geological Society, London, Special Publications, 58(1): 1-24.
- Urlwin, B., 1992. Carbon isotope stratigraphy of the Late Proterozoic Wonoka Formation of the Adelaide Fold Belt: diagenetic assessment and interpretation of isotopic signature and correlations with previously measured isotopic curves.
- Veizer, J., 1983. Trace elements and isotopes in sedimentary carbonates. 11: 265-300.
- Verdel, C., Wernicke, B.P. and Bowring, S.A., 2011. The Shuram and subsequent Ediacaran carbon isotope excursions from southwest Laurentia, and implications for environmental stability during the metazoan radiation. Geological Society of America Bulletin, 123(7-8): 1539-1559.
- Vernhet, E., Heubeck, C., Zhu, M.Y. and Zhang, J.M., 2006. Large-scale slope instability at the southern margin of the Ediacaran Yangtze platform (Hunan province, central China). Precambrian Research, 148(1-2): 32-44.
- Walter, M., Veevers, J., Calver, C., Gorjan, P. and Hill, A., 2000. Dating the 840-544 Ma Neoproterozoic interval by isotopes of strontium, carbon, and sulfur in seawater, and some interpretative models. Precambrian Research, 100(1-3): 371-433.
- Wang, J. and Li, Z.X., 2003. History of Neoproterozoic rift basins in South China: implications for Rodinia break-up. Precambrian Research, 122(1-4): 141-158.
- Wang, L., Shi, X.Y. and Jiang, G.Q., 2012a. Pyrite morphology and redox fluctuations recorded in the Ediacaran Doushantuo Formation. Palaeogeography Palaeoclimatology Palaeoecology, 333: 218-227.
- Wang, P., Algeo, T.J., Zhou, Q., Yu, W., Du, Y., Qin, Y., Xu, Y., Yuan, L. and Pan, W., 2019a. Large accumulations of 34S-enriched pyrite in a low-sulfate marine basin: The Sturtian Nanhua Basin, South China. Precambrian Research, 335.
- Wang, W., Guan, C., Zhou, C., Peng, Y., Pratt, L.M., Chen, X., Chen, L., Chen, Z., Yuan, X. and Xiao, S., 2017a. Integrated carbon, sulfur, and nitrogen isotope chemostratigraphy of the Ediacaran Lantian Formation in South China: Spatial gradient, ocean redox oscillation, and fossil distribution. Geobiology, 15(4): 552-571.
- Wang, W., Guan, C.G., Hu, Y.L., Cui, H., Muscente, A.D., Chen, L. and Zhou, C.M., 2020. Spatial and temporal evolution of Ediacaran carbon and sulfur cycles in the Lower Yangtze Block, South China. Palaeogeography Palaeoclimatology Palaeoecology, 537.
- Wang, W., Hu, Y.L., Muscente, A.D., Cui, H., Guan, C.G., Hao, J.L. and Zhou, C.M., 2021. Revisiting Ediacaran sulfur isotope chemostratigraphy with in situ nanoSIMS analysis of sedimentary pyrite. Geology, 49(6): 611-616.
- Wang, W., Zhou, C., Yuan, X., Chen, Z. and Xiao, S., 2012b. A pronounced negative $\delta^{13}\text{C}$ excursion in an Ediacaran succession of western Yangtze Platform: A possible equivalent to the Shuram event and its implication for chemostratigraphic correlation in South China. Gondwana Research, 22(3-4): 1091-1101.
- Wang, X., Shi, X., Jiang, G. and Tang, D., 2014. Organic carbon isotope gradient and ocean stratification across the late Ediacaran-Early Cambrian Yangtze

- Platform. *Science China Earth Sciences*, 57(5): 919-929.
- Wang, X.Q., Jiang, G.G., Shi, X.Y. and Xiao, S.H., 2016. Paired carbonate and organic carbon isotope variations of the Ediacaran Doushantuo Formation from an upper slope section at Siduping, South China. *Precambrian Research*, 273: 53-66.
- Wang, X.Q., Shi, X.Y., Jiang, G.Q. and Zhang, W.H., 2012c. New U-Pb age from the basal Niutitang Formation in South China: Implications for diachronous development and condensation of stratigraphic units across the Yangtze platform at the Ediacaran-Cambrian transition. *Journal of Asian Earth Sciences*, 48: 1-8.
- Wang, Y.F., Zhai, G.Y., Lu, Y.C., Ma, Y.Q., Li, J., Liu, G.H. and Zhang, Y.X., 2019b. Sedimentary lithofacies characteristics and sweet-spot interval characterization of the Sinian Doushantuo Formation in Upper Yangtze Platform, South China. *China Geology*, 2(3): 261-275.
- Wang, Z., Wang, J., Suess, E., Wang, G., Chen, C. and Xiao, S., 2017b. Silicified glendonites in the Ediacaran Doushantuo Formation (South China) and their potential paleoclimatic implications. *Geology*, 45(2): 115-118.
- Wanty, R.B. and Goldhaber, M.B., 1992. Thermodynamics and kinetics of reactions involving vanadium in natural systems: Accumulation of vanadium in sedimentary rocks. *Geochimica et Cosmochimica Acta*, 56(4): 1471-1483.
- Webb, G.E. and Kamber, B.S., 2000. Rare earth elements in Holocene reefal microbialites: a new shallow seawater proxy. *Geochimica et Cosmochimica Acta*, 64(9): 1557-1565.
- Wei, G.-Y., Ling, H.-F., Shields, G.A., Hohl, S.V., Yang, T., Lin, Y.-B. and Zhang, F., 2021a. Revisiting stepwise ocean oxygenation with authigenic barium enrichments in marine mudrocks. *Geology*.
- Wei, G.-Y., Planavsky, N.J., Tarhan, L.G., Chen, X., Wei, W., Li, D. and Ling, H.-F., 2018a. Marine redox fluctuation as a potential trigger for the Cambrian explosion. *Geology*, 46(7): 587-590.
- Wei, G.-Y., Planavsky, N.J., Tarhan, L.G., He, T., Wang, D., Shields, G.A., Wei, W. and Ling, H.-F., 2020a. Highly dynamic marine redox state through the Cambrian explosion highlighted by authigenic $\delta^{238}\text{U}$ records. *Earth and Planetary Science Letters*, 544.
- Wei, G.Y., Planavsky, N.J., He, T.C., Zhang, F.F., Stockey, R.G., Cole, D.B., Lin, Y.B. and Ling, H.F., 2021b. Global marine redox evolution from the late Neoproterozoic to the early Paleozoic constrained by the integration of Mo and U isotope records. *Earth-Science Reviews*, 214.
- Wei, H., Tang, Z., Qiu, Z., Yan, D. and Bai, M., 2020b. Formation of large carbonate concretions in black cherts in the Gufeng Formation (Guadalupian) at Enshi, South China. *Geobiology*, 18(1): 14-30.
- Wei, H., Wang, X., Shi, X., Jiang, G., Tang, D., Wang, L. and An, Z., 2019. Iodine content of the carbonates from the Doushantuo Formation and shallow ocean redox change on the Ediacaran Yangtze Platform, South China. *Precambrian Research*, 322: 160-169.
- Wei, W., Frei, R., Gilleaudeau, G.J., Li, D., Wei, G.Y., Chen, X. and Ling, H.F., 2018b. Oxygenation variations in the atmosphere and shallow seawaters of the

- Yangtze Platform during the Ediacaran Period: Clues from Cr-isotope and Ce-anomaly in carbonates. *Precambrian Research*, 313: 78-90.
- Wei, W., Frei, R., Gilleaudeau, G.J., Li, D., Wei, G.Y., Huang, F. and Ling, H.F., 2020c. Variations of redox conditions in the atmosphere and Yangtze Platform during the Ediacaran-Cambrian transition: Constraints from Cr isotopes and Ce anomalies. *Palaeogeography Palaeoclimatology Palaeoecology*, 543.
- Werne, J.P., Lyons, T.W., Hollander, D.J., Formolo, M.J. and Damste, J.S.S., 2003. Reduced sulfur in euxinic sediments of the Cariaco Basin: sulfur isotope constraints on organic sulfur formation. *Chemical Geology*, 195(1-4): 159-179.
- Weyer, S., Anbar, A.D., Gerdes, A., Gordon, G.W., Algeo, T.J. and Boyle, E.A., 2008. Natural fractionation of $^{238}\text{U}/^{235}\text{U}$. *Geochimica et Cosmochimica Acta*, 72(2): 345-359.
- Williams, G.E. and Schmidt, P.W., 2018. Shuram-Wonoka carbon isotope excursion: Ediacaran revolution in the world ocean's meridional overturning circulation. *Geoscience Frontiers*, 9(2): 391-402.
- Williams, J.J., Mills, B.J.W. and Lenton, T.M., 2019. A tectonically driven Ediacaran oxygenation event. *Nat Commun*, 10(1): 2690.
- Wood, R., Liu, A.G., Bowyer, F., Wilby, P.R., Dunn, F.S., Kenchington, C.G., Cuthill, J.F.H., Mitchell, E.G. and Penny, A., 2019. Integrated records of environmental change and evolution challenge the Cambrian Explosion. *Nat Ecol Evol*, 3(4): 528-538.
- Wood, R.A., Poulton, S.W., Prave, A.R., Hoffmann, K.H., Clarkson, M.O., Guilbaud, R., Lyne, J.W., Tostevin, R., Bowyer, F., Penny, A.M., Curtis, A. and Kasemann, S.A., 2015. Dynamic redox conditions control late Ediacaran metazoan ecosystems in the Nama Group, Namibia. *Precambrian Research*, 261: 252-271.
- Worden, R.H., Smalley, P.C. and Oxtoby, N.H., 1995. Gas souring by thermochemical sulfate reduction at 140 C. *Aapg Bulletin*, 79(6): 854-863.
- Wortmann, U.G. and Chernyavsky, B.M., 2007. Effect of evaporite deposition on Early Cretaceous carbon and sulphur cycling. *Nature*, 446(7136): 654-6.
- Wotte, T., Shields-Zhou, G.A. and Strauss, H., 2012a. Carbonate-associated sulfate: Experimental comparisons of common extraction methods and recommendations toward a standard analytical protocol. *Chemical Geology*, 326: 132-144.
- Wotte, T., Strauss, H., Fugmann, A. and Garbe-Schönberg, D., 2012b. Paired $\delta^{34}\text{S}$ data from carbonate-associated sulfate and chromium-reducible sulfur across the traditional Lower-Middle Cambrian boundary of W-Gondwana. *Geochimica et Cosmochimica Acta*, 85: 228-253.
- Wu, H.P., Jiang, S.Y., Palmer, M.R., Wei, H.Z. and Yang, J.H., 2019. Positive cerium anomaly in the Doushantuo cap carbonates from the Yangtze platform, South China: Implications for intermediate water column manganese conditions in the aftermath of the Marinoan glaciation. *Precambrian Research*, 320: 93-110.
- Wu, N., Farquhar, J. and Fike, D.A., 2015. Ediacaran sulfur cycle: Insights from sulfur isotope measurements ($\Delta^{33}\text{S}$ and $\delta^{34}\text{S}$) on paired sulfate-pyrite in the Huqf

- Supergroup of Oman. *Geochimica et Cosmochimica Acta*, 164: 352-364.
- Xiao, S., Knoll, A.H., Yuan, X. and Poeschel, C.M., 2004. Phosphatized multicellular algae in the Neoproterozoic Doushantuo Formation, China, and the early evolution of florideophyte red algae. *American Journal of Botany*, 91(2): 214-227.
- Xiao, S.H., Chen, Z., Pang, K., Zhou, C.M. and Yuan, X.L., 2021. The Shibantan Lagerstätte: insights into the Proterozoic-Phanerozoic transition. *Journal of the Geological Society*, 178(1): jgs2020-135.
- Xiao, S.H., Droser, M., Gehling, J.G., Hughes, I.V., Wan, B., Chen, Z. and Yuan, X.L., 2013. Affirming life aquatic for the Ediacara biota in China and Australia. *Geology*, 41(10): 1095-1098.
- Xiao, S.H., McFadden, K.A., Peek, S., Kaufman, A.J., Zhou, C.M., Jiang, G.Q. and Hu, J., 2012. Integrated chemostratigraphy of the Doushantuo Formation at the northern Xiaofenghe section (Yangtze Gorges, South China) and its implication for Ediacaran stratigraphic correlation and ocean redox models. *Precambrian Research*, 192-95: 125-141.
- Xiao, S.H., Muscente, A.D., Chen, L., Zhou, C.M., Schiffbauer, J.D., Wood, A.D., Polys, N.F. and Yuan, X.L., 2014. The Weng'an biota and the Ediacaran radiation of multicellular eukaryotes. *National Science Review*, 1(4): 498-520.
- Yang, C., Li, X.-H., Zhu, M. and Condon, D.J., 2016. SIMS U-Pb zircon geochronological constraints on upper Ediacaran stratigraphic correlations, South China. *Geological Magazine*, 154(6): 1202-1216.
- Yang, C., Rooney, A.D., Condon, D.J., Li, X.-H., Grazhdankin, D.V., Bowyer, F.T., Hu, C., Macdonald, F.A. and Zhu, M., 2021. The tempo of Ediacaran evolution. *Science Advances*, 7(45): eabi9643.
- Yang, C., Zhu, M.Y., Condon, D.J. and Li, X.H., 2017. Geochronological constraints on stratigraphic correlation and oceanic oxygenation in Ediacaran-Cambrian transition in South China. *Journal of Asian Earth Sciences*, 140: 75-81.
- Yang, F., Qin, S., Ding, W., Xu, Y. and Shen, B., 2018. New Discovery of Macroscopic Algae Fossils from Shibantan Bituminous Limestone of Dengying Formation in the Yangtze Gorges Area, South China. *Beijing Da Xue Xue Bao*, 54(3): 563-572.
- Yano, M., Yasukawa, K., Nakamura, K., Ikehara, M. and Kato, Y., 2020. Geochemical Features of Redox-Sensitive Trace Metals in Sediments under Oxygen-Depleted Marine Environments. *Minerals*, 10(11).
- Yao, W.H., Li, Z.X., Li, W.X., Li, X.H. and Yang, J.H., 2014. From Rodinia to Gondwanaland: A Tale of Detrital Zircon Provenance Analyses from the Southern Nanhua Basin, South China. *American Journal of Science*, 314(1): 278-313.
- Ye, Y.T., Wang, H.J., Wang, X.M., Zhai, L., Wu, C.D., Canfield, D.E. and Zhang, S.C., 2020. Tracking the evolution of seawater Mo isotopes through the Ediacaran-Cambrian transition. *Precambrian Research*, 350.
- Yin, L., Zhu, M., Knoll, A.H., Yuan, X., Zhang, J. and Hu, J., 2007. Doushantuo embryos preserved inside diapause egg cysts. *Nature*, 446(7136): 661-3.
- Yuan, X., Chen, Z., Xiao, S., Wan, B., Guan, C., Wang, W., Zhou, C. and Hua, H., 2012. The Lantian biota: A new window onto the origin and early evolution of




- multicellular organisms. *Chinese Science Bulletin*, 58(7): 701-707.
- Zhang, F., Xiao, S., Kendall, B., Romaniello, S.J., Cui, H., Meyer, M., Gilleaudeau, G.J., Kaufman, A.J. and Anbar, A.D., 2018. Extensive marine anoxia during the terminal Ediacaran Period. *Sci Adv*, 4(6): eaan8983.
- Zhang, F., Xiao, S., Romaniello, S.J., Hardisty, D., Li, C., Melezhik, V., Pokrovsky, B., Cheng, M., Shi, W., Lenton, T.M. and Anbar, A.D., 2019. Global marine redox changes drove the rise and fall of the Ediacara biota. *Geobiology*, 17(6): 594-610.
- Zhang, F.F., Dahl, T.W., Lenton, T.M., Luo, G.M., Shen, S.Z., Algeo, T.J., Planavsky, N., Liu, J.S., Cui, Y., Qie, W.K., Romaniello, S.J. and Anbar, A.D., 2020a. Extensive marine anoxia associated with the Late Devonian Hangenberg Crisis. *Earth and Planetary Science Letters*, 533.
- Zhang, F.F., Lenton, T.M., del Rey, A., Romaniello, S.J., Chen, X.M., Planavsky, N.J., Clarkson, M.O., Dahl, T.W., Lau, K.V., Wang, W.Q., Li, Z.H., Zhao, M.Y., Isson, T., Algeo, T.J. and Anbar, A.D., 2020b. Uranium isotopes in marine carbonates as a global ocean paleoredox proxy: A critical review. *Geochimica Et Cosmochimica Acta*, 287: 27-49.
- Zhang, S.H., Evans, D.A.D., Li, H.Y., Wu, H.C., Jiang, G.G., Dong, J., Zhao, Q.L., Raub, T.D. and Yang, T.S., 2013. Paleomagnetism of the late Cryogenian Nantuo Formation and paleogeographic implications for the South China Block. *Journal of Asian Earth Sciences*, 72: 164-177.
- Zhang, S.H., Li, H.Y., Jiang, G.Q., Evans, D.A.D., Dong, J., Wu, H.C., Yang, T.S., Liu, P.J. and Xiao, Q.S., 2015. New paleomagnetic results from the Ediacaran Doushantuo Formation in South China and their paleogeographic implications. *Precambrian Research*, 259: 130-142.
- Zhang, X.-G. and Pratt, B.R., 2015. Possible algal origin and life cycle of Ediacaran Doushantuo microfossils with dextral spiral structure. *Journal of Paleontology*, 88(1): 92-98.
- Zhang, X.L., Zhou, X. and Hu, D.P., 2020c. High-resolution paired carbon isotopic records from the Meishucun section in South China: Implications for carbon cycling and environmental changes during the Ediacaran-Cambrian transition. *Precambrian Research*, 337.
- Zhao, Y.L., Chen, M., Peng, J., Yu, M.Y., He, M.H., Wang, Y., Yang, R.J., Wang, P.L. and Zhang, Z.H., 2004. Discovery of a Miaohu-type Biota from the Neoproterozoic Doushantuo formation in Jiangkou County, Guizhou Province, China. *Chinese Science Bulletin*, 49(20): 2224-2226.
- Zheng, Y., Anderson, R.F., van Geen, A. and Fleisher, M.Q., 2002. Remobilization of authigenic uranium in marine sediments by bioturbation. *Geochimica et Cosmochimica Acta*, 66(10): 1759-1772.
- Zhou, C. and Xiao, S., 2007. Ediacaran $\delta^{13}\text{C}$ chemostratigraphy of South China. *Chemical Geology*, 237(1-2): 89-108.
- Zhou, C., Yuan, X., Xiao, S., Chen, Z. and Hua, H., 2018. Ediacaran integrative stratigraphy and timescale of China. *Science China Earth Sciences*, 62(1): 7-24.
- Zhou, C.M., Jiang, S.Y., Xiao, S.H., Chen, Z. and Yuan, X.L., 2012. Rare earth elements and carbon isotope geochemistry of the Doushantuo Formation in South




- China: Implication for middle Ediacaran shallow marine redox conditions. *Chinese Science Bulletin*, 57(16): 1998-2006.
- Zhou, C.M., Li, X.H., Xiao, S.H., Lan, Z.W., Ouyang, Q., Guan, C.G. and Chen, Z., 2017a. A new SIMS zircon U-Pb date from the Ediacaran Doushantuo Formation: age constraint on the Weng'an biota. *Geological Magazine*, 154(6): 1193-1201.
- Zhou, C.M., Xiao, S.H., Wang, W., Guan, C.G., Ouyang, Q. and Chen, Z., 2017b. The stratigraphic complexity of the middle Ediacaran carbon isotopic record in the Yangtze Gorges area, South China, and its implications for the age and chemostratigraphic significance of the Shuram excursion. *Precambrian Research*, 288: 23-38.
- Zhou, Y., von Strandmann, P.A.P., Zhu, M., Ling, H., Manning, C., Li, D., He, T. and Shields, G.A., 2020. Reconstructing Tonian seawater $^{87}\text{Sr}/^{86}\text{Sr}$ using calcite microspar. *Geology*, 48(5): 462-467.
- Zhu, M.Y., Gehling, J.G., Xia, S.H., Zhao, Y.L. and Droser, M.L., 2008. Eight-armed Ediacara fossil preserved in contrasting taphonomic windows from China and Australia. *Geology*, 36(11): 867-870.
- Zhu, M.Y. and Li, X.H., 2017. Introduction: from snowball Earth to the Cambrian explosion-evidence from China. *Geological Magazine*, 154(6): 1187-1192.
- Zhu, M.Y., Lu, M., Zhang, J.M., Zhao, F.C., Li, G.X., Aihua, Y., Zhao, X. and Zhao, M.J., 2013. Carbon isotope chemostratigraphy and sedimentary facies evolution of the Ediacaran Doushantuo Formation in western Hubei, South China. *Precambrian Research*, 225: 7-28.
- Zhu, M.Y., Zhang, J.M. and Yang, A.H., 2007. Integrated Ediacaran (Sinian) chronostratigraphy of South China. *Palaeogeography Palaeoclimatology Palaeoecology*, 254(1-2): 7-61.
- Zhuravlev, A.Y., Vintaned, J.A.G. and Ivantsov, A.Y., 2009. First finds of problematic Ediacaran fossil Gaojiashania in Siberia and its origin. *Geological Magazine*, 146(5): 775-780.





APPENDIX A: ROCK DESCRIPTIONS





Qinglinkou Section: GPS: N30.7967285 E110.916404

Table S1. Detailed outcrop observation of the Qinglinkou section

Depth (m)	Photos	Description	Notes
210.7 - 302.9		Light grey thin-bedded limestone	Upper Shibantan Member, Dengying Formation
199.1 - 209.8		Dark colour thin-bedded limestone with elliptical siliceous concretion (7-12cm).	Lower Shibantan Member, Dengying Formation
195.3 - 199.1		Dark colour thin-bedded limestone with spherical siliceous concretion (4-8cm).	Lower Shibantan Member, Dengying Formation

186.2 -194		The lift side is grey medium bedded dolostone with siliceous bands.	The boundary between Doushantu o Member IV black shale and Dengying HMJ Member dolostone
176.9 - 185.9		Thick dark shale layer with carbonate concretion (0.8-1.5m).	Doushantu o Member IV. This is the 'second shale' layer, which shows the lift side is thicker than the right side.
157.8 - 175.9		Grey unbedded dolostone with a thin dark shale layer	Middle carbonate and 'first shale' layer, which clearly shows a slumping feature. The shale layer is not a continuous layer and the lift side is thicker than the right side

148.3 - 157.8		Grey unbedded dolostone	Doushantu o Member III
125.4 - 147.8		Grey medium- thick bedded dolostone	Upper Doushantu o Member III
105.2 -114		Grey medium bedded dolostone layer interbedde d with shale layers	Upper Doushantu o Member II
92.1- 101.2		Thin- medium bedded dolostone folds	Upper Doushantu o Member II

40.95 -92.		Medium-thin interbedded shale and carbonate	Middle Doushantu o Member II
18.75 -40.55		Medium bedded carbonate with calcite veins	Lower Doushantu o Member II
3.55-17.95		Very fine bedded carbonate interbedded with chert bands. Has small silicate concretions	Lower Doushantu o Member II
0-3.55		Cap carbonate	Doushantu o Member I

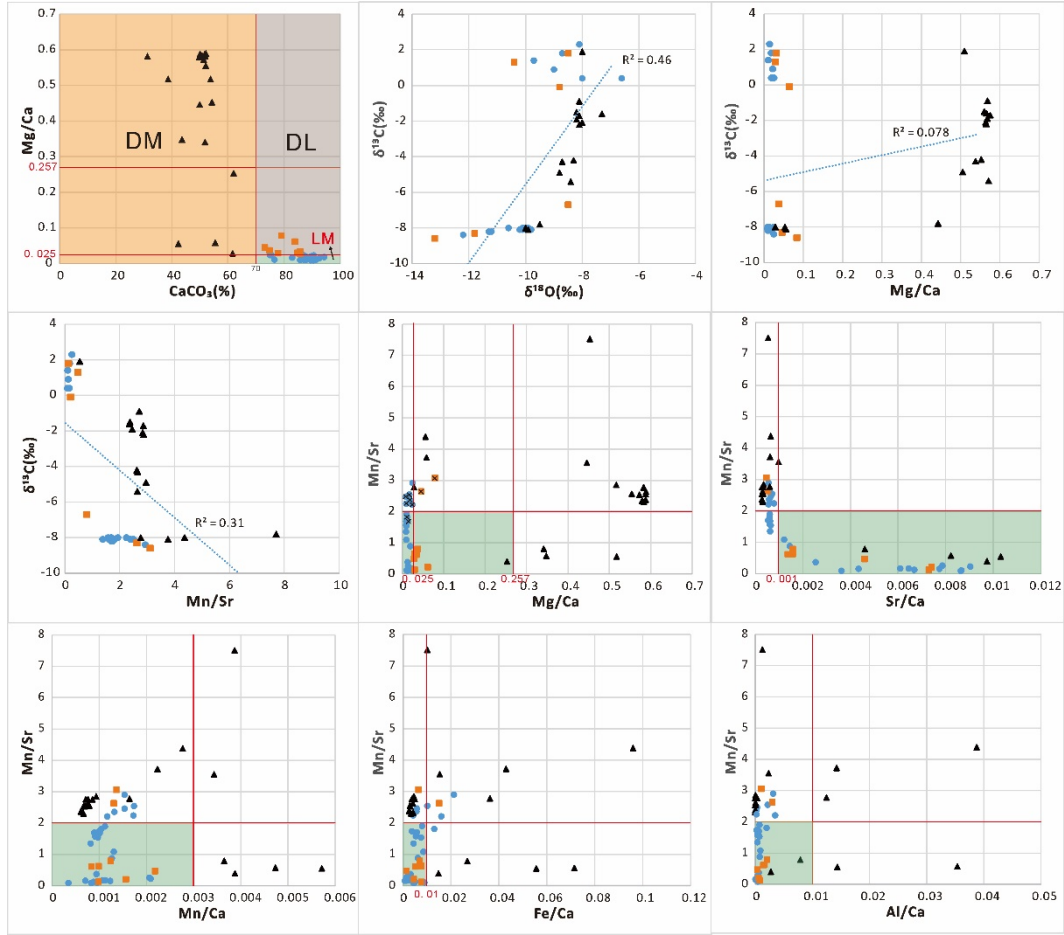


Fig. S1: Cross-plot of the Lianghong section samples with $\text{Mn/Sr} < 10$. DM: dolomite (calcium carbonate content $< 70\%$); DL: dolomitic limestone (calcium carbonate content $> 70\%$; $\text{Mg/Ca} > 0.025$); LM: limestone (calcium carbonate content $> 70\%$; $\text{Mg/Ca} < 0.025$). Thresholds for the green shaded area (best-preserved samples) are $\text{Mn/Sr} < 2$, $\text{Mg/Ca} < 0.257$, $\text{Sr/Ca} > 0.001$, $\text{Mn/Ca} < 0.003$, $\text{Fe/Ca} < 0.01$ and $\text{Al/Ca} < 0.05$.

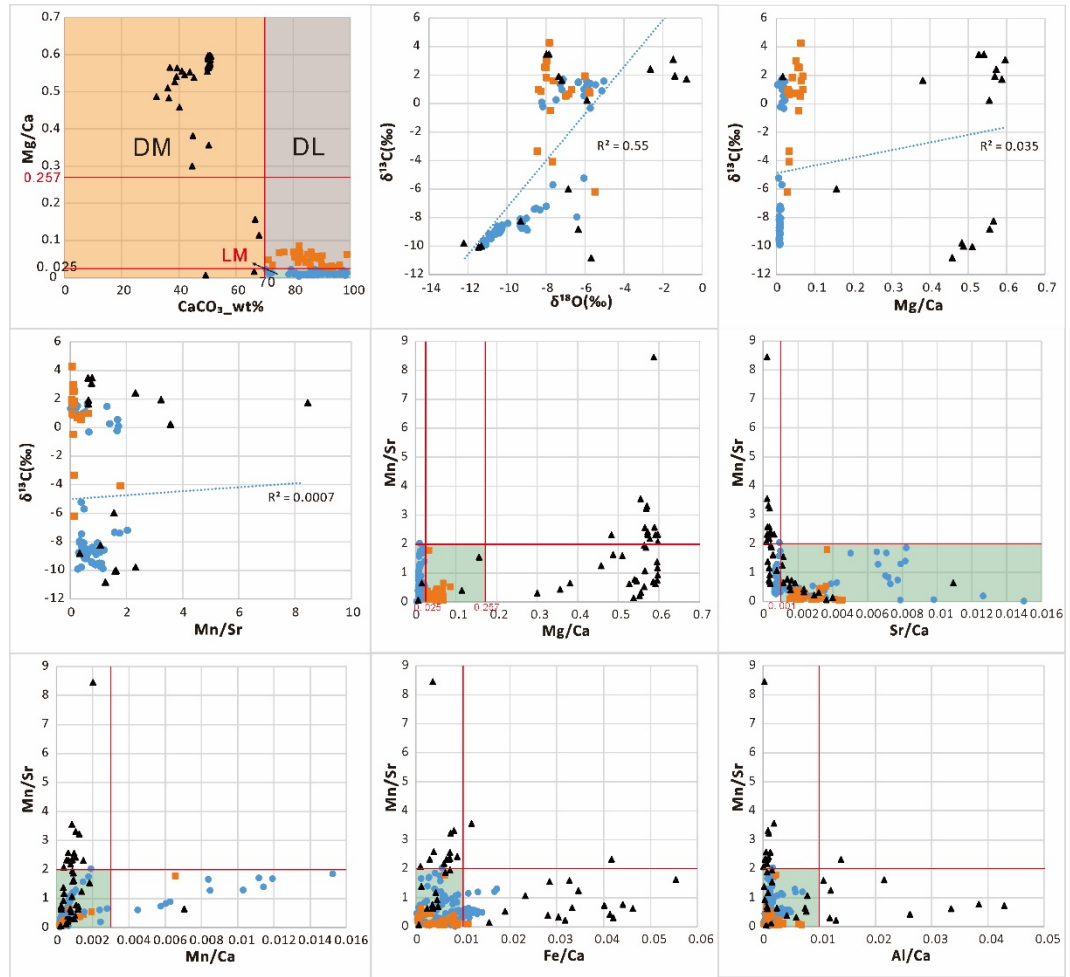


Fig. S2: Cross-plot of the Sishang section samples with $Mn/Sr < 10$. DM: dolomite (calcium carbonate content $< 70\%$); DL: dolomitic limestone (calcium carbonate content $> 70\%$; $Mg/Ca > 0.025$); LM: limestone (calcium carbonate content $> 70\%$; $Mg/Ca < 0.025$). Thresholds for the green shaded area (best-preserved samples) are $Mn/Sr < 2$, $Mg/Ca < 0.257$, $Sr/Ca > 0.001$, $Mn/Ca < 0.003$, $Fe/Ca < 0.01$ and $Al/Ca < 0.05$.

APPENDIX B: RAW DATA FROM ICP-OES TEST

Lianghong section

GPS position: N29°04'53.2", E102°49'01.7"

Sample [↵]	Age [↵] (Ma) [↵]	Height [↵] (m) [↵]	Ca [↵] wt% [↵]	Mg [↵] wt% [↵]	Al [↵] ppm [↵]	Na [↵] ppm [↵]	K [↵] ppm [↵]	Fe [↵] ppm [↵]	Mn [↵] ppm [↵]	Sr [↵] ppm [↵]
LHC21.7 [↵]	543.2 [↵]	49.7 [↵]	33.52 [↵]	0.53 [↵]	148.16 [↵]	5.59 [↵]	27.25 [↵]	479.16 [↵]	735.25 [↵]	3223.24 [↵]
LHC21.0 [↵]	543.5 [↵]	49 [↵]	34.54 [↵]	0.48 [↵]	138.39 [↵]	1.46 [↵]	77.25 [↵]	519.58 [↵]	740.64 [↵]	2863.62 [↵]
LHC20.0 [↵]	543.94 [↵]	48 [↵]	32.07 [↵]	0.94 [↵]	116.42 [↵]	5.7 [↵]	30.61 [↵]	540.04 [↵]	735.55 [↵]	1552.44 [↵]
LHC19.0 [↵]	544.37 [↵]	47 [↵]	34.84 [↵]	0.58 [↵]	20.85 [↵]	3.49 [↵]	-- [↵]	499.69 [↵]	450.42 [↵]	2866.47 [↵]
LHC18.0 [↵]	544.8 [↵]	46 [↵]	35.54 [↵]	0.68 [↵]	8.62 [↵]	7.76 [↵]	-- [↵]	340.34 [↵]	261.32 [↵]	1610.18 [↵]
LHC17.0 [↵]	545.24 [↵]	45 [↵]	15.79 [↵]	8.05 [↵]	2230.54 [↵]	95.76 [↵]	862.42 [↵]	8325.21 [↵]	868.84 [↵]	1589.9 [↵]
LHC16.0 [↵]	545.67 [↵]	44 [↵]	31.96 [↵]	0.99 [↵]	254.76 [↵]	15.94 [↵]	42.93 [↵]	2663.32 [↵]	326.19 [↵]	2459.27 [↵]
LHC15.0 [↵]	546.11 [↵]	43 [↵]	33.51 [↵]	0.6 [↵]	109.44 [↵]	12.52 [↵]	11.89 [↵]	1486.7 [↵]	393.85 [↵]	2287.61 [↵]
LHC14.0 [↵]	546.54 [↵]	42 [↵]	32.22 [↵]	0.71 [↵]	224.73 [↵]	5.42 [↵]	57.83 [↵]	1879.11 [↵]	306.61 [↵]	2383.9 [↵]
LHC13.0 [↵]	546.98 [↵]	41 [↵]	34.14 [↵]	0.37 [↵]	182.77 [↵]	8.58 [↵]	43.14 [↵]	3279.86 [↵]	339.68 [↵]	3169.19 [↵]
LHC12.0 [↵]	547.41 [↵]	40 [↵]	32.6 [↵]	0.82 [↵]	165.2 [↵]	21.27 [↵]	4.01 [↵]	1716 [↵]	281.57 [↵]	3000.63 [↵]
LHC11.0 [↵]	547.84 [↵]	39 [↵]	31.73 [↵]	2.04 [↵]	186.27 [↵]	36.61 [↵]	88.53 [↵]	1573.42 [↵]	514.93 [↵]	2467.79 [↵]
LHC10.0 [↵]	548.28 [↵]	38 [↵]	33.84 [↵]	0.82 [↵]	154.67 [↵]	9.48 [↵]	105.96 [↵]	1060.31 [↵]	383.07 [↵]	2190.3 [↵]
LHC9.0 [↵]	548.71 [↵]	37 [↵]	25.08 [↵]	6.33 [↵]	671.61 [↵]	18.76 [↵]	368.45 [↵]	3713.2 [↵]	942.89 [↵]	2404.35 [↵]
LHC8.0 [↵]	549.15 [↵]	36 [↵]	17.76 [↵]	6.06 [↵]	6184.39 [↵]	69.85 [↵]	3025.01 [↵]	12050.89 [↵]	804.5 [↵]	1416.59 [↵]
LHC7.1 [↵]	549.54 [↵]	35.1 [↵]	21.15 [↵]	7.11 [↵]	1641.38 [↵]	82.52 [↵]	794.76 [↵]	5518.3 [↵]	741.34 [↵]	922.83 [↵]
LHC6.0 [↵]	550.01 [↵]	34 [↵]	33.71 [↵]	0.46 [↵]	212.53 [↵]	8.61 [↵]	129.71 [↵]	1184.04 [↵]	329.67 [↵]	870.43 [↵]
LHC5.0 [↵]	550.45 [↵]	33 [↵]	32.26 [↵]	1.16 [↵]	475.53 [↵]	46.17 [↵]	205.41 [↵]	1857.2 [↵]	279.52 [↵]	454.7 [↵]
LHC4.0 [↵]	550.88 [↵]	32 [↵]	28.88 [↵]	1.07 [↵]	607.22 [↵]	41.33 [↵]	200.5 [↵]	2130.97 [↵]	370.82 [↵]	461.08 [↵]
LHC3.5 [↵]	551.1 [↵]	31.5 [↵]	20.41 [↵]	8.87 [↵]	460.1 [↵]	61.55 [↵]	323 [↵]	3062.69 [↵]	686.65 [↵]	190.51 [↵]

LHC2.0 [⊖]	551.75 [⊖]	30 [⊖]	33.09 [⊖]	0.66 [⊖]	281.81 [⊖]	45.93 [⊖]	137.07 [⊖]	2181.37 [⊖]	441.87 [⊖]	487.02 [⊖]
LHC1.5 [⊖]	551.97 [⊖]	29.5 [⊖]	29.45 [⊖]	0.88 [⊖]	508.7 [⊖]	18.66 [⊖]	247.24 [⊖]	2406.82 [⊖]	307.9 [⊖]	468.51 [⊖]
LHC1.1 [⊖]	552.14 [⊖]	29.1 [⊖]	33.07 [⊖]	0.32 [⊖]	310.19 [⊖]	50.65 [⊖]	114.24 [⊖]	3007.11 [⊖]	457.21 [⊖]	415.77 [⊖]
LHC0.6 [⊖]	552.36 [⊖]	28.6 [⊖]	34.77 [⊖]	0.44 [⊖]	166.65 [⊖]	10.44 [⊖]	43.55 [⊖]	1578.5 [⊖]	128.13 [⊖]	1308.41 [⊖]
LHC-0.7 [⊖]	552.92 [⊖]	27.3 [⊖]	34.22 [⊖]	0.34 [⊖]	67.2 [⊖]	10.11 [⊖]	18.31 [⊖]	1580.56 [⊖]	621.47 [⊖]	275.09 [⊖]
LHC-1.1 [⊖]	553.1 [⊖]	26.9 [⊖]	31.42 [⊖]	0.53 [⊖]	710.79 [⊖]	26.08 [⊖]	397.15 [⊖]	3349.82 [⊖]	574.16 [⊖]	223.2 [⊖]
LHA10.5 [⊖]	553.27 [⊖]	26.5 [⊖]	32.98 [⊖]	0.36 [⊖]	259.59 [⊖]	39.35 [⊖]	90.22 [⊖]	2832.76 [⊖]	394.72 [⊖]	204.68 [⊖]
LHA10.0 [⊖]	553.49 [⊖]	26 [⊖]	23.86 [⊖]	0.68 [⊖]	3081.02 [⊖]	33.49 [⊖]	954.9 [⊖]	8521.11 [⊖]	397.46 [⊖]	143.7 [⊖]
LHA9.5 [⊖]	553.7 [⊖]	25.5 [⊖]	17.07 [⊖]	0.91 [⊖]	6579.11 [⊖]	52.38 [⊖]	2071.08 [⊖]	15135.04 [⊖]	456.47 [⊖]	104.48 [⊖]
LHA9.0 [⊖]	553.92 [⊖]	25 [⊖]	32.43 [⊖]	0.32 [⊖]	253.26 [⊖]	56.27 [⊖]	101.85 [⊖]	2613.07 [⊖]	334.47 [⊖]	212.18 [⊖]
LHA8.5 [⊖]	554.14 [⊖]	24.5 [⊖]	34.24 [⊖]	0.45 [⊖]	172.86 [⊖]	39.97 [⊖]	107.22 [⊖]	1978.37 [⊖]	364.51 [⊖]	215.77 [⊖]
LHA8.0 [⊖]	554.36 [⊖]	24 [⊖]	33.84 [⊖]	0.32 [⊖]	121.15 [⊖]	25.86 [⊖]	56.25 [⊖]	2082.99 [⊖]	551.3 [⊖]	219.91 [⊖]
LHA7.5 [⊖]	554.57 [⊖]	23.5 [⊖]	22.37 [⊖]	1.25 [⊖]	3159.99 [⊖]	36.17 [⊖]	1438.22 [⊖]	9051.42 [⊖]	489.97 [⊖]	130.18 [⊖]
LHA7.0 [⊖]	554.79 [⊖]	23 [⊖]	29.33 [⊖]	0.33 [⊖]	608.15 [⊖]	10.03 [⊖]	443.53 [⊖]	3918.76 [⊖]	318.78 [⊖]	174.97 [⊖]
LHA6.5 [⊖]	555.01 [⊖]	22.5 [⊖]	33.97 [⊖]	0.34 [⊖]	130.19 [⊖]	12.5 [⊖]	91.19 [⊖]	1940.9 [⊖]	333.85 [⊖]	207.06 [⊖]
LHA6.0 [⊖]	555.22 [⊖]	22 [⊖]	34.73 [⊖]	0.36 [⊖]	73.89 [⊖]	16.39 [⊖]	51.62 [⊖]	1420.07 [⊖]	363.31 [⊖]	206.88 [⊖]
LHA5.5 [⊖]	555.44 [⊖]	21.5 [⊖]	34.2 [⊖]	0.31 [⊖]	143.34 [⊖]	22.87 [⊖]	58.83 [⊖]	1646.96 [⊖]	297.03 [⊖]	214.49 [⊖]
LHA5.0 [⊖]	555.66 [⊖]	21 [⊖]	33.24 [⊖]	0.62 [⊖]	51.33 [⊖]	21.64 [⊖]	-- [⊖]	2001.41 [⊖]	464.49 [⊖]	193.79 [⊖]
LHA4.5 [⊖]	555.88 [⊖]	20.5 [⊖]	28.6 [⊖]	0.7 [⊖]	1045.7 [⊖]	22.01 [⊖]	811.15 [⊖]	4871.97 [⊖]	347.31 [⊖]	154.61 [⊖]
LHA4.0 [⊖]	556.09 [⊖]	20 [⊖]	33.53 [⊖]	0.33 [⊖]	141.48 [⊖]	92.96 [⊖]	217.01 [⊖]	1959.05 [⊖]	340.28 [⊖]	200.51 [⊖]
LHA3.5 [⊖]	556.31 [⊖]	19.5 [⊖]	32.99 [⊖]	0.38 [⊖]	214.43 [⊖]	45.78 [⊖]	236.35 [⊖]	2056 [⊖]	313.67 [⊖]	179.86 [⊖]
LHA2.5 [⊖]	556.74 [⊖]	18.5 [⊖]	27.95 [⊖]	1.29 [⊖]	862.41 [⊖]	37.23 [⊖]	617.92 [⊖]	4403.79 [⊖]	372.14 [⊖]	141.47 [⊖]
LHA1.9 [⊖]	557 [⊖]	17.9 [⊖]	28.69 [⊖]	0.71 [⊖]	935.57 [⊖]	27.95 [⊖]	517.19 [⊖]	6471.75 [⊖]	456.08 [⊖]	155.37 [⊖]
LHA1.0 [⊖]	557.4 [⊖]	17 [⊖]	29.73 [⊖]	2.49 [⊖]	332.7 [⊖]	37.14 [⊖]	212.47 [⊖]	2045.78 [⊖]	423.37 [⊖]	136.26 [⊖]
LHA0.4 [⊖]	557.66 [⊖]	16.4 [⊖]	21.97 [⊖]	9.72 [⊖]	264.2 [⊖]	85.73 [⊖]	310.9 [⊖]	2228.55 [⊖]	834.37 [⊖]	108.26 [⊖]

LHA0.05 [⊂]	557.81 [⊂]	16.05 [⊂]	21.76 [⊂]	11 [⊂]	7.68 [⊂]	167.93 [⊂]	141.72 [⊂]	996.26 [⊂]	200.96 [⊂]	67.88 [⊂]
LHA0.0 [⊂]	557.83 [⊂]	16 [⊂]	21.17 [⊂]	11.39 [⊂]	2.24 [⊂]	199.96 [⊂]	109.44 [⊂]	599.63 [⊂]	163.7 [⊂]	61.59 [⊂]
LHA-0.2 [⊂]	557.92 [⊂]	15.8 [⊂]	20.98 [⊂]	11.59 [⊂]	-- [⊂]	80.54 [⊂]	61.59 [⊂]	637.6 [⊂]	143.57 [⊂]	54.66 [⊂]
LHA-1.0 [⊂]	558.26 [⊂]	15 [⊂]	20.39 [⊂]	11.65 [⊂]	7.54 [⊂]	52.74 [⊂]	54.12 [⊂]	602.35 [⊂]	133.66 [⊂]	50.59 [⊂]
LHA-1.6 [⊂]	558.52 [⊂]	14.4 [⊂]	21.1 [⊂]	11.91 [⊂]	60.92 [⊂]	63.27 [⊂]	85.25 [⊂]	776.45 [⊂]	156.33 [⊂]	55.07 [⊂]
LHA-2.3 [⊂]	558.83 [⊂]	13.7 [⊂]	21.06 [⊂]	11.96 [⊂]	-- [⊂]	91.65 [⊂]	85.97 [⊂]	530.9 [⊂]	124.68 [⊂]	50.76 [⊂]
LHA-3.0 [⊂]	559.13 [⊂]	13 [⊂]	20.66 [⊂]	11.67 [⊂]	-- [⊂]	41.83 [⊂]	123.75 [⊂]	841.34 [⊂]	143 [⊂]	49.77 [⊂]
LHA-3.5 [⊂]	559.35 [⊂]	12.5 [⊂]	20.56 [⊂]	11.64 [⊂]	3.29 [⊂]	65.74 [⊂]	89.8 [⊂]	666.83 [⊂]	131.31 [⊂]	55.87 [⊂]
LHA-4.0 [⊂]	559.57 [⊂]	12 [⊂]	12.62 [⊂]	7.25 [⊂]	-- [⊂]	16.58 [⊂]	87.18 [⊂]	621.27 [⊂]	106.81 [⊂]	37.31 [⊂]
LHA-4.5 [⊂]	559.78 [⊂]	11.5 [⊂]	20.32 [⊂]	11.38 [⊂]	34.7 [⊂]	53.54 [⊂]	144.49 [⊂]	850.38 [⊂]	128.14 [⊂]	53.91 [⊂]
LHA-5.0 [⊂]	560 [⊂]	11 [⊂]	21.22 [⊂]	0.57 [⊂]	0 [⊂]	91.57 [⊂]	855.68 [⊂]	0.0040 [⊂]	2.72 [⊂]	0.00027 [⊂]

Sishang Section

GPS position: N32°51'05.7", E107°54'08.2"

Sample [↵]	Age [↵] (Ma) [↵]	Height [↵] (m) [↵]	Ca [↵] wt% [↵]	Mg [↵] wt% [↵]	Al [↵] ppm [↵]	Na [↵] ppm [↵]	K [↵] ppm [↵]	Fe [↵] ppm [↵]	Mn [↵] ppm [↵]	Sr [↵] ppm [↵]
S21 [↵]	535.44 [↵]	124 [↵]	20.18 [↵]	11.86 [↵]	51.2 [↵]	148.03 [↵]	[↵]	727.89 [↵]	405.26 [↵]	47.95 [↵]
S20 [↵]	535.78 [↵]	122 [↵]	20.28 [↵]	12.12 [↵]	11.04 [↵]	118.41 [↵]	[↵]	194.13 [↵]	81.48 [↵]	39.27 [↵]
S19 [↵]	536.12 [↵]	120 [↵]	20.39 [↵]	12.18 [↵]	64.32 [↵]	182.02 [↵]	[↵]	601.36 [↵]	110.08 [↵]	47.4 [↵]
S18 [↵]	536.46 [↵]	118 [↵]	20.1 [↵]	11.85 [↵]	102.44 [↵]	132.05 [↵]	[↵]	765.53 [↵]	131.09 [↵]	50.78 [↵]
S17 [↵]	537.15 [↵]	114 [↵]	20.06 [↵]	11.86 [↵]	158.3 [↵]	253.2 [↵]	[↵]	470.04 [↵]	53.46 [↵]	85.38 [↵]
S16 [↵]	537.49 [↵]	112 [↵]	20.1 [↵]	12 [↵]	55.47 [↵]	264 [↵]	[↵]	905 [↵]	74.69 [↵]	80.44 [↵]
S15 [↵]	538.52 [↵]	106 [↵]	20.44 [↵]	11.97 [↵]	142.86 [↵]	297.5 [↵]	[↵]	969.85 [↵]	54.85 [↵]	79 [↵]
S14 [↵]	538.83 [↵]	104.2 [↵]	20.23 [↵]	12.06 [↵]	121.25 [↵]	282.28 [↵]	[↵]	714.23 [↵]	54.92 [↵]	72.99 [↵]
S13 [↵]	539.17 [↵]	102.2 [↵]	20.27 [↵]	11.99 [↵]	123.88 [↵]	441.13 [↵]	[↵]	1319.93 [↵]	136.17 [↵]	58.95 [↵]
S12 [↵]	539.34 [↵]	101.2 [↵]	20.3 [↵]	12.11 [↵]	182.84 [↵]	309.23 [↵]	23.39 [↵]	849.26 [↵]	82.96 [↵]	70.73 [↵]
S11 [↵]	539.56 [↵]	99.9 [↵]	20.52 [↵]	12.23 [↵]	42.43 [↵]	305.19 [↵]	[↵]	239.52 [↵]	77.16 [↵]	55.83 [↵]
S10 [↵]	539.73 [↵]	98.9 [↵]	20.38 [↵]	11.77 [↵]	140.54 [↵]	307.14 [↵]	[↵]	1220.02 [↵]	156.69 [↵]	71.9 [↵]
S9 [↵]	539.99 [↵]	97.4 [↵]	20.09 [↵]	11.46 [↵]	176.96 [↵]	337.32 [↵]	9.72 [↵]	1632.94 [↵]	214.28 [↵]	64.64 [↵]
S8 [↵]	540.09 [↵]	96.8 [↵]	20.17 [↵]	11.48 [↵]	200.89 [↵]	329.32 [↵]	26.45 [↵]	1496.2 [↵]	252.34 [↵]	78.19 [↵]
S7 [↵]	540.2 [↵]	96.2 [↵]	20.17 [↵]	11.53 [↵]	167.82 [↵]	346.17 [↵]	[↵]	1457.58 [↵]	176.87 [↵]	75.44 [↵]
S6 [↵]	540.32 [↵]	95.5 [↵]	20.08 [↵]	11.37 [↵]	256.17 [↵]	370.34 [↵]	77.08 [↵]	1459.95 [↵]	193.56 [↵]	75.4 [↵]
S5 [↵]	540.52 [↵]	94.3 [↵]	20.13 [↵]	11.52 [↵]	201.78 [↵]	414.9 [↵]	14.77 [↵]	1768.35 [↵]	209.75 [↵]	86.69 [↵]
S4 [↵]	540.64 [↵]	93.6 [↵]	20.29 [↵]	11.53 [↵]	141.15 [↵]	544.96 [↵]	[↵]	1272.93 [↵]	188.58 [↵]	100.45 [↵]
S3 [↵]	540.79 [↵]	92.7 [↵]	20.15 [↵]	11.36 [↵]	318.56 [↵]	440.63 [↵]	76.74 [↵]	1466.11 [↵]	176.97 [↵]	90.61 [↵]
S2 [↵]	540.91 [↵]	92 [↵]	20.41 [↵]	11.69 [↵]	96.91 [↵]	336.62 [↵]	[↵]	1417.15 [↵]	170.39 [↵]	73.61 [↵]
S1 [↵]	541 [↵]	91.5 [↵]	20.02 [↵]	11.1 [↵]	393.76 [↵]	546.98 [↵]	157.31 [↵]	2368.34 [↵]	169.16 [↵]	47.5 [↵]
M92 [↵]	543.76 [↵]	75.4 [↵]	35.84 [↵]	0.54 [↵]	110.31 [↵]	[↵]	76 [↵]	87.88 [↵]	165.26 [↵]	669.9 [↵]

M91	543.91	74.5	34.79	0.8	278.73		195.66	1861.82	213.49	768.48
M90	544.06	73.6	36.81	0.55	102.83		68.14	52.27	352.71	774.54
M89	544.17	73	36.66	1.08	184.49		165.3	354.07	290.11	781.67
M88	544.42	71.5	35.96	0.56	279.12		235.52	1593.73	165.24	1298.48
M87	544.61	70.4	38.13	0.32	116.13		79.14	407.23	224.66	1076.2
M86	544.78	69.4	37.15	0.46	185.86		156.61	463.64	184.72	965.67
M85	544.89	68.8	35.97	1.21	231.73		216.85	133.07	227.76	854.84
M84	545.09	67.6	34.51	2.38	207.33		150.81	353.59	250.35	388.66
M83	545.19	67	39.48	2.46	278.41		249.48	220.95	257.81	687.98
M82	545.37	66	19.79	0.13	100.66		62.92	123	45.49	722.37
M81	545.64	64.4	37.97	0.39	179.97		159.56	755.43	251.24	600.81
M80	545.71	64	35.73	0.81	190.37		163.72	1508.11	216.71	1141.44
M79	545.76	63.7	0.4	0.23	1869.84		1620.88	1045.48	33.26	6.82
M78	545.81	63.4	36.2	0.73	170.25		134.16	505.55	240.87	1137.83
M77	545.9	62.9	28.53	1.37	282.37		319.93	2156.19	206.09	689.23
M76	546.02	62.2	35.56	0.46	234.44		180.25	111.76	166.46	1009.85
M75	546.1	61.7	28.2	0.65	402.95		317.43	3693.77	433.14	809.23
M74	546.22	61	36.43	0.82	152.26		104.8	774.25	133.17	826.53
M73	546.39	60	32.81	0.1	325.64		276.59	2721.49	63.46	4919.25
M72	546.53	59.2	30.07	2.03	447.93		413.51	573.48	427.18	976.96
M71	547.25	55	33.37	1.69	533.99		384.14	2693.03	433.16	1128.8
M70	547.39	54.2	38.98	0.77	296.64		256.76	501.57	503.5	1370.2
M69	547.51	53.5	34.66	1.81	471.6		312.39	1116	518.3	1153.4
M68	547.76	52	32.88	2.82	375.27		348.48	802.45	633.91	1190.38
M67	547.93	51	34.69	0.34	443.32		408.88	1024.1	134.4	2733.64

M66	548.1	50	29.07	0.36	144.39		100.53	577.59	184.9	2851.74
M65	548.28	49	35.11	0.77	539.74		359.71	251.14	832.55	1370.99
M64	548.53	47.5	35.61	0.68	231.89		181.32	193.12	993.52	1509.43
M63	549.23	43.4	35.24	0.4	395.26		217.93	653.22	2126.15	2541.49
M62	549.34	42.8	34.22	0.29	446.69		256.33	1332.98	832.99	4330.7
M61	549.37	42.6	34.42	0.48	439.84		269.42	789.8	2157.5	2423.07
M60	549.47	42	36.74	0.69	438.22		275.05	1495.32	#VALUE!	3020.73
M59	549.56	41.5	34.91	0.64	315.87		155.68	952.33	4156.49	2472.53
M58	549.64	41	35.81	0.45	351.94		233.47	1496.7	3031.18	2367.48
M56	549.82	40	37.71	0.4	295.07		120.44	335.91	2171.21	2916.09
M55	549.87	39.7	38.68	0.56	367.63		146.97	1509.7	3980.16	3059.3
M54	549.99	39	39.57	0.54	314.21		109	343.62	1775.73	2897.88
M53	550.09	38.4	38.87	0.39	304.97		94.22	417.4	3256.04	1957.57
M52	550.14	38.1	31.7	0.71	516.84		295.41	766.22	3618.22	2588.38
M51	550.21	37.7	31.76	0.49	620.03		222.7	890.86	3548.31	2074.49
M49	550.42	36.5	26.54	0.43	661.6		342.52	950.96	1868.36	2902.96
M48	550.67	35	29.11	0.98	654.19		329.86	1781.79	1909.81	1071.31
M46	550.84	34	36.74	0.52	152.96		65.26	419.22	308.05	632.54
M45	550.93	33.5	39.31	0.23	165.74		77.95	382.94	223.41	581.2
M44	551.01	33	37.04	0.34	200.01		78	470.1	220.59	439.14
M43	551.1	32.5	38.57	0.33	176.74		61.01	547.56	209.28	531.16
M42	551.21	32	26.72	4.19	430.82		330.45	7614.69	485.77	313.7
M41	551.33	31.5	35.91	0.43	501.45		94.11	1819.31	632.99	360.86
M40	551.44	31	37.52	0.37	650.1		135.26	2081.8	712.32	350.98
M39	551.55	30.5	35.13	0.32	434.25		127.83	1835.46	510.46	324.21

M38	551.66	30	35.68	0.34	499.09		146.66	1573.48	186.07	327.96
M37	551.78	29.5	34.87	0.38	441.54		134.64	1497.82	113.82	350.52
M36	552.34	27	35.97	0.34	508.03		186.51	2826.39	234.29	300.23
M35	552.56	26	33.38	0.28	578.55		204.68	2930.68	217.35	260.42
M32	552.9	24.5	36.03	0.33	513.25		173	2310.87	264.65	294.9
M31	553.02	24	35.25	0.28	562.24		208.72	2202.92	236.95	258.19
M30	553.24	23	37.78	0.29	556.54		212	2299.46	280.99	264.78
S22	553.35	22.5	32.68	0.32	1348.24	80.91	330.2	3779.17	147.55	253.5
S23	553.47	22	32.12	0.33	1210.7	93.24	444.75	3094.75	147.62	265.46
M29	553.51	21.8	35.55	0.35	463.49		138.12	1912.73	314.92	260.38
S24	553.58	21.5	32.72	0.32	1100.39	108.4	226.01	3437.3	138.69	230.15
S25	553.69	21	32.18	0.31	1165.48	76.78	301.4	2983	124.39	250.95
S26	553.8	20.5	33.06	0.33	1341.9	92.36	580.35	2838.27	136.08	246.24
M27	553.89	20.1	33.65	0.27	549.31	169.32	75.61	2137.61	259.7	265.49
S27	553.92	20	33.27	0.33	1185.69	76.85	258.81	3738.26	119.17	248.88
S28	554.03	19.5	33.73	0.33	1257.08	77.87	243.8	3869.48	134.94	246.67
M26	554.12	19.1	32.32	0.38	2258.15	190.29	94.61	5419.27	294.53	244.07
S29	554.14	19	33.26	0.29	930.5	87.34	202.69	3463.58	112.19	249.33
S30	554.25	18.5	33.37	0.32	1270.6	96.99	373.44	4010.59	112.44	238.05
S31	554.37	18	33.85	0.29	994.95	72.21	271.51	3446.13	114.35	251.88
S32	554.48	17.5	31.37	0.29	1195.03	76.25	312.82	3782.19	131.55	224.98
S33	554.59	17	33.83	0.27	692.94	70.38	135.16	3048.52	132.61	257.79
M23	554.64	16.8	34.63	0.24	233.67	178.88	112.03	1629.65	239.01	290.97
S34	554.71	16.5	33.57	0.31	1110.82	71.75	247.11	3756.58	157.83	248.51
S35	554.82	16	32.88	0.3	1243.75	245.87	280.04	4116.79	143.97	251.86

S36	554.93	15.5	33.85	0.27	611.51	325.96	278.02	2585.21	125.62	237.78
S37	555.04	15	34.53	0.27	610.98	88.82	281.83	2593.98	127.5	252.4
S38	555.16	14.5	33.55	0.29	947.08	248.44	309.51	3746.84	137.96	247.19
S39	555.27	14	32.52	0.26	612.85	92.28	286.22	2879.15	137.26	263.49
S40	555.38	13.5	33.8	0.3	1257.09	433.83	657.87	3973.58	136.29	263.34
S41	555.49	13	34.02	0.31	1163.81	106.04	522.3	3567.62	137.71	265.61
S42	555.61	12.5	34.27	0.32	990.6	111.98	408.27	3494.58	132.46	255.9
S43	555.72	12	32.84	0.26	857.54	72.44	430.91	2824.92	127.85	246.95
M18	555.72	12	28.64	0.29	1645.26	145.41	631.95	3791.23	268.56	225.19
S44	555.83	11.5	34.73	0.28	790.73	68.97	299.11	3143.1	144.24	253.73
S45	555.94	11	33.92	0.28	847.48	97.72	373.23	3044.52	129.63	254.76
S46	556.06	10.5	34.15	0.33	1690.85	148.6	496.09	4815.77	124.87	250.2
S47	556.17	10	34.63	0.31	1098.83	147.54	445.94	3383.54	103.04	250.29
S48	556.26	9.6	34.56	0.31	1183.11	141.59	417.09	3674.11	126.04	250.04
S49	556.39	9	36.81	0.33	1296.69	180.48	968.71	3796.46	139.86	262.2
S50	556.51	8.5	34.41	0.34	1603.57	147.66	460.26	4100.23	140.67	246.1
M13	556.62	8	34.66	0.26	445.99	485.61	357.62	1936.71	222.42	294.3
S51	556.67	7.8	33.56	0.26	699.61	149.53	414.63	2092.3	108.22	234.94
M12	556.73	7.5	35.34	0.25	341.59	246.04	374.14	1969.89	257.21	286.83
S52	556.85	7	33.56	0.25	739.44	193.73	465.89	4384.27	102.26	237.33
M11	556.91	6.7	34.11	0.24	285.89	156.56	334.76	1769.66	229.9	301.07
S53	556.98	6.4	33.87	0.25	819.48	112.5	380.04	3613.97	97.56	244.22
M10	557.09	5.9	34.12	0.24	357.08	122.05	384.47	1953.42	273.56	266.69
S54	557.12	5.8	34.9	0.26	506.59	104.34	204.22	3440.58	101.51	234.49
M9	557.18	5.5	33.91	0.28	1204.28	159.78	881.19	3041.98	272.34	246.54

S55	557.23	5.3	34.61	0.28	832.58	627.25	206.83	3510.19	77.93	234.16
M8	557.3	5	34.77	0.27	634.9	178.39	309.96	2635.03	239.08	246.79
S56	557.32	4.9	33.6	0.29	841.84	99.75	232.01	3826.59	77.5	252.19
M7	557.41	4.5	35.19	0.29	881.39	127.52	239.27	2982.58	246.8	230.5
S57	557.43	4.4	35.14	0.27	897.69	76.79	490.38	3639.4	99.31	230.87
S58	557.52	4	33.72	0.31	1155.93	77.64	439.41	3739.95	90.95	234.15
M5	557.63	3.5	35.1	0.32	1133.24	131.78	334.66	3911.74	295.95	256.35
S59	557.75	3	34.43	0.29	775.31	134.44	432.93	1727.78	69.65	232.34
S60	557.86	2.5	34.62	0.31	863.03	69.58	388.6	3115.19	68.32	259.68
M2	557.95	2.1	33.69	0.34	1897.14	213.88	370.17	5798.68	356.22	273.67
S61	557.97	2	34.13	0.33	1210.53	76.39	401.69	3342.48	120.83	279.62
S62	558.06	1.6	14.63	7.07	2023.14	86.13	1323.67	6100.32	215.36	92.84
S63	558.2	1	12.89	6.29	2779.61	70.62	1396.62	7148.04	121.8	75.07
S64	558.29	0.6	14.47	7.38	1551.82	165	1019.33	4741.61	129.44	81.23
S65	558.42	0	14.76	8.35	1162.1	116.1	718.86	3444.72	124.54	116.58
S66	558.47	-0.2	15.79	8.9	1216.43	100.46	905.33	3002.45	128.16	240.83
S67	558.56	-0.6	33.51	0.28	977.2	112.13	369.86	3672.28	91.2	223.28
S68	558.65	-1	33.77	0.26	722.87	104.93	181.78	3323.55	74.45	224.3
S69	558.78	-1.6	16.47	9.16	971.64	132.28	434.57	5013.18	128.09	386.81
S70	558.92	-2.2	17.58	9.72	2283.33	177.24	1387.98	5591.02	114.09	515.77
S71	559.03	-2.7	18.11	9.74	259.97		146.46	2825.94	96.95	724.24
S72	559.12	-3.1	16.13	7.39	1939.02		1273.7	5587.5	222.95	178.81
S74	559.23	-3.6	27.25	3.12	1145.13		502.45	7668.94	169.86	434.81
S75	559.28	-3.8	30.69	2.1	731.01		401.84	1677.01	127.41	605.18
S76	559.32	-4	37.5	1.07	968.12		524.62	1302.51	105.91	809.08

S77	559.37	-4.2	32.24	1.75	883.53		439.02	2187.48	125.24	531.64
S80	559.57	-5.1	38.49	1.29	364.76		157.85	1496.24	113.25	912.17
S81	559.82	-6.2	38.39	1.17	173.38		57.75	1038.64	77.89	1070.18
S82	559.91	-6.6	33.91	1.5	633.04		275.55	2713.26	133.47	972.77
S83	560	-7	34.41	1.12	275.97		115.05	959.1	66.11	757.39
S84	560.09	-7.4	37.37	1.2	198.6		36.86	831.54	65.7	743.81
S85	560.32	-8.4	32.97	2.25	1179.44		313.15	3674.45	118.92	1357.99
S86	560.45	-9	32.65	1.36	1143.01		318.94	2637.66	92.39	690.28
S87	560.54	-9.4	35.81	1.77	669.4		179.55	1936.67	66.47	648.99
S88	560.68	-10	36.08	2.14	913.29		315.85	3224.6	99.76	804.25
S90	560.92	-11.1	33	1.84	405.63		61.31	1170.28	63.43	710.75
S91	561.15	-12.1	35.5	1.82	2223.52		403.9	3880.58	116.7	1211.27
S92	561.28	-12.7	20.19	7.2	5269.06		1288.89	8346.61	204.08	474.9
S93	561.35	-13	15.7	8.48	--		1339.17	6929.43	169.48	219.74
S94	561.46	-13.5	35.92	1.87	669.47		124.42	2843.41	80.69	1563.62
S95	561.55	-13.9	15.43	8.14	5157.37		877.41	7136.53	180.29	287.49
S96	561.62	-14.2	16.83	9.17	--		1139.9	6764.81	203.18	277.71
S97	561.76	-14.8	34.08	2.18	941.67		130.82	1732.65	88.84	1477.43
S98	561.83	-15.1	32.04	2.21	2200.86		377.39	2794.6	76.43	1458.6
16SS7	563.61	-23	35.39	2.04	50.96	163.28	121.66	189.39	51.68	541.56
16ss5.5	563.94	-24.5	33.77	1.38	225.02	150.67	207.4	2051.09	74.05	1039.41
16ss4	564.28	-26	32.44	0.4	314.47	132.35	168.5	2371.72	79.56	1448.04
16ss3	564.51	-27	32.9	2.11	520.18	132.35	250.76	1496.77	114.94	1146.87
16ss2	564.73	-28	17.99	6.86	1338.24	28.95	1303.07	5995.72	135.45	210.16
16ss0.8	565	-29.2	17.91	5.38	2126.19	59.8	1393.72	7537.17	175.91	574.7

Qinglinkou Section

GPS position: N30°47'45.22", E110°55'15.81"

Sample [↵]	Age [↵] (Ma) [↵]	Height [↵] (m) [↵]	Ca [↵] wt% [↵]	Mg [↵] wt% [↵]	Al [↵] ppm [↵]	Na [↵] ppm [↵]	K [↵] ppm [↵]	Fe [↵] ppm [↵]	Mn [↵] ppm [↵]	Sr [↵] ppm [↵]
Q218 [↵]	543.4 [↵]	302.9 [↵]	35.76 [↵]	2.9 [↵]	126.37 [↵]	223.19 [↵]	[↵]	206.35 [↵]	48.33 [↵]	1556.73 [↵]
Q217 [↵]	543.56 [↵]	300.4 [↵]	37.11 [↵]	0.55 [↵]	81.84 [↵]	271.56 [↵]	[↵]	22.79 [↵]	18.01 [↵]	2245.71 [↵]
Q216 [↵]	543.8 [↵]	296.9 [↵]	38.52 [↵]	1.38 [↵]	96.46 [↵]	232.88 [↵]	[↵]	27.48 [↵]	40.41 [↵]	2061.77 [↵]
Q215 [↵]	543.91 [↵]	295.1 [↵]	36.1 [↵]	0.79 [↵]	52.29 [↵]	194.4 [↵]	[↵]	19.63 [↵]	19.24 [↵]	2127.5 [↵]
Q214 [↵]	544.07 [↵]	292.8 [↵]	38.94 [↵]	1.15 [↵]	100.22 [↵]	185.06 [↵]	[↵]	159.25 [↵]	15.63 [↵]	2179.11 [↵]
Q213 [↵]	544.36 [↵]	288.3 [↵]	34.53 [↵]	3.2 [↵]	124.33 [↵]	152.02 [↵]	[↵]	123.54 [↵]	12.85 [↵]	709.59 [↵]
Q212 [↵]	544.49 [↵]	286.4 [↵]	33.96 [↵]	1.74 [↵]	68.11 [↵]	178.69 [↵]	[↵]	59.68 [↵]	35.08 [↵]	706.31 [↵]
Q211 [↵]	545.41 [↵]	272.4 [↵]	34.5 [↵]	0.66 [↵]	47.31 [↵]	103.66 [↵]	[↵]	66.89 [↵]	50.63 [↵]	1064.67 [↵]
Q210 [↵]	545.54 [↵]	270.5 [↵]	36.7 [↵]	0.5 [↵]	39.33 [↵]	56.23 [↵]	19.66 [↵]	8.26 [↵]	37.85 [↵]	480.43 [↵]
Q209 [↵]	545.8 [↵]	266.5 [↵]	34.32 [↵]	1.78 [↵]	82.86 [↵]	309.15 [↵]	[↵]	134.63 [↵]	26.67 [↵]	932.53 [↵]
Q208 [↵]	546 [↵]	263.5 [↵]	36.42 [↵]	2.92 [↵]	122.39 [↵]	499.85 [↵]	[↵]	120.65 [↵]	31.21 [↵]	1016.89 [↵]
Q207 [↵]	546.16 [↵]	261 [↵]	34.81 [↵]	0.72 [↵]	126.83 [↵]	201.82 [↵]	61.18 [↵]	45.39 [↵]	29.82 [↵]	1027.58 [↵]
Q206 [↵]	546.4 [↵]	257.4 [↵]	34.84 [↵]	0.31 [↵]	65.66 [↵]	103 [↵]	[↵]	47.56 [↵]	14.04 [↵]	1060.78 [↵]
Q205 [↵]	546.58 [↵]	254.7 [↵]	34.35 [↵]	2.29 [↵]	103.39 [↵]	99.87 [↵]	[↵]	57.53 [↵]	30.76 [↵]	466.77 [↵]
Q204 [↵]	546.77 [↵]	251.9 [↵]	36.75 [↵]	1.2 [↵]	73.75 [↵]	144.41 [↵]	[↵]	99.19 [↵]	35.41 [↵]	955.13 [↵]
Q203 [↵]	546.91 [↵]	249.7 [↵]	37.21 [↵]	0.37 [↵]	44 [↵]	88.37 [↵]	[↵]	12.34 [↵]	20.13 [↵]	757.1 [↵]
Q202 [↵]	547.04 [↵]	247.7 [↵]	37.28 [↵]	1.33 [↵]	83.33 [↵]	106.59 [↵]	12.73 [↵]	52.74 [↵]	33.28 [↵]	767.06 [↵]
Q201 [↵]	547.34 [↵]	243.2 [↵]	36.16 [↵]	1.84 [↵]	158.42 [↵]	276.51 [↵]	20.06 [↵]	116.75 [↵]	17.73 [↵]	1772.64 [↵]
Q200 [↵]	547.52 [↵]	240.4 [↵]	37.24 [↵]	0.35 [↵]	66.24 [↵]	99.31 [↵]	33.55 [↵]	16.65 [↵]	20.33 [↵]	665.63 [↵]
Q199 [↵]	547.65 [↵]	238.5 [↵]	34.63 [↵]	1.01 [↵]	41.18 [↵]	233.56 [↵]	22.53 [↵]	147.72 [↵]	92 [↵]	396.59 [↵]
Q198 [↵]	547.85 [↵]	235.4 [↵]	36.9 [↵]	1.25 [↵]	51.57 [↵]	127.34 [↵]	[↵]	24.41 [↵]	11.27 [↵]	723.5 [↵]
Q197 [↵]	548 [↵]	233.2 [↵]	36.09 [↵]	1.73 [↵]	148.02 [↵]	212.74 [↵]	[↵]	17.58 [↵]	34.48 [↵]	1642.78 [↵]

Q196	548.13	231.2	39.32	0.51	86.01	205.39		54.06	26.39	1582.5
Q195	548.31	228.5	36.46	1.19	83.12	188.82	14.52	87.37	23.7	1324.06
Q194	548.44	226.5	35.22	1.17	132.25	236.08	27.65	82.34	66.56	1263
QLKS8	548.62	223.8	35.4	1.93	93.55			29.54	40.37	1358.94
QLKS7	548.66	223.2	28.5	6.45	106.69			4.85	151.79	320.08
QLKS6	548.7	222.5	36.65	1.19	47.71			4.77	32.92	1125.95
Q193	548.77	221.5	33.71	3.42	231.99	220.89	40.65	104.82	11.33	1900.23
Q191	548.98	218.4	31.73	3.26	173.82	216.6		190.96	22.32	819.79
Q190	549.08	216.8	33.33	2.52	113.9	298.19		62.1	8.98	1731.69
Q189	549.18	215.3	39.16	0.6	74.22	257.28		87.31	14.58	1843.35
Q188	549.28	213.8	35.44	2.82	118.57	382.61	23.97	162.74	12.79	1132.98
Q187	549.36	212.5	35.37	2.05	155.45	394.46	14.48	193	12.13	1745.57
Q186	549.48	210.7	33.99	3.4	153.36	436.83		83.49	17.26	915.5
Q185	549.54	209.8	35.71	2.36	163.89	253.35	35.72	441.5	36.07	1244.24
Q184	549.63	208.5	37.23	0.18	48.86	199.87		158.13	14.61	1285.72
Q183	549.77	206.3	35.29	1.12	78.68	354.08	40.36	87.39	6.44	1705.01
Q182	549.89	204.5	34.94	0.13	42.23	60.97		172.5	25.51	593.77
Q181	550	202.9	38.33	0.59	54.67	249.39	15.63	99.24	14.6	1808.72
Q180	550.1	201.4	27.91	7.06	225.6	131.65		172.29	26.87	220.7
Q179	550.18	200.2	36.3	1.31	48.41	96.95		31.08	6.42	263.75
Q178	550.25	199.1	38	0.59	45.42	92.89	26.12	82.46	7.46	372.63
Q177	550.31	198.1	38.76	0.45	40.53	121.52		16.81	7.93	662.34
Q176	550.43	196.3	33.4	0.37	284.95	120.34	178.67	673.53	19.54	1763.86
Q175	550.5	195.3	38.87	0.74	110.76	171.01	63.86	54.68	10.81	1305.63
Q174	550.59	194	34.74	0.35	66.81	137.68		56.27	13.29	672.26

Q173	550.68	192.5	29.59	4.19	365.46	236.17	197	336.58	36.66	992.51
Q172	550.76	191.3	29.2	5.04	184.91	220.62	77.41	23.08	53.55	343.23
Q171	550.86	189.8	21.78	11.51	219.13	275.67	71.02	53.28	73.93	88.15
Q170	550.93	188.8	19.07	10.59	149.48	347.68		187.46	45.33	89.29
Q169	551.05	187	16.33	9.14	159.16	145.17	44.97	108.23	43.89	63.57
Q168	551.1	186.2	15.19	8.6	124.71	184.49	54.76	602.61	64.81	60.62
Q163	556.6	178.4	19.53	11.06	123.48	182.73	34.11	4912.37	208.02	89.67
Q160	556.89	175.9	19.32	10.88	432.01	351.85	249.56	569.78	247.65	77.87
Q158	557.76	167.4	19.61	11.15	418.34	275.54	272.85	795.97	235.47	70.62
Q157	558.02	164.9	20.41	11.38	225.3	211.9	72.66	336.51	151.58	103.76
Q156	558.53	159.9	21.06	12.05	128.68	251.99	36.58	661.45	613.83	64.55
Q154	558.75	157.8	18.47	10.44	318.27	196.18	305.76	2470.23	227.95	55.16
Q153	559.45	151	17.12	9.68	463.37	192.32	456.6	1525.35	173.73	54.19
Q152	559.72	148.3	16.71	9.58	489.75	166.62	506.11	1264.52	139.8	44.22
Q151	559.77	147.8	21.46	12.4	53.43	131.27		980.89	129.09	58.79
Q150	559.86	147	20.2	11.59	147.46	155.88	106.13	1060.41	142.91	65.41
Q149	560	145.6	20.55	11.79	145.35	182	91.46	1871.11	200.32	63.93
Q148	560.18	143.8	21.1	11.84	207.76	143.23	179.06	1480.15	259.26	96.75
Q147	560.37	142	20.24	11.24	135.05	200.86	72.82	4994.51	276.24	49.01
Q145	560.57	140.1	19.3	11.08	105.97	124.11	124.6	972.34	184.13	36.49
Q144	560.79	137.9	18.73	10.61	277.71	210.8	302.69	995.47	163.58	44.21
Q143	560.87	137.1	17.11	9.64	1296.43	189.35	646.33	749.04	151	92.27
Q142	561.02	135.7	18.96	10.05	384.08	279.33	164.74	534.46	112.63	101.99
Q141	561.15	134.4	18.13	9.77	405.4	205.3	115.57	434.03	114.77	157.42
Q140	561.34	132.6	17.54	9.4	2502.77	556.3	1047.74	851.28	122.37	172.84

Q139	561.63	129.7	19.3	9.19	352.31	408.82	130.96	736.55	109.61	169.5
Q138	561.77	128.4	18.5	8.91	1316.24	512.44	409.18	738.23	101.75	235.86
Q137	561.89	127.2	19.27	9.4	184.42	379.96	62.24	593.09	76.06	186.14
Q73	568.74	105.2	15.35	9.5	2016.1	293.04	319.62	6333.75	149.07	476.18
Q72	571.23	101.2	17.54	10.25	825.43	248.3	221.55	1502.54	122.37	394.45
Q71	571.92	100.1	14.77	8.7	1194.38		235.19	3139.21	103.01	372.5
Q70	572.67	98.9	16.16	9.95	3225.25		614.53	2062.5	105.37	492.7
Q69	576.35	93	14.27	8.14	1327.8		109.53	5190.85	159.11	632.24
Q68	576.91	92.1	16.59	10.15	3456.06		201.44	10061.82	208.34	523.72
Q67	577.78	90.7	16.24	9.78	4778.31		716.27	6188.16	188.53	687.66
Q66	578.53	89.5	17.46	7.52	606.82			3579.41	209.78	629.37
Q61	583.58	81.4	14.18	8.26	912.8		207.63	2455.92	196.39	462.39
Q59	586.14	77.3	11.86	7.14	1236.75		60.19	4167.94	214.36	404.08
Q57	590.13	70.9	15.6	9.15	581.74			5967.57	290.03	635.68
Q56	596.05	61.4	13.54	7.64	888.77		57.84	8324.2	215.11	408.83
Q55	596.43	60.8	18.15	10.43	469.9		87.55	4722.59	314.6	565.99
Q52	600.35	54.5	13.77	7.62	424.48		197.54	4198.52	263.45	513.78
Q51	600.73	53.9	13.78	7.68	749.9		123.27	5627.99	271.33	491.11
Q47	606.22	45.1	28.25	1.41	560.38			2253.94	324.35	501.29
Q45	607.34	43.3	28.57	1.3	699.18			2524.71	273.06	644.91
Q43	608.09	42.1	23.8	1.04	283.99		32.75	770.76	167.17	547.07
Q41	608.68	41.15	20.12	0.46	183.16			415.47	143.98	374.95
Q39	608.80	40.95	17.25	1.42	541.75		164.35	1245.68	138.85	319.17
Q36	610.42	38.35	15.96	4.9	733.2		77.79	6981.83	1199.13	273.95
Q35	611.11	37.25	15.63	3.64	1119.09		102.84	8018.86	869.8	288.78

Q32	614.54	31.75	9.94	4.83	2026.74		335.08	14062.62	2075.74	75.54
Q31	615.54	30.15	25.5	2.56	538.89		38.01	6624.27	1975.75	190.88
Q30	616.41	28.75	9.9	4.63	2276.15		432.14	12324.95	1460.08	94.6
Q29	616.79	28.15	14.76	6.25	880.91		98.95	9970.39	1371.42	108.72
Q28	617.10	27.65	13.71	6.38	1085.67		197.17	14755.11	2326.75	129.16
Q27	617.91	26.35	11.86	5.08	785.59		106.23	12559.74	1509.31	197.78
Q26	618.34	25.65	11.31	5.18	1193.92		298.32	11165.61	1528.53	148.84
Q24	619.53	23.75	31.6	0.96	181.01		48.55	3858.41	2972	268.15
Q23	620.09	22.85	12.94	6	863.15		104.99	11086.46	2337.65	68.67
Q22	620.65	21.95	8.47	3.31	1866.6		694.18	6755.42	1422.95	82.37
Q21	621.34	20.85	9.69	4.81	1715.82		458.28	9434.1	1757.58	44.59
Q20	622.09	19.65	13.11	6.47	1616.62		254.46	8143.98	1411.26	60.82
Q19	622.65	18.75	13.01	5.34	2177.83		281.2	14327.53	2560.29	86.63
Q17	624.27	16.15	8.23	3.79	1680.06		815.26	4071.57	842.94	43.91
Q15	625.17	14.7	13.36	5.64	733.2		153.69	9837.49	965.67	91.74
Q14	626.01	13.35	11.53	5.16	912.23		157.44	10278.97	1279.59	69.23
Q13	626.83	12.05	12.84	6.26	2365.41		157.12	10213.07	1229.69	80.45
Q12	627.26	11.35	8.99	4.81	4981.58		323.14	13080.49	541.25	36.67
Q11	627.76	10.55	12.4	5.35	1714.83		202.32	12539.89	2266.07	103.18
Q10N	627.94	10.27	22.86	0.76	1429.92		239.47	4317.6	3796.65	150.07
Q10	628.04	10.1	10.64	5.04	2734.03		484.85	10225.14	1403.52	70.57
Q4	632.50	2.95	19.62	10.63	221.31		182.12	4626.87	2968.69	50.72
Q3	633.23	2.15	21.03	10.17	237.57		159.46	3860.9	3010.79	76.27
Q2	634.61	0.65	19.55	10.18	265.88		155.23	4508.84	2991.03	64.5
Q1	635.20	0	19.67	9.66	383.08		178.17	2362.95	1728.85	80.94

APPENDIX C: RAW DATA FROM ICP-MS TEST

Lianghong section

GPS position: N29°04'53.2", E102°49'01.7"

Sample	Age Ma	Height m	U ppt	V ppt	Mo ppt	U/Sc w/w	V/Sc w/w	Mo/Sc w/w
LHC21.7	543.2	49.7	0.58	6.78	0.23	1.08	12.65	0.44
LHC21.0	543.5	49						
LHC20.0	543.94	48	0.64	6.84	0.18	1.22	13.16	0.34
LHC19.0	544.37	47						
LHC18.0	544.8	46	0.57	7.34	0.18	1.35	17.46	0.42
LHC17.0	545.24	45						
LHC16.0	545.67	44						
LHC15.0	546.11	43	1.33	8.20	0.59	2.02	12.46	0.90
LHC14.0	546.54	42						
LHC13.0	546.98	41						
LHC12.0	547.41	40	0.92	7.22	0.29	1.30	10.16	0.41
LHC11.0	547.84	39						
LHC10.0	548.28	38	0.43	7.72	0.25	0.80	14.21	0.45
LHC9.0	548.71	37						
LHC8.0	549.15	36						
LHC7.1	549.54	35.1	0.84	15.34	6.76	0.57	10.39	4.58
LHC6.0	550.01	34	1.96	7.65	0.34	3.09	12.04	0.54

LHC5.0↵	550.45↵	33↵	1.50 ↵	11.97 ↵	0.92 ↵	1.87 ↵	14.98 ↵	1.15 ↵
LHC4.0↵	550.88↵	32↵	2.81 ↵	8.84 ↵	0.75 ↵	3.52 ↵	11.09 ↵	0.94 ↵
LHC3.5↵	551.1↵	31.5↵	↵	↵	↵	↵	↵	↵
LHC2.0↵	551.75↵	30↵	3.16 ↵	11.51 ↵	0.60 ↵	3.33 ↵	12.11 ↵	0.63 ↵
LHC1.5↵	551.97↵	29.5↵	↵	↵	↵	↵	↵	↵
LHC1.1↵	552.14↵	29.1↵	↵	↵	↵	↵	↵	↵
LHC0.6↵	552.36↵	28.6↵	3.39 ↵	7.97 ↵	0.15 ↵	5.42 ↵	12.74 ↵	0.24 ↵
LHC-0.7↵	552.92↵	27.3↵	↵	↵	↵	↵	↵	↵
LHC-1.1↵	553.1↵	26.9↵	0.36 ↵	9.30 ↵	0.10 ↵	0.20 ↵	5.15 ↵	0.05 ↵
LHA10.5↵	553.27↵	26.5↵	0.36 ↵	7.66 ↵	0.07 ↵	0.30 ↵	6.34 ↵	0.06 ↵
LHA10.0↵	553.49↵	26↵	↵	↵	↵	↵	↵	↵
LHA9.5↵	553.7↵	25.5↵	0.34 ↵	5.41 ↵	0.09 ↵	0.27 ↵	4.31 ↵	0.07 ↵
LHA9.0↵	553.92↵	25↵	↵	↵	↵	↵	↵	↵
LHA8.5↵	554.14↵	24.5↵	0.28 ↵	7.69 ↵	0.41 ↵	0.20 ↵	5.65 ↵	0.30 ↵
LHA8.0↵	554.36↵	24↵	↵	↵	↵	↵	↵	↵
LHA7.5↵	554.57↵	23.5↵	0.48 ↵	6.81 ↵	0.22 ↵	0.27 ↵	3.87 ↵	0.13 ↵
LHA7.0↵	554.79↵	23↵	↵	↵	↵	↵	↵	↵
LHA6.5↵	555.01↵	22.5↵	0.22 ↵	7.52 ↵	0.11 ↵	0.21 ↵	7.20 ↵	0.10 ↵
LHA6.0↵	555.22↵	22↵	0.20 ↵	7.65 ↵	0.31 ↵	0.18 ↵	7.01 ↵	0.28 ↵
LHA5.5↵	555.44↵	21.5↵	0.20 ↵	7.79 ↵	0.07 ↵	0.17 ↵	6.74 ↵	0.06 ↵
LHA5.0↵	555.66↵	21↵	0.19 ↵	7.71 ↵	0.18 ↵	0.13 ↵	5.35 ↵	0.12 ↵
LHA4.5↵	555.88↵	20.5↵	0.30 ↵	7.12 ↵	0.13 ↵	0.17 ↵	4.09 ↵	0.08 ↵

LHA4.0↵	556.09↵	20↵	0.22 ↵	7.52 ↵	0.24 ↵	0.21 ↵	7.10 ↵	0.23 ↵
LHA3.5↵	556.31↵	19.5↵	0.22 ↵	7.78 ↵	0.10 ↵	0.19 ↵	6.69 ↵	0.09 ↵
LHA2.5↵	556.74↵	18.5↵	0.30 ↵	7.73 ↵	0.14 ↵	0.18 ↵	4.57 ↵	0.08 ↵
LHA1.9↵	557↵	17.9↵	0.35 ↵	7.39 ↵	0.20 ↵	0.17 ↵	3.50 ↵	0.09 ↵
LHA1.0↵	557.4↵	17↵	0.22 ↵	9.52 ↵	0.05 ↵	0.14 ↵	6.17 ↵	0.03 ↵
LHA0.4↵	557.66↵	16.4↵	↵	↵	↵	↵	↵	↵
LHA0.05↵	557.81↵	16.05↵	0.41 ↵	10.71 ↵	0.20 ↵	1.37 ↵	35.45 ↵	0.65 ↵
LHA0.0↵	557.83↵	16↵	↵	↵	↵	↵	↵	↵
LHA-0.2↵	557.92↵	15.8↵	0.32 ↵	11.49 ↵	0.08 ↵	1.15 ↵	41.35 ↵	0.29 ↵
LHA-1.0↵	558.26↵	15↵	↵	↵	↵	↵	↵	↵
LHA-1.6↵	558.52↵	14.4↵	0.29 ↵	11.84 ↵	0.07 ↵	1.11 ↵	44.88 ↵	0.26 ↵
LHA-2.3↵	558.83↵	13.7↵	0.28 ↵	19.46 ↵	0.10 ↵	0.92 ↵	63.84 ↵	0.33 ↵
LHA-3.0↵	559.13↵	13↵	↵	↵	↵	↵	↵	↵
LHA-3.5↵	559.35↵	12.5↵	0.29 ↵	12.81 ↵	0.09 ↵	1.17 ↵	52.46 ↵	0.38 ↵
LHA-4.0↵	559.57↵	12↵	↵	↵	↵	↵	↵	↵
LHA-4.5↵	559.78↵	11.5↵	0.12 ↵	12.30 ↵	0.10 ↵	0.40 ↵	41.45 ↵	0.33 ↵
LHA-5.0↵	560↵	11↵	↵	↵	↵	↵	↵	↵

Sishang Section

GPS position: N32°51'05.7", E107°54'08.2"

Sample	Age (Ma)	Height (m)	U ppm	V ppm	Mo ppm	U/Sc w/w	V/Sc w/w	Mo/Sc w/w
S21	535.44	124	0.14	11.07	0.61	0.07	6.04	0.33
S20	535.78	122						
S19	536.12	120	0.29	10.40	0.24	0.17	5.87	0.13
S18	536.46	118						
S17	537.15	114	0.99	11.26	0.20	0.56	6.36	0.11
S16	537.49	112						
S15	538.52	106						
S14	538.83	104.2	0.59	10.78	0.54	0.36	6.55	0.33
S13	539.17	102.2						
S12	539.34	101.2	0.45	15.16	0.12	0.26	8.63	0.07
S11	539.56	99.9						
S10	539.73	98.9	2.30	20.17	0.22	1.14	10.00	0.11
S9	539.99	97.4						
S8	540.09	96.8						
S7	540.2	96.2	1.41	12.25	0.14	0.78	6.76	0.08
S6	540.32	95.5						
S5	540.52	94.3						
S4	540.64	93.6	3.45	14.63	3.45	2.03	8.59	2.03
S3	540.79	92.7						
S2	540.91	92	3.61	20.92	0.26	1.97	11.41	0.14
S1	541	91.5						
M92	543.76	75.4	1.23	13.61	0.36	0.38	4.18	0.11
M91	543.91	74.5						

M90	544.06	73.6						
M89	544.17	73	1.37	13.61	0.51	0.41	4.09	0.15
M88	544.42	71.5						
M87	544.61	70.4	1.13	13.02	0.34	0.34	3.88	0.10
M86	544.78	69.4						
M85	544.89	68.8	1.30	13.23	0.43	0.35	3.52	0.12
M84	545.09	67.6						
M83	545.19	67	1.27	13.48	0.53	0.30	3.13	0.12
M82	545.37	66						
M81	545.64	64.4						
M80	545.71	64	1.62	12.92	0.29	0.45	3.57	0.08
M79	545.76	63.7						
M78	545.81	63.4						
M77	545.9	62.9						
M76	546.02	62.2						
M75	546.1	61.7	1.52	10.21	2.73	0.44	2.92	0.78
M74	546.22	61						
M73	546.39	60						
M72	546.53	59.2	1.29	11.64	4.76	0.31	2.83	1.16
M71	547.25	55	1.79	12.36	0.83	0.38	2.62	0.18
M70	547.39	54.2						
M69	547.51	53.5	1.58	13.46	0.60	0.36	3.03	0.14
M68	547.76	52						
M67	547.93	51	2.79	11.75	1.01	0.80	3.36	0.29
M66	548.1	50						
M65	548.28	49						

M64	548.53	47.5	1.20	11.79	0.53	0.34	3.36	0.15
M63	549.23	43.4						
M62	549.34	42.8						
M61	549.37	42.6	1.94	13.52	0.44	0.55	3.81	0.12
M60	549.47	42						
M59	549.56	41.5	1.57	13.28	1.24	0.48	4.11	0.38
M58	549.64	41						
M56	549.82	40						
M55	549.87	39.7	2.64	14.96	0.94	0.68	3.84	0.24
M54	549.99	39						
M53	550.09	38.4	2.07	15.76	0.31	0.48	3.64	0.07
M52	550.14	38.1						
M51	550.21	37.7	3.09	12.17	1.11	0.79	3.12	0.28
M49	550.42	36.5	3.03	11.52	2.07	0.80	3.05	0.55
M48	550.67	35	4.03	16.44	3.92	1.09	4.44	1.06
M46	550.84	34	4.04	18.04	2.82	1.12	5.00	0.78
M45	550.93	33.5	4.60	16.74	1.12	1.09	3.96	0.26
M44	551.01	33	4.51	13.62	0.20	1.23	3.70	0.06
M43	551.1	32.5	5.50	15.97	0.32	1.22	3.54	0.07
M42	551.21	32	3.49	26.83	0.35	1.04	8.03	0.10
M41	551.33	31.5	3.86	13.69	1.20	0.86	3.05	0.27
M40	551.44	31	2.83	16.33	0.55	0.65	3.76	0.13
M39	551.55	30.5						
M38	551.66	30						
M37	551.78	29.5	0.81	12.75	0.30	0.23	3.57	0.08
M36	552.34	27						

M35	552.56	26	0.23	12.01	0.44	0.05	2.88	0.11
M32	552.9	24.5						
M31	553.02	24	0.12	13.50	0.32	0.03	3.33	0.08
M30	553.24	23						
S22	553.35	22.5	0.28	13.98	0.29	0.08	3.75	0.08
S23	553.47	22						
M29	553.51	21.8						
S24	553.58	21.5						
S25	553.69	21						
S26	553.8	20.5	0.22	15.21	0.16	0.06	3.89	0.04
M27	553.89	20.1						
S27	553.92	20						
S28	554.03	19.5						
M26	554.12	19.1						
S29	554.14	19						
S30	554.25	18.5	0.24	13.71	1.21	0.06	3.62	0.32
S31	554.37	18						
S32	554.48	17.5						
S33	554.59	17						
M23	554.64	16.8						
S34	554.71	16.5	0.14	13.34	0.21	0.04	3.70	0.06
S35	554.82	16						
S36	554.93	15.5						
S37	555.04	15						
S38	555.16	14.5	0.13	13.40	0.29	0.03	3.41	0.07
S39	555.27	14						

S40 [↵]	555.38 [↵]	13.5 [↵]	↵	↵	↵	↵	↵	↵
S41 [↵]	555.49 [↵]	13 [↵]	↵	↵	↵	↵	↵	↵
S42 [↵]	555.61 [↵]	12.5 [↵]	0.25 ↵	14.37 ↵	0.60 ↵	0.06 ↵	3.46 ↵	0.14 ↵
S43 [↵]	555.72 [↵]	12 [↵]	↵	↵	↵	↵	↵	↵
M18 [↵]	555.72 [↵]	12 [↵]	↵	↵	↵	↵	↵	↵
S44 [↵]	555.83 [↵]	11.5 [↵]	↵	↵	↵	↵	↵	↵
S45 [↵]	555.94 [↵]	11 [↵]	↵	↵	↵	↵	↵	↵
S46 [↵]	556.06 [↵]	10.5 [↵]	↵	↵	↵	↵	↵	↵
S47 [↵]	556.17 [↵]	10 [↵]	0.18 ↵	13.95 ↵	0.47 ↵	0.05 ↵	3.82 ↵	0.13 ↵
S48 [↵]	556.26 [↵]	9.6 [↵]	↵	↵	↵	↵	↵	↵
S49 [↵]	556.39 [↵]	9 [↵]	↵	↵	↵	↵	↵	↵
S50 [↵]	556.51 [↵]	8.5 [↵]	0.19 ↵	15.06 ↵	0.09 ↵	0.05 ↵	3.95 ↵	0.02 ↵
M13 [↵]	556.62 [↵]	8 [↵]	↵	↵	↵	↵	↵	↵
S51 [↵]	556.67 [↵]	7.8 [↵]	↵	↵	↵	↵	↵	↵
M12 [↵]	556.73 [↵]	7.5 [↵]	0.09 ↵	11.85 ↵	0.39 ↵	0.02 ↵	3.13 ↵	0.10 ↵
S52 [↵]	556.85 [↵]	7 [↵]	↵	↵	↵	↵	↵	↵
M11 [↵]	556.91 [↵]	6.7 [↵]	↵	↵	↵	↵	↵	↵
S53 [↵]	556.98 [↵]	6.4 [↵]	0.16 ↵	12.78 ↵	2.34 ↵	0.04 ↵	3.09 ↵	0.57 ↵
M10 [↵]	557.09 [↵]	5.9 [↵]	↵	↵	↵	↵	↵	↵
S54 [↵]	557.12 [↵]	5.8 [↵]	↵	↵	↵	↵	↵	↵
M9 [↵]	557.18 [↵]	5.5 [↵]	↵	↵	↵	↵	↵	↵
S55 [↵]	557.23 [↵]	5.3 [↵]	0.16 ↵	12.93 ↵	0.17 ↵	0.04 ↵	3.14 ↵	0.04 ↵
M8 [↵]	557.3 [↵]	5 [↵]	↵	↵	↵	↵	↵	↵
S56 [↵]	557.32 [↵]	4.9 [↵]	0.13 ↵	12.15 ↵	0.18 ↵	0.03 ↵	3.20 ↵	0.05 ↵
M7 [↵]	557.41 [↵]	4.5 [↵]	↵	↵	↵	↵	↵	↵
S57 [↵]	557.43 [↵]	4.4 [↵]	↵	↵	↵	↵	↵	↵

S58 [↵]	557.52 [↵]	4 [↵]	0.19 [↵]	12.54 [↵]	0.52 [↵]	0.04 [↵]	2.95 [↵]	0.12 [↵]
M5 [↵]	557.63 [↵]	3.5 [↵]	[↵]	[↵]	[↵]	[↵]	[↵]	[↵]
S59 [↵]	557.75 [↵]	3 [↵]	0.14 [↵]	12.13 [↵]	1.49 [↵]	0.03 [↵]	3.05 [↵]	0.37 [↵]
S60 [↵]	557.86 [↵]	2.5 [↵]	0.16 [↵]	12.80 [↵]	0.57 [↵]	0.04 [↵]	3.05 [↵]	0.14 [↵]
M2 [↵]	557.95 [↵]	2.1 [↵]	[↵]	[↵]	[↵]	[↵]	[↵]	[↵]
S61 [↵]	557.97 [↵]	2 [↵]	[↵]	[↵]	[↵]	[↵]	[↵]	[↵]
S62 [↵]	558.06 [↵]	1.6 [↵]	0.07 [↵]	4.93 [↵]	0.12 [↵]	0.07 [↵]	5.05 [↵]	0.12 [↵]
S63 [↵]	558.2 [↵]	1 [↵]	[↵]	[↵]	[↵]	[↵]	[↵]	[↵]
S64 [↵]	558.29 [↵]	0.6 [↵]	0.07 [↵]	8.15 [↵]	0.33 [↵]	0.03 [↵]	3.97 [↵]	0.16 [↵]
S65 [↵]	558.42 [↵]	0 [↵]	[↵]	[↵]	[↵]	[↵]	[↵]	[↵]
S66 [↵]	558.47 [↵]	-0.2 [↵]	0.09 [↵]	11.11 [↵]	0.27 [↵]	0.04 [↵]	4.76 [↵]	0.12 [↵]
S67 [↵]	558.56 [↵]	-0.6 [↵]	6.53 [↵]	50.02 [↵]	2.15 [↵]	1.04 [↵]	8.00 [↵]	0.34 [↵]
S68 [↵]	558.65 [↵]	-1 [↵]	0.94 [↵]	37.60 [↵]	1.36 [↵]	0.15 [↵]	5.82 [↵]	0.21 [↵]
S69 [↵]	558.78 [↵]	-1.6 [↵]	0.75 [↵]	25.78 [↵]	1.09 [↵]	0.35 [↵]	12.00 [↵]	0.51 [↵]
S70 [↵]	558.92 [↵]	-2.2 [↵]	1.18 [↵]	15.48 [↵]	4.06 [↵]	0.50 [↵]	6.61 [↵]	1.74 [↵]
S71 [↵]	559.03 [↵]	-2.7 [↵]	0.10 [↵]	13.97 [↵]	0.49 [↵]	0.06 [↵]	7.43 [↵]	0.26 [↵]
S72 [↵]	559.12 [↵]	-3.1 [↵]	0.36 [↵]	12.32 [↵]	0.82 [↵]	0.13 [↵]	4.63 [↵]	0.31 [↵]
S74 [↵]	559.23 [↵]	-3.6 [↵]	[↵]	[↵]	[↵]	[↵]	[↵]	[↵]
S75 [↵]	559.28 [↵]	-3.8 [↵]	0.21 [↵]	15.37 [↵]	0.26 [↵]	0.04 [↵]	3.19 [↵]	0.05 [↵]
S76 [↵]	559.32 [↵]	-4 [↵]	[↵]	[↵]	[↵]	[↵]	[↵]	[↵]
S77 [↵]	559.37 [↵]	-4.2 [↵]	0.29 [↵]	8.43 [↵]	0.68 [↵]	0.06 [↵]	1.81 [↵]	0.15 [↵]
S80 [↵]	559.57 [↵]	-5.1 [↵]	0.30 [↵]	9.74 [↵]	0.60 [↵]	0.05 [↵]	1.69 [↵]	0.10 [↵]
S81 [↵]	559.82 [↵]	-6.2 [↵]	0.42 [↵]	9.34 [↵]	2.24 [↵]	0.09 [↵]	1.90 [↵]	0.46 [↵]
S82 [↵]	559.91 [↵]	-6.6 [↵]	0.29 [↵]	8.89 [↵]	0.29 [↵]	0.07 [↵]	2.03 [↵]	0.07 [↵]
S83 [↵]	560 [↵]	-7 [↵]	0.29 [↵]	8.55 [↵]	0.36 [↵]	0.08 [↵]	2.25 [↵]	0.10 [↵]
S84 [↵]	560.09 [↵]	-7.4 [↵]	0.25 [↵]	9.19 [↵]	0.32 [↵]	0.06 [↵]	2.18 [↵]	0.08 [↵]

S85↵	560.32↵	-8.4↵	0.37 ↵	9.49 ↵	0.23 ↵	0.10 ↵	2.46 ↵	0.06 ↵
S86↵	560.45↵	-9↵	0.26 ↵	8.24 ↵	3.73 ↵	0.07 ↵	2.07 ↵	0.94 ↵
S87↵	560.54↵	-9.4↵	↵	↵	↵	↵	↵	↵
S88↵	560.68↵	-10↵	0.30 ↵	9.60 ↵	0.39 ↵	0.06 ↵	2.07 ↵	0.08 ↵
S90↵	560.92↵	-11.1↵	0.30 ↵	8.50 ↵	0.18 ↵	0.09 ↵	2.54 ↵	0.05 ↵
S91↵	561.15↵	-12.1↵	0.28 ↵	10.49 ↵	0.26 ↵	0.06 ↵	2.42 ↵	0.06 ↵
S92↵	561.28↵	-12.7↵	↵	↵	↵	↵	↵	↵
S93↵	561.35↵	-13↵	0.34 ↵	9.14 ↵	0.25 ↵	0.15 ↵	4.03 ↵	0.11 ↵
S94↵	561.46↵	-13.5↵	↵	↵	↵	↵	↵	↵
S95↵	561.55↵	-13.9↵	↵	↵	↵	↵	↵	↵
S96↵	561.62↵	-14.2↵	0.26 ↵	10.63 ↵	0.58 ↵	0.12 ↵	4.94 ↵	0.27 ↵
S97↵	561.76↵	-14.8↵	↵	↵	↵	↵	↵	↵
S98↵	561.83↵	-15.1↵	0.31 ↵	11.09 ↵	0.48 ↵	0.09 ↵	3.29 ↵	0.14 ↵
16SS7↵	563.61↵	-23↵	↵	↵	↵	↵	↵	↵
16ss5.5↵	563.94↵	-24.5↵	↵	↵	↵	↵	↵	↵
16ss4↵	564.28↵	-26↵	↵	↵	↵	↵	↵	↵
16ss3↵	564.51↵	-27↵	↵	↵	↵	↵	↵	↵
16ss2↵	564.73↵	-28↵	↵	↵	↵	↵	↵	↵
16ss0.8↵	565↵	-29.2↵	↵	↵	↵	↵	↵	↵

Qinglinkou Section

GPS position: N30°47'45.22", E110°55'15.81"

Sample [↵]	Age [↵] (Ma) [↵]	Height [↵] (m) [↵]	U [↵] ppm [↵]	V [↵] ppm [↵]	Mo [↵] ppm [↵]	U/Sc [↵] w/w [↵]	V/Sc [↵] w/w [↵]	Mo/Sc [↵] w/w [↵]
Q218 [↵]	543.4 [↵]	302.9 [↵]	3.75 [↵]	9.85 [↵]	1.23 [↵]	1.05 [↵]	2.76 [↵]	0.35 [↵]
Q217 [↵]	543.56 [↵]	300.4 [↵]	[↵]	[↵]	[↵]	[↵]	[↵]	[↵]
Q216 [↵]	543.8 [↵]	296.9 [↵]	1.62 [↵]	6.30 [↵]	0.43 [↵]	0.42 [↵]	1.63 [↵]	0.11 [↵]
Q215 [↵]	543.91 [↵]	295.1 [↵]	[↵]	[↵]	[↵]	[↵]	[↵]	[↵]
Q214 [↵]	544.07 [↵]	292.8 [↵]	0.43 [↵]	6.84 [↵]	0.48 [↵]	0.10 [↵]	1.66 [↵]	0.12 [↵]
Q213 [↵]	544.36 [↵]	288.3 [↵]	[↵]	[↵]	[↵]	[↵]	[↵]	[↵]
Q212 [↵]	544.49 [↵]	286.4 [↵]	0.85 [↵]	6.19 [↵]	0.38 [↵]	0.25 [↵]	1.83 [↵]	0.11 [↵]
Q211 [↵]	545.41 [↵]	272.4 [↵]	[↵]	[↵]	[↵]	[↵]	[↵]	[↵]
Q210 [↵]	545.54 [↵]	270.5 [↵]	0.58 [↵]	6.51 [↵]	0.33 [↵]	0.14 [↵]	1.56 [↵]	0.08 [↵]
Q209 [↵]	545.8 [↵]	266.5 [↵]	1.17 [↵]	7.68 [↵]	3.19 [↵]	0.35 [↵]	2.32 [↵]	0.96 [↵]
Q208 [↵]	546 [↵]	263.5 [↵]	[↵]	[↵]	[↵]	[↵]	[↵]	[↵]
Q207 [↵]	546.16 [↵]	261 [↵]	1.19 [↵]	6.77 [↵]	0.25 [↵]	0.32 [↵]	1.83 [↵]	0.07 [↵]
Q206 [↵]	546.4 [↵]	257.4 [↵]	[↵]	[↵]	[↵]	[↵]	[↵]	[↵]
Q205 [↵]	546.58 [↵]	254.7 [↵]	1.23 [↵]	7.41 [↵]	0.49 [↵]	0.36 [↵]	2.13 [↵]	0.14 [↵]
Q204 [↵]	546.77 [↵]	251.9 [↵]	[↵]	[↵]	[↵]	[↵]	[↵]	[↵]
Q203 [↵]	546.91 [↵]	249.7 [↵]	0.55 [↵]	6.99 [↵]	0.20 [↵]	0.15 [↵]	1.89 [↵]	0.05 [↵]
Q202 [↵]	547.04 [↵]	247.7 [↵]	[↵]	[↵]	[↵]	[↵]	[↵]	[↵]
Q201 [↵]	547.34 [↵]	243.2 [↵]	1.54 [↵]	8.30 [↵]	0.45 [↵]	0.39 [↵]	2.12 [↵]	0.12 [↵]
Q200 [↵]	547.52 [↵]	240.4 [↵]	[↵]	[↵]	[↵]	[↵]	[↵]	[↵]
Q199 [↵]	547.65 [↵]	238.5 [↵]	2.27 [↵]	7.16 [↵]	0.31 [↵]	0.66 [↵]	2.07 [↵]	0.09 [↵]
Q198 [↵]	547.85 [↵]	235.4 [↵]	[↵]	[↵]	[↵]	[↵]	[↵]	[↵]
Q197 [↵]	548 [↵]	233.2 [↵]	1.00 [↵]	9.12 [↵]	0.22 [↵]	0.31 [↵]	2.83 [↵]	0.07 [↵]

Q196	548.13	231.2						
Q195	548.31	228.5	1.26	8.28	0.47	0.39	2.54	0.14
Q194	548.44	226.5						
QLKS8	548.62	223.8						
QLKS7	548.66	223.2						
QLKS6	548.7	222.5						
Q193	548.77	221.5	2.85	10.35	0.24	0.91	3.29	0.08
Q191	548.98	218.4						
Q190	549.08	216.8	0.80	9.92	0.83	0.26	3.20	0.27
Q189	549.18	215.3	1.41	9.84	1.16	0.39	2.68	0.32
Q188	549.28	213.8						
Q187	549.36	212.5	1.32	11.76	0.40	0.36	3.23	0.11
Q186	549.48	210.7	0.43	10.08	0.30	0.14	3.22	0.10
Q185	549.54	209.8	1.39	11.57	0.17	0.38	3.16	0.05
Q184	549.63	208.5	1.63	10.76	0.25	0.42	2.75	0.06
Q183	549.77	206.3	1.12	11.21	0.15	0.33	3.28	0.04
Q182	549.89	204.5						
Q181	550	202.9	1.35	10.17	0.71	0.34	2.56	0.18
Q180	550.1	201.4	1.21	11.34	0.20	0.46	4.29	0.07
Q179	550.18	200.2	0.57	8.03	0.22	0.17	2.41	0.07
Q178	550.25	199.1	0.82	9.89	0.55	0.23	2.82	0.16
Q177	550.31	198.1	0.67	8.35	0.21	0.19	2.33	0.06
Q176	550.43	196.3	2.48	13.55	0.47	0.75	4.10	0.14
Q175	550.5	195.3	2.03	14.48	2.90	0.55	3.89	0.78
Q174	550.59	194	0.63	9.02	0.47	0.19	2.79	0.15
Q173	550.68	192.5	1.38	12.39	0.26	0.48	4.31	0.09

Q172	550.76	191.3	0.88	12.76	0.33	0.32	4.58	0.12
Q171	550.86	189.8	1.20	22.35	0.52	0.56	10.49	0.24
Q170	550.93	188.8	0.40	10.41	0.24	0.23	5.96	0.14
Q169	551.05	187	0.38	10.65	0.43	0.24	6.62	0.27
Q168	551.1	186.2	0.15	8.76	0.16	0.10	5.47	0.10
Q163	556.6	178.4	1.11	21.32	0.32	0.30	5.86	0.09
Q160	556.89	175.9	0.46	14.46	0.41	0.12	3.70	0.10
Q158	557.76	167.4	1.78	22.70	0.21	0.44	5.65	0.05
Q157	558.02	164.9	0.68	11.67	0.44	0.32	5.53	0.21
Q156	558.53	159.9	1.31	10.60	0.28	0.58	4.68	0.13
Q154	558.75	157.8	0.46	38.24	0.14	0.20	16.56	0.06
Q153	559.45	151	0.85	45.76	0.09	0.32	17.17	0.03
Q152	559.72	148.3	0.92	30.09	0.27	0.33	10.95	0.10
Q151	559.77	147.8	0.80	17.25	0.13	0.35	7.55	0.05
Q150	559.86	147	0.93	17.19	0.12	0.36	6.62	0.05
Q149	560	145.6	0.36	13.77	0.16	0.13	5.01	0.06
Q148	560.18	143.8	0.33	22.65	0.34	0.11	7.46	0.11
Q147	560.37	142	0.12	12.52	3.75	0.05	4.88	1.46
Q145	560.57	140.1	0.10	12.55	0.18	0.04	4.62	0.07
Q144	560.79	137.9	0.32	10.04	0.28	0.10	3.14	0.09
Q143	560.87	137.1	0.08	8.71	0.12	0.03	3.29	0.04
Q142	561.02	135.7	0.14	9.83	0.07	0.05	3.26	0.02
Q141	561.15	134.4	0.10	9.05	0.13	0.04	3.56	0.05
Q140	561.34	132.6	0.95	10.41	0.09	0.33	3.60	0.03
Q139	561.63	129.7	0.40	9.49	0.30	0.15	3.61	0.12
Q138	561.77	128.4						

Q137↵	561.89↵	127.2↵	0.53 ↵	8.92 ↵	0.09 ↵	0.25 ↵	4.22 ↵	0.04 ↵
↵	↵	↵	↵	↵	↵	↵	↵	↵
Q73↵	568.74 ↵	105.2↵	0.18 ↵	10.03 ↵	0.21 ↵	0.08 ↵	4.73 ↵	0.10 ↵
Q72↵	571.23 ↵	101.2↵	0.24 ↵	9.97 ↵	0.40 ↵	0.11 ↵	4.43 ↵	0.18 ↵
Q71↵	571.92 ↵	100.1↵	↵	↵	↵	↵	↵	↵
Q70↵	572.67 ↵	98.9↵	0.69 ↵	12.71 ↵	0.18 ↵	0.30 ↵	5.48 ↵	0.08 ↵
Q69↵	576.35 ↵	93↵	0.35 ↵	8.54 ↵	0.24 ↵	0.18 ↵	4.35 ↵	0.12 ↵
Q68↵	576.91 ↵	92.1↵	↵	↵	↵	↵	↵	↵
Q67↵	577.78 ↵	90.7↵	↵	↵	↵	↵	↵	↵
Q66↵	578.53 ↵	89.5↵	0.17 ↵	9.05 ↵	0.18 ↵	0.08 ↵	4.18 ↵	0.08 ↵
Q61↵	583.58 ↵	81.4↵	0.39 ↵	9.23 ↵	0.39 ↵	0.17 ↵	4.00 ↵	0.17 ↵
Q59↵	586.14 ↵	77.3↵	0.26 ↵	7.44 ↵	0.22 ↵	0.10 ↵	3.00 ↵	0.09 ↵
Q57↵	590.13 ↵	70.9↵	0.20 ↵	10.22 ↵	0.41 ↵	0.08 ↵	3.91 ↵	0.16 ↵
Q56↵	596.05 ↵	61.4↵	↵	↵	↵	↵	↵	↵
Q55↵	596.43 ↵	60.8↵	0.12 ↵	11.19 ↵	0.17 ↵	0.04 ↵	4.10 ↵	0.06 ↵
Q52↵	600.35 ↵	54.5↵	↵	↵	↵	↵	↵	↵
Q51↵	600.73 ↵	53.9↵	0.21 ↵	9.51 ↵	0.20 ↵	0.07 ↵	3.19 ↵	0.07 ↵
Q47↵	606.22 ↵	45.1↵	↵	↵	↵	↵	↵	↵
Q45↵	607.34 ↵	43.3↵	↵	↵	↵	↵	↵	↵
Q43↵	608.09 ↵	42.1↵	0.09 ↵	8.55 ↵	0.14 ↵	0.03 ↵	2.44 ↵	0.04 ↵
Q41↵	608.68 ↵	41.15↵	↵	↵	↵	↵	↵	↵
Q39↵	608.80 ↵	40.95↵	0.20 ↵	7.07 ↵	0.73 ↵	0.06 ↵	2.29 ↵	0.24 ↵
Q36↵	610.42 ↵	38.35↵	↵	↵	↵	↵	↵	↵
Q35↵	611.11 ↵	37.25↵	0.11 ↵	10.46 ↵	0.42 ↵	0.03 ↵	2.35 ↵	0.09 ↵
Q32↵	614.54 ↵	31.75↵	↵	↵	↵	↵	↵	↵
Q31↵	615.54 ↵	30.15↵	0.22 ↵	10.59 ↵	0.31 ↵	0.04 ↵	1.95 ↵	0.06 ↵

Q30↵	616.41 ↵	28.75↵	↵	↵	↵	↵	↵	↵
Q29↵	616.79 ↵	28.15↵	↵	↵	↵	↵	↵	↵
Q28↵	617.10 ↵	27.65↵	↵	↵	↵	↵	↵	↵
Q27↵	617.91 ↵	26.35↵	0.25 ↵	7.75 ↵	0.37 ↵	0.09 ↵	2.68 ↵	0.13 ↵
Q26↵	618.34 ↵	25.65↵	↵	↵	↵	↵	↵	↵
Q24↵	619.53 ↵	23.75↵	↵	↵	↵	↵	↵	↵
Q23↵	620.09 ↵	22.85↵	0.05 ↵	6.41 ↵	0.34 ↵	0.01 ↵	1.72 ↵	0.09 ↵
Q22↵	620.65 ↵	21.95↵	↵	↵	↵	↵	↵	↵
Q21↵	621.34 ↵	20.85↵	↵	↵	↵	↵	↵	↵
Q20↵	622.09 ↵	19.65↵	↵	↵	↵	↵	↵	↵
Q19↵	622.65 ↵	18.75↵	0.09 ↵	7.76 ↵	0.23 ↵	0.02 ↵	1.57 ↵	0.05 ↵
Q17↵	624.27 ↵	16.15↵	↵	↵	↵	↵	↵	↵
Q15↵	625.17 ↵	14.7↵	0.07 ↵	7.56 ↵	0.38 ↵	0.02 ↵	2.22 ↵	0.11 ↵
Q14↵	626.01 ↵	13.35↵	↵	↵	↵	↵	↵	↵
Q13↵	626.83 ↵	12.05↵	↵	↵	↵	↵	↵	↵
Q12↵	627.26 ↵	11.35↵	0.06 ↵	9.04 ↵	0.20 ↵	0.02 ↵	2.77 ↵	0.06 ↵
Q11↵	627.76 ↵	10.55↵	↵	↵	↵	↵	↵	↵
Q10N↵	627.94 ↵	10.27↵	0.12 ↵	10.02 ↵	0.20 ↵	0.02 ↵	1.64 ↵	0.03 ↵
Q10↵	628.04 ↵	10.1↵	↵	↵	↵	↵	↵	↵
Q4↵	632.50 ↵	2.95↵	0.22 ↵	11.78 ↵	1.25 ↵	0.09 ↵	4.66 ↵	0.49 ↵
Q3↵	633.23 ↵	2.15↵	0.27 ↵	11.41 ↵	0.33 ↵	0.10 ↵	4.11 ↵	0.12 ↵
Q2↵	634.61 ↵	0.65↵	0.35 ↵	9.80 ↵	0.33 ↵	0.12 ↵	3.38 ↵	0.12 ↵
Q1↵	635.20 ↵	0↵	0.23 ↵	9.44 ↵	0.17 ↵	0.09 ↵	3.78 ↵	0.07 ↵

APPENDIX D: CARBON, OXYGEN, SULFUR, URANIUM ISOTOPES DATA

Lianghong Section

GPS: N29°04'53.2" E102°49'01.7"

Sample [↕]	Height [↕] (m) [↕]	$\delta^{13}\text{C}$ [↕] (‰) [↕]	$\delta^{18}\text{O}$ [↕] (‰) [↕]	$\delta^{238}\text{U}$ [↕] (‰) [↕]	$\delta^{34}\text{S}_{\text{CAS}}$ [↕] (‰) [↕]	[CAS] [↕] (ppm) [↕]	Carbonate [↕] (wt%) [↕]
LHC21.7 [↕]	49.7 [↕]	3.04 [↕]	-11.33 [↕]	-0.7 [↕]	[↕]	[↕]	86.56 [↕]
LHC21.0 [↕]	49 [↕]	2.3 [↕]	-8.1 [↕]	[↕]	[↕]	[↕]	88.83 [↕]
LHC20.0 [↕]	48 [↕]	1.3 [↕]	-10.4 [↕]	-0.63 [↕]	32.27 [↕]	30.77 [↕]	85.01 [↕]
LHC19.0 [↕]	47 [↕]	2.07 [↕]	-8.7 [↕]	[↕]	[↕]	[↕]	90.08 [↕]
LHC18.0 [↕]	46 [↕]	0.4 [↕]	-6.6 [↕]	-0.82 [↕]	[↕]	13.26 [↕]	92.35 [↕]
LHC17.0 [↕]	45 [↕]	1.9 [↕]	-8 [↕]	[↕]	[↕]	[↕]	81.09 [↕]
LHC16.0 [↕]	44 [↕]	1.8 [↕]	-8.5 [↕]	[↕]	[↕]	[↕]	83.37 [↕]
LHC15.0 [↕]	43 [↕]	1.8 [↕]	-8.7 [↕]	-0.46 [↕]	26.07 [↕]	30.67 [↕]	85.88 [↕]
LHC14.0 [↕]	42 [↕]	0.9 [↕]	-9 [↕]	[↕]	[↕]	[↕]	83.06 [↕]
LHC13.0 [↕]	41 [↕]	1.4 [↕]	-9.7 [↕]	[↕]	[↕]	[↕]	86.66 [↕]
LHC12.0 [↕]	40 [↕]	0.4 [↕]	-8 [↕]	-0.7 [↕]	[↕]	20.65 [↕]	84.37 [↕]
LHC11.0 [↕]	39 [↕]	-0.1 [↕]	-8.8 [↕]	[↕]	[↕]	[↕]	86.44 [↕]
LHC10.0 [↕]	38 [↕]	0.15 [↕]	-8.81 [↕]	-0.55 [↕]	[↕]	21.39 [↕]	87.49 [↕]
LHC9.0 [↕]	37 [↕]	-1.99 [↕]	-8.18 [↕]	[↕]	[↕]	[↕]	84.86 [↕]
LHC8.0 [↕]	36 [↕]	-1.74 [↕]	-7.85 [↕]	[↕]	[↕]	[↕]	65.62 [↕]
LHC7.1 [↕]	35.1 [↕]	-1.8 [↕]	-7.96 [↕]	[↕]	23.77 [↕]	46.02 [↕]	77.75 [↕]
LHC6.0 [↕]	34 [↕]	-2.54 [↕]	-8.45 [↕]	-0.63 [↕]	[↕]	[↕]	85.87 [↕]
LHC5.0 [↕]	33 [↕]	-6.1 [↕]	-8.73 [↕]	[↕]	24.97 [↕]	72.31 [↕]	84.7 [↕]
LHC4.0 [↕]	32 [↕]	-6.7 [↕]	-8.5 [↕]	-0.61 [↕]	16.26 [↕]	77.29 [↕]	75.96 [↕]
LHC3.5 [↕]	31.5 [↕]	-7.45 [↕]	-7.62 [↕]	[↕]	[↕]	[↕]	82.05 [↕]
LHC2.0 [↕]	30 [↕]	-9.6 [↕]	-9.24 [↕]	-0.34 [↕]	[↕]	[↕]	85.04 [↕]
LHC1.5 [↕]	29.5 [↕]	-7.51 [↕]	-8.96 [↕]	[↕]	[↕]	[↕]	76.72 [↕]
LHC1.1 [↕]	29.1 [↕]	-8.77 [↕]	-9.25 [↕]	-0.35 [↕]	[↕]	[↕]	83.8 [↕]
LHC0.6 [↕]	28.6 [↕]	-6.21 [↕]	-9.17 [↕]	-0.45 [↕]	27.76 [↕]	51.45 [↕]	88.46 [↕]
LHC-0.7 [↕]	27.3 [↕]	-8.07 [↕]	-9.14 [↕]	-0.43 [↕]	[↕]	[↕]	86.76 [↕]
LHC-1.1 [↕]	26.9 [↕]	-8.44 [↕]	-9.66 [↕]	[↕]	[↕]	[↕]	80.38 [↕]
LHA10.5 [↕]	26.5 [↕]	-8 [↕]	-10.1 [↕]	-0.46 [↕]	19.85 [↕]	78.36 [↕]	83.73 [↕]
LHA10.0 [↕]	26 [↕]	-8 [↕]	-10 [↕]	[↕]	[↕]	[↕]	62.03 [↕]
LHA9.5 [↕]	25.5 [↕]	-8 [↕]	-10 [↕]	[↕]	21.35 [↕]	26.32 [↕]	45.84 [↕]
LHA9.0 [↕]	25 [↕]	-8 [↕]	-10 [↕]	[↕]	[↕]	[↕]	82.2 [↕]
LHA8.5 [↕]	24.5 [↕]	-8 [↕]	-9.9 [↕]	-0.36 [↕]	18.49 [↕]	139.96 [↕]	87.19 [↕]
LHA8.0 [↕]	24 [↕]	-8.1 [↕]	-9.8 [↕]	[↕]	[↕]	[↕]	85.7 [↕]
LHA7.5 [↕]	23.5 [↕]	-8.1 [↕]	-9.9 [↕]	[↕]	21.1 [↕]	59.6 [↕]	60.3 [↕]
LHA7.0 [↕]	23 [↕]	-8.1 [↕]	-10 [↕]	-0.42 [↕]	[↕]	[↕]	74.49 [↕]
LHA6.5 [↕]	22.5 [↕]	-8.1 [↕]	-9.8 [↕]	[↕]	20.21 [↕]	78.84 [↕]	86.11 [↕]
LHA6.0 [↕]	22 [↕]	-8.1 [↕]	-10 [↕]	[↕]	19.25 [↕]	88.48 [↕]	88.09 [↕]
LHA5.5 [↕]	21.5 [↕]	-8.1 [↕]	-10.2 [↕]	-0.51 [↕]	19.72 [↕]	155.12 [↕]	86.57 [↕]
LHA5.0 [↕]	21 [↕]	-8.1 [↕]	-10.1 [↕]	[↕]	21.28 [↕]	183.38 [↕]	85.26 [↕]

LHA4.5 [±]	20.5 [±]	-8 [±]	-10.6 [±]	±	20.97 [±]	101.05 [±]	73.97 [±]
LHA4.0 [±]	20 [±]	-8.2 [±]	-11.2 [±]	±	±	±	84.99 [±]
LHA3.5 [±]	19.5 [±]	-8.2 [±]	-11.3 [±]	-0.45 [±]	20.17 [±]	181.94 [±]	83.81 [±]
LHA2.5 [±]	18.5 [±]	-8.3 [±]	-11.8 [±]	±	20.99 [±]	212.99 [±]	74.38 [±]
LHA1.9 [±]	17.9 [±]	-8.4 [±]	-12.2 [±]	-0.58 [±]	22.15 [±]	96.73 [±]	74.23 [±]
LHA1.0 [±]	17 [±]	-8.6 [±]	-13.2 [±]	±	±	±	83.05 [±]
LHA0.4 [±]	16.4 [±]	-7.8 [±]	-9.5 [±]	-0.22 [±]	±	±	88.93 [±]
LHA0.05 [±]	16.05 [±]	-4.9 [±]	-8.8 [±]	-0.46 [±]	±	±	92.92 [±]
LHA0.0 [±]	16 [±]	-4.3 [±]	-8.7 [±]	±	±	±	92.78 [±]
LHA-0.2 [±]	15.8 [±]	-4.2 [±]	-8.3 [±]	-0.35 [±]	±	±	93.02 [±]
LHA-1.0 [±]	15 [±]	-5.4 [±]	-8.4 [±]	±	±	±	91.74 [±]
LHA-1.6 [±]	14.4 [±]	-2.1 [±]	-8 [±]	-0.45 [±]	±	±	94.44 [±]
LHA-2.3 [±]	13.7 [±]	-1.9 [±]	-8.2 [±]	±	±	±	94.49 [±]
LHA-3.0 [±]	13 [±]	-2.2 [±]	-8.1 [±]	±	±	±	92.49 [±]
LHA-3.5 [±]	12.5 [±]	-1.6 [±]	-7.3 [±]	-0.46 [±]	±	15.08 [±]	92.12 [±]
LHA-4.0 [±]	12 [±]	-1.7 [±]	-8.1 [±]	±	±	±	56.93 [±]
LHA-4.5 [±]	11.5 [±]	-1.5 [±]	-8.2 [±]	±	±	23.9 [±]	90.63 [±]
LHA-5.0 [±]	11 [±]	-0.9 [±]	-8.1 [±]	±	±	±	55.03 [±]

Sishang Section

GPS: N32°51'05.7" E107°54'08.2"

Sample [↕]	Height [↕] (m) [↕]	$\delta^{13}\text{C}$ [↕] (‰) [↕]	$\delta^{18}\text{O}$ [↕] (‰) [↕]	$\delta^{238}\text{U}$ [↕] (‰) [↕]	$\delta^{34}\text{S}_{\text{CAS}}$ [↕] (‰) [↕]	[CAS] (ppm) [↕]	Carbonate [↕] (%) [↕]
S21 [↕]	124 [↕]	1.73 [↕]	-0.79 [↕]	[↕]	[↕]	[↕]	91.95 [↕]
S20 [↕]	122 [↕]	[↕]	[↕]	[↕]	[↕]	[↕]	93.11 [↕]
S19 [↕]	120 [↕]	[↕]	[↕]	[↕]	42.60 [↕]	33.82 [↕]	93.6 [↕]
S18 [↕]	118 [↕]	[↕]	[↕]	[↕]	[↕]	[↕]	91.7 [↕]
S17 [↕]	114 [↕]	[↕]	[↕]	[↕]	43.66 [↕]	31.22 [↕]	91.66 [↕]
S16 [↕]	112 [↕]	[↕]	[↕]	[↕]	[↕]	[↕]	92.25 [↕]
S15 [↕]	106 [↕]	[↕]	[↕]	[↕]	[↕]	[↕]	93 [↕]
S14 [↕]	104.2 [↕]	3.1 [↕]	-1.47 [↕]	[↕]	43.03 [↕]	64.26 [↕]	92.78 [↕]
S13 [↕]	102.2 [↕]	[↕]	[↕]	[↕]	42.64 [↕]	60.00 [↕]	92.67 [↕]
S12 [↕]	101.2 [↕]	[↕]	[↕]	[↕]	43.16 [↕]	72.94 [↕]	93.15 [↕]
S11 [↕]	99.9 [↕]	[↕]	[↕]	[↕]	42.71 [↕]	32.55 [↕]	94.11 [↕]
S10 [↕]	98.9 [↕]	[↕]	[↕]	[↕]	44.40 [↕]	88.01 [↕]	92.13 [↕]
S9 [↕]	97.4 [↕]	[↕]	[↕]	[↕]	0.00 [↕]	69.82 [↕]	90.34 [↕]
S8 [↕]	96.8 [↕]	1.95 [↕]	-1.39 [↕]	[↕]	42.31 [↕]	117.93 [↕]	90.62 [↕]
S7 [↕]	96.2 [↕]	[↕]	[↕]	[↕]	43.22 [↕]	78.08 [↕]	90.78 [↕]
S6 [↕]	95.5 [↕]	[↕]	[↕]	[↕]	[↕]	[↕]	89.99 [↕]
S5 [↕]	94.3 [↕]	[↕]	[↕]	[↕]	43.74 [↕]	131.97 [↕]	90.66 [↕]
S4 [↕]	93.6 [↕]	[↕]	[↕]	[↕]	45.00 [↕]	139.97 [↕]	91.07 [↕]
S3 [↕]	92.7 [↕]	[↕]	[↕]	[↕]	43.61 [↕]	202.10 [↕]	90.15 [↕]
S2 [↕]	92 [↕]	2.43 [↕]	-2.64 [↕]	[↕]	43.87 [↕]	60.16 [↕]	91.94 [↕]
S1 [↕]	91.5 [↕]	0.24 [↕]	-5.9 [↕]	[↕]	[↕]	[↕]	88.9 [↕]
M92 [↕]	75.4 [↕]	1.53 [↕]	-6.33 [↕]	-1 [↕]	30.83 [↕]	22.05 [↕]	91.47 [↕]
M91 [↕]	74.5 [↕]	[↕]	[↕]	[↕]	[↕]	[↕]	89.8 [↕]
M90 [↕]	73.6 [↕]	1.01 [↕]	-6.05 [↕]	[↕]	[↕]	[↕]	93.96 [↕]
M89 [↕]	73 [↕]	0.87 [↕]	-5.78 [↕]	[↕]	35.32 [↕]	57.53 [↕]	95.45 [↕]
M88 [↕]	71.5 [↕]	1.19 [↕]	-5.93 [↕]	[↕]	[↕]	[↕]	91.85 [↕]
M87 [↕]	70.4 [↕]	1.38 [↕]	-7.27 [↕]	-0.75 [↕]	34.62 [↕]	46.49 [↕]	96.47 [↕]
M86 [↕]	69.4 [↕]	[↕]	[↕]	[↕]	[↕]	[↕]	94.46 [↕]
M85 [↕]	68.8 [↕]	0.68 [↕]	-6.81 [↕]	[↕]	32.05 [↕]	22.77 [↕]	94.16 [↕]
M84 [↕]	67.6 [↕]	1 [↕]	-6.69 [↕]	[↕]	[↕]	[↕]	94.61 [↕]
M83 [↕]	67 [↕]	0.55 [↕]	-6.98 [↕]	-0.64 [↕]	31.50 [↕]	48.07 [↕]	107.32 [↕]
M82 [↕]	66 [↕]	[↕]	[↕]	[↕]	[↕]	[↕]	49.94 [↕]
M81 [↕]	64.4 [↕]	[↕]	[↕]	[↕]	[↕]	[↕]	96.29 [↕]
M80 [↕]	64 [↕]	0.98 [↕]	-7.18 [↕]	-0.69 [↕]	33.75 [↕]	43.79 [↕]	92.16 [↕]
M79 [↕]	63.7 [↕]	1.8 [↕]	-6.23 [↕]	[↕]	[↕]	[↕]	1.78 [↕]
M78 [↕]	63.4 [↕]	1.58 [↕]	-5.91 [↕]	[↕]	[↕]	[↕]	93.06 [↕]
M77 [↕]	62.9 [↕]	[↕]	[↕]	[↕]	[↕]	[↕]	76.12 [↕]
M76 [↕]	62.2 [↕]	[↕]	[↕]	[↕]	[↕]	[↕]	90.51 [↕]
M75 [↕]	61.7 [↕]	1.09 [↕]	-5.86 [↕]	[↕]	21.53 [↕]	94.46 [↕]	72.77 [↕]
M74 [↕]	61 [↕]	[↕]	[↕]	[↕]	[↕]	[↕]	93.95 [↕]
M73 [↕]	60 [↕]	1.33 [↕]	-5.45 [↕]	-0.35 [↕]	[↕]	[↕]	82.36 [↕]

M72	59.2				27.81	42.54	82.28
M71	55	0.74	-5.77		25.05	25.81	89.35
M70	54.2	0.9	-5.12	-0.58			100.15
M69	53.5				30.72	77.74	93.01
M68	52						92.05
M67	51				33.64	68.35	87.91
M66	50						73.94
M65	49	1.58	-5.03	-0.83			90.47
M64	47.5	-0.32	-5.72		29.35	53.45	91.4
M63	43.4			-0.84			89.5
M62	42.8	1.42	-5.74				86.58
M61	42.6				27.80	55.15	87.73
M60	42						94.28
M59	41.5	0.55	-6.05		26.44	70.86	89.52
M58	41						91.08
M56	40						95.68
M55	39.7	1.48	-6.34	-0.99	25.04	9.52	98.67
M54	39	1.7	-7.11				100.82
M53	38.4	-0.22	-8.15		28.91	48.34	98.56
M52	38.1	0.27	-7.49				81.72
M51	37.7	0.1	-8.22	-0.79			81.1
M49	36.5	1.92	-7.35				67.86
M48	35	-4.07	-7.66	-0.2			76.21
M46	34	-5.69	-7.65	-0.32			93.65
M45	33.5	-5.22	-6.05				99.07
M44	33						93.79
M43	32.5	-7.45	-8.3	-0.45	24.39	59.28	97.59
M42	32	-5.98	-6.85				81.46
M41	31.5	-7.4	-8.6				91.27
M40	31	-7.19	-7.98		20.68	67.28	95.1
M39	30.5	-7.34	-8.51				88.94
M38	30						90.39
M37	29.5	-8.04	-9		19.24	63.93	88.51
M36	27	-8.39	-9.96				91.13
M35	26	-8.64	-10.46		19.13	174.06	84.44
M32	24.5	-8.6	-10.49	-0.25	19.34	197.87	91.23
M31	24	-8.88	-8.96				89.12
M30	23	-8.72	-9.17				95.49
S22	22.5				19.77	84.63	82.83
S23	22	-8.71	-9.2		19.75	53.21	81.45
M29	21.8						90.09
S24	21.5	-8.52	-10.25	-0.47	20.06	77.10	82.93
S25	21	-8.65	-9.19		20.15	102.48	81.52
S26	20.5				20.01	85.00	83.8
M27	20.1						85.07

S27	20	-8.08	-9.31		20.18	107.00	84.31
S28	19.5	-8.68	-10.32		19.97	132.81	85.47
M26	19.1				20.15	110.09	82.13
S29	19	-8.75	-9.25		20.58	125.38	84.18
S30	18.5	-8.68	-10.26		19.85	84.34	84.55
S31	18	-8.71	-10.31		20.13	79.81	85.64
S32	17.5	-8.65	-10.36		19.90	109.72	79.41
S33	17	-8.69	-10.38		0.00	0.00	85.51
M23	16.8				19.70	109.76	87.42
S34	16.5	-8.77	-10.39	-0.36	19.61	142.25	85.01
S35	16	-8.64	-9.28		20.07	125.79	83.25
S36	15.5	-8.88	-10.41		19.67	144.96	85.56
S37	15	-8.87	-10.39		19.52	69.93	87.26
S38	14.5				19.75	127.67	84.88
S39	14	-8.89	-10.3				82.2
S40	13.5	-8.91	-10.62		19.73	126.12	85.53
S41	13	-8.58	-9.31		20.64	90.29	86.12
S42	12.5				20.28	94.16	86.8
S43	12	-8.58	-9.31		19.91	65.27	83
M18	12	-8.58	-9.31				72.6
S44	11.5	-8.99	-10.59		19.49	65.47	87.79
S45	11	-9.03	-10.56		20.07	175.10	85.78
S46	10.5	-9.08	-10.38		20.59	127.70	86.52
S47	10	-8.32	-9.2		20.54	84.42	87.64
S48	9.6	-9.15	-10.57	-0.38	20.13	136.69	87.49
S49	9	-9.17	-10.61		20.18	125.76	93.18
S50	8.5	-9.14	-10.93		20.10	93.23	87.24
M13	8	-9.4	-10.88		21.28	36.26	87.57
S51	7.8				20.40	46.06	84.81
M12	7.5	-9.6	-11.21		21.42	86.52	89.22
S52	7	-8.2	-9.2		20.43	83.25	84.78
M11	6.7	-9.46	-10.81				86.12
S53	6.4				21.40	75.38	85.57
M10	5.9	-9.49	-10.95				86.13
S54	5.8						88.15
M9	5.5	-9.51	-10.96		21.09	49.66	85.78
S55	5.3				20.91	114.93	87.51
M8	5	-8.08	-9.31		20.91	100.24	87.86
S56	4.9				21.27	60.99	85
M7	4.5	-9.72	-11.23		20.74	88.87	89.01
S57	4.4						88.82
S58	4	-9.77	-11.19		21.67	125.20	85.38
M5	3.5	-9.86	-11.18		21.09	72.87	88.86
S59	3	-8.76	-9.02		20.16	105.00	87.07
S60	2.5	-9.91	-11.08	-0.41	20.45	61.96	87.62

M2 [±]	2.1 [±]	±	±	±	21.54 [±]	64.08 [±]	85.42 [±]
S61 [±]	2 [±]	-8.36 [±]	-9.32 [±]	±	18.77 [±]	167.79 [±]	86.47 [±]
S62 [±]	1.6 [±]	-9.78 [±]	-12.21 [±]	±	21.87 [±]	171.17 [±]	61.32 [±]
S63 [±]	1 [±]	-9.99 [±]	-11.31 [±]	±	22.81 [±]	138.87 [±]	54.23 [±]
S64 [±]	0.6 [±]	-10.05 [±]	-11.46 [±]	±	23.23 [±]	72.27 [±]	62.02 [±]
S65 [±]	0 [±]	-8.23 [±]	-9.3 [±]	±	±	±	66.12 [±]
S66 [±]	-0.2 [±]	±	±	±	27.20 [±]	23.89 [±]	70.62 [±]
S67 [±]	-0.6 [±]	±	±	-0.12 [±]	±	±	84.73 [±]
S68 [±]	-1 [±]	-7.95 [±]	-6.42 [±]	-0.67 [±]	±	±	85.35 [±]
S69 [±]	-1.6 [±]	-8.81 [±]	-6.34 [±]	±	±	±	73.24 [±]
S70 [±]	-2.2 [±]	±	±	±	±	±	77.95 [±]
S71 [±]	-2.7 [±]	±	±	±	±	±	79.38 [±]
S72 [±]	-3.1 [±]	-10.82 [±]	-5.68 [±]	±	±	±	66.21 [±]
S74 [±]	-3.6 [±]	±	±	±	±	±	79.03 [±]
S75 [±]	-3.8 [±]	±	±	±	±	±	84.07 [±]
S76 [±]	-4 [±]	-6.2 [±]	-5.49 [±]	-0.5 [±]	±	±	97.51 [±]
S77 [±]	-4.2 [±]	±	±	±	±	±	86.72 [±]
S80 [±]	-5.1 [±]	-3.33 [±]	-8.45 [±]	-0.52 [±]	±	±	100.73 [±]
S81 [±]	-6.2 [±]	0.99 [±]	-8.38 [±]	±	±	±	100.08 [±]
S82 [±]	-6.6 [±]	±	±	±	±	±	90.01 [±]
S83 [±]	-7 [±]	0.86 [±]	-8.25 [±]	-0.68 [±]	±	±	89.97 [±]
S84 [±]	-7.4 [±]	±	±	±	±	±	97.64 [±]
S85 [±]	-8.4 [±]	±	±	±	±	±	90.29 [±]
S86 [±]	-9 [±]	1.84 [±]	-7.98 [±]	-0.82 [±]	±	±	86.39 [±]
S87 [±]	-9.4 [±]	±	±	±	±	±	95.73 [±]
S88 [±]	-10 [±]	2.56 [±]	-8.06 [±]	±	±	±	97.68 [±]
S90 [±]	-11.1 [±]	2.53 [±]	-8.01 [±]	±	±	±	88.95 [±]
S91 [±]	-12.1 [±]	3.02 [±]	-7.97 [±]	±	±	±	95.11 [±]
S92 [±]	-12.7 [±]	±	±	±	±	±	75.66 [±]
S93 [±]	-13 [±]	3.48 [±]	-7.98 [±]	±	±	±	68.94 [±]
S94 [±]	-13.5 [±]	±	±	±	±	±	96.32 [±]
S95 [±]	-13.9 [±]	3.48 [±]	-7.85 [±]	±	±	±	67.06 [±]
S96 [±]	-14.2 [±]	±	±	±	±	±	74.18 [±]
S97 [±]	-14.8 [±]	4.27 [±]	-7.82 [±]	±	±	±	92.82 [±]
S98 [±]	-15.1 [±]	1.94 [±]	-6 [±]	±	±	±	87.81 [±]
16SS7 [±]	-23 [±]	-0.49 [±]	-7.76 [±]	±	±	±	95.61 [±]
16ss5.5 [±]	-24.5 [±]	±	±	±	±	±	89.26 [±]
16ss4 [±]	-26 [±]	1.61 [±]	-7.61 [±]	±	±	±	82.49 [±]
16ss3 [±]	-27 [±]	4.52 [±]	-8.26 [±]	±	±	±	89.63 [±]
16ss2 [±]	-28 [±]	1.65 [±]	-7.19 [±]	±	±	±	69 [±]
16ss0.8 [±]	-29.2 [±]	±	±	±	±	±	63.61 [±]

Qinglinkou Section

GPS: N30°47'45.22", E110°55'15.81"

Sample	Height (m)	$\delta^{13}\text{C}$ (‰)	$\delta^{18}\text{O}$ (‰)	$\delta^{238}\text{U}$ (‰)	$\delta^{34}\text{S}_{\text{CAS}}$ (‰)	[CAS] (ppm)	Carbonate (%)
Q218	302.9	2.43	-7.05		45.61	43.51	99.56
Q217	300.4	3.12	-5.7				94.7
Q216	296.9	3.05	-6.24		42.61	25.13	101.14
Q215	295.1	3.25	-6.18				93
Q214	292.8	2.79	-6.38				101.36
Q213	288.3	2.66	-7.7	-1.35			97.54
Q212	286.4	2.39	-7.59				91
Q211	272.4	3.26	-7.22				88.54
Q210	270.5	4.13	-8.02				93.5
Q209	266.5	2.45	-5.94	-1.34	49.89	74.23	92.02
Q208	263.5	3.82	-6.03				101.28
Q207	261	3.4	-6.83				89.57
Q206	257.4	4.07	-5.16				88.18
Q205	254.7	3.13	-6.3				93.91
Q204	251.9	2.1	-7.16		42.86	12.64	96.08
Q203	249.7	3.34	-7.84				94.33
Q202	247.7	2.64	-7.18				97.87
Q201	243.2	2.96	-5.48				96.84
Q200	240.4	3.55	-5.62		39.18	32.61	94.3
Q199	238.5	2.74	-6.43				90.1
Q198	235.4	3.77	-5.66				96.63
Q197	233.2	3.86	-5.69				96.26
Q196	231.2	3.08	-6.05				100.07
Q195	228.5	3.16	-6.47		40.02	22.15	95.3
Q194	226.5	2.63	-7.03		44.39	75.88	92.15
QLKS8	223.8				43.81	48.05	95.25
QLKS7	223.2				43.74	67.48	93.83
QLKS6	222.5				46.79	53.42	95.8
Q193	221.5	3.06	-5.16		46.81	82.8	96.25
Q191	218.4	3.74	-5.63				90.74
Q190	216.8	3.65	-4.89				92.15
Q189	215.3	3.3	-5.1		53.57	142.54	100
Q188	213.8	4.32	-4.16				98.49
Q187	212.5	4.07	-4.94	-1.02	56.17	104.09	95.61
Q186	210.7	4.79	-4.31				96.88
Q185	209.8	2.7	-5.64	-1.18	51.18	135.66	97.51
Q184	208.5	3	-7.65	-1.18	47.72	164.65	93.7
Q183	206.3	5.15	-4.54				92.13
Q182	204.5	1.93	-10.36		47.59	67.24	87.8
Q181	202.9	2.52	-6.88				97.88
Q180	201.4	4.2	-4.35				94.5

Q179	200.2	4.5	-5.2				95.34
Q178	199.1	3.96	-4.72	-1.22			97.08
Q177	198.1	3.78	-4.35				98.47
Q176	196.3	2.57	-5.58		43.95	307.44	84.79
Q175	195.3	2.98	-5.31				99.76
Q174	194	3.67	-4.47	-1.15			88.1
Q173	192.5	3.25	-6.06				88.64
Q172	191.3	3.01	-7.37		49.06	74.35	90.64
Q171	189.8	0.86	-6.06				94.74
Q170	188.8	-0.33	-5.99		35.48	19.79	84.71
Q169	187	-1.23	-5.64	-1.02			72.81
Q168	186.2	-3.1	-5.51				68.09
Q163	178.4	-4.6	-1.54		30.72	67.24	87.52
Q160	175.9	1.81	-2.09		37.55	146.74	86.4
Q158	167.4	1.29	-2.61				88.06
Q157	164.9	2.97	-1.03		43.52	24.09	90.86
Q156	159.9	1.21	-1.12		42.16	101.01	94.83
Q154	157.8	-1.26	-1.51		33.64	91	82.73
Q153	151	-2.51	-2.32	-0.6	33.6	100.73	76.67
Q152	148.3	-1.09	-2.86	-0.98	34.42	47.29	75.31
Q151	147.8	-0.96	-4.9				97.04
Q150	147	0.06	-4.32		34.37	26.45	91.06
Q149	145.6	0	-5.07	-0.93	35.04	35.78	92.65
Q148	143.8	0.2	-4.08	-1.02	34.74	23.95	94.17
Q147	142	0.36	-6.04				89.93
Q145	140.1	2.51	-5.52				87
Q144	137.9	3.44	-4.9	-1.04	36.86	73.19	83.95
Q143	137.1	4.17	-3.92		39.04	135.46	76.49
Q142	135.7	4.4	-4.06		40.57	170.89	82.6
Q141	134.4	4.44	-4.18				79.51
Q140	132.6	4.29	-2.71		35.72	319.24	76.73
Q139	129.7	3.7	-4.43		36.69	440.52	80.41
Q138	128.4	3.87	-2.87	-1.13	34.76	470.82	77.43
Q137	127.2	2.03	-4.22		37.96	219.77	81.1
Q73	105.2	1.5	-2.18				71.63
Q72	101.2	1.25	-2.56				79.71
Q71	100.1	0.73	-2.54				67.39
Q70	98.9	0.33	-2.69	-1.25			75.21
Q69	93	-0.17	-3.05				64.15
Q68	92.1	-0.99	-1.94				76.99
Q67	90.7	1.33	-2.98				74.83
Q66	89.5	1.02	-3.39				69.97
Q61	81.4	2.98	-4.36				64.37
Q59	77.3	2.68	-4.44				54.62

Q57 [±]	70.9 [±]	1.37 [±]	-4.55 [±]	±	±	±	71.03 [±]
Q56 [±]	61.4 [±]	3.06 [±]	-5.77 [±]	±	±	±	60.61 [±]
Q55 [±]	60.8 [±]	2.67 [±]	-4.42 [±]	±	±	±	81.9 [±]
Q52 [±]	54.5 [±]	2.58 [±]	-4.99 [±]	±	±	±	61.1 [±]
Q51 [±]	53.9 [±]	±	±	±	36.52 [±]	225.290 [±]	61.33 [±]
Q47 [±]	45.1 [±]	0.89 [±]	-2.4 [±]	±	34.01 [±]	71.887 [±]	75.54 [±]
Q45 [±]	43.3 [±]	0.68 [±]	-10.17 [±]	±	±	±	75.96 [±]
Q43 [±]	42.1 [±]	-0.03 [±]	-10.84 [±]	±	±	±	63.14 [±]
Q41 [±]	41.15 [±]	-1.92 [±]	-10.66 [±]	±	±	±	51.93 [±]
Q39 [±]	40.95 [±]	-2.01 [±]	-10.17 [±]	±	±	±	48.1 [±]
Q36 [±]	38.35 [±]	-5.02 [±]	-8.43 [±]	±	±	±	57.06 [±]
Q35 [±]	37.25 [±]	-1.69 [±]	-8.11 [±]	±	±	±	51.83 [±]
Q32 [±]	31.75 [±]	1.18 [±]	-4.04 [±]	-0.51 [±]	±	±	41.77 [±]
Q31 [±]	30.15 [±]	-3.37 [±]	-7.86 [±]	±	±	±	72.71 [±]
Q30 [±]	28.75 [±]	0.87 [±]	-5.63 [±]	±	±	±	40.97 [±]
Q29 [±]	28.15 [±]	1.6 [±]	-4.06 [±]	±	±	±	58.77 [±]
Q28 [±]	27.65 [±]	0.98 [±]	-5.65 [±]	±	±	±	56.61 [±]
Q27 [±]	26.35 [±]	1.48 [±]	-7.87 [±]	±	±	±	47.42 [±]
Q26 [±]	25.65 [±]	-0.27 [±]	-5.11 [±]	±	±	±	46.39 [±]
Q24 [±]	23.75 [±]	-6.99 [±]	-10.92 [±]	±	±	±	82.35 [±]
Q23 [±]	22.85 [±]	±	±	±	±	±	53.35 [±]
Q22 [±]	21.95 [±]	0.84 [±]	-4.83 [±]	±	±	±	32.76 [±]
Q21 [±]	20.85 [±]	1.44 [±]	-3.79 [±]	±	±	±	41.06 [±]
Q20 [±]	19.65 [±]	2.67 [±]	-2.13 [±]	±	±	±	55.45 [±]
Q19 [±]	18.75 [±]	0.46 [±]	-4.86 [±]	±	±	±	51.22 [±]
Q17 [±]	16.15 [±]	2.41 [±]	-2.24 [±]	±	±	±	33.83 [±]
Q15 [±]	14.7 [±]	1.71 [±]	-3.55 [±]	±	±	±	53.14 [±]
Q14 [±]	13.35 [±]	1.59 [±]	-4.62 [±]	±	±	±	46.88 [±]
Q13 [±]	12.05 [±]	2.79 [±]	-2.14 [±]	±	±	±	54.01 [±]
Q12 [±]	11.35 [±]	4.22 [±]	-0.94 [±]	±	±	±	39.31 [±]
Q11 [±]	10.55 [±]	1.3 [±]	-4.21 [±]	±	±	±	49.73 [±]
Q10N [±]	10.27 [±]	-9.28 [±]	-12.51 [±]	±	±	±	59.83 [±]
Q10 [±]	10.1 [±]	±	±	±	±	±	44.23 [±]
Q4 [±]	2.95 [±]	-4.42 [±]	-7.79 [±]	-0.73 [±]	±	±	86.28 [±]
Q3 [±]	2.15 [±]	-3.91 [±]	-8.11 [±]	±	±	±	88.17 [±]
Q2 [±]	0.65 [±]	-3.12 [±]	-7.81 [±]	-0.95 [±]	±	±	84.5 [±]
Q1 [±]	0 [±]	-2.94 [±]	-6.72 [±]	±	35.65 [±]	111.527 [±]	83 [±]